

博士論文

A study on thermal radiation control by  
microstructures and phase-change materials  
(微細構造と相転移材料を用いた熱輻射  
制御に関する研究)

東京大学大学院 工学系研究科 先端学際工学専攻  
37-137284

伊藤 晃太



博士論文

A study on thermal radiation control by microstructures and  
phase-change materials

(微細構造と相転移材料を用いた熱輻射制御に関する研究)

Kota Ito

伊藤 晃太

in

Department of Advanced Interdisciplinary Studies

先端学際工学専攻

in

Graduate School of Engineering

工学系研究科

of

The University of Tokyo

東京大学大学院

Supervisor:

Professor Hiroshi Toshiyoshi

年吉洋教授

June 2016



# Abstract

This work deals with a study on thermal radiation control, which is enabled by using subwavelength structures or phase-change materials. Thermal radiation is one of the three heat transfer modes, and its control opens possibilities in various applications such as thermophotovoltaics, thermal management, and mid-infrared light sources. In this study, four types of thermal radiation control, namely dynamic control, monochromatic light source, thermal rectification, and near-field thermal radiation are investigated theoretically and/or experimentally, toward mid-infrared light source for chemical sensing and thermal management in artificial satellites.

Firstly, a novel coupling mechanism between surface waves and guided mode resonances are theoretically proposed for dynamic thermal radiation control. A developed modal analysis shows that the guided mode in a silicon grating couples to the surface phonon polariton on a silicon carbide substrate or surface plasmon polariton on a doped silicon slab via evanescent waves. The modulation of the grating height from  $36.2\ \mu\text{m}$  to  $37.3\ \mu\text{m}$  allows us to control emissivity with an amplitude larger than 0.9 at a wavelength of  $12.13\ \mu\text{m}$ . Such a dynamic modulation improves the signal-to-noise ratio of infrared chemical sensing.

Secondary, a quasi-monochromatic incandescent light source is demonstrated theoretically and experimentally. The proximity interaction between densely-placed metal-insulator-metal (MIM) metamaterial resonators enables the suppression of the parasitic modes. The integrated parasitic heat flux decreases from  $11.8\ \text{Wsr}^{-1}\text{m}^{-2}$  to  $4.0\ \text{Wsr}^{-1}\text{m}^{-2}$  at an angle of  $60^\circ$  by adopting densely-tiled square resonators. The mechanism of the suppression is theoretically investigated, and the measured thermal emission

spectra of the fabricated metamaterial verify the presented suppression. Such a quasi-monochromatic source contributes the design of non-dispersed infrared sensing (NDIR) systems.

Thirdly, radiative thermal rectifiers are developed based on the phase-change of vanadium dioxide ( $\text{VO}_2$ ).  $\text{VO}_2$  in the insulating state works as a good infrared absorber in the forward scenario, while it in the metallic state works as an emitter with low efficiency in the reverse scenario. The variation of the optical response between the insulating and the metallic states enables a high thermal rectification contrast ratio of 2 in our measurement system. The presented thermal rectification will allow novel thermal management systems.

Finally, a methodology to form submicron gaps for near-field thermal radiation is proposed. Microfabricated spacers with a height of 0.5  $\mu\text{m}$ , 1  $\mu\text{m}$ , or 2  $\mu\text{m}$ , are employed to determine the gap width between opposing substrates with an area of  $19 \times 8.6$  mm. Applied pressure as high as 6 kPa compensates the intrinsic mechanical deflection of substrates to keep a uniform gap, while the planarity of the gap is monitored by optical reflection spectra. The proposed methodology is applicable to thermal management utilizing photon-tunneling.

The achievements obtained for the four types of thermal radiation control will contribute to scientific communities as well as industrial implementations. Especially, dynamic and monochromatic mid-infrared light source for NDIR and thermal management system for artificial satellites will be realized. Moreover, the achievements in this thesis open a pathway to more versatile thermal radiation control.

|  |    |
|--|----|
| <i>Chapter 1 Introduction</i> .....  | 1  |
| 1.1 Background.....  | 2  |
| 1.1.1 Thermal radiation.....   | 2  |
| 1.1.2 Application of thermal radiation control.....                          | 6  |
| 1.1.2.1 Thermophotovoltaics .....  | 6  |
| 1.1.2.2 Light source.....  | 7  |
| 1.1.2.3 Radiative cooling .....  | 8  |
| 1.1.2.4 Radiative heating .....  | 9  |
| 1.2. Justification of this work.....   | 10 |
| 1.3. Purpose of this work .....  | 12 |
| 1.4. Originality of this work.....   | 14 |
| 1.5. Thesis organization.....  | 15 |
| <i>Chapter 2 Theory and methodologies</i> .....                              | 23 |
| 2.1. Theory of thermal radiation.....  | 24 |
| 2.1.1 Maxwell's equation and electric current density .....                  | 24 |
| 2.1.2 Spectral intensity and spectral power.....                             | 26 |
| 2.1.3 Emissivity and Kirchhoff's law.....                                    | 27 |
| 2.1.4 View factor .....  | 28 |
| 2.2 Simulation of electromagnetic wave .....                                 | 30 |
| 2.2.1 Multilayered system: Transmission matrix method .....                  | 32 |
| 2.2.2 Multilayered system: scattering matrix method .....                    | 34 |
| 2.2.3 Grating: modal analysis and rigorous coupled wave analysis (RCWA)..... | 36 |
| 2.2.4 Near-field radiative heat transfer.....                                | 41 |
| 2.3 Microfabrication technologies.....                                       | 45 |

|   |           |
|---|-----------|
| 2.3.1 Lithography techniques .....  | 45        |
| 2.3.2 Etching techniques.....   | 48        |
| 2.4 Evaluation methodologies.....   | 49        |
| 2.4.1 Fourier-transform infrared spectroscopy (FT-IR).....                                | 50        |
| 2.4.2 Steady-state heat flux measurement system.....                                      | 51        |
| 2.5 Chapter summary .....   | 54        |
| <i>Chapter 3 Dynamic modulation of thermal radiation .....</i>                            | <i>57</i> |
| 3.1. Introduction.....  | 58        |
| 3.1.1 Motivation .....  | 58        |
| 3.1.2 Preceding works on emissivity control by subwavelength structures.....              | 59        |
| 3.2 Coupling of guided mode resonance and surface polariton .....                         | 61        |
| 3.2.1 Guided mode resonance (GMR).....  | 62        |
| 3.2.2 Surface polariton .....   | 63        |
| 3.3 Thermal emitter with surface phonon polariton (SPhP) .....                            | 64        |
| 3.3.1 Permittivity of silicon carbide (SiC).....  | 64        |
| 3.3.2 Structure of the thermal emitter.....   | 66        |
| 3.3.3 Modal analysis formalism .....  | 67        |
| 3.3.4 Magnetic field at resonance .....   | 69        |
| 3.3.5 Emissivity profile .....  | 71        |
| 3.3.6 Distance-dependent emissivity and dynamic modulation of thermal radiation.....      | 73        |
| 3.3.7 Asymmetric emission.....  | 75        |
| 3.4 Thermal emitter with surface plasmon polariton (SPP).....                             | 78        |
| 3.4.1 Permittivity of doped silicon and the dispersion of surface plasmon polariton ..... | 78        |
| 3.4.2 Structure of thermal emitter.....   | 80        |

|  |     |
|--|-----|
| 3.4.3 Magnetic field at resonance .....  | 82  |
| 3.4.4 Thermal radiation spectra .....  | 83  |
| 3.4.5 Possible fabrication process.....  | 85  |
| 3.4.6 Electrostatic actuation of the distance between the grating and the slab.....    | 86  |
| 3.5 Discussion on the sharpness of the resonance .....                                 | 87  |
| 3.6 Chapter summary .....  | 89  |
| <i>Chapter 4 Monochromatic thermal emitter</i> .....                                   | 97  |
| 4.1 Introduction.....  | 98  |
| 4.1.1 Motivation .....   | 98  |
| 4.1.2 Metal-insulator-metal (MIM) metamaterial.....                                    | 98  |
| 4.1.3 Fundamental and parasitic mode.....  | 100 |
| 4.1.4 Focus of this chapter .....  | 103 |
| 4.2 Second-order control by a diagonal arrangement .....                               | 104 |
| 4.2.1 Geometry.....  | 104 |
| 4.2.2 Second-order resonance control .....   | 105 |
| 4.2.3 Asymmetrically-shifted resonators .....  | 108 |
| 4.3 Densely placed square resonators .....   | 110 |
| 4.3.1 Geometry.....  | 110 |
| 4.3.2 Parasitic control toward monochromatic emission.....                             | 110 |
| 4.3.3 Gap dependence .....   | 115 |
| 4.4 Experimental investigations .....  | 116 |
| 4.4.1 Fabrication of the metamaterials .....   | 116 |
| 4.4.2 Reflection spectra of diagonally arranged metamaterials.....                     | 117 |
| 4.4.3 Thermal radiation and reflection spectra of densely-placed square emitters ..... | 120 |

|   |     |
|---|-----|
| 4.5 Chapter summary .....   | 124 |
| <i>Chapter 5 Thermal rectification</i> .....  | 131 |
| 5.1. Introduction .....   | 132 |
| 5.2. Phase-change material .....  | 133 |
| 5.3. Proposal of the thermal rectifier based on the phase-change of VO <sub>2</sub> ..... | 135 |
| 5.4. Deposition of the VO <sub>2</sub> film .....   | 136 |
| 5.5. Analysis of infrared response .....  | 137 |
| 5.6. Numerical prediction of heat flux .....  | 139 |
| 5.7. Heat flux measurement .....  | 141 |
| 5.8. Tailoring the operation temperature range .....                                      | 144 |
| 5.9. Chapter summary .....  | 146 |
| <i>Chapter 6 Near-field radiative heat transfer</i> .....                                 | 151 |
| 6.1. Introduction .....   | 152 |
| 6.2. Gap formation methodology .....  | 156 |
| 6.2.1. Analysis of heat transfer .....  | 156 |
| 6.2.2. Evaluation of the wafer surface .....  | 157 |
| 6.2.3. Selection of spacer material .....   | 160 |
| 6.2.4. Microfabrication of spacers .....  | 161 |
| 6.2.5. Mechanical tolerance of spacers .....  | 164 |
| 6.3. Evaluation of the gap .....  | 165 |
| 6.3.1. Optical setup .....  | 165 |
| 6.3.2. Interferometric optical spectra .....  | 166 |
| 6.4. Developed apparatus .....  | 168 |
| 6.5. Measurement of the heat flux across the gap .....                                    | 169 |

|   |     |
|---|-----|
| 6.5.1. Calibration of the thermal series resistance ( $R_S$ ).....            | 169 |
| 6.5.2. Heat flux as a function of temperature difference .....                | 171 |
| 6.5.3. Heat transfer coefficient .....  | 172 |
| 6.6. Discussion.....  | 173 |
| 6.7. Chapter summary.....   | 175 |
| <i>Chapter 7 Discussion and Conclusion</i> .....                              | 181 |
| 7.1 Summary of this work.....   | 182 |
| 7.2 Comparison with other works.....  | 184 |
| 7.3 Discussion on the fabrication error.....                                  | 186 |
| 7.4 Significant implication of this work and future research directions ..... | 189 |
| 7.4.1 Mid-infrared light source for NDIR.....                                 | 189 |
| 7.4.2 Thermal management in artificial satellites .....                       | 190 |
| 7.5 Conclusion.....   | 194 |
| <i>Publications</i> .....   | 199 |
| <i>Acknowledgements</i> .....   | 203 |



## *Chapter 1 Introduction*

This chapter introduces the work in a general view. This chapter begins from a review of the basic characteristics of thermal radiation. The concept of the emissivity and near-field radiative heat transfer are explained. The application of thermal radiation control spans from mid-infrared light source to thermal management, and they are discussed in detail. Four types of thermal radiation control, namely dynamic modulation, monochromatic emission, thermal rectification, and near-field radiative heat transfer, are tackled in this work for mid-infrared light source for chemical sensing and thermal management in artificial satellites. The justification, the purpose, and the originality of the work are explained for the four types of thermal radiation control. Finally, the organization of this thesis is described.

## 1.1 Background

### 1.1.1 Thermal radiation

Thermal radiation or radiative heat transfer [1][2] is one of the three principal mechanisms of heat transfer. It is mediated by the transport of electromagnetic waves, unlike the other two mechanisms, namely convection and conduction, each of which needs materials to transport heat. In all the materials having finite temperature, electrons and atoms are thermally agitated, resulting in electromagnetic emission to the surroundings. For example, it is well known that the sunlight is thermal radiation from the sun, whose surface temperature is around 5800 K. In everyday life, we feel thermal radiation from incandescent lamps, infrared heaters, and wood-fire ovens. In nature, snakes have organs that are sensitive to infrared radiation, thus they can detect radiative heat from homeothermic animals [3].

The investigation of the radiation spectrum opened the era of quantum physics. Max Planck explained the spectrum from a blackbody, which is an ideally absorptive body, by introducing the quantization of energy [4]. The quantized electromagnetic wave is called photons, and has the energy of  $hc/\lambda$ , where  $h = 6.63 \times 10^{-34} \text{ m}^2\text{kg/s}$  is the Planck constant,  $c = 3.00 \times 10^8 \text{ m/s}$  the speed of light, and  $\lambda$  the wavelength. The hemispherical spectral emissive power from a blackbody  $e_{\lambda b}$  is the function of the wavelength  $\lambda$  and the temperature  $T$ , and is given by Planck's law [1][2]:

$$e_{\lambda b}(\lambda, T) = \frac{2\pi hc^2}{\lambda^5} \frac{1}{\exp(hc/\lambda k_B T) - 1}, \quad (1.1)$$

where  $k_B$  is the Boltzmann constant. The spectral emissive power is shown as a function of wavelength with several temperatures in Figure 1. 1. With increasing the temperature, the power increases and its peak shifts to the shorter wavelength. The

integration of the hemispherical spectral emissive power over all wavelengths gives a total heat flux from the blackbody  $e_b(T)$ . The relationship between the temperature and the flux is called Stephan-Boltzmann law [1][2]:

$$e_b(T) = \frac{2\pi^5 k_B^4}{15c^2 h^3} T^4. \quad (1.2)$$

The rapid increase of the flux with the temperature is quantitatively shown in Figure 1.

2. The peak wavelength of the blackbody radiation  $\lambda_{\max}$  is achieved by taking the derivative of  $e_{\lambda b}(\lambda, T)$ . The relationship between the temperature and the peak wavelength is called Wien's displacement law [1][2]:

$$\lambda_{\max} = \frac{b_W}{T}, \quad (1.3)$$

where  $b_W = 2.90 \times 10^{-3}$  mK is Wien's displacement constant. The peak wavelength is shown in Figure 1. 3. The peak wavelength is found to be around  $10 \mu\text{m}$  at room temperature (300 K), while it is in visible range ( $\sim 500$  nm) at 6000 K, which is close to the temperature of the sun.

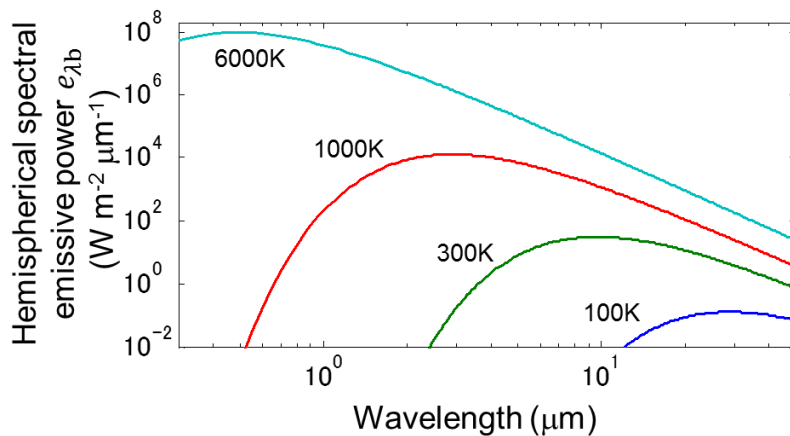


**Figure 1. 1 Hemispherical spectral emissive power derived from Planck's law**

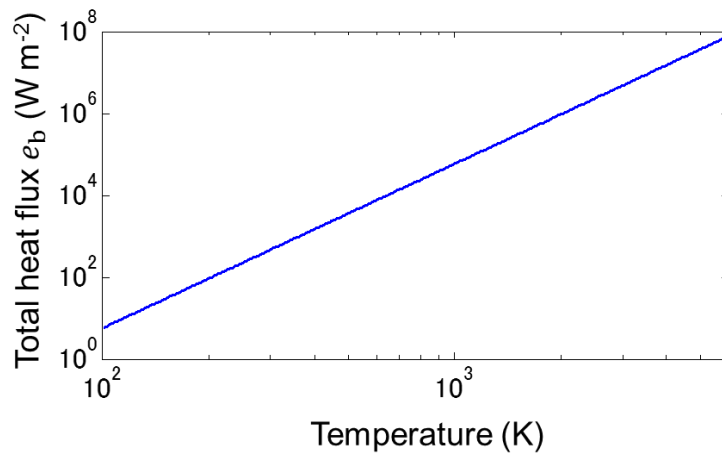


**Figure 1. 2 Total heat flux derived from Stefan-Boltzmann law**

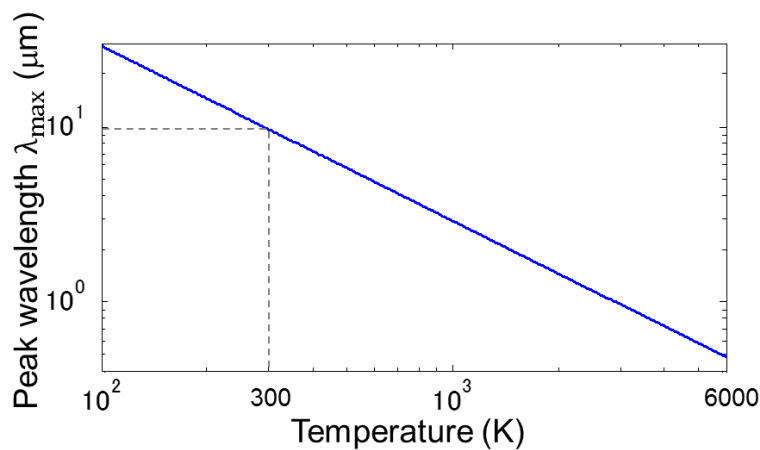


**Figure 1. 3 Peak wavelength derived from Wien's displacement law**

The real body in our world is not an ideal blackbody but has nonzero reflectance and transmittance. The ability to emit thermal radiation compared to a blackbody is defined as emissivity. Generally, metals have low emissivity while organic materials have high emissivity. One of the goals of the study on thermal radiation is to control spectral emissivity as needed. Both material research and surface structuring have been investigated to achieve desired spectral emissivity in various applications, such as thermophotovoltaics [6]-[12], mid-infrared light source [13]-[19], and radiative cooling

[23]-[26].

The above mentioned Planck's law, its derivative, and the concept of emissivity rely on one assumption that the electromagnetic waves couple only in the far-field. If the distance  $d$  between a hot body and a cold body is smaller than the peak wavelength obtained from the Wien's displacement law, the near-field components start to be transferred as shown in Figure 1. 4 [4]. Then, the heat flux  $Q$  is no more constant over the distance between bodies as described by Planck's law but it increases rapidly as the decrease of the gap. The heat flux across the gap exceeds the Stefan-Boltzmann law in the case that the gap is small enough. This phenomenon, which is called near-field radiative heat transfer (NFRHT), is expected to overwhelm the relatively small power density of thermal radiation compared to thermal conduction and convection.

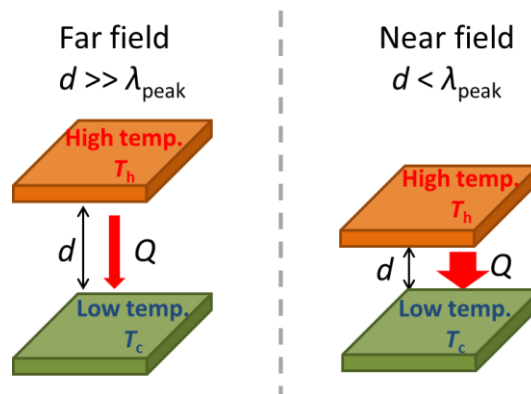


**Figure 1. 4 Near-field radiative heat transfer**

### 1.1.2 Application of thermal radiation control

There are numbers of engineering fields, where the control of thermal radiation adds new functionalities or improves system performances. These include thermophotovoltaics [6]-[12], mid-infrared light source [13]-[19], and radiative cooling [23]-[26], as depicted in Figure 1. 5.

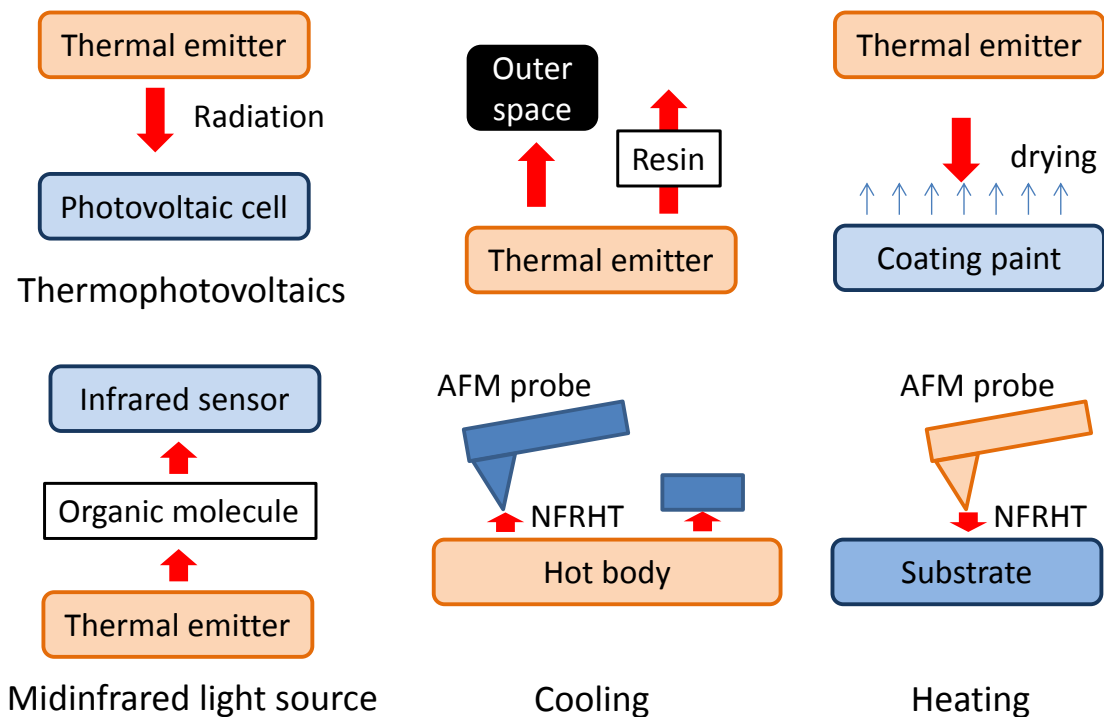


**Figure 1. 5 Application of thermal radiation control**

#### 1.1.2.1 Thermophotovoltaics

Thermophotovoltaics [6][7] is one of energy conversion schemes, where electricity is generated from thermal photons. Photons from a thermal emitter are absorbed by a photovoltaic cell, where photo-excited carriers flow as an electric current. The spectral response of the thermal emitter is ideally designed to be quasi-monochromatic with a wavelength close to the bandgap of the photovoltaic cell. In a photovoltaic system, the

photon energy which is considerably larger than the bandgap is partly lost as heat by the mechanism called thermalization loss. The photon whose energy is smaller than the bandgap is not absorbed by the cell but absorbed by other parts of the apparatus. This mechanism is called radiative loss. These two losses are engineered by the spectral control of thermal emission toward conversion systems with high efficiency [7]-[9]. Thermophotovoltaics is applicable to waste heat recovery or portable power sources [7]. It is also expected to enhance the efficiency of solar energy conversions with the combination of solar absorbers [9].

#### 1.1.2.2 Light source

Another application is mid-infrared light sources for chemical sensing [13][14]. Organic molecules absorb mid-infrared light at specific wavelengths corresponding to their vibrational modes. These specific absorptions allow us to identify unknown material by using a database such as spectral database for organic compounds (SDBS) [15] from National Institute of Advanced Industrial Science and Technology (AIST). Although Fourier-transform infrared spectrometers (FT-IR) are widely utilized for the measurement of absorption spectra, the compact system with mid-infrared light sources and infrared detectors is required to bring the analysis to consumer markets such as alcoholic gas detections in cars. Light-emitting diodes [16] and quantum cascade lasers [17] show satisfactory performance, but their cost hampers the wide usage. Alternatively, the spectral control of the thermal emitter enables quasi-monochromatic light sources because the peak wavelength of blackbody radiation is in the mid-infrared range around room temperature. Miyazaki and his colleagues determined the concentration of a chemical compound using a thermal emitter composed of resonant high-aspect cavities [18]. Inoue and his colleagues used emitters based on multiple quantum wells and

two-dimensional photonic crystal for the discrimination of acetone from trichloroethylene [19].

The emissivity control of the incandescent lamps improves the efficiency of the visible light sources [21][22]. The unwanted spectral band is suppressed without absorptive or reflective filters. Cold incandescent lamp is achieved by suppressing the infrared radiation to the near-zero level.

### 1.1.2.3 Radiative cooling

Cooling heat engines, electronic devices, and building is the key demand for highly-integrated modern technologies. Especially, artificial satellites need well-designed thermal emitters for cooling [20] because radiative transfer is only the path to exhaust heat in outer space. Interestingly, it is also possible to radiatively couple a body on the earth to outer space by utilizing the atmospheric transmission windows spanning from 3  $\mu\text{m}$  to 5  $\mu\text{m}$  and from 8  $\mu\text{m}$  to 13  $\mu\text{m}$ . The infrared light from the body runs away to outer space, whose temperature is around 3 K. A properly designed spectrally selective thermal radiator was demonstrated to be cooled down 10 K compared to the ambient in the night [23]. Recently, Raman and his colleagues manufactured a multilayered structure which reflects visible photons and emits infrared photons in the atmospheric window [24]. The device is cooled to 5 K below the ambient air temperature under strong sunlight.

The radiative cooling is not limited to the coupling with outer space. Shimizu and his colleagues proposed radiative cooling of electronic devices packaged in resin [25]. The cooling is achieved by radiatively coupling to the ambient through the IR transmission windows of the resin. Spectrally selective emitter enhances radiative heat flux, thus the emitter is cooled down more than 2 K. There should be plenty of rooms for the

investigation on the radiative cooler.

Selective cooling of nanostructures are of interest for the miniaturized circuits and microelectromechanical systems (MEMS). In the modern very large scale integrated circuits (VLSI), the transistors with small size and high power consumption can be quite hot. The temperatures of suspended MEMS structures such as resonators and bolometers are sometimes considerably high, especially in vacuum conditions. To cool down such hot spots, a probe positioned in proximity is used to couple through NFRHT. Additionally, the heat flux is controlled by changing the distance between the probe and the hot spot. Recently, Guha and his colleague achieved selective cooling of suspended silicon dioxide membrane by using an oxidized probe [26].

Near-field radiative heat transfer across a planar gap significantly increases the heat flux per area. The technique to produce a uniform gap enables the control of heat flow in more bulky systems. Such a planar gap has been long awaited from the theoretical community [27] although the experimental realization of a submicron gap has not been intensively studied. Recently, St-Gelais and his colleagues achieved monolithic thermal circuit where near field is transferred between microfabricated beams positioned across a submicron gap [28]. The usage of near-field radiative heat transfer would add new perspective in the next generation heat management systems.

#### 1.1.2.4 Radiative heating

Probe-based nanolithography, which utilizes a cantilever for atomic force microscopy (AFM), is an emerging technology to overcome the diffraction limit of the conventional photolithography. The heat transfer from probes to polymers for drying [29] is a promising candidate among numbers of patterning physics. Although fine patterning requires precise physical modelling, the heat transfer between the probe and the

polymer is not fully understood. The investigations of near-field radiative heat transfer contribute the improvement of the system, especially in vacuum conditions. The same applies to the heat assisted magnetic recording [30][31]. Also, the probing of temperature distribution in nanoscale with AFM cantilever [32] is a promising application of near-field radiative heat transfer.

Infrared drying process of painting [33] can be improved by using controlled thermal emitter. The matching of the emission wavelength with the absorption band of paint improves the power efficiency and/or drying time.

## 1. 2. Justification of this work

Although numbers of researchers have investigated the control of thermal radiation [6]-[12][18]-[28][32][34], there are types of control where more solutions should be provided. Here, two application scenarios are picked up in order to set the goal of this thesis. The first scenario is the mid-infrared light source for chemical sensing. The dynamic control of thermal radiation and the monochromaticity are required for the portable and sensitive non-dispersive infrared sensing (NDIR) system. Another scenario is the thermal management in the artificial satellites, where thermal convection does not exist. An intelligent thermal management device such as thermal rectifier as well as the heat flux enhancement are required to realize efficient management system without increasing payload.

In NDIR systems, signal-to-background ratio is improved by the modulation of the light. Conventionally, the amplitude of thermal radiation is modulated by changing temperature, thus the modulation frequency is limited by the heat capacity of the radiator. The direct modulation of emissivity by external stimuli enables an emitter with

a modulation frequency higher than 1 kHz, which suppresses low-frequency noise.

Numbers of thermal emitters based on electromagnetic resonance have been presented [8][18][19][33] toward the realization of monochromatic, designable thermal emission. On the other hand, electromagnetic resonances are excited at several mode frequencies in these thermal emitters. Although the design of the fundamental mode has been well studied, the control of parasitic modes have rarely been investigated albeit their importance for monochromatic thermal emitters.

Thermal radiation is utilized as a thermal path in thermal management systems, especially in artificial satellites. In future, more efficient, more intelligent, and adaptive thermal devices are required to satisfy increasing demands such as portability and payload. Thermal rectifier is a candidate of such devices [35]. They can modulate the heat flow according to their direction without any power input from outside. This intelligent heat flow controller adds more flexibility on the system design. Although conductive rectifiers with low rectification contrast ratio have been demonstrated [36]-[38], radiative rectifiers or rectifiers with high contrast have rarely been experimentally presented.

As for the radiative thermal management, the maximum heat flux is limited by Stefan-Boltzmann law. One needs to increase the temperature difference between the emitter and the receiver in order to increase the heat flux. The same applies to thermophotovoltaics systems. Near-field radiative heat transfer overcomes these limits by using the tunneling of thermal photons. Theoretical works predicted that near-field radiative heat transfer contributes both the spectral control and the enhancement of the power density of thermophotovoltaics system [10]-[12]. On the experimental side, the fabrication of a uniform gap is quite difficult because of the alignment problem as well

as the deviation from the ideal flat surfaces. With the parallel-plate configurations, the most of experimental achievements fall over 1  $\mu\text{m}$ . The sphere-plate configuration achieves the gap as small as 30 nm by bypassing the alignment problem, but the amount of heat transfer is significantly smaller than that in the parallel-plate configuration. The technology to produce a uniform submicron gap for near-field radiative heat transfer is quite important for thermophotovoltaics and radiative thermal management system.

### 1. 3. Purpose of this work

The purpose of this work is to realize four types of thermal radiation control depicted in Figure 1. 6, toward two application scenarios namely mid-infrared light source for chemical sensing and thermal management in artificial satellites. They are the dynamic control of thermal emission, the control of parasitic emission modes, the rectification of radiative heat transfer, and the experimental investigation of near-field thermal radiation. The dynamic control and the suppression of parasitic modes contributes to improve the sensitivity and the power efficiency of the chemical sensing system using thermal emitters as light sources. A thermal rectifier with enhanced heat flux by near-field coupling enables intelligent thermal management system in artificial satellites.

Although numbers of researchers have investigated the spectral control, dynamic control of thermal radiation is still limited. Dynamic control allows us to modulate mid-infrared light source with a high frequency, thus a higher signal-to-noise ratio is achieved. In this work, such a dynamic control is proposed by using the coupling of guided mode resonance and surface polaritons.

Spectral selectivity of the thermal emitter is attained by electromagnetic resonances. Metal-insulator-metal (MIM) metamaterials, which consist of MIM trilayers, are

promising because of their omnidirectional response and the simplicity on the fabrication. The top metal is patterned to form electromagnetic resonators, and multiple resonances are generally excited at the fundamental and higher mode frequencies. In this work, proximity coupling between resonators is introduced to suppress parasitic modes including the second-order mode harmonics. The control of higher modes improves monochromaticity of the emitter.

Thermal rectifiers are attracting more interest as a key component in intelligent thermal management systems [35]. They modulate heat flow according to their direction without any power input from outside. This intelligent heat flow controller adds more flexibility to the system design. In this work, a radiative thermal rectifier based on a phase-change material is demonstrated. The transition from the insulating state to the metallic state controls the transfer of infrared photons.

As discussed before, near-field radiative thermal radiation boosts the amount of heat transfer. The critical challenge on this field is the formation of the uniform submicron gap. Because the alignment of a pair of planar surfaces is extremely difficult, most of the experimental investigation have utilized the heat transfer between a sphere and a plate with the cost of small heat flux enhancement. Several works have investigated the parallel-plate configuration, but submicron gaps have not been quantitatively evaluated. In this work, a new methodology to form submicron gaps is presented.

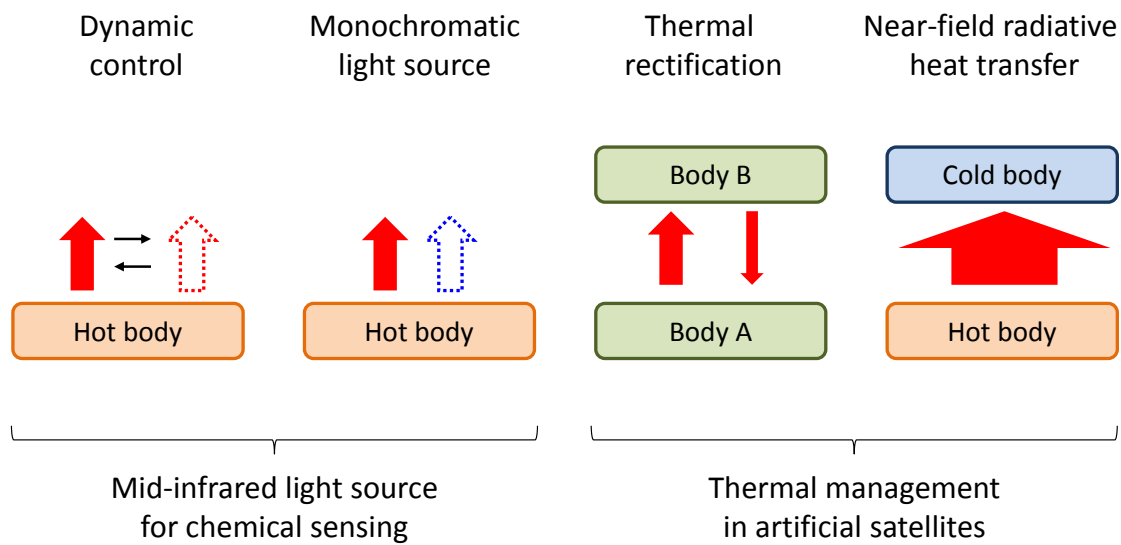


**Figure 1. 6 Purpose of this work**

#### 1. 4. Originality of this work

The coupling of guided more resonances in gratings and surface polaritons is firstly proposed to control the optical characteristics of structures. They are applicable to mid-infrared range, where thermal radiation takes place. Dynamic modulation is theoretically demonstrated by changing the distance between the grating and the interface which supports the surface polariton. Two kinds of surface polaritons, namely the surface phonon polariton on a silicon carbide substrate and the surface plasmon polariton on a doped silicon slab are presented.

A methodology to control parasitic modes, including the control of the frequency interval between the fundamental and the second-order modes, is firstly presented. The resonators are proximity-coupled so as to lower the fundamental frequency and to raise the second-order frequency. The small gap between resonators is shown to suppress other parasitic modes. The measured emission spectra clearly indicate the contribution of the proposed methodology toward a single-peaked emitter.

At the beginning of this work, the thermal rectification contrast ratio was limited to be smaller than 1. This is because of the difficulty to control diffusive thermal conduction. We adopt radiation as the thermal path to achieve more designable heat transfer properties. The phase change of vanadium dioxide provides large permittivity change, thus a large contrast on heat flux is experimentally achieved. Such a radiative thermal diode based on the phase-change material has not been experimentally obtained. The measured rectification ratio of 2 is the highest value ever reported to the best of our knowledge.

A novel methodology which utilizes sparsely placed spacers is proposed for the uniform gap formation. The exerted force compensates the intrinsic deflection of the diced chips. The gap separation and its uniformity are quantitatively examined by optical measurements based on interference. The heat flux across a submicron gap is evaluated for the first time to the best of our knowledge.

### 1. 5. Thesis organization

This thesis is organized as shown in Figure 1. 7. As discussed in Subsection 1. 3., we demonstrate four types of thermal radiation control: dynamic control, monochromatic light source, thermal rectification, and near-field radiative heat transfer.

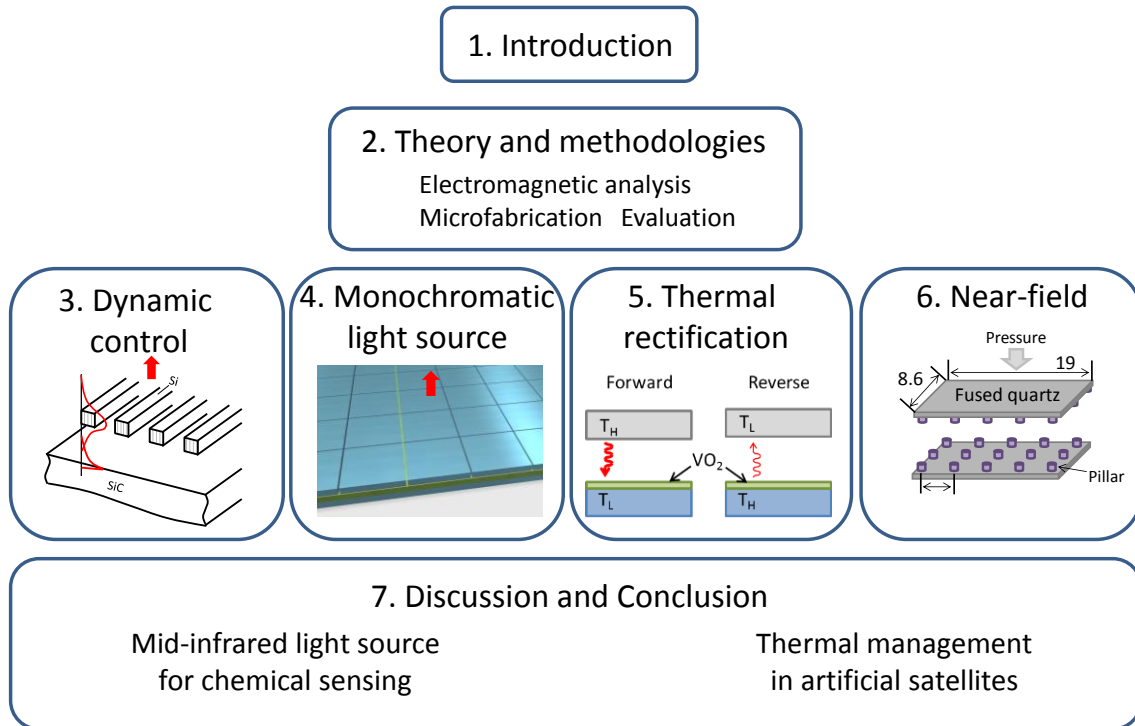


**Figure 1. 7 Thesis organization**

Chapter 2 starts from the theory of thermal radiation. Then, methodologies to analyze, control, and evaluate radiative heat transfer utilized in the following sections are discussed. They are theoretical analysis of electromagnetic waves, microfabrication technologies for microstructures, and evaluation methodology including Fourier-transform infrared spectroscopy and steady-state heat flux measurement.

In Chapter 3, the dynamic control of thermal radiation is theoretically presented. The coupling between guided mode resonances and surface polaritons is utilized to control emissivity. Both the surface phonon polariton on a silicon carbide substrate and the surface plasmon polariton on a doped silicon slab are investigated for the active modulation of thermal emission.

In Chapter 4, a quasi-monochromatic thermal emitter is obtained by controlling parasitic modes of the metal-insulator-metal metamaterials. The proximity interactions

in two arrangements suppress and/or blue-shift parasitic modes. As one arrangement, diagonally-arranged MIM absorbers are investigated for the enhancement of the ratio of the second-order frequency to the fundamental frequency. As another arrangement, densely-placed square resonators are presented as a polarization-independent MIM thermal emitter. The numerically proposed suppression is supported by the fabricated MIM metamaterials.

In Chapter 5, a thermal rectifier with a high rectification contrast ratio is experimentally demonstrated. Vanadium dioxide films deposited on a silicon substrate and a fused quartz are used as the emitter and receiver. The measured heat flux is explained by the theoretical analysis based on the fluctuation electrodynamics. Tungsten doping into vanadium dioxide lowers the transition temperature.

In Chapter 6, a method to form a submicron gap for near-field radiative heat transfer is proposed. Microfabricated spacers are sparsely placed between two fused quartz substrates to achieve uniform submicron gaps with suppressed parasitic heat conduction. The uniformity of the gap is verified by the optical interferometry. The heat flux is evaluated and compared with the theoretical calculation of radiative heat transfer. The contribution of the parasitic spacer conduction is revealed to be smaller than radiation. The heat transfer is analyzed by utilizing an equivalent thermal circuit model.

In Chapter 7, the results obtained in Chapter 3-6 are summarized and compared with other works. Then, their impacts on the two application scenarios, namely mid-infrared light source for chemical sensing and intelligent thermal management in artificial satellites, are investigated. Finally, this work is concluded.

**Reference**

- [1] J. R. Howell, R. Siegel, and M. P. Menguc. Thermal radiation heat transfer. CRC press, 2010.
- [2] M. F. Modest, Radiative heat transfer, Academic press, 2013
- [3] J. F. Harris and R. I. Gamow, "Snake infrared receptors: thermal or photochemical mechanism?" Science **172**, 1252 (1971).
- [4] M. Planck, Theory of heat radiation, 1914.
- [5] D. Polder and M. Van Hove, Theory of radiative heat transfer between closely spaced bodies , Phys. Rev. B **4**, 3303 (1971).
- [6] L. M. Fraas, J. E. Avery, and H. X. Huang. "Thermophotovoltaic furnace-generator for the home using low bandgap GaSb cells." Semicond. Sci. Tech. **18**, S247 (2003).
- [7] W. R. Chan, P. Bermel, R. C. N. Pilawa-Podgurski, C. H. Marton, K. F. Jensen, J. J. Senkevich, J. D. Joannopoulos, M. Soljačić, and I. Celanovic. "Toward high-energy-density, high-efficiency, and moderate-temperature chip-scale thermophotovoltaics." Proc. Nat. Acad. Sci. **110**, 5309 (2013).
- [8] H. Sai and H. Yugami. "Thermophotovoltaic generation with selective radiators based on tungsten surface gratings." Appl. Phys. Lett. **85**, 3399 (2004).
- [9] A. Lenert, D. M. Bierman, Y. Nam, W. R. Chan, I. Celanović, M. Soljačić, and E. N. Wang. "A nanophotonic solar thermophotovoltaic device." Nat. Nano. **9**, 126 (2014).
- [10] A. Narayanaswamy and G. Chen. Surface modes for near field thermophotovoltaics, Appl. Phys. Lett. **82**, 3544 (2003).

- [11] M. Laroche, R. Carminati, and J-J. Greffet. "Near-field thermophotovoltaic energy conversion." *J. Appl. Phys.* **100**, 063704 (2006).
- [12] K. Park, S. Basu, W. P. King, and Z. M. Zhang. "Performance analysis of near-field thermophotovoltaic devices considering absorption distribution." *J. Quant. Spec. Rad. Trans.* **109**, 305 (2008).
- [13] J. Meléndez, A. J. De Castro, F. López, and J. Meneses. "Spectrally selective gas cell for electrooptical infrared compact multigas sensor." *Sens. Act. A* **47**, 417 (1995).
- [14] J. Hodgkinson, and R. P. Tatam. "Optical gas sensing: a review." *Meas. Sci. Tech.* **24**, 012004 (2013).
- [15] <http://sdfs.db.aist.go.jp/>
- [16] A. Krier, and V. V. Sherstnev. "Powerful interface light emitting diodes for methane gas detection." *J. Phys. D* **33**, 101 (2000).
- [17] Y. Yao, A. J. Hoffman, and C. F. Gmachl. "Mid-infrared quantum cascade lasers." *Nat. Photo.* **6**, 432 (2012).
- [18] H. T. Miyazaki, K. Ikeda, T. Kasaya, K. Yamamoto, Y. Inoue, K. Fujimura, T. Kanakugi, M. Okada, K. Hatade, and S. Kitagawa. "Thermal emission of two-color polarized infrared waves from integrated plasmon cavities." *Appl. Phys. Lett.* **92**, 141114 (2008).
- [19] T. Inoue, M. De Zoysa, T. Asano, and S. Noda. "Filter-free nondispersive infrared sensing using narrow-bandwidth mid-infrared thermal emitters." *Appl. Phys. Exp.* **7**, 012103 (2014).

- [20] R. Osiander, S. L. Firebaugh, J. L. Champion, D. Farrar, and M. Darrin. "Microelectromechanical devices for satellite thermal control." *IEEE Sensors J.* **4**, 525 (2004).
- [21] T. Matsumoto and M. Tomita. "Modified blackbody radiation spectrum of a selective emitter with application to incandescent light source design." *Opt. Exp.* **18**, A192 (2010).
- [22] O. Ilic, P. Bermel, G. Chen, J. D. Joannopoulos, I. Celanovic, and M. Soljačić. "Tailoring high-temperature radiation and the resurrection of the incandescent source." *Nature nanotechnology* (2016).
- [23] C. G. Granqvist, and A. Hjortsberg. "Surfaces for radiative cooling: Silicon monoxide films on aluminum." *Appl. Phys. Lett.* **36**, 139 (1980).
- [24] A. P. Raman, M. A. Anoma, L. Zhu, E. Rephaeli, and S. Fan. "Passive radiative cooling below ambient air temperature under direct sunlight." *Nature* **515**, 540 (2014).
- [25] M. Shimizu, and H. Yugami. "Thermal Radiation Control by Surface Gratings as an Advanced Cooling System for Electronic Devices." *J. Therm. Sci. Tech.* **6**, 297 (2011).
- [26] B. Guha, C. Otey, C. B. Poitras, S. Fan, and M. Lipson. "Near-field radiative cooling of nanostructures." *Nano Lett.* **12**, 4546 (2012).
- [27] S. A. Biehs, F. S. S. Rosa, and P. Ben-Abdallah. "Modulation of near-field heat transfer between two gratings." *Appl. Phys. Lett.* **98**, 243102 (2011).
- [28] R. St-Gelais, B. Guha, L. Zhu, S. Fan, and M. Lipson. "Demonstration of strong near-field radiative heat transfer between integrated nanostructures." *Nano Lett.* **14**, 6971 (2014).

- [29] O. Coulembier, A. Knoll, D. Pires, B. Gotsmann, U. Duerig, J. Frommer, R. D. Miller, P. Dubois, and J. L. Hedrick. "Probe-based nanolithography: self-amplified depolymerization media for dry lithography." *Macromolecules* **43**, 572 (2009).
- [30] M. A. Seigler, W. Challener, E. Gage, N. Gokemeijer, G. Ju, B. Lu, K. Pelhos et al. "Integrated heat assisted magnetic recording head: Design and recording demonstration." *IEEE Magnetics* **44**, 119 (2008).
- [31] M. H. Kryder, E. C. Gage, T. W. McDaniel, W. Challener, R. E. Rottmayer, G. Ju, Y. T. Hsia, and M. F. Erden. "Heat assisted magnetic recording." *Proc. IEEE* **96**, 1810 (2008).
- [32] Y. D. Wilde, F. Formanek, R. Carminati, B. Gralak, P. A. Lemoine, K. Joulain, J. P. Mulet, Y. Chen, J. J. Greffet, "Thermal radiation scanning tunnelling microscopy." *Nature* **444**, 740 (2006).
- [33] P. Dufour, D. Blanc, Y. Touré, and P. Laurent. "Infrared drying process of an experimental water painting: Model predictive control." *Dry. Tech.* **22**, 269 (2004).
- [34] J. J. Greffet, R. Carminati, K. Joulain, J. P. Mulet, S. Mainguy, and Y. Chen. "Coherent emission of light by thermal sources." *Nature* **416**, 61 (2002).
- [35] N. A. Roberts and D. G. Walker. "A review of thermal rectification observations and models in solid materials." *Int. J. Therm. Sci.* **50**, 648 (2011).
- [36] C. W. Chang, D. Okawa, A. Majumdar, and A. Zettl, Solid-state thermal rectifier. *Science*, **314**, 1121 (2006).
- [37] W. Kobayashi, Y. Teraoka, and I. Terasaki, An oxide thermal rectifier. *Appl. Phys. Lett.* **95**, 171905 (2009).

- [38] R. Nakayama, T. Takeuchi, “Thermal Rectification in Bulk Material Through Unusual Behavior of Electron Thermal Conductivity of Al-Cu-Fe Icosahedral Quasicrystal” *J. Electronic Materials* **44**, 356 (2015).

## *Chapter 2 Theory and methodologies*

This chapter describes the theory of thermal radiation and the methodologies utilized in this work. Firstly, the Maxwell's equations are briefly reviewed stressing the relation with thermally excited electric current. The concepts of spectral intensity, emissivity, and view factor are introduced. Secondary, electromagnetic simulation techniques are described. They include transmission matrix method, scattering matrix method, modal analysis, and fluctuation electrodynamics for near-field radiative heat transfer. Thirdly, microfabrication technologies, especially lithography and etching, are briefly reviewed. Finally, evaluation methodologies employed in this work are illustrated. Fourier-transform infrared spectrometer is briefly explained, and the custom-built heat flux measurement system in vacuum is described.

## 2.1. Theory of thermal radiation

### 2.1.1 Maxwell's equation and electric current density

Thermal radiation is the electromagnetic wave excited by thermal energy. The generation and the propagation of electromagnetic waves are explained by Maxwell's equations: [1][2]

Gauss's law for the electric field:

$$\nabla \cdot \mathbf{E} = \frac{\rho}{\varepsilon}, \quad (2.1)$$

Gauss's law for the magnetic field:

$$\nabla \cdot \mathbf{B} = 0, \quad (2.2)$$

Faraday's law:

$$\nabla \times \mathbf{E} = -\frac{\partial \mathbf{B}}{\partial t}, \quad (2.3)$$

Ampere's law:

$$\nabla \times \mathbf{B} = \mu \left( \mathbf{J} + \varepsilon \frac{\partial \mathbf{E}}{\partial t} \right), \quad (2.4)$$

where  $\mathbf{E}$  is the electric field,  $\mathbf{B}$  the magnetic field,  $\rho$  the charge density,  $\varepsilon$  the permittivity,  $\mu$  the permeability, and  $\mathbf{J}$  the current density. Thermal energy vibrates charges like free electrons and the atoms of polar materials, and these vibrating charges excite the oscillating magnetic field according to Ampere's law. The electric field and magnetic field are generated following Faraday's law and Ampere's law. The propagative sinusoidal waves are called far-field components and reach far from the emitting material. Other fields are localized around materials and called evanescent waves or near-field components.

The distribution of thermally excited electric current density in any material follows the Bose-Einstein statistics. According to fluctuation dissipation theorem [3], the cross

product of the spectral current densities  $\mathbf{j}(\mathbf{x}, \omega)$  at two locations  $\mathbf{x}'$  and  $\mathbf{x}''$  at certain frequency  $\omega$  satisfies following relationship:

$$\langle \mathbf{j}(\mathbf{x}', \omega) \times \mathbf{j}^*(\mathbf{x}'', \omega) \rangle = \frac{4\omega \text{Im}(\varepsilon)}{\pi} \theta(\omega, T) \delta(\mathbf{x}' - \mathbf{x}''), \quad (2.5)$$

where  $\theta(\omega, T) = \hbar\omega / (\exp(\hbar\omega/k_B T) - 1)$  is the mean energy of the Planck oscillator at the temperature  $T$ , and  $k_B$  is the Boltzmann constant. The derivation of the spectral heat flux in the far-field from the equation (2.5) gives the Planck's law, and the formalism will be shown in the subsection 2.2.4.

### 2.1.2 Spectral intensity and spectral power

There are two variables which describe the spectrum of thermal radiation, as shown in Figure 2. 1. The first one is the emitted spectral intensity  $i'_{\lambda_b}(\lambda)$  and is defined as the power which is emitted into a unit solid angle from a unit projected surface area normal to the emission direction. The spectral intensity is angularly independent because thermodynamic requirement does not allow the rotation of the emitter to change the intensity. The second one is the directive spectral emissive power  $e'_{\lambda_b}(\lambda, \theta)$  and is defined as the power which is emitted into a unit solid angle from a unit actual area. The directive spectral emissive power is angularly dependent, and the geometrical analysis gives us Lambert's cosine law as described as follows:

$$e'_{\lambda_b}(\lambda, \theta) = i'_{\lambda_b}(\lambda) \cos \theta . \quad (2.6)$$

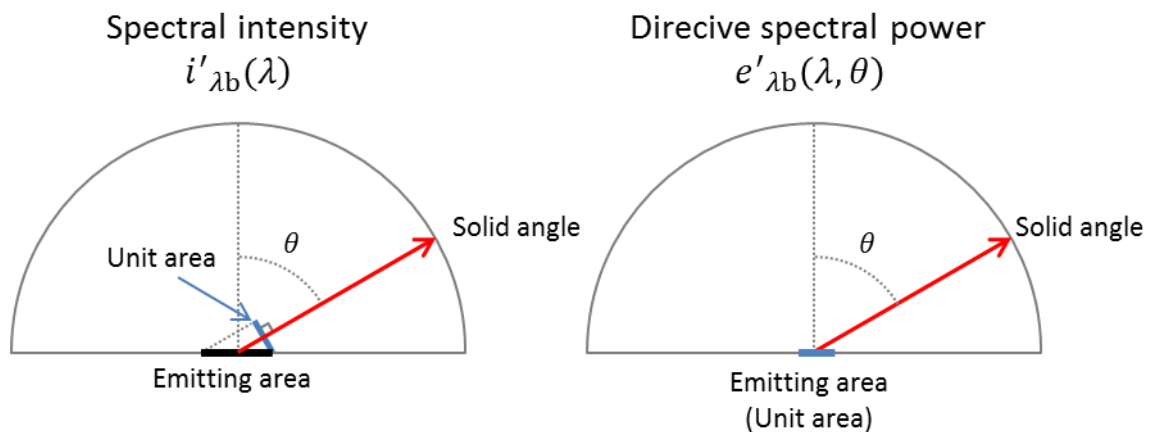


**Figure 2. 1 Spectral intensity and directive spectral power**

## 2.1.3 Emissivity and Kirchoff's law

Emissivity  $E_M(\lambda, \theta, j)$  is the emitting ability of a material and is a function of wavelength  $\lambda$ , angle  $\theta$ , and polarization  $j$ . As shown in Figure 2. 2, emissivity is defined by using the emitted power from a blackbody  $P_B(\lambda, \theta, j, T)$  and the emitted power from the material  $P_M(\lambda, \theta, j, T)$  as follows:

$$E_M(\lambda, \theta, j) = \frac{P_M(\lambda, \theta, j, T)}{P_B(\lambda, \theta, j, T)}, \quad (2.7)$$

where  $T$  is the temperature. For most materials, emissivity is independent of temperature, which allows us to analyze the thermal radiation phenomenon simply.

Thermodynamic requirement gives us the Kirchoff's law [4], which explains the relationship between emissivity and absorptivity. Now consider that a material is facing a blackbody. In thermal equilibrium, the material emits exactly the same numbers of photons as it absorbs from the blackbody to keep the temperature constant. Thus, emitted power  $P_E$  and absorbed power  $P_A$  are equal:

$$P_E(\lambda, \theta, j, T) = P_A(\lambda, \theta, j, T). \quad (2.8)$$

By dividing both sides of Eq. (2.8) by the blackbody radiation  $P_B(\lambda, \theta, j, T)$ , we achieve

$$E_M(\lambda, \theta, j) = A_M(\lambda, \theta, j), \quad (2.9)$$

where  $A_M(\lambda, \theta, j)$  is the absorptivity of the body.

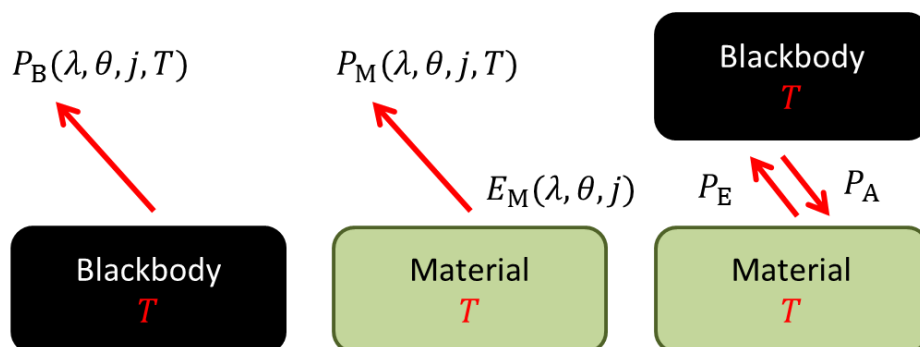


**Figure 2. 2 Thermal radiation and optical absorption by a material**

## 2.1.4 View factor

Considering the heat transfer between two surfaces, thermal radiation which does not hit the cold surface should be taken into account. The view factor is defined as the ratio of the flux that hits the cold surface to the emitted flux from the hot surface. In case that the two surfaces are placed in proximity in parallel, the view factor is close to unity. If two surfaces are perpendicularly placed and that their distance is large, the view factor is close to zero. Complexed surfaces can be treated as the sum of the small and simple structure for the calculation. Considering two infinitesimal patches  $dA_i$  and  $dA_j$  in arbitrary positions and orientations as shown in Figure 2. 3, the infinitesimal view factor between these patches  $dF_{dA_i-dA_j}$  depends only on geometry:

$$dF_{dA_i-dA_j} = \frac{\cos \theta_i \cos \theta_j}{\pi S^2} dA_j , \quad (2.10)$$

where  $S$  is the length of the straight line between the two infinitesimal patches,  $\theta_i$  and  $\theta_j$  are the angles between the line and patches  $dA_i$  and  $dA_j$ , respectively. By integrating the infinitesimal view factor over areas  $A_i$  and  $A_j$ , the view factor between two areas  $F_{A_i-A_j}$  is derived.

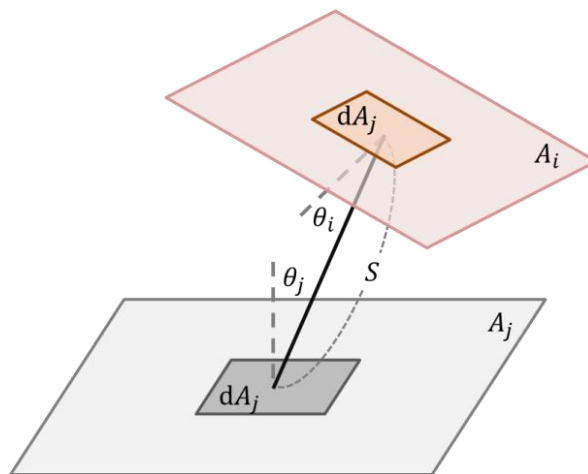


**Figure 2. 3 Calculation of the view factor**

Alternative to carry out the integrations, there are rules for simple geometries. Catalogs of these rules can be found in the literature [2][5] or in the website [6][7]. For example, if the emitter and the receiver are the identical square surfaces placed in parallel, the view factor can be written as: [2][6][7]

$$F_{12} = \frac{1}{\pi x^2} \left[ \ln \frac{(1+x^2)^2}{1+2x^2} + 4x(\sqrt{1+x^2} \tan^{-1} \frac{x}{\sqrt{1+x^2}} - \tan^{-1} x) \right], \quad (2.11)$$

where  $x$  is the ratio between the square length and the separation. The calculated view factor against  $x$  is shown in Figure 2. 4. The square length should be larger than 2.58 times the separation in order to receive the half of the radiation by the cold surface.

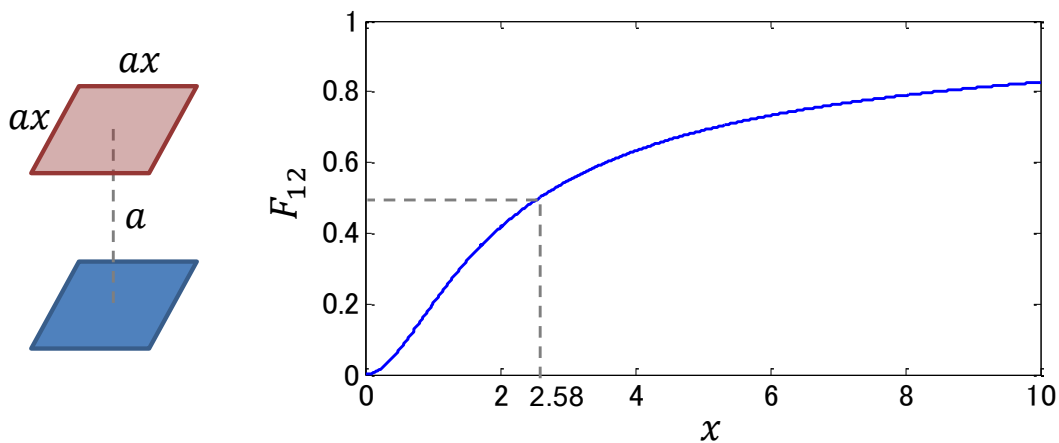


**Figure 2. 4 View factor between identical square surfaces**

## 2.2 Simulation of electromagnetic wave

In principle, one may find solutions of thermal radiation problems by solving Maxwell's equations with thermally generated currents described by fluctuation dissipation theorem, but this falls in problematic complexity on calculation and/or troublesome convergence. Alternatively, the absorptivity of the body is calculated and it is translated to emissivity according to Kirchhoff's law for the problem in the far-field.

The calculation of absorptivity can be classified in three categories based on the structure of bodies as shown in Figure 2. 5: multilayered system, grating structure, and 3D structures. These structures have variance in one-direction, two-directions, and three-directions, respectively.

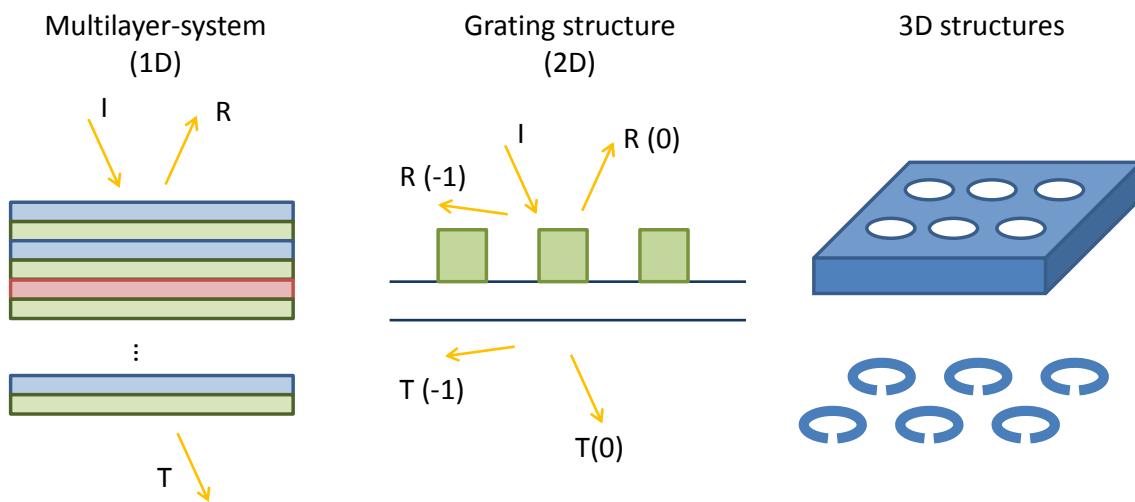


**Figure 2. 5 Three categories of electromagnetic simulation**

Most of smooth surfaces including bulk materials, coated thin films on a substrate, one-dimensional photonic crystals, is modelled as infinite in the direction parallel to the surface. In other words, by defining the direction perpendicular to the surface as the z-direction and the other two directions as the x- and y-directions, the material is modelled as invariant in the x- and y-directions. Such bodies are analyzed by transmission matrix method or scattering matrix method.

Classical surface-relief grating and subwavelength grating manufactured by modern microfabrication technology can be treated as invariant in the y-direction. In the case they are modelled as periodic in the x-direction, modal analysis or rigorous coupled wave analysis (RCWA) is widely utilized to analyze the electromagnetic response.

More complex structures, which do not have any invariant directions, are simulated based on mesh-based methods including finite domain time difference method (FDTD) and finite element method (FEM). These methods segmentalize the structure into meshes, and solve Maxwell's equations inside a mesh. To satisfy the boundary conditions and the continuity between meshes, a solver iterates calculations. These methods allow us to simulate complex problems such as photonic crystal with defects, gigahertz response of cars, and random structures. In this thesis, a commercial software based on finite integration technique, CST microwave studio [9], is utilized.

## 2.2.1 Multilayered system: Transmission matrix method

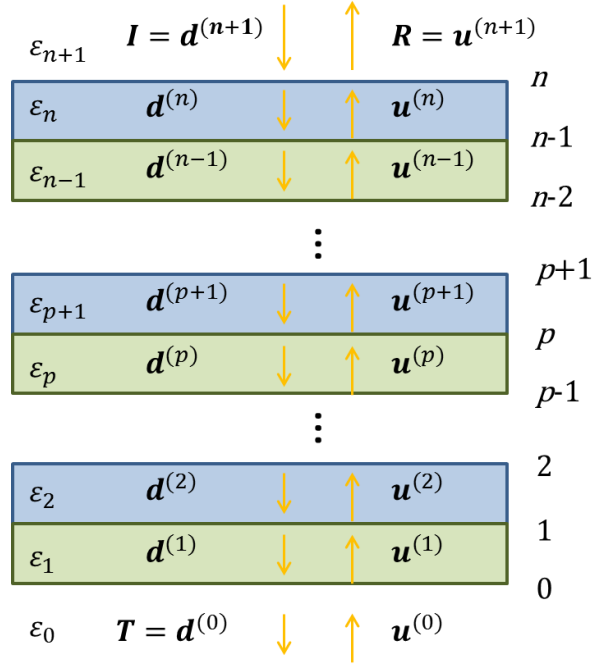


**Figure 2. 6 Multilayered system and electromagnetic waves inside.**

Now consider a multilayered system comprises  $n$  layers suspended in vacuum as shown in Figure 2. 6. The  $p$ -th layer has the permittivity  $\varepsilon_p$  and all the layers are nonmagnetic in the frequency range of interest ( $\mu_p = 1$ ). There are  $n + 1$  interfaces and they are named as interface 0 ~ interface  $n$ . The upward and downward waves in the  $p$ -th layer from the bottom are denoted as  $u^{(p)}$  and  $d^{(p)}$ , respectively. The amplitudes of electric fields in the  $(p+1)$ -th layer close to  $z_p$  are described as

$$\begin{bmatrix} u^{(p+1)}(z_p + 0) \\ d^{(p+1)}(z_p + 0) \end{bmatrix} = t^{(p)} \begin{bmatrix} u^{(p)}(z_p - 0) \\ d^{(p)}(z_p - 0) \end{bmatrix}, \quad (2.12)$$

where  $t^{(p)}$  is interface transmission matrix and is written as

$$t^{(p)} = \begin{bmatrix} t_{p,p+1} - \frac{r_{p+1,p} r_{p,p+1}}{t_{p+1,p}} & \frac{r_{p+1,p}}{t_{p+1,p}} \\ -\frac{r_{p,p+1}}{t_{p+1,p}} & \frac{1}{t_{p+1,p}} \end{bmatrix}. \quad (2.13)$$

Here,  $r_{ij}$  and  $t_{ij}$  are reflection and transmission coefficients at each interface, respectively, and are written differently in each polarization as shown in equations (2.14) and (2.15):

$$r_{ij} = \begin{cases} \frac{\gamma_i - \gamma_j}{\gamma_i + \gamma_j} \text{ (s-pol.)} \\ \frac{\varepsilon_j \gamma_i - \varepsilon_i \gamma_j}{\varepsilon_j \gamma_i + \varepsilon_i \gamma_j} \text{ (p-pol.)} \end{cases} \text{ and} \quad (2.14)$$

$$t_{ij} = \begin{cases} \frac{2\gamma_i}{\gamma_i + \gamma_j} \text{ (s-pol.)} \\ \frac{2\sqrt{\varepsilon_i \varepsilon_j} \gamma_i}{\varepsilon_j \gamma_i + \varepsilon_i \gamma_j} \text{ (p-pol.)} \end{cases}, \quad (2.15)$$

where the wavevector in the z-direction  $\gamma_i$  is written by the wavevector in vacuum  $k_0$  and the wavevector in the xy-plane  $\beta$ :

$$\gamma_i = \sqrt{\varepsilon_i k_0^2 - \beta^2}. \quad (2.16)$$

The phase rotation in the case of propagative wave or the decay in the case of evanescent wave inside the  $p$ -th layer is written as

$$\begin{bmatrix} u^{(p)}(z_p - 0) \\ d^{(p)}(z_p - 0) \end{bmatrix} = \phi^{(p)} \begin{bmatrix} u^{(p)}(z_{p-1} + 0) \\ d^{(p)}(z_{p-1} + 0) \end{bmatrix}, \quad (2.17)$$

where

$$\phi^{(p)} = \begin{bmatrix} \exp(i\gamma_p h_p) & 0 \\ 0 & \exp(-i\gamma_p h_p) \end{bmatrix}. \quad (2.18)$$

Thus, by defining layer t-matrix  $\tilde{t}^{(p)} = t^{(p)}\phi^{(p)}$ , we write

$$\begin{bmatrix} u^{(n+1)}(z_n + 0) \\ d^{(n+1)}(z_n + 0) \end{bmatrix} = \tilde{t}^{(n)}\tilde{t}^{(n-1)} \dots \tilde{t}^{(1)}t^{(0)} \begin{bmatrix} u^{(0)}(z_0 - 0) \\ d^{(0)}(z_0 - 0) \end{bmatrix}. \quad (2.19)$$

In the case that the incident is from the top, then  $d^{(n+1)} = I$ . Thus reflectance  $R$  and transmittance  $T$  are derived by analyzing the equation (2.20).

$$\begin{bmatrix} R \\ I \end{bmatrix} = \tilde{t}^{(n)}\tilde{t}^{(n-1)} \dots \tilde{t}^{(1)}t^{(0)} \begin{bmatrix} 0 \\ T \end{bmatrix} \quad (2.20)$$

### 2.2.2 Multilayered system: scattering matrix method

An alternative way to solve multilayered structure is scattering matrix method [10]. In the S-matrix method, the outgoing waves from the  $p$ -th interface are described by the incoming waves.

$$\begin{bmatrix} u^{(p+1)}(z_p + 0) \\ d^{(p)}(z_p - 0) \end{bmatrix} = s^{(p)} \begin{bmatrix} u^{(p)}(z_p - 0) \\ d^{(p+1)}(z_p + 0) \end{bmatrix}, \quad (2.21)$$

where  $s^{(p)}$  is the interface s-matrix and described by Fresnel's coefficient with a relatively simple manner:

$$s^{(p)} = \begin{bmatrix} t_{p,p+1} & r_{p+1,p} \\ r_{p,p+1} & t_{p+1,p} \end{bmatrix}. \quad (2.22)$$

The layer s-matrix  $\tilde{s}^{(p)}$  is described as follows:

$$\tilde{s}^{(p)} = \begin{bmatrix} 1 & 0 \\ 0 & \exp(i\gamma_p h_p) \end{bmatrix} s^{(p)} \begin{bmatrix} \exp(i\gamma_p h_p) & 0 \\ 0 & 1 \end{bmatrix}. \quad (2.23)$$

The convergence of the S-matrix method is much better than T-matrix method because layer s-matrix does not have components linear to  $\exp(-i\gamma_p h_p)$ . Furthermore, the internal component of S-matrix method is physically meaningful. On the other hand, the calculation of iteratively stacked layers by S-matrix method is more complex than that

by T-matrix method, where the matrix product expresses the solution of the multilayer problem. The stack S matrix is calculated from the bottom layers iteratively, and the stack S matrix of the  $p$ -th layer  $S^{(p)}$  are described by using the stack S matrix of the  $(p-1)$ -th layer  $S^{(p-1)}$  as follows:

$$S_{11}^{(p)} = \tilde{s}_{11}^{(p)} \left[ 1 - S_{12}^{(p-1)} \tilde{s}_{21}^{(p)} \right]^{-1} S_{11}^{(p-1)}, \quad (2.24)$$

$$S_{12}^{(p)} = \tilde{s}_{12}^{(p)} + \tilde{s}_{11}^{(p)} S_{12}^{(p-1)} \left[ 1 - \tilde{s}_{21}^{(p)} S_{12}^{(p-1)} \right]^{-1} \tilde{s}_{22}^{(p)}, \quad (2.25)$$

$$S_{21}^{(p)} = S_{21}^{(p-1)} + S_{22}^{(p-1)} \tilde{s}_{21}^{(p)} \left[ 1 - S_{12}^{(p-1)} \tilde{s}_{21}^{(p)} \right]^{-1} S_{11}^{(p-1)}, \quad (2.26)$$

$$S_{22}^{(p)} = S_{22}^{(p-1)} \left[ 1 - \tilde{s}_{21}^{(p)} S_{12}^{(p-1)} \right]^{-1} \tilde{s}_{22}^{(p)}. \quad (2.27)$$

In case that the incident is from the top, then  $I = d^{(n+1)}$ . Thus the reflectance  $R$  and transmittance  $T$  are respectively derived as

$$R = S_{12}^{(n)}, \quad (2.28)$$

and

$$T = S_{22}^{(n)}. \quad (2.29)$$

### 2.2.3 Grating: modal analysis and rigorous coupled wave analysis (RCWA)

Periodic structure in the direction parallel to the surface adds more flexibility in design. In case that the periodicity is only in one direction, the structure is called a grating. The optical response of a grating is calculated by modal analysis [11]-[14] or rigorous coupled wave analysis (RCWA) [15]-[17], which is also called Fourier modal method.

In this subsection, modal analysis is explained following the analysis of the reflective double-groove grating shown in Figure 2. 7 [18]. The geometrical parameters are:  $p = 895$  nm,  $w_1 = 200$  nm,  $w_2 = 110$  nm,  $w_3 = 300$  nm,  $w_4 = 285$  nm, and  $h_g = 1030$  nm. The refractive indexes are:  $n_s = 1.45$  and  $n_g = 3.48$ . The incident angle and wavelength are  $\theta_{in} = 60^\circ$  and  $\lambda_0 = 1550$  nm, respectively.

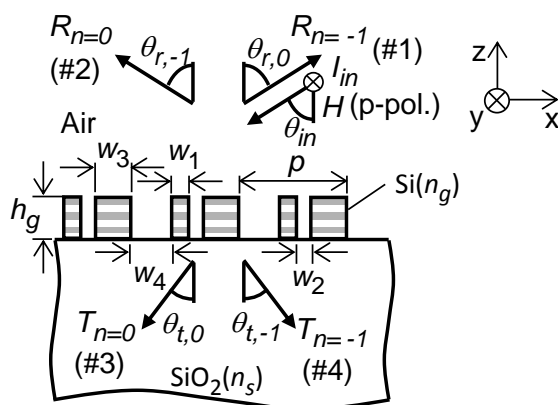


**Figure 2. 7 Reflective double-groove grating [18].**

Here, the p-polarized incidence from the  $xz$  plane is discussed. Then, magnetic fields do not have the  $x$ -component or the  $z$ -component, and thus the electromagnetic problem is reduced to the solution of the  $y$ -component of the magnetic field  $H_y$ . In homogeneous layers, the magnetic fields are expressed as the sum of diffracted plane waves. In other words, Rayleigh expansion is applied.

$$H_y^{(1)} = H_{\text{in}} \exp(-i\beta_0 x - i\gamma_0^{(1)} z) + \sum_n H_{\text{Rn}} \exp(-i\beta_n x + i\gamma_n^{(1)} z), \quad (2.30)$$

$$H_y^{(3)} = \sum_n H_{\text{Tn}} \exp(-i\beta_n x - i\gamma_n^{(3)} z), \quad (2.31)$$

where  $\beta_n$  and  $\gamma_n^{(l)}$  are the x-component and the z-component of the wavevector of

the  $n$ -th order diffraction, respectively:

$$\beta_n = (\omega/c) \sin(\theta) + n(2\pi/p), \quad (2.32)$$

$$\gamma_n^{(l)} = \begin{cases} \sqrt{\varepsilon^{(l)}(\omega/c)^2 - \beta_n^2} & (\varepsilon^{(l)}(\omega/c)^2 \geq \beta_n^2) \\ i\sqrt{\beta_n^2 - \varepsilon^{(l)}(\omega/c)^2} & (\varepsilon^{(l)}(\omega/c)^2 < \beta_n^2) \end{cases}. \quad (2.33)$$

In grating layers, the electromagnetic fields are decomposed of eigenmodes, which are characterized by the eigenfunction  $X_m(x)$  and the eigenvalue  $\Lambda_m$ . These eigenmodes are waves whose development in the  $z$ -direction is expressed by the wavenumber  $\Lambda_m$ , and development in the  $x$ -direction satisfies the periodicity of the structure. The requirement for the periodicity yields the eigenvalue equation:

$$\begin{aligned}
 & \prod_{i=1}^4 \cos \zeta_i - (\cos \zeta_1 \sin \zeta_2 \cos \zeta_3 \sin \zeta_4 + \sin \zeta_1 \cos \zeta_2 \sin \zeta_3 \cos \zeta_4) \\
 & + \frac{1}{2} \left\{ \left( \frac{k_{xa} t_g}{k_{xg}} \right)^2 + \left( \frac{k_{xg}}{k_{xa} t_g} \right)^2 \right\} \prod_{i=1}^4 \sin \zeta_i \\
 & - \frac{1}{2} \left\{ \frac{k_{xa} t_g}{k_{xg}} + \frac{k_{xg}}{k_{xa} t_g} \right\} (\cos \zeta_1 \cos \zeta_2 \sin \zeta_3 \sin \zeta_4 \\
 & + \sin \zeta_1 \sin \zeta_2 \cos \zeta_3 \cos \zeta_4 + \cos \zeta_1 \sin \zeta_2 \sin \zeta_3 \cos \zeta_4 \\
 & + \sin \zeta_1 \cos \zeta_2 \cos \zeta_3 \sin \zeta_4) = \cos(k_0 p \sin \theta_{in}),
 \end{aligned} \tag{2.34}$$

where

$$\zeta_i = \begin{cases} k_{xg} w_i & (i = 1, 3) \\ k_{xa} w_i & (i = 2, 4) \end{cases} \tag{2.35}$$

$$k_{xg} = \sqrt{(n_g \omega / c)^2 - \Lambda_m^2} \text{ and } k_{xa} = \sqrt{(\omega / c)^2 - \Lambda_m^2} \text{ and}$$

$$t_g = \begin{cases} n_g^2 & (\text{p-pol.}) \\ 1 & (\text{s-pol.}) \end{cases} \tag{2.36}$$

In this specific problem, only the first three eigenvalues are real numbers, which means that these three modes are propagative modes. Other eigenvalues are imaginary numbers, which means these modes are evanescent modes. The first three eigenfunctions and eigenvalues are shown in Figure 2. 8.

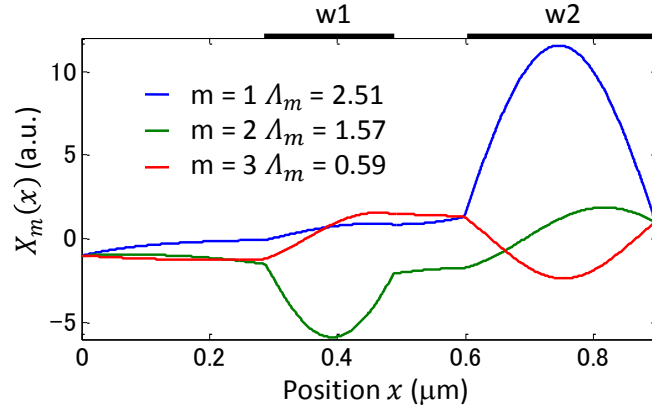


**Figure 2. 8** The first three eigenfunctions of the grating shown in Figure 2. 7

The mode  $m = 1$  has the large amplitude in the wide edge, while the mode  $m = 2$  has that in the small ridge. These three modes are dominant in this case and explain the diffraction efficiency with the accuracy of 10 %. Thus, the behavior of these three modes would give us a physical insight of the grating diffraction phenomena. By using these eigenmodes, the magnetic field in the grating layer is expressed as follows:

$$H_y^{(2)} = \sum_m X_m(x) [U_m^{(2)} \exp(i\Lambda_m z) + D_m^{(2)} \exp(-i\Lambda_m z)]. \quad (2.37)$$

Then, the diffraction problem reduces to the determination of the magnetic field amplitude vectors  $\mathbf{H}_R$ ,  $\mathbf{H}_T$ ,  $\mathbf{U}^{(2)}$ , and  $\mathbf{D}^{(2)}$ , which satisfy the boundary condition at two interfaces. In this specific problem, 17 diffraction orders and 17 modes are considered in the calculation, thus 4 equations with 4 unknown  $17 \times 17$  matrices are numerically solved.

$$\chi(\mathbf{U}^{(2)} + \mathbf{D}^{(2)}) - \mathbf{H}_R = \mathbf{I}, \quad (2.38)$$

$$\chi(\Sigma \mathbf{U}^{(2)} + \Sigma^{-1} \mathbf{D}^{(2)}) - \Delta \mathbf{H}_T = \mathbf{0}, \quad (2.39)$$

$$\Omega(\mathbf{U}^{(2)} - \mathbf{D}^{(2)}) - \Pi \mathbf{H}_R = -\Pi \mathbf{I}, \quad (2.40)$$

$$\mathbf{\Omega}(\mathbf{\Sigma}\mathbf{U}^{(2)} - \mathbf{\Sigma}^{-1}\mathbf{D}^{(2)}) + \xi\mathbf{\Delta}\mathbf{H}_T = \mathbf{0}, \quad (2.41)$$

where

$$\chi_{nm} = \int_0^p X_m(x) \exp(-i\beta_n x) dx, \quad (2.42)$$

$$\Sigma_{nm} = \exp(-i\Lambda_m h_g) \delta_{nm}, \quad (2.43)$$

$$\Delta_{nm} = \exp(i\gamma_n^{(3)} h_g) \delta_{nm}, \quad (2.44)$$

$$\Omega_{nm} = \begin{cases} \Lambda_m \int_0^p \frac{X_m(x)}{\varepsilon(x)} \exp(-i\beta_n x) dx & (\text{p-pol.}) \\ \Lambda_m \int_0^p X_m(x) \exp(-i\beta_n x) dx & (\text{s-pol.}) \end{cases}, \quad (2.45)$$

$$\Pi_{nm} = \gamma_n^{(1)} \delta_{nm}, \quad (2.46)$$

$$\xi_{nm} = \begin{cases} \gamma_n^{(3)} & (\text{p-pol.}) \\ \varepsilon^{(3)} & (\text{s-pol.}) \\ \gamma_n^{(3)} & (\text{s-pol.}) \end{cases}, \quad (2.47)$$

and  $\delta_{nm}$  is the Kronecker delta. The boundary condition problem is solved through the system of equations as shown in equations (2.38)-(2.41). Alternatively, the t-matrix as well as s-matrix method extended with a vector formalism could be utilized to solve boundary condition problems. The complexed formalism or the convergence problem in case of the multilayer structure can be avoided by matrix methods with reasonable simplicity and convergence.

Rigorous coupled wave analysis (RCWA) is similar to modal analysis. In homogeneous layers, the electromagnetic fields are decomposed by Rayleigh expansion like modal analysis. In non-homogeneous layers, the permittivity profile is Fourier-transformed in the x-direction. The electromagnetic profile in the non-homogeneous layer is expressed as the sum of spatial harmonics. The amplitude of each harmonic is derived from the boundary conditions like modal method. MATLAB

codes [19] following the textbook [17] is available.

#### 2.2.4 Near-field radiative heat transfer

The concept of emissivity is not applicable to the calculation of near-field radiative heat transfer. Fluctuational electrodynamics [20][21] has been utilized to calculate near-field coupling. Here, the heat flux across a planar gap is derived, assuming that both hot and cold bodies are semi-infinite substrate and both bodies do not have temperature gradient inside. In the following discussion, the coordinated system depicted in Figure 2. 9 is utilized.

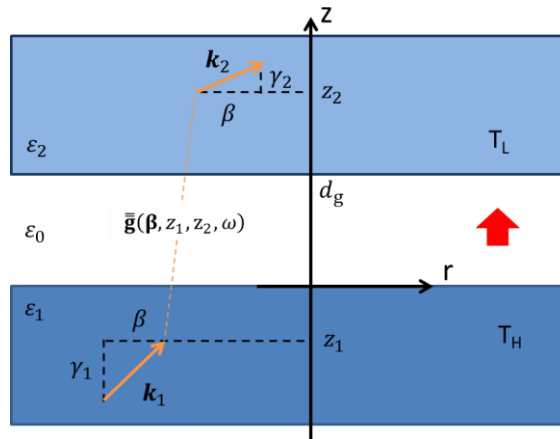


**Figure 2. 9** Two semi-infinite substrates separated with a gap.

The electric dyadic Green function  $\bar{\bar{\mathbf{G}}}(\mathbf{x}, \mathbf{x}', \omega)$  helps us write down the electric field  $\mathbf{E}(\mathbf{x}, \omega)$ .

$$\mathbf{E}(\mathbf{x}, \omega) = i\omega\mu_0 \int_V \bar{\bar{\mathbf{G}}}(\mathbf{x}, \mathbf{x}', \omega) \cdot \mathbf{j}(\mathbf{x}', \omega) d\mathbf{x}', \quad (2.48)$$

where  $\mu_0$  is permeability of vacuum and  $V$  is the region where the body exists. Thanks to the Maxwell-Farady equation, the magnetic field  $\mathbf{H}(\mathbf{x}, \omega)$  is derived from

the electric field:

$$\mathbf{H}(\mathbf{x}, \omega) = \frac{1}{i\omega\mu_0} \nabla \times \mathbf{E}(\mathbf{x}, \omega). \quad (2.49)$$

The emitted energy flux from the body observed at the point  $\mathbf{x}$ ,  $\langle \mathbf{S}(\mathbf{x}, \omega) \rangle$ , is calculated by the ensemble average of the Poynting vectors:

$$\begin{aligned} \langle \mathbf{S}(\mathbf{x}, \omega) \rangle &= \frac{1}{2} \langle \text{Re}[\mathbf{E}(\mathbf{x}, \omega) \times \mathbf{H}^*(\mathbf{x}, \omega)] \rangle \\ &= \frac{1}{2} \text{Re} \left[ i\omega\mu_0 \int_V d\mathbf{x}' \int_V d\mathbf{x}'' \bar{\bar{\mathbf{G}}}(\mathbf{x}, \mathbf{x}', \omega) \langle \mathbf{j}(\mathbf{x}', \omega) \right. \\ &\quad \left. \times \mathbf{j}^*(\mathbf{x}'', \omega) [\nabla \times \bar{\bar{\mathbf{G}}}(\mathbf{x}, \mathbf{x}'', \omega)]^* \right] \end{aligned} \quad (2.50)$$

The position  $\mathbf{x}$  can be rewritten as

$$\mathbf{x} = \mathbf{R} + z\hat{\mathbf{z}}, \quad (2.51)$$

where  $\mathbf{R}$  does not have  $z$ -component, and  $\hat{\mathbf{z}}$  is the unit vector in the  $z$  direction. The absolute value of  $\mathbf{R}$  is omitted because of the one-dimensional structure. Thus, two-dimensional spatial Fourier transform can be applied to Green functions:

$$\bar{\bar{\mathbf{G}}}(\mathbf{R} - \mathbf{R}', z, z', \omega) = \iint_{-\infty}^{\infty} \frac{d\boldsymbol{\beta}}{(2\pi)^2} \bar{\bar{\mathbf{g}}}(\boldsymbol{\beta}, z, z', \omega) e^{i\boldsymbol{\beta} \cdot (\mathbf{R} - \mathbf{R}')}, \quad (2.52)$$

where  $\boldsymbol{\beta}$  is the wavevector in the  $x$ - and  $y$ - directions. Thanks to the azimuthal symmetry of the structure, a cylindrical coordinate system  $(\rho, \varphi, z)$  is utilized for the modelling. Then the integration over wavevector is written as:

$$\iint_{-\infty}^{\infty} d\boldsymbol{\beta} = \int_{\beta=0}^{\infty} \int_{\varphi=0}^{2\pi} \beta d\beta d\varphi = 2\pi \int_{\beta=0}^{\infty} \beta d\beta, \quad (2.53)$$

where  $\beta = |\boldsymbol{\beta}|$ .

Furthermore, Weyl components of the dyadic Green function  $\bar{\bar{\mathbf{g}}}$  are expressed as:

$$\bar{\mathbf{g}}(\boldsymbol{\beta}, z, z', \omega) = -\frac{i}{2\gamma_1} [\hat{\mathbf{s}} t_{12}^s \hat{\mathbf{s}} + \hat{\mathbf{p}}_2 t_{12}^p \hat{\mathbf{p}}_1] e^{i\gamma_2 z - i\gamma_1 z'}, \quad (2.54)$$

where  $\hat{\mathbf{s}}$  and  $\hat{\mathbf{p}}_i$  are the s-polarized and the p-polarized unit vectors, respectively,

$$\hat{\mathbf{s}} = \begin{pmatrix} -\sin(\varphi) \\ \cos(\varphi) \\ 0 \end{pmatrix}, \quad (2.55)$$

$$\hat{\mathbf{p}}_i = \frac{c}{n_i \omega} \begin{pmatrix} -\gamma_i \cos(\varphi) \\ -\gamma_i \sin(\varphi) \\ \beta \end{pmatrix}, \quad (2.56)$$

and  $t_{12}^s$  and  $t_{12}^p$  are the transfer function from the body 1 to the body 2 in the s and p polarizations, respectively. The z-component Poynting vector observed at  $z = d_g$  is expressed as the integration of the exchange function over all the wavenumbers as follows:

$$\langle S_z(z = d_g, \omega) \rangle = \theta(\omega, T) \sum_{j=s,p} \int_0^{+\infty} Z(\omega, \beta, j) \beta d\beta, \quad (2.57)$$

where the Planck's oscillator is written as:

$$\theta(\omega, T) = \frac{\hbar\omega}{\exp(\hbar\omega/k_B T) - 1}, \quad (2.58)$$

and the exchange function in the polarization  $j$  is written as:

$$Z(\omega, \beta, j = s) = \frac{1}{4\pi^2} |t_{12}^s|^2 \frac{\text{Re}(\gamma_1) \text{Re}(\gamma_2)}{|\gamma_1|^2}, \quad (2.59)$$

$$Z(\omega, \beta, j = p) = \frac{1}{4\pi^2} |t_{12}^p|^2 \frac{\text{Re}(\varepsilon_1 \gamma_1^*) \text{Re}(\varepsilon_2 \gamma_2^*)}{|n_1|^2 |n_2|^2 |\gamma_1|^2}. \quad (2.60)$$

$Z(\omega, \beta, j)$  is further simplified by discriminating the case of the propagative coupling and evanescent coupling:

$$Z(\omega, \beta < k_0) = \frac{(1 - |r_{01}|^2)(1 - |r_{02}|^2)}{4|1 - r_{01}r_{02}e^{2i\gamma_0 d_g}|^2}, \quad (2.61)$$

$$Z(\omega, \beta > k_0) = \frac{\text{Im}(r_{01})\text{Im}(r_{02})e^{-2\text{Im}(\gamma_0)d_g}}{|1 - r_{01}r_{02}e^{-2\text{Im}(\gamma_0)d_g}|^2}. \quad (2.62)$$

Radiative heat flux is calculated from the integral of the z-component Poynting vector over all frequencies. Net heat flux  $\phi$  is derived by subtracting the downward heat flux from the upward heat flux:

$$\phi = \frac{1}{\pi^2} \int_0^{+\infty} d\omega [\theta(\omega, T_H) - \theta(\omega, T_L)] \sum_{j=s,p} \int_0^{+\infty} Z(\omega, \beta, j) \beta d\beta. \quad (2.63)$$

If distance  $d$  is large enough, the evanescent components are eliminated and the interference inside the gap can be neglected. The exchange function is approximated as:

$$\int_0^{+\infty} Z(\omega, \beta, j) \beta d\beta \approx \int_0^{\frac{\omega}{c}} \frac{(1 - |r_{01}|^2)(1 - |r_{02}|^2)}{4} \beta d\beta. \quad (2.64)$$

In case that the reflectance is independent of frequency, wavevector, and polarization, we can define the constant emissivity  $E_i$ :

$$E_i = 1 - |r_{0i}|^2. \quad (2.65)$$

Then heat flux is approximated as

$$\begin{aligned} \phi &\approx \int_0^{+\infty} d\omega \frac{\hbar\omega^3}{4\pi^2 c^2} \left[ \frac{1}{\exp(\hbar\omega/k_B T_H) - 1} - \frac{1}{\exp(\hbar\omega/k_B T_L) - 1} \right] E_1 E_2 \\ &= \frac{\pi^2 k_B^4}{60 c^2 \hbar^3} (T_H^4 - T_L^4) E_1 E_2, \end{aligned} \quad (2.66)$$

which is consistent with the Planck's law, and Stefan-Boltzmann law.

### 2.3 Microfabrication technologies

In the last two decades, the precision of microfabrication technology is improved due to the large demand from VLSI industries. Tremendous efforts have been paid to follow Moore's law by inventing numbers of new microfabrication techniques including reactive-ion-etching (RIE) and deep ultraviolet lithography. Such technologies enable subwavelength structure with novel nanophotonic response to control thermal emission and absorption. These technologies contribute to manufacture submicron gaps, which is mandatory for near-field radiative heat transfer.

In this work, electron-beam lithography, reactive-ion-etching, sputtering, deep ultraviolet lithography, and wet-etching were utilized. In this subsection, the general procedure and remarks on lithography and etching are explained.

#### 2.3.1 Lithography techniques

Lithography is the technique to pattern the photosensitive organic film, or photoresist, for subsequent processes including etching and implantation. In general, it contains six steps as shown in Figure 2. 10. Taking the deep-ultraviolet-photolithography with positive resist as an example, these steps are explained.

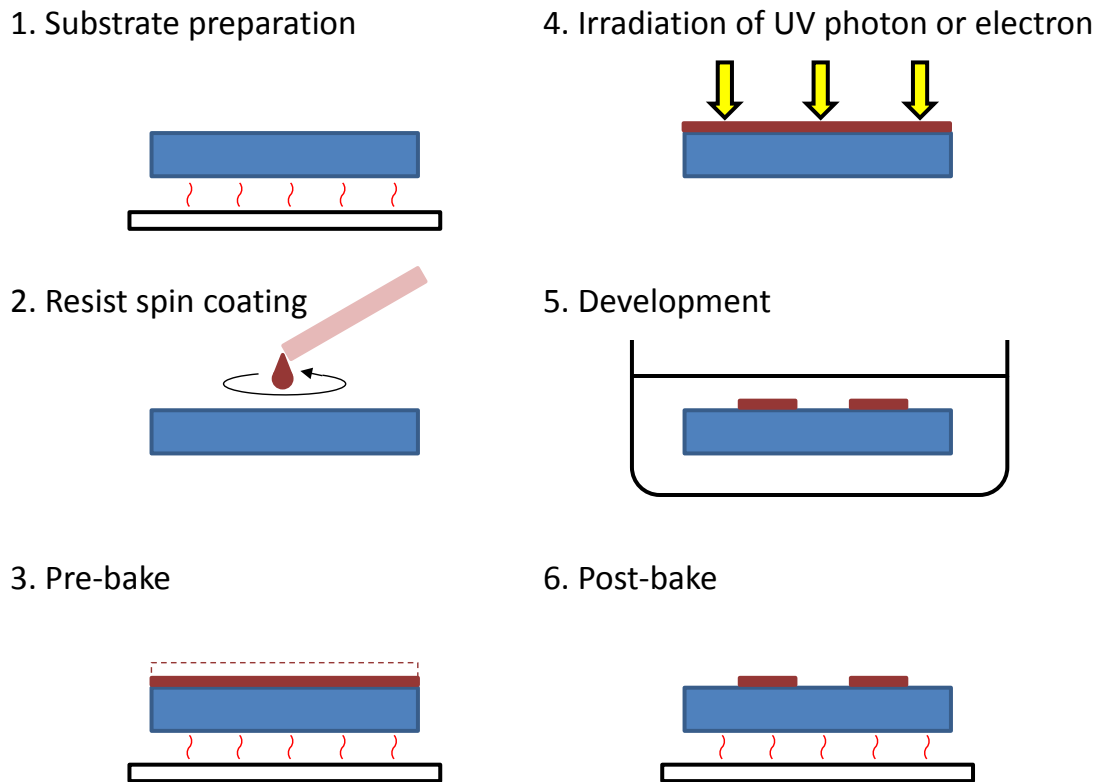


**Figure 2. 10 Six steps of lithography.**

The first step of lithography is the substrate preparation. This is one of the important steps because the adhesion between the photoresist and the substrate might affect the yield, especially in case that isolated resist patterns are planned to be formed. The isolated patterns with weak adhesion might be washed away during subsequent processes. To improve the adhesion, the substrate should be cleaned with a proper chemical solution like sulfuric acid with hydrogen peroxide or acetone. After cleaning, the remaining water molecules should be removed by dehydration bake at the temperature higher than 100 °C. Finally, the surface bonds of the substrate are terminated with an organic functional group, by coating hexamethyl disilazane (HMDS). Such organic functional group provides good adhesion between photoresist and the substrates.

The second step is spin-coating of photoresist. The rotation speed of spin-coating controls the thickness of the resist. In general, thinner resist film is preferred for lithography with fine patterns. The resist pattern with high aspect-ratio would be blurred because of the finite depth-of-focus or fragility against development procedure. On the other hand, resist pattern should have enough thickness for subsequent process such as etching or lift-off. Etching chemicals do not only attack the film beneath the resist, but also damage the photoresist. The photoresist should be sufficiently thick to be tolerant against the designed etching time. Lift-off process needs thicker resist than the deposited film, otherwise the opening at the edge of the pattern would disappear, i.e. the failure of the lift-off. The rotation speed should be designed to coat the photoresist with the required thickness.

The third step is pre-bake, which evaporates the residual solvent from the resist film. Without this procedure, the resist does not become solid enough. In the case of contact lithography, the substrate and the mask might stick to each other.

The fourth step is exposure. In the case of contact photolithography, the photomask made of glass plate and chromium patterns is impressed towards the substrate. The ultraviolet light illuminates the substrate through the photomask, and the organic molecules in the resist film change its structure according to the illumination. In the case of the electron-beam lithography, electrons affect organic molecules. Highly-accelerated electron beam is scanned over the substrate to achieve designed patterns. As well-known, the proximity effect deviates the resist pattern from the designed pattern. The physical origins of the proximity effect are [22]: the diffraction limit, the distance between photomask and the substrate, the non-ideality of the optical beam, and the scattering of the electron. To eliminate such proximity effect, the dose or

the exposure time should be optimized.

The fifth step is the development, which dissolves the part of the resist film. If the resist have positive tone, the illuminated part is dissolved because the exposure induce solubility to the development chemicals. On the other hand, the illumination links the molecules of the negative resist to decrease the solubility to the developer solution. The development time and the exposure dose should be simultaneously optimized to minimize the proximity effect. Chemically amplified resist needs the post-exposure-bake before development.

The sixth step is the post-bake. The remaining development chemical and the rinse solution are evaporated for the subsequent processes.

As explained, each step of lithography as well as exposed patterns should be optimized to achieve the best results.

### 2.3.2 Etching techniques

There are two types of etching techniques. The first one, wet-etching utilizes the chemicals in liquid-phase. The substrate is immersed for certain minutes calculated from the measured etch-rate and the desired etching thickness.

The ratio of the etch rate between two materials is called selectivity, and the etchant with high selectivity is generally required. Selectivity against both the film underneath the etched film and the mask for etching is important. For example, buffered hydrofluoric acid (BHF) is widely utilized to etch silicon dioxide without damaging silicon substrate because of the high selectivity against the silicon and the photoresist. Furthermore, the etch-rate of BHF is relatively constant because BHF consists of hydrofluoric acid (HF) and buffering agent such as ammonium fluoride ( $\text{NH}_4\text{F}$ ).

Wet etching is known as an isotropic process. Because the chemical agent etches the target material isotropically, etchant undercuts the masking layer. The resulting sidewalls are slopes, and they are ideally round-shaped. The masking layer should be designed considering the effect of the undercut.

The second etching technique, dry-etching, utilizes plasma to etch films. In case that the pressure of plasma is high and acceleration voltage is low, the etching is driven by chemical reaction between the free radicals from plasma and the material consist of the target film. High-selectivity and isotropic etching profile is achieved by such a process condition. In the other extreme where the pressure is low and the acceleration voltage is high, the etching is driven by the sputtering against the film. Highly anisotropic etching enables high-aspect trenches with the cost of low selectivity. The operation point of the reactive-ion-etching (RIE) is set in the middle of these two extreme to achieve acceptable selectivity and anisotropy. The chemicals of plasma, the ratio of these, the pressure, and the RF power are optimized to find a compromise in the tradeoff.

#### 2.4 Evaluation methodologies

The spectral response or the integrated heat flux of manufactured thermal radiation devices is evaluated. The spectral response was measured by Fourier-transform infrared spectrometer. A steady-state heat flux measurement system was developed to measure the integrated heat flux.

### 2.4.1 Fourier-transform infrared spectroscopy (FT-IR)

Fourier-transform infrared spectrometer consists of a light source, a Michelson interferometer, a sample chamber, and a detector as depicted in Figure 2. 11. The light source needs to cover a broad spectrum, thus blackbody radiator with an elevated temperature is normally utilized. The Michelson interferometer splits the light from the source evenly between toward the stationary mirror and the moving mirror. The light reflected back from the mirrors interfere each other, and the interfered light illuminates the sample. The spectrum of the interfered light depends on the position of the moving mirror. The amount of the light pass through the sample is recorded by the detector. The iterative measurement while moving the mirror achieves the relationship between the position of the mirror and the amount of the light. The Fourier transform of this relationship gives us transmittance spectrum of the sample by comparing the data with and without the sample.

In this work, Nicolet iS50 FT-IR spectrometer from Thermo Scientific was utilized. For the reflectivity measurement, a specular reflectance accessory (VeeMax II, 10 Spec) was utilized.

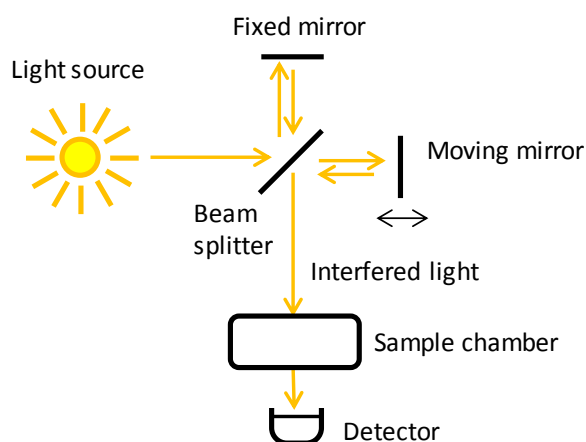


**Figure 2. 11 Schematic illustration of Fourier-transform infrared spectrometer**

### 2.4.2 Steady-state heat flux measurement system

The heat flux measurement system built and utilized in this thesis works in the steady-state. For ease of analysis, the heat is designed to flow in one-dimensional i.e. the temperature distribution perpendicular to heat flow is quasi-uniform.

The schematic illustration of the apparatus is shown in Figure 2. 12. The heat generated by the heater (Sakaguchi E.H. Voc. Corp., MS-M1000) is homogenized by the copper heat spreader. Then heat flows into the emitter substrate through thermal gap pad. The flux is radiatively transferred from the emitter surface to the receiver surface. The heat flux is measured by the heat flux sensor (Concept Engineering) based on a thermopile, in which thermocouples are connected in series to generate large voltage according to the temperature difference of the opposing side of the sensor. The temperatures of the substrates are monitored by the K-thermocouples (Okazaki manufacturing company) inserted into the pads. The temperatures are controlled to be constant by the heater and the thermoelectric device (Z-max, FPH1-12708AC) to enable steady-state measurement. The bottom side of the thermoelectric device is cooled by the refrigerant circulated by a chiller (Taitec, CL-150R). The diameter of the thermocouples is only 0.15 mm, thus the parasitic heat conduction through the thermocouples is smaller than 0.5% of the blackbody radiation.

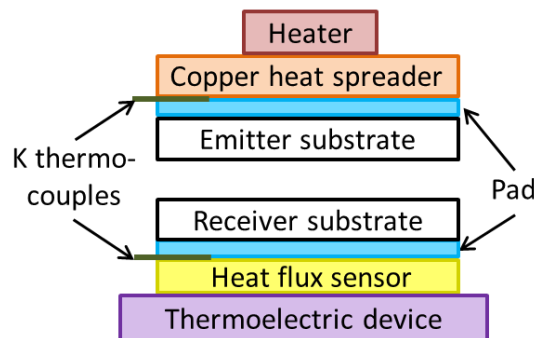


**Figure 2. 12 Schematic illustration of the steady-state heat flux measurement**

The photograph of the apparatus is shown in Figure 2. 13. The size of the emitter and the receiver is 19 mm×8.6 mm to fit the size of the heat flux sensor. The copper heat spreader is supported by the post made of ceramics.

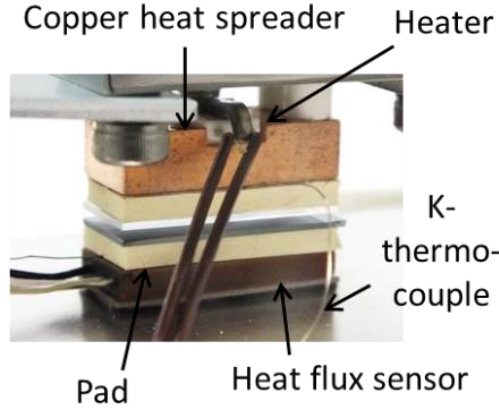


**Figure 2. 13 Photograph of the steady-state heat flux measurement**

The conductive heat flux  $\Phi$  through the rarefied air at a pressure  $P$  is calculated as:

$$\Phi = (T_H - T_L) \frac{\lambda_{\text{air}}}{d} \frac{P/P_0}{1 + P/P_0}, \quad (2.67)$$

$$P_0 = \frac{\lambda_{\text{air}}(T_H + T_L)/2}{dv_{\text{air}}}, \quad (2.68)$$

$$v_{\text{air}} = \sqrt{\frac{3k_B(T_H + T_L)/2}{\pi m_{\text{air}}}}, \quad (2.69)$$

where  $P_0$  is the critical pressure,  $\lambda_{\text{air}} = 0.0241 \text{ Wm}^{-1}\text{K}^{-1}$  is the thermal conductivity of the air,  $v_{\text{air}}$  is the averaged velocity of the molecules, and  $m_{\text{air}} = 4.78 \times 10^{-26} \text{ kg}$  is the averaged molecular weight.  $T_H$  is the temperature of the emitter substrate,  $T_L$  is the temperature of the receiver substrate,  $d$  is the distance between the emitter and the receiver,  $k_B$  is the Boltzmann constant. The calculated conductive heat flux across the

air gap is shown in Figure 2. 14. The heat fluxes across 1 mm gap and 1  $\mu\text{m}$  gap are the same at the pressures lower than 1 Pa, which indicates that the heat transfer is almost ballistic in this pressure range.

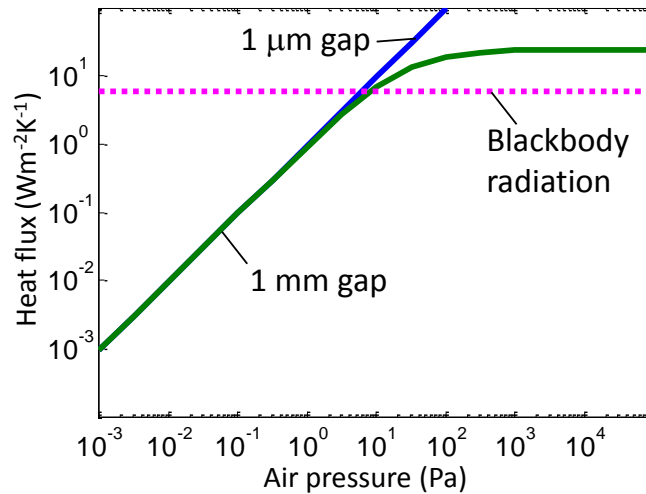


**Figure 2. 14** Conductive heat flux through air as a function of air pressure.

In order to eliminate the conductive flux smaller than 0.5 % of the blackbody radiation, whole the system are installed in a vacuum chamber evacuated to a pressure lower than  $5 \times 10^{-3}$  Pa. Two turbo molecular pumps connected in series and a rotary pump are utilized to realize the required vacuum condition.

### 2.5 Chapter summary

This chapter has introduced the theory of thermal radiation and the methodologies employed in this work. The Maxwell's equation, spectral intensity, emissivity, and view factor were explained for the discussion in the subsequent chapters. Electromagnetic simulation techniques were described for the design and modelling of thermal radiation devices. Fabrication methodologies were explained for the experimental demonstration of microstructured thermal devices. Evaluation methodologies including Fourier-transform infrared spectrometer and heat flux measurement system were also described.

**Reference**

- [1] H. A. Haus, "Waves and Fields in Optoelectronics (Prentice-Hall series in solid state physical electronics)." (1984).
- [2] J. R. Howell, R. Siegel, and M. P. Menguc. Thermal radiation heat transfer. CRC press, 2010.
- [3] D. Polder and M. Van Hove, Theory of radiative heat transfer between closely spaced bodies , Phys. Rev. B **4**, 3303 (1971).
- [4] J. J. Greffet, and M. Nieto-Vesperinas. "Field theory for generalized bidirectional reflectivity: derivation of Helmholtz's reciprocity principle and Kirchhoff's law." JOSAA **15**, 2735-2744 (1998).
- [5] M. F. Modest, Radiative heat transfer. Academic press, 2013.
- [6] <http://www.thermalradiation.net/indexCat.html>
- [7] <http://webserver.dmt.upm.es/~isidoro/tc3/Radiation%20View%20factors.pdf>
- [8] J. J. Greffet and M. Nieto-Vesperinas. "Field theory for generalized bidirectional reflectivity: derivation of Helmholtz's reciprocity principle and Kirchhoff's law." J. Opt. Soc. Am. A **15**, 2735 (1998).
- [9] CST microwave studio 2013, <https://www.cst.com/>
- [10] L. Li, "Formulation and comparison of two recursive matrix algorithms for modeling layered diffraction gratings." J. Opt. Soc. Am. A **13**, 1024 (1996).
- [11] P. Sheng, R. S. Stepleman, and P. N. Sanda. "Exact eigenfunctions for square-wave gratings: Application to diffraction and surface-plasmon calculations." Phys. Rev. B **26**, 2907 (1982).
- [12] L. Li, "A modal analysis of lamellar diffraction gratings in conical mountings." J. Mod. Opt. **40**, 553 (1993).

- [13] T. Clausnitzer, T. Kämpfe, E. B. Kley, A. Tünnermann, U. Peschel, A. V. Tishchenko, and O. Parriaux. "An intelligible explanation of highly-efficient diffraction in deep dielectric rectangular transmission gratings." *Opt. Exp.* **13**, 10448 (2005).
- [14] H. Iizuka, N. Engheta, H. Fujikawa, K. Sato, and Y. Takeda. "Role of propagating modes in a double-groove grating with a+ 1st-order diffraction angle larger than the substrate–air critical angle." *Opt. Lett.* **35**, 3973 (2010).
- [15] M. G. Moharam, and T. K. Gaylord. "Rigorous coupled-wave analysis of planar-grating diffraction." *J. Opt. Soc. Am. A* **71**, 811 (1981).
- [16] M. G. Moharam, T. K. Gaylord, E. B. Grann, and D. A. Pommet. "Formulation for stable and efficient implementation of the rigorous coupled-wave analysis of binary gratings." *J. Opt. Soc. Am. A* **12**, 1068 (1995).
- [17] H. Kim, J. Park, and B. Lee. *Fourier modal method and its applications in computational nanophotonics*. CRC Press, 2012.
- [18] K. Ito and H. Iizuka. "Highly efficient-1st-order reflection in Littrow mounted dielectric double-groove grating." *AIP Adv.* **3**, 062119 (2013).
- [19] [https://www.crcpress.com/downloads/88386/MATLAB\\_codes.zip](https://www.crcpress.com/downloads/88386/MATLAB_codes.zip)
- [20] D. Polder and M. Van Hove, Theory of radiative heat transfer between closely spaced bodies , *Phys. Rev. B* **4**, 3303 (1971).
- [21] C. J. Fu, and Z. M. Zhang. "Nanoscale radiation heat transfer for silicon at different doping levels." *International Journal of Heat and Mass Transfer* **49**, 1703 (2006).
- [22] 佐々木実、”レジストプロセスの基本”電気学会論文誌. E, センサ・マイクログラフ部門誌 **131**, 2-7 (2011).

## *Chapter 3 Dynamic modulation of thermal radiation*

This chapter theoretically demonstrates dynamic modulation of thermal radiation. The guided mode resonance in a grating and the surface polariton on an interface are resonantly coupled to each other in order to control emissivity. The coupling strength is tuned by changing the distance between the grating and the interface, resulting in the dynamic modulation of thermal radiation. The amplitude of emissivity modulation at a wavelength of 12.13  $\mu\text{m}$  is larger than 0.9, which exceeds those reported in preceding works. As practical implementations, surface phonon polariton on a silicon carbide substrate and surface plasmon polariton on a doped silicon slab are investigated. The factors which affect the sharpness of the resonance is also discussed.

### 3.1. Introduction

#### 3.1.1 Motivation

In the field of automotive engineering, various types of gases are measured for monitoring the exhaust and the ambient of car-cabin. Nondispersive infrared (NDIR) sensing [1]-[3], where the gas concentration is estimated from the absorption of infrared light, has advantages of high reliability and selectivity compared to electrochemical [4], catalytic [5], or metal-oxide gas sensors [6]. Each gas has a characteristic absorption spectrum, thus the spectroscopic analysis gives us not only the concentration but also the composition of the ambient. In this field, thermal emitter is widely utilized as a light source, and the amplitude of infrared light is dynamically modulated in order to eliminate the low frequency noise from background.

Conventionally, such dynamic modulation of the thermal radiation is achieved by modulating the emitter temperature or by using a mechanical chopper. Thus, the speed of the modulation is limited by the heat capacity of the thermal emitter or the rotation speed of the chopper. In contrast, the modulation of emissivity provides faster modulation of thermal radiation. To this end, the deformation of a resonant subwavelength structure is employed in this study. Because the electromagnetic resonant frequency and strength are dependent on the geometrical parameters of subwavelength structures, the deformation of the structure enables the dynamic control of emissivity. The dynamic control of electromagnetic response is demonstrated in the terahertz regime by utilizing microfabricated electrostatic actuators [7]. The next subsection presents a brief review of emissivity control by subwavelength structures.

### 3.1.2 Preceding works on emissivity control by subwavelength structures

Taming emissivity by subwavelength structures is attracting broad interest because of its controllability through geometrical parameters. Pioneering works have shown that emissivity is designed by utilizing several types of electromagnetic resonances around the turn of the millennium [8][15][39].

Yugami and his colleagues utilized resonance in cubic microcavities made of metals [8][9]. In each microcavity, standing waves are thermally excited at certain wavelengths determined by the cavity length, and these waves are emitted as thermal radiation. Arrayed microcavities made of metals were micromachined to enhance the emissivity in a specific frequency band while suppressing that in lower frequencies. Numbers of modes additively contribute to the enhancement, and thus the thermal emission become broadband rather than monochromatic. The thermal emitter was designed for thermophotovoltaics.

Lately, high-aspect metallic microcavities have been presented [10]-[14]. Selected resonant modes are excited in these cavities, resulting in more monochromatic emission. Miyazaki and his colleagues manufactured vertical grating cavities made of gold [10][11]. The emission is observed around 5  $\mu\text{m}$ , and it is highly polarized due to the grating structure. Padilla and his colleagues investigated horizontal cavities [14]. A gold top layer is cross-shaped and it is placed on an insulator layer and a gold ground plane, which form metal-insulator-metal (MIM) trilayer. Such MIM metamaterials are discussed in Chapter 4 in this thesis.

Dielectric photonic crystal slabs have been utilized for the control [15]-[21]. The guided mode inside the slab is diffracted by the periodically perforated holes, to couple to propagative wave according to the dispersion relationship of the photonic crystal. If

the permittivity of the slab has an imaginary part, the guided mode is thermally excited. Thus, the resulting thermal emission characteristics show resonant behavior. Especially, Noda and his colleagues have controlled the permittivity of the slab by multiple quantum well [18]-[20]. The imaginary part of the permittivity is set to be large around the emission wavelength, whereas it is low at the other part of spectrum. Thus, monochromatic thermal emission is obtained by utilizing such a structure. The group has also investigated the dynamic control [21]. The depletion of the quantum well is achieved by applying a reverse bias voltage, thus thermal emission is suppressed. Their thermal emitters demonstrate promising performance with the cost of the expensive component: the quantum well based on epitaxial GaInAs.

Other subwavelength structures including metallic photonic crystals [22][23], nano-antennas made of polar materials [24][25], and graphene [26]-[28] have been presented. Recently, electronic modulation of thermal radiation was demonstrated by doping graphene nano-ribbons [28]. The emissivity modulation with an amplitude of 4 % was observed.

### 3.2 Coupling of guided mode resonance and surface polariton

This work presents a thermal emitter profiting from the coupling between the surface polariton on a flat surface and the guided mode resonance in a dielectric grating. A schematic of such coupling is shown in Figure 3. 1. This coupling enables the dynamic modulation of emissivity and directional emission. The coupling is mediated by the evanescent waves, and is achieved by carefully matching the lateral wavevector of the surface polariton and that of the guided mode resonance. The coupling strength is determined by the distance between the surface which supports the polariton and the grating where the guided mode is excited, and thus the emissivity is also controlled by the distance. A double-grooved asymmetric grating is employed to obtain asymmetric thermal radiation, through asymmetric coupling between propagative wave and guided mode resonance.

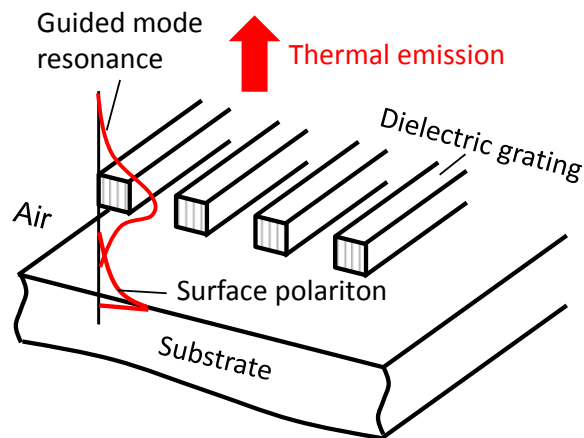


**Figure 3. 1 Coupling of guided mode resonance and surface polariton [56]**

### 3.2.1 Guided mode resonance (GMR)

A properly designed subwavelength grating reflects the incident light with the efficiency close to unity [29]-[34]. Upon reflection, strong electromagnetic field is excited in the grating layer. The excited resonant electromagnetic field is regarded as a guided mode propagating in the grating layer, in the direction perpendicular to grating stripes. The incident light couples to the guided mode through the diffraction phenomena. Figure 3. 2 shows the reflectivity of subwavelength gratings. Resonant reflection is attained by selecting the width and the height of the grating. Guided-mode resonant gratings have potential applications of filters [29]-[31] and reflectors [32][33]. In this study, the grating for the guided mode resonance is set to be lossless i.e. thermally transparent.

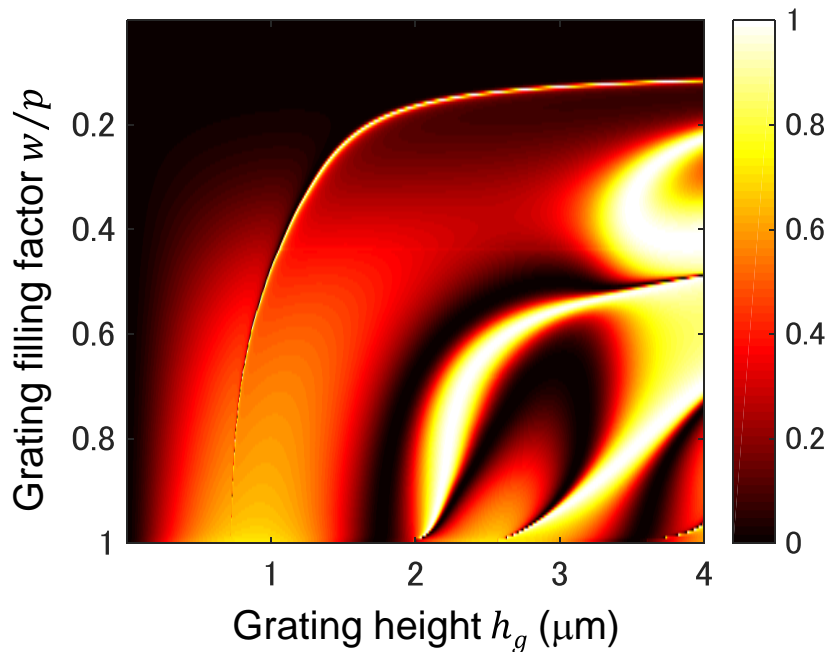


**Figure 3. 2 Reflectivity of a subwavelength grating with silicon ridges ( $n = 3.48$ ).**

**Grating period is  $11.9 \mu\text{m}$ , and incident wavelength is  $12.13 \mu\text{m}$ .**

### 3.2.2 Surface polariton

Surface polariton is the collective oscillation of electromagnetic field around a surface and charges in a material. It is excited at the frequencies where the real part of the permittivity of the material is negative. In case that free electrons in metals or semiconductors cause the resonance, it is called surface plasmon polariton (SPP). Likewise, a polariton with a certain vibration mode of ionic atoms in a polar material is called surface phonon polariton (SPhP). SPP is excited at the frequencies lower than the plasma frequency, while SPhP is excited only around the resonant frequency of optical phonon. Some surface polariton exhibit extremely high-Q resonance: SPP on noble metals [35], SPP on graphene [36][37], and SPhP on a silicon carbide (SiC) substrate [38].

Greffet and his colleagues employed SPhP on SiC for the control of thermal radiation [38]-[41]. The authors etched an SiC substrate to achieve a surface relief grating, and diffracted SPhP to couple to p-polarized propagative wave. The emissivity is quasi-monochromatic when observed at a certain angle, and the relation of the emission frequencies and the emission angles follows the dispersion relationship of SPhP. Recently, the group investigated the electric modulation of emissivity through the intersubband transition in a quantum-well [42]. The quantum-well is composed of polar materials, namely GaAs/AlGaAs. The surface phonon mode around the quantum-well decays through the intersubband transition, and it couples to the propagative wave through the grating. By applying a voltage, the emissivity varies with an amplitude of 9 %.

### 3.3 Thermal emitter with surface phonon polariton (SPhP)

#### 3.3.1 Permittivity of silicon carbide (SiC)

The permittivity of silicon carbide is governed by optical phonons around the frequency of  $1.5 \times 10^{14}$  rad/s. The optical phonon of 3C-SiC splits into two modes, namely longitudinal optical (LO) phonon and transverse optical (TO) phonon. The relative permittivity of 3C-SiC is described as:

$$\varepsilon_{\text{SiC}} = \varepsilon_{\text{inf}} \left\{ 1 + \frac{\omega_{\text{LO}}^2 - \omega_{\text{TO}}^2}{\omega_{\text{TO}}^2 - \omega^2 - i\gamma\omega} \right\}, \quad (3.1)$$

where  $\varepsilon_{\text{inf}}$  is the permittivity in the high frequency limit,  $\omega_{\text{LO}}$  and  $\omega_{\text{TO}}$  are the frequency of LO- and TO-phonon, respectively, and  $\gamma = 8.92 \times 10^{11}$  rad/s is the damping coefficient. The parameters of  $\omega_{\text{LO}}$ ,  $\omega_{\text{TO}}$  and  $\varepsilon_{\text{inf}}$  are described as [43]:

$$\omega_{\text{LO}} = \frac{2\pi c}{98100 - 2.9T} \text{ (rad/s)}, \quad (3.2)$$

$$\omega_{\text{TO}} = \frac{2\pi c}{80400 - 2.18T} \text{ (rad/s)}, \quad (3.3)$$

$$\varepsilon_{\text{inf}} = 6.52 + 0000326(T - 300) \quad (3.4)$$

where  $T$  is the temperature of 3C-SiC.  $T = 773$  K is employed to model the thermal emitter using 3C-SiC. The permittivity of 3C-SiC is shown in Figure 3. 3.

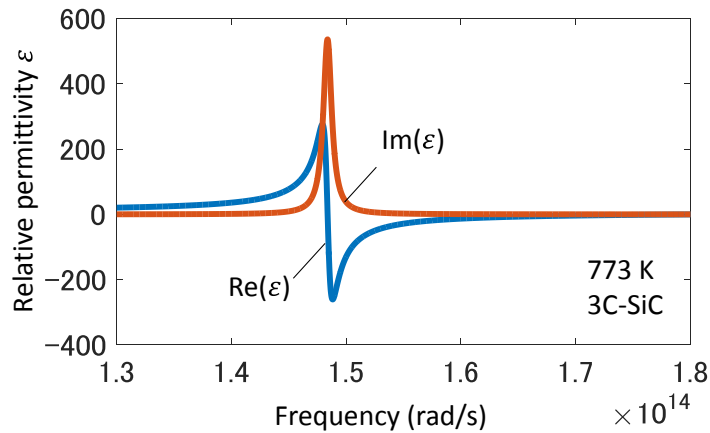


**Figure 3. 3 Relative permittivity of 3C-SiC**

As shown in Figure 3. 3, the permittivity drastically changes according to the frequency. This resonant permittivity induces a highly resonant SPhP at the interface between SiC and dielectrics. The dispersion relationship of SPhP on SiC is calculated as:

$$\beta = \frac{\omega}{c} \sqrt{\frac{\varepsilon_{\text{SiC}}\varepsilon_{\text{d}}}{\varepsilon_{\text{SiC}} + \varepsilon_{\text{d}}}}, \quad (3.5)$$

where  $\beta$  is the lateral wavenumber,  $c$  the speed of light,  $\varepsilon_{\text{d}}$  the permittivity of dielectrics. The dispersion relationship is calculated with  $\varepsilon_{\text{d}} = 1$ , and is shown in Figure 3. 4. The wavevector is highly enhanced around  $930 \text{ cm}^{-1}$ , owing to the resonant permittivity of SiC.

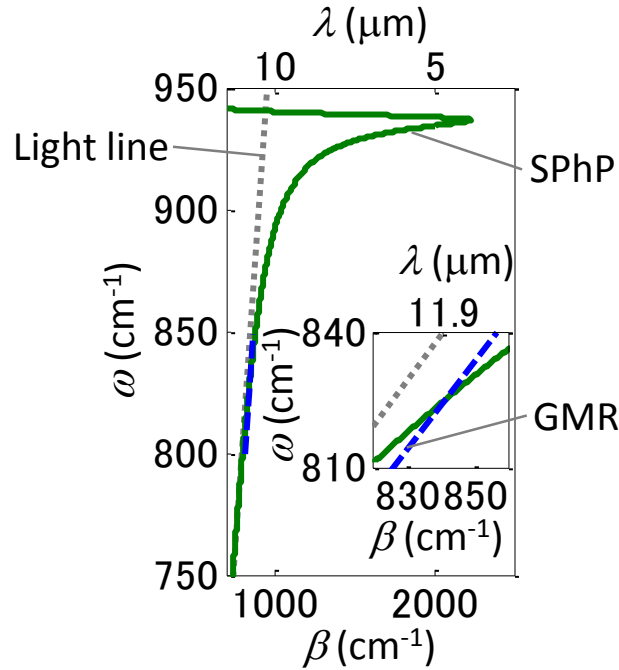


**Figure 3. 4 Dispersion relation of the SiC-SPhP (green line) and the guided mode resonance (GMR) (blue dotted line) [56]**

## 3.3.2 Structure of the thermal emitter

The thermal emitter utilizing SiC-SPhP is shown in Figure 3. 5. The thermal emitter comprises a silicon grating and a semi-infinite SiC substrate. The emitter consists of 4 layers, and these layers are named from Layer 1 to Layer 4 as shown in Figure 3. 5. The grating period  $p$  is designed so as to excite a diffracted wave with a lateral wavenumber which matches with the dispersion relation of the SPhP. As shown in Figure 3. 4, the dispersion relation of the SPhP and that of the guided mode resonance crosses out of the light line, indicating that the guided mode and the SPhP interact with each other through evanescent waves in Layer 3. The distance between the grating and the SiC substrate  $d_a$  is chosen such that the interaction is constructive, i.e. normal incident light is totally absorbed at the SiC/air interface. At first, the p-polarized incidence from the normal direction is considered i.e., the Poynting vector is directed to the negative z-direction and the magnetic field is parallel to the y-axis. Owing to the Kirchhoff's law, the optical absorption is translated to the thermal radiation toward the positive z-direction.

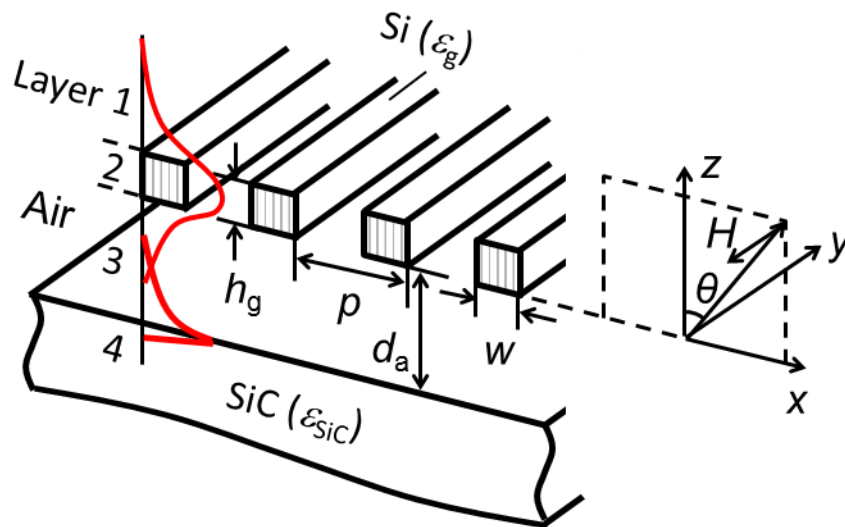


**Figure 3. 5 Thermal emitter utilizing a resonant grating and SPhP on SiC substrate**

[56]

### 3.3.3 Modal analysis formalism

A modal analysis [48]-[51] was developed to calculate the emissivity of the emitter. In the modal analysis, the electromagnetic field is written by the expansion of modes in Layer 2 and that of plane waves in the other layers, as discussed in Section 2.2.3. The  $y$  component of the magnetic field in each layer is given by

$$H_y^{(1)} = H_{\text{in}} \exp(-i\beta_0 x - i\gamma_0^{(1)} z) + \sum_n H_{\text{Rn}} \exp(-i\beta_n x + i\gamma_n^{(1)} z), \quad (3.6)$$

$$H_y^{(2)} = \sum_m X_m(x) [U_m^{(2)} \exp(i\Lambda_m z) + D_m^{(2)} \exp(-i\Lambda_m z)], \quad (3.7)$$

$$H_y^{(3)} = \sum_n U_n^{(3)} \exp(-i\beta_n x + i\gamma_n^{(3)} z) + \sum_n D_n^{(3)} \exp(-i\beta_n x - i\gamma_n^{(3)} z), \quad (3.8)$$

$$H_y^{(4)} = \sum_n H_{\text{Tn}} \exp(-i\beta_n x - i\gamma_n^{(4)} z), \quad (3.9)$$

where

$$\beta_n = (\omega/c) \sin(\theta) + n(2\pi/p), \quad (3.10)$$

$$\gamma_n^{(l)} = \begin{cases} \sqrt{\varepsilon^{(l)}(\omega/c)^2 - \beta_n^2} & (\varepsilon^{(l)}(\omega/c)^2 \geq \beta_n^2) \\ i\sqrt{\beta_n^2 - \varepsilon^{(l)}(\omega/c)^2} & (\varepsilon^{(l)}(\omega/c)^2 < \beta_n^2) \end{cases}. \quad (3.11)$$

$H_y^{(i)}$  denotes the magnetic field in layer  $i$ .  $H_{\text{Tn}}$  and  $H_{\text{Rn}}$  respectively represent transmitted and reflected fields of the  $n$ -th order diffraction, and  $H_{\text{in}}$  is the incidence.  $\Lambda_m$  and  $X_m(x)$  are the  $m$ -th eigenvalue and eigenfunction, respectively.  $\Lambda_m$  is the propagation constant in the  $z$  direction.  $X_m(x)$  corresponds to the mode profile of the magnetic field.  $U_m^{(2)}$  and  $D_m^{(2)}$  are the amplitudes of the mode in the grating layer,

respectively.  $U_n^{(3)}$  and  $D_n^{(3)}$  are the amplitudes of the plane wave of the  $n$ -th order diffraction in Layer 3 for the upward (+z) and downward (-z) directions, respectively. The magnetic fields of the whole structure are determined by six equations derived from the boundary conditions at three interfaces of the four layer structure.

The developed modal analysis was utilized to select geometrical parameters of the presented thermal emitter. Firstly, the period of the grating  $p$  was calculated from the dispersion relation of the SiC-SPhP. Secondary, the reflectivity of the grating without SiC substrate was calculated by modal analysis, and the grating width  $w$  and the grating height  $h_g$  were determined so as to reflect the normal incidence while exciting guided mode resonance. Finally, the distance  $d_a$  between the grating and the SiC substrate was selected through the modal analysis of the whole structure. The selected geometrical parameters are  $p = 11.9 \mu\text{m}$ ,  $w = 5.7 \mu\text{m}$ ,  $h_g = 1.01 \mu\text{m}$ , and  $d_a = 36.2 \mu\text{m}$ , so as to maximize the coupling at  $12.13 \mu\text{m}$  in normal incidence. Note that the thermal emitter is characterized by the absorptivity, then it is translated to emissivity according to the Kirchhoff's law [52], as discussed in Section 2.2. In the following simulation, the absorption of incident light was simulated in order to understand the physics on the thermal emitter.

## 3.3.4 Magnetic field at resonance

Magnetic fields at resonances were simulated by CST microwave studio [53] as shown in Figure 3. 6. Without the SiC substrate, resonant electromagnetic field is excited only around the grating structure with the unity reflection as shown in Figure 3. 6 (a). With the SiC substrate, on the other hand, the evanescent wave from the grating structure excites SPhP at the surface of the SiC substrate as shown in Figure 3. 6 (b). The magnetic field at the interface clearly indicates the signature of SPhP. The amplitude of the first-order diffraction in the Layer 3 is plotted as red lines, and indicates that strong evanescent field is excited due to guide mode resonance. The green dashed line in Figure 3. 6 (b) illustrates that SPhP is excited with significant amplitude.

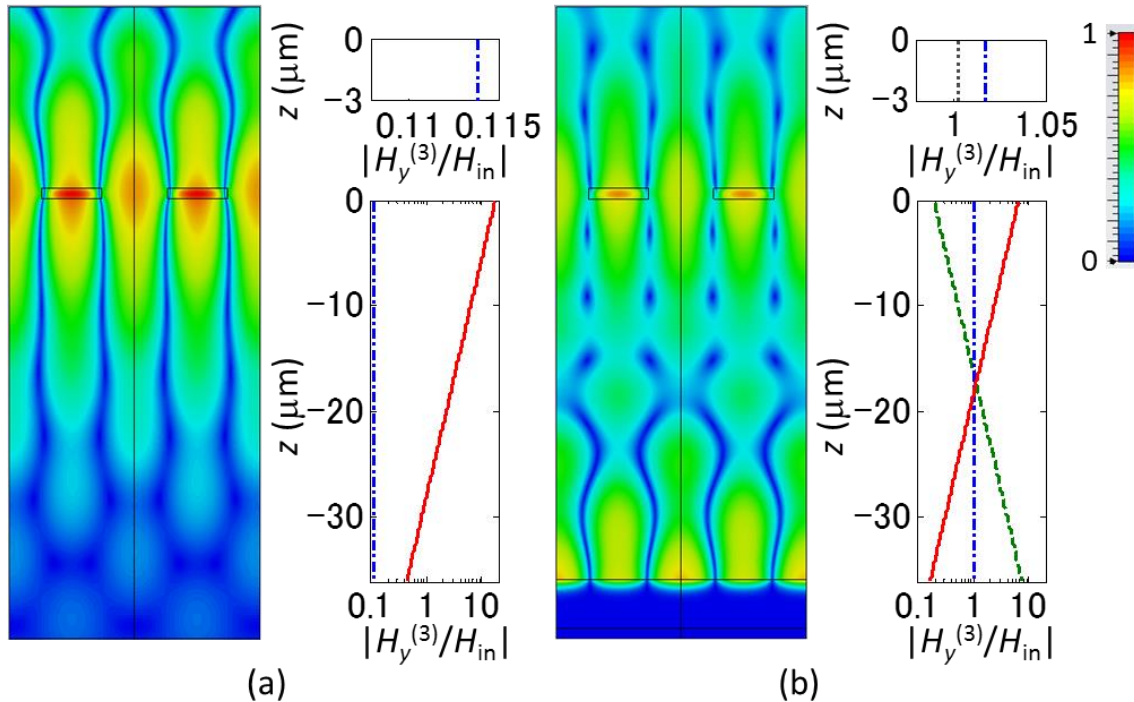


**Figure 3. 6 Magnetic field at resonance. (a) Without SiC substrate. (b) With SiC substrate. The amplitude of each diffraction order in Layer 3 is calculated by the modal analysis, and is plotted as a line in the right panel. [56]**

In case that the wavelength is different from the resonant condition, the grating is almost transparent, and SiC acts as a simple mirror. The emitter reflects the propagative wave without significant absorption as shown in Figure 3. 7 (a). If the distance between the grating and the SiC is modulated, the evanescent wave and SPhP interfere destructively, thus the excitation of the guided mode resonance and SPhP is weak as shown in Figure 3. 7 (b). The modulation amplitude of emissivity exceeds 90 %, which is enabled by the coupling through thermally transparent silicon grating. In both cases, SPhP excitation is almost 2 orders of magnitude smaller than the resonant case (Figure 3. 6 (b)).

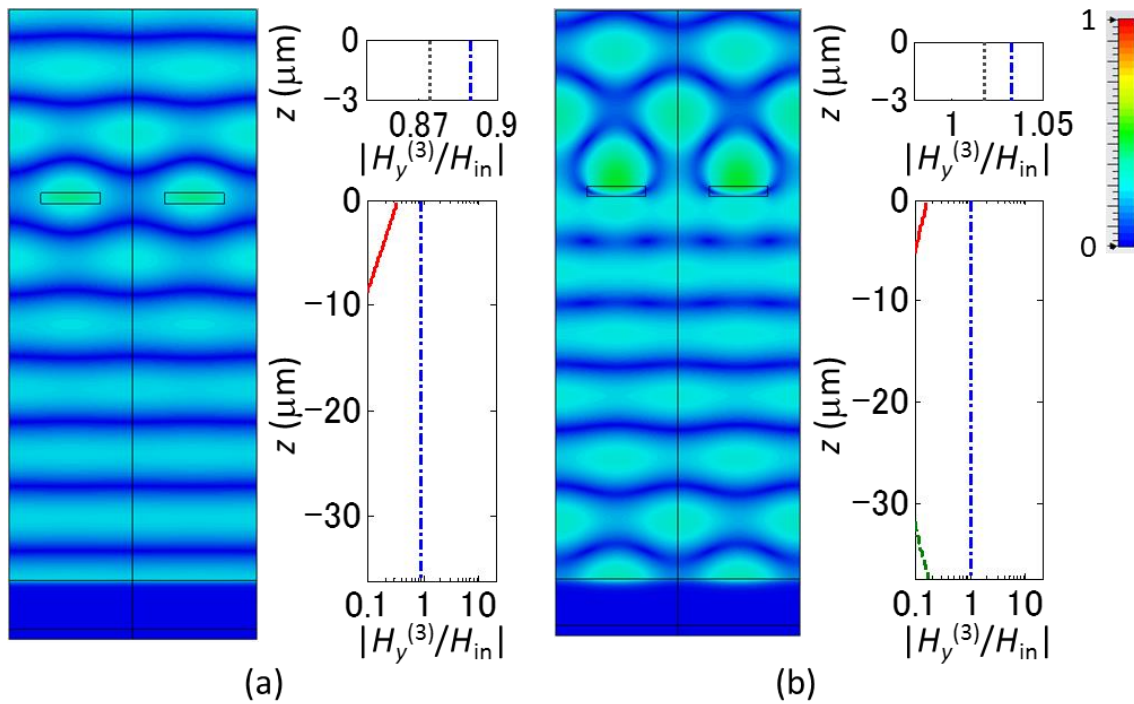


**Figure 3. 7 Magnetic field. (a) At an off-resonant wavelength of  $12.4 \mu\text{m}$ . (b) With a different distance between the grating and the substrate of  $37.3 \mu\text{m}$ . [56]**

## 3.3.5 Emissivity profile

Figure 3. 8 shows spectral thermal emissivity with a variation of angle  $\theta$ . The incident angle  $\theta$  is defined as the angle between the incidence and the z-axis, and the incidence in the xz-plane is considered in Figure 3. 8. The emissivity is almost unity around  $\lambda = 12.13 \mu\text{m}$  and normal incidence. The emissivity is almost zero at off-resonance conditions.

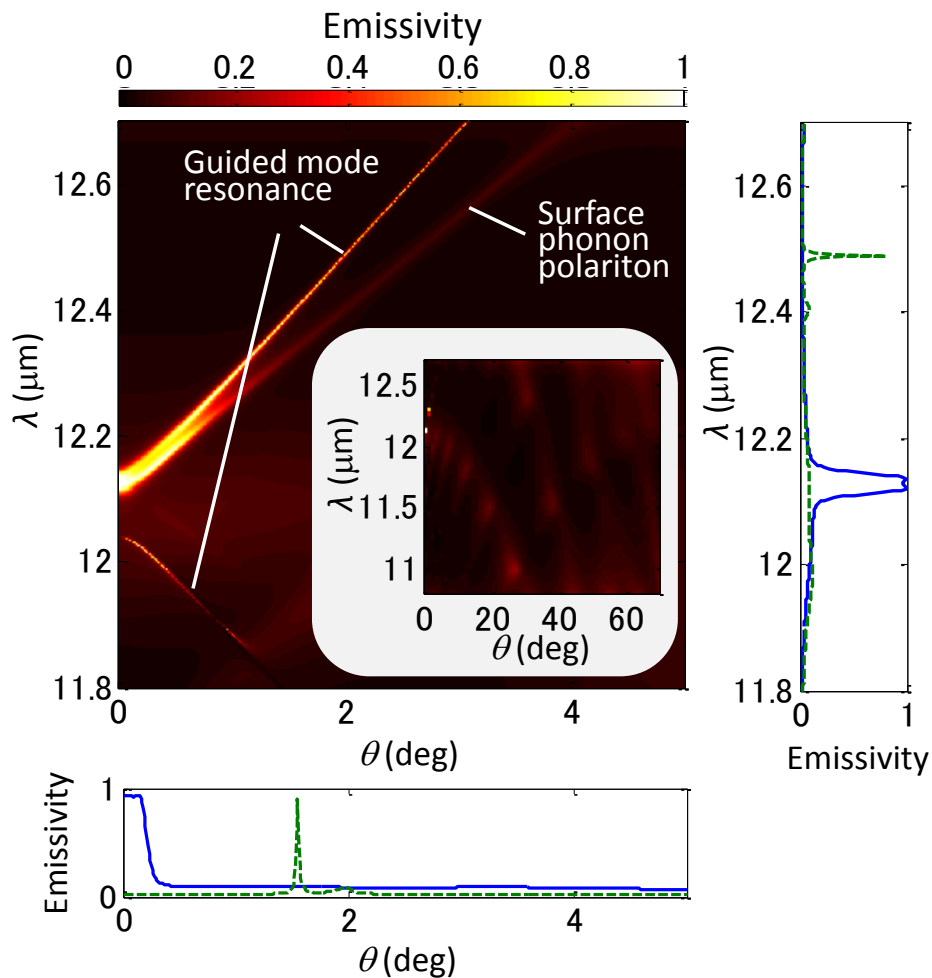


**Figure 3. 8 Emissivity as functions of wavelength and angle in p-polarization. The bottom panel shows emissivity as a function of angle  $\theta$  at  $\lambda = 12.13 \mu\text{m}$  (blue solid line) and  $12.4 \mu\text{m}$  (green dashed line). The right panel shows emissivity as a function of  $\lambda$  at  $\theta = 0^\circ$  (blue solid line) and  $2^\circ$  (green dashed line). [56]**

Guided mode resonance which does not match the dispersion relationship of SPhP causes high emissivity, but the emission peak is too narrow to affect the integrated emission spectra. The incidence which couples to SPhP but does not excite a guided mode resonance is slightly absorbed, because the evanescent wave is not excited with sufficient amplitude. Such characteristics of the parasitic emission are also shown in right and bottom panels in Figure 3. 8.

The emissivity profile at whole angles, i.e. azimuth rotation is considered, was calculated by the extended modal analysis [49] and shown in Figure 3. 9. In p-polarization, significant emission occurs around the normal incidence. In s-polarization, significant emission around the normal incidence is extended like the arcs of circle. These arcs are explained by the phase matching as discussed in Ref. [41]. In both polarizations, there are several circles centered at  $(k_x/k_0, k_y/k_0) = (0, 0)$ ,  $(1.02, 0)$ , and  $(-1.02, 0)$ . They correspond to the Fabry-Perot resonance of the propagative mode in the air region between the grating and the substrate.

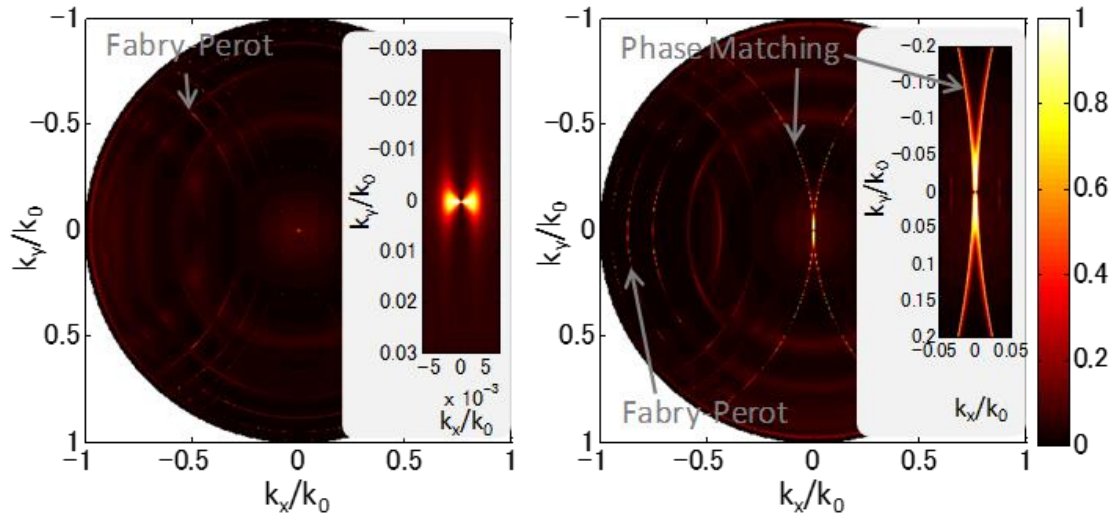


**Figure 3. 9 Emissivity at whole angles. (a) p-polarization. (b) s-polarization.**

## 3.3.6 Distance-dependent emissivity and dynamic modulation of thermal radiation

The emissivity at a wavelength of  $12.13 \mu\text{m}$  and at normal as a function of the distance between the grating and the substrate is shown in Figure 3. 10. We see that the emissivity is almost unity at  $d_a = 36.2 \mu\text{m}$ , while the emission is suppressed at  $d_a = 37.3 \mu\text{m}$ . This suppression is due to the destructive interference between the evanescent wave and the propagative wave, because the contribution of the propagative waves is suggested by the fact that the dips appear with a period equal to half the wavelength. For further verification, an approximate calculation based on the scattering matrix method, wherein the propagative components are removed, was developed. The calculation allows us to investigate the contribution of the evanescent wave alone, and the approximately-calculated result is plotted in Figure 3. 10 with the blue dotted curve. The dips disappear, and the approximately-calculated result follows the emission peaks well.

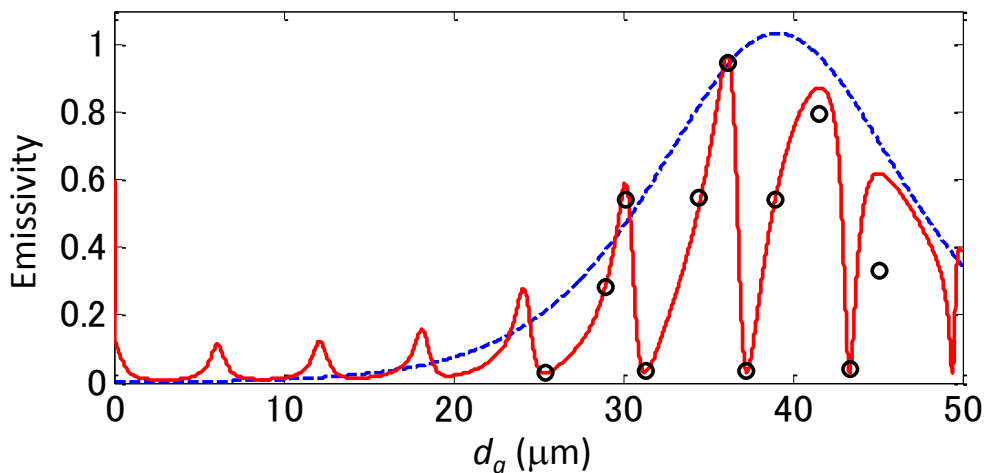


**Figure 3. 10 Emissivity as a function of distance  $d_a$  at  $\lambda = 12.13 \mu\text{m}$  and  $\theta = 0^\circ$ . (red solid line: modal analysis, black circles: CST, blue dashed line: approximation)**

[56]

One may argue that there could be coupling at other wavelengths and angles even if the distance is set to suppress the emissivity at a specific wavelength and an angle. In order to answer such a question, the emissivity profile at  $d_a = 37.3 \mu\text{m}$  is calculated as shown in Figure 3. 11. The coupling between GMR and SPhP is not observed because they have a different dispersion relationship and cross at only one point in the wavenumber-frequency plane, as shown in Figure 3. 4. Note that the bright line observed in Figure 3. 11 (b) is the excitation of GMR only.

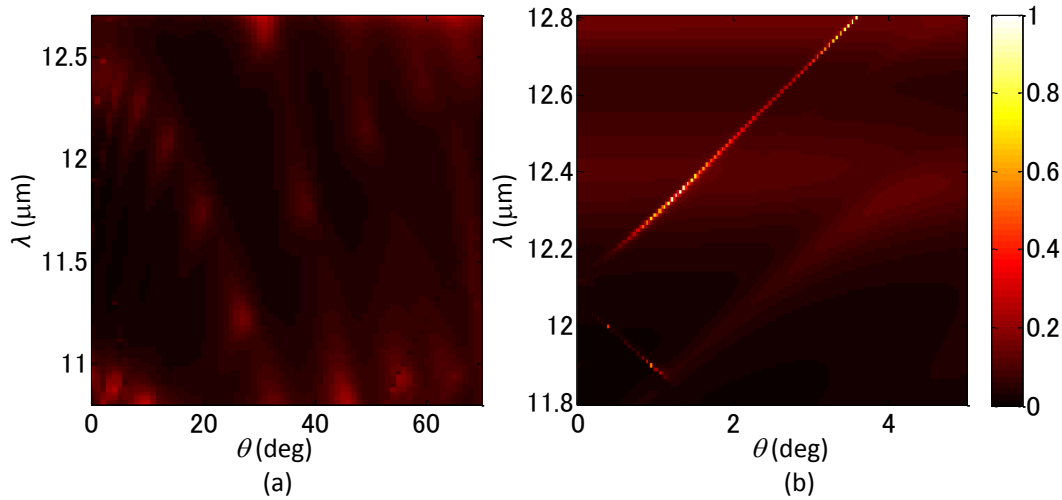


**Figure 3. 11 Emissivity profile at  $d_a = 37.3 \mu\text{m}$  in (a) wide and (b) narrow wavelength and angle ranges.**

The distance dependent emissivity enables the dynamic modulation of the emissivity. MEMS actuators can be designed to control the distance between the grating and the SiC substrate. For example, electrostatic actuator is easily implemented to achieve such dynamic modulation. Tuning of electromagnetic response through the modulation of the vertical distance by electrostatic force is also shown in Ref. [7][44][45].

The modulation amplitude of thermal emissivity exceeds 90 % according to the

theoretical calculation. One may compare the value with the value reported in Ref. [28][42] ( $< 10\%$ ) and that in Ref. [21] (50%). The large contrast is owing to the presented coupling between guided mode resonance and SPhP.

### 3.3.7 Asymmetric emission

Figure 3. 12 shows the thermal emitter comprising an asymmetric grating. The emitter exhibits asymmetric thermal radiation profile due to the asymmetric excitation of the guided mode resonance [34]. The geometrical parameters were optimized so as to absorb the incidence at the wavelength of  $11.32\ \mu\text{m}$  and at the incident angle of  $+21^\circ$ . The geometrical parameters are:  $p = 15.4\ \mu\text{m}$ ,  $w_1 = 6.8\ \mu\text{m}$ ,  $w_2 = 2.8\ \mu\text{m}$ ,  $h_g = 3.5\ \mu\text{m}$ ,  $g_r = 0.8\ \mu\text{m}$ , and  $d_a = 6.3\ \mu\text{m}$ . The magnetic field at the resonance is shown in Figure 3. 13 (a). Strong SPhP is observed at the surface of the SiC substrate with the absorptivity of 0.95. At the incident angle of  $-21^\circ$ , the incident light is reflected back into the incident direction as observed in Figure 3. 13 (b), without exciting SPhP. This reflective coupling to the -1st order is due to the unique diffraction phenomena of the asymmetric grating [34].

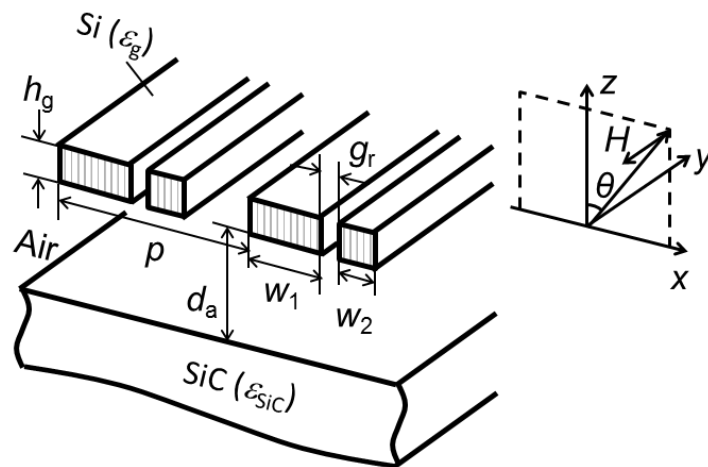


Figure 3. 12 Asymmetric thermal emitter. [56]

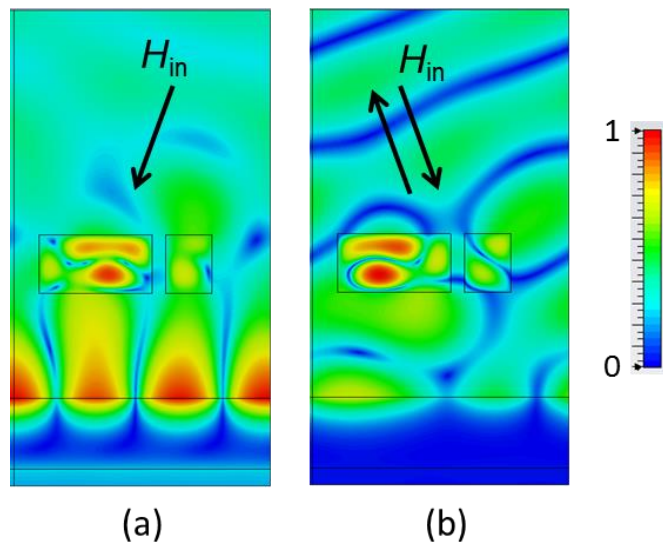
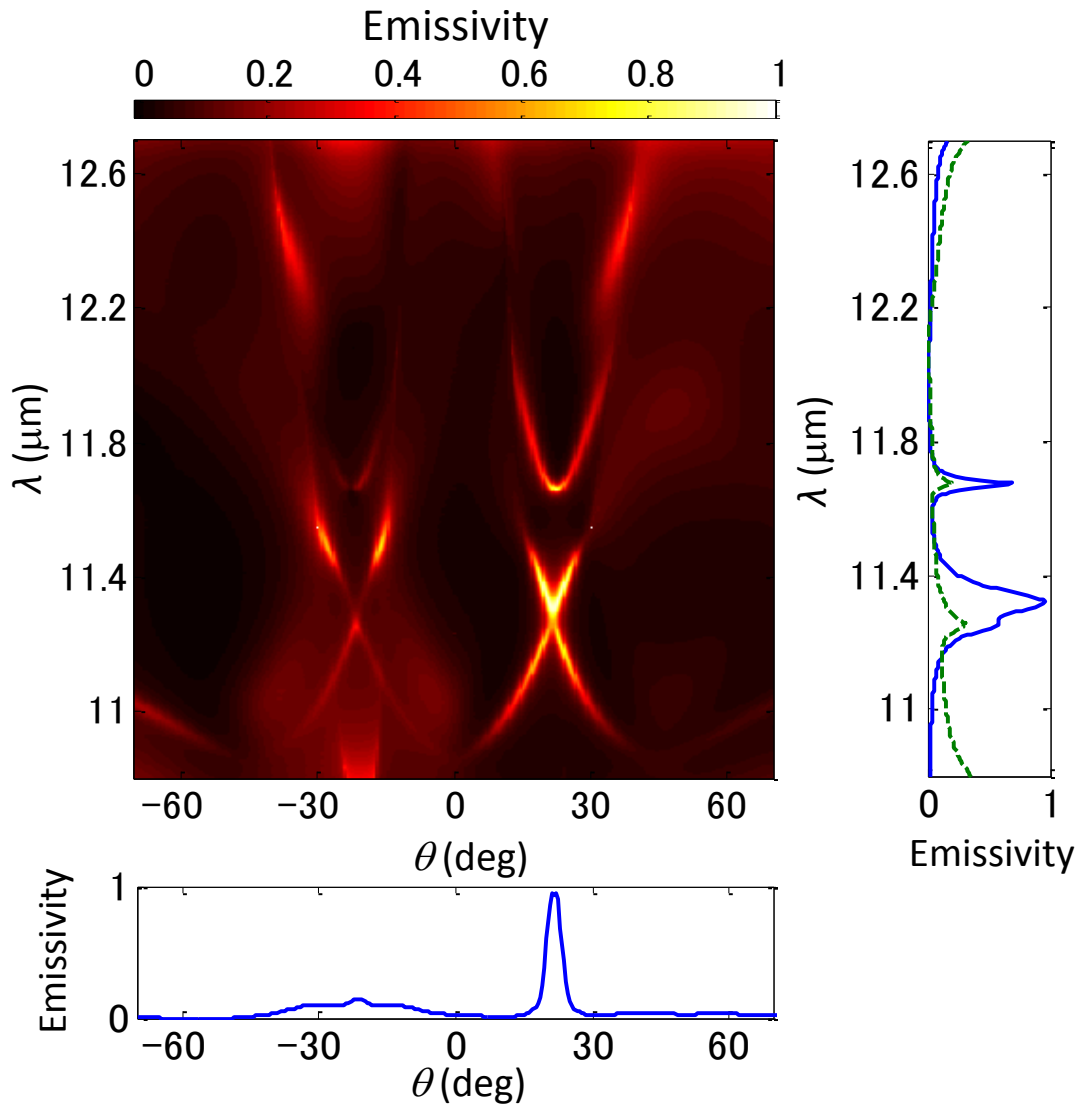


Figure 3. 13 Magnetic field profile at  $\lambda = 11.32 \mu\text{m}$ . (a)  $\theta = +21^\circ$ . (b)  $\theta = -21^\circ$ . [56]

Figure 3. 14 shows the emissivity profile with a variation of the wavelength and the angle. High emissivity is observed around an incident angle of  $+20^\circ$  and the wavelength of  $11.3 \mu\text{m}$  though the resonant excitation of SPhP. Emissivity is successfully suppressed at negative angles, although lines with nonzero amplitude is seen.



**Figure 3. 14** Emissivity profile of the asymmetric thermal emitter. The right panel shows emissivity as a function of  $\lambda$  at  $\theta = +21^\circ$  (blue solid line) and  $-21^\circ$  (green dashed line). The bottom panel shows emissivity as a function of  $\theta$  at  $\lambda = 11.32 \mu\text{m}$ .

[56]

### 3.4 Thermal emitter with surface plasmon polariton (SPP)

#### 3.4.1 Permittivity of doped silicon and the dispersion of surface plasmon polariton

In recent years, CMOS-compatible MEMS, integrated MEMS or silicon photonics is attracting interests from academia and industry because they are manufactured by the conventional silicon technologies. From this viewpoint, silicon-based surface polariton is favorable. Highly-doped silicon exhibits metallic optical response in the mid-infrared region and widely investigated as “engineered metal” in the plasmonics community owing to the benefit that the plasma frequency is tuned by doping concentration [46].

The relative permittivity of doped silicon is expressed by the Drude model [54]:

$$\varepsilon_{\text{DSi}}(\omega) = \varepsilon_{\text{inf}} - \frac{\omega_p^2}{\omega(\omega + i\gamma)}, \quad (3.12)$$

where  $\varepsilon_{\text{inf}}$  is the permittivity in the high frequency limit,  $\omega_p$  is the plasma frequency,  $\gamma$  is the scattering rate. In the first-order approximation, the plasma frequency  $\omega_p$  and the damping coefficient  $\gamma$  is expressed as follows:

$$\omega_p = \sqrt{\frac{Ne^2}{m^*\varepsilon_0}} \quad (3.13)$$

$$\gamma = \frac{e}{m^*\mu_c} \quad (3.14)$$

where  $N$  is the carrier concentration,  $e$  is the elemental charge,  $m^*$  is the effective mass of the carrier,  $\varepsilon_0$  is the permittivity of vacuum,  $\mu_c$  is the mobility of the carrier.

A doped silicon slab supports two SPP modes: symmetric and antisymmetric. The symmetric SPP satisfies the following relationship:

$$\varepsilon_{\text{DSi}}\gamma_0 + \varepsilon_0\gamma_{\text{DSi}} \tanh\left(\frac{\gamma_{\text{DSi}}t_d}{2i}\right) = 0, \quad (3.15)$$

where

$$\gamma_0^2 = (\omega/c)^2 - \beta^2, \quad (3.16)$$

$$\gamma_{\text{DSi}}^2 = \epsilon_{\text{DSi}}(\omega/c)^2 - \beta^2, \quad (3.17)$$

where  $\beta$  is the SPP wavenumber parallel to the slab,  $\gamma_0$  and  $\gamma_{\text{DSi}}$  are the SPP wavenumber perpendicular to the slab in vacuum and in doped silicon, respectively, and  $t_d = 1 \mu\text{m}$  is the thickness of the doped silicon slab. Likewise, the antisymmetric SPP satisfies the following relationship:

$$\epsilon_{\text{DSi}}\gamma_0 + \epsilon_0\gamma_{\text{DSi}} \coth\left(\frac{\gamma_{\text{DSi}}t_d}{2i}\right) = 0. \quad (3.18)$$

Assuming that the silicon slab is doped such that free electron is excited with a concentration of  $5 \times 10^{19} \text{ cm}^{-3}$ , the dispersion relation is calculated as shown in Figure 3. 15. For the symmetric SPP, the real part of the wavenumber lies outside of light line, indicating that the mode is confined around the slab. The imaginary part is relatively small in the frequency of interest, due to the symmetric excitation of SPP. The symmetric and antisymmetric SPP are also called the long-range surface plasmon (LRSP) and the short-range surface plasmon (SRSP), respectively, according to their imaginary part of wavenumbers.

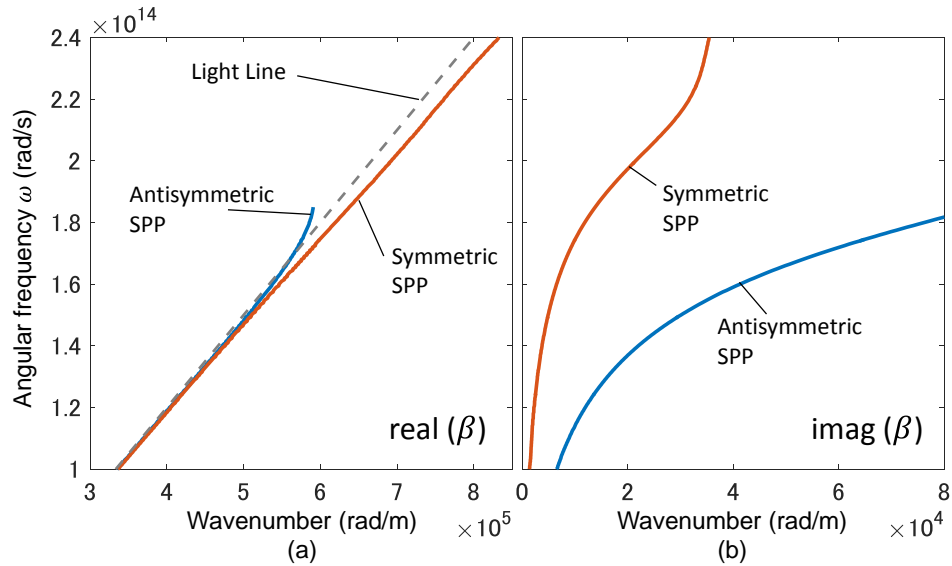


**Figure 3. 15 Dispersion of SPP (a) real part (b) imaginary part of wavenumber  $\beta$**

[57]

## 3.4.2 Structure of thermal emitter

A thermal emitter utilizing surface plasmon polariton (SPP) on a doped silicon slab is shown in Figure 3. 16. Firstly, the grating period was determined such that the wavenumber of guided mode matches with the dispersion relation of SPP. Secondary, the reflectivity of silicon grating was calculated as a function of grating width and thickness (Figure 3. 17), and they were chosen to excite the resonant guided mode. Finally, the grating height was selected so as to maximize the evanescent coupling. For the thermal emission at  $9.35 \mu\text{m}$  in the normal direction, the geometrical parameters were set to be  $p = 8.4 \mu\text{m}$ ,  $w = 4.79 \mu\text{m}$ ,  $h_g = 1.09 \mu\text{m}$ , and  $d_a = 3.9 \mu\text{m}$ .

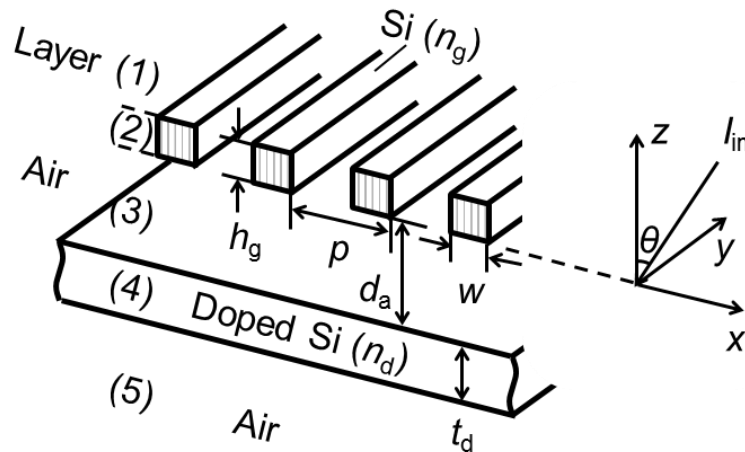


**Figure 3. 16 Thermal emitter with surface plasmon polariton on a doped silicon slab [57]**

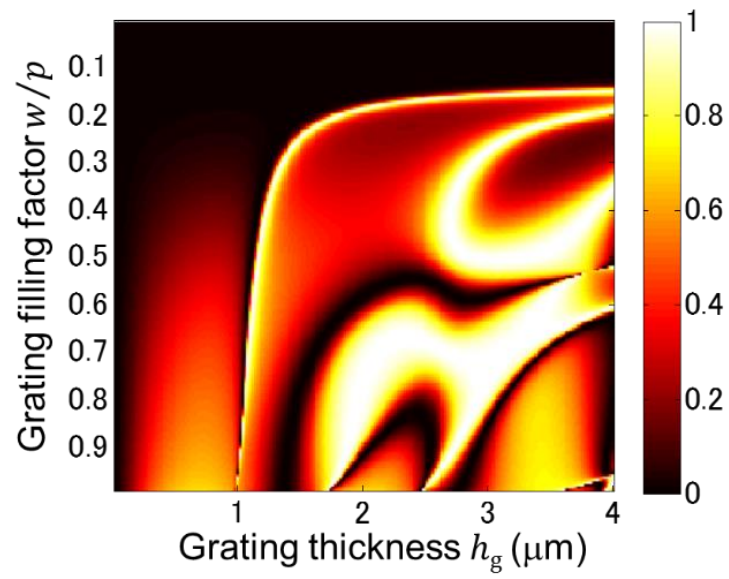


**Figure 3. 17 Reflectivity of silicon subwavelength gratings with a period of  $8.4 \mu\text{m}$ .**

[57]

## 3.4.3 Magnetic field at resonance

The magnetic field in the thermal emitter was simulated by CST microwave studio as shown in Figure 3. 18. At  $d_a = 3.9 \mu\text{m}$ , a strong magnetic field is excited in the grating ridge and around the doped silicon slab. This indicates that an SPP is excited through the guided mode resonance in the grating layer. Absorptivity is observed to be almost unity at this condition. Such excitation is suppressed at  $d_a = 1.4 \mu\text{m}$  as shown in Figure 3. 18 (b); periodic excitation around doped silicon slab is not observed, and absorptivity is around 0.3.

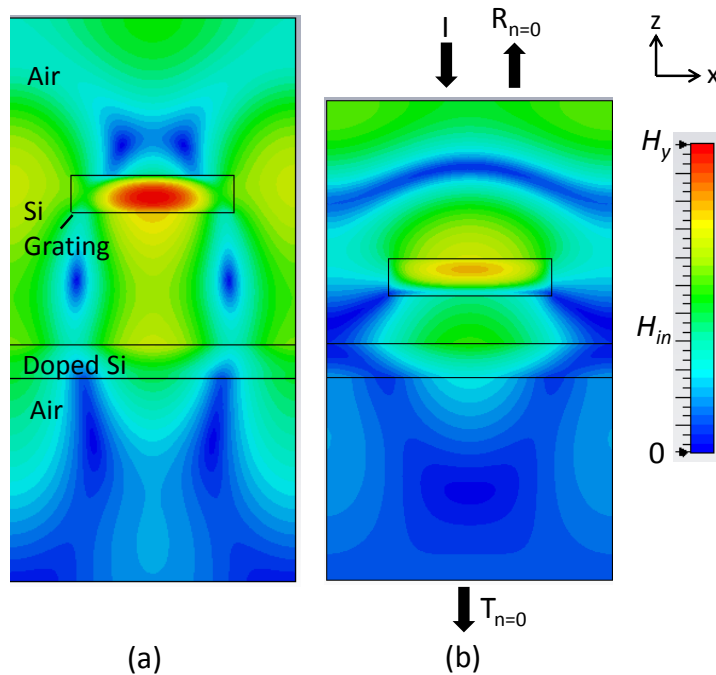


**Figure 3. 18 Magnetic field amplitude at  $9.35 \mu\text{m}$  normal incidence, p-polarization.**

**(a)  $d_a = 3.9 \mu\text{m}$ . (b)  $d_a = 1.4 \mu\text{m}$ . [57]**

## 3.4.4 Thermal radiation spectra

Thermal radiation spectra at  $d_a = 3.9 \mu\text{m}$  and  $d_a = 1.4 \mu\text{m}$  are shown in Figure 3. 19. Heat flux was derived by multiplying the emissivity by the blackbody spectrum. Heat flux is successfully modulated in the spectral range from  $8.5 \mu\text{m}$  to  $10.5 \mu\text{m}$ .

Emissivity as a function of the distance is shown in Figure 3. 20. Emissivity maximum is larger than 0.9, while the minimum is smaller than 0.35. The incomplete suppression is because of the finite imaginary part of the permittivity of doped silicon, which works as an absorptive mirror. The dips with the period of half the wavelength at larger distances are attributed to the Fabry-Perot resonance of the propagative wave.

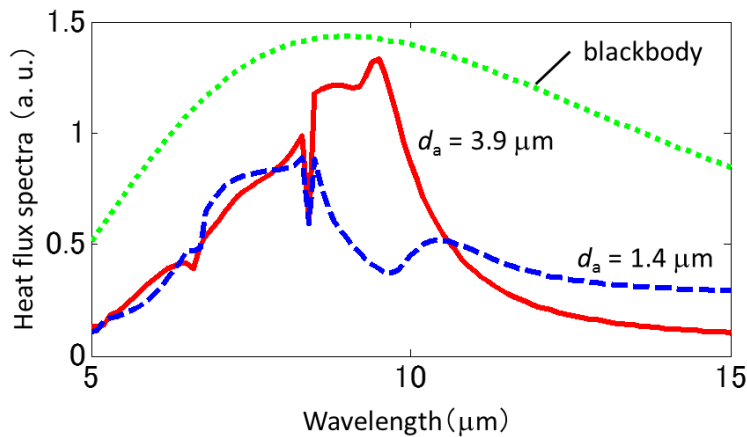


**Figure 3. 19 Thermal radiation spectra with different height. [57]**

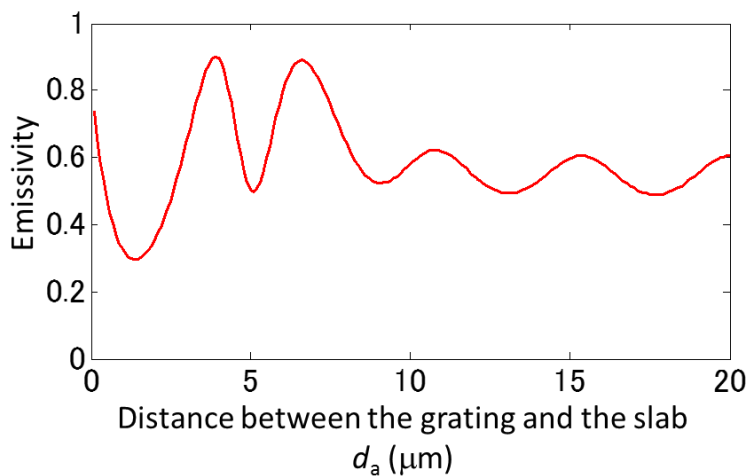


**Figure 3. 20 Emissivity as a function of the distance at  $\lambda = 9.35 \mu\text{m}$ . [57]**

Emissivity as functions of wavelength and angle is shown in Figure 3. 21. Strong bright spot around 9  $\mu\text{m}$  is observed when  $d_a = 3.9 \mu\text{m}$ , whereas it disappears when  $d_a = 1.4 \mu\text{m}$ . There exist several parasitic emission modes at  $d_a = 1.4 \mu\text{m}$ . The parasitic mode A is attributed to the Fabry-Perot resonance as shown in Figure 3. 22 (a). The parasitic mode B is attributed to the guided mode resonance as shown in Figure 3. 22 (b).

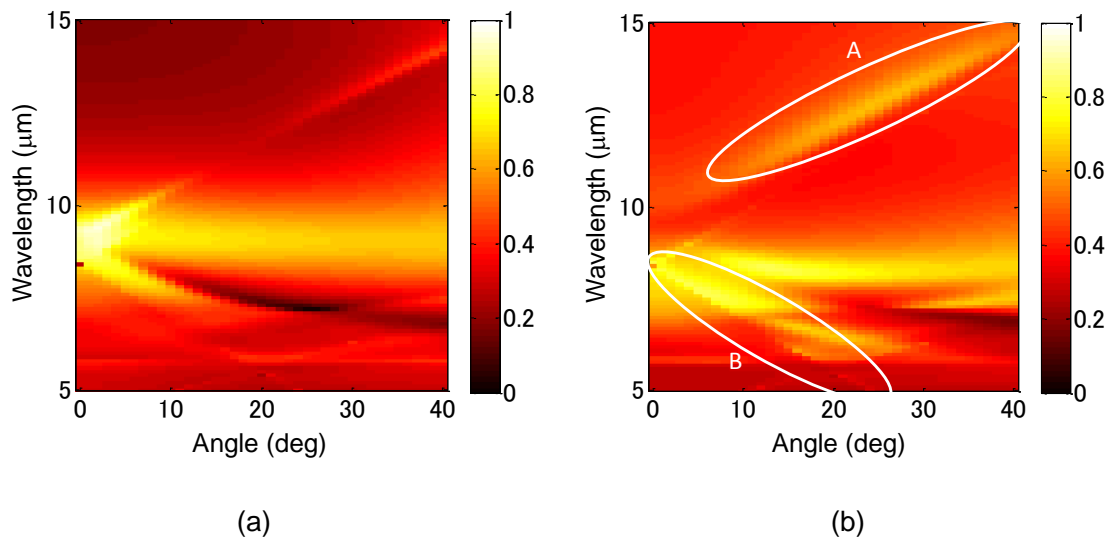


Figure 3. 21 Emissivity profile (a)  $d_a = 3.9 \mu\text{m}$  (b)  $d_a = 1.4 \mu\text{m}$ . [57]

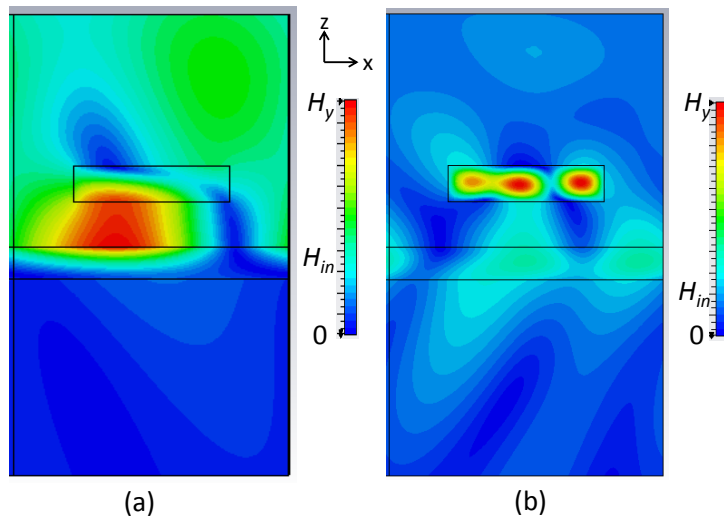
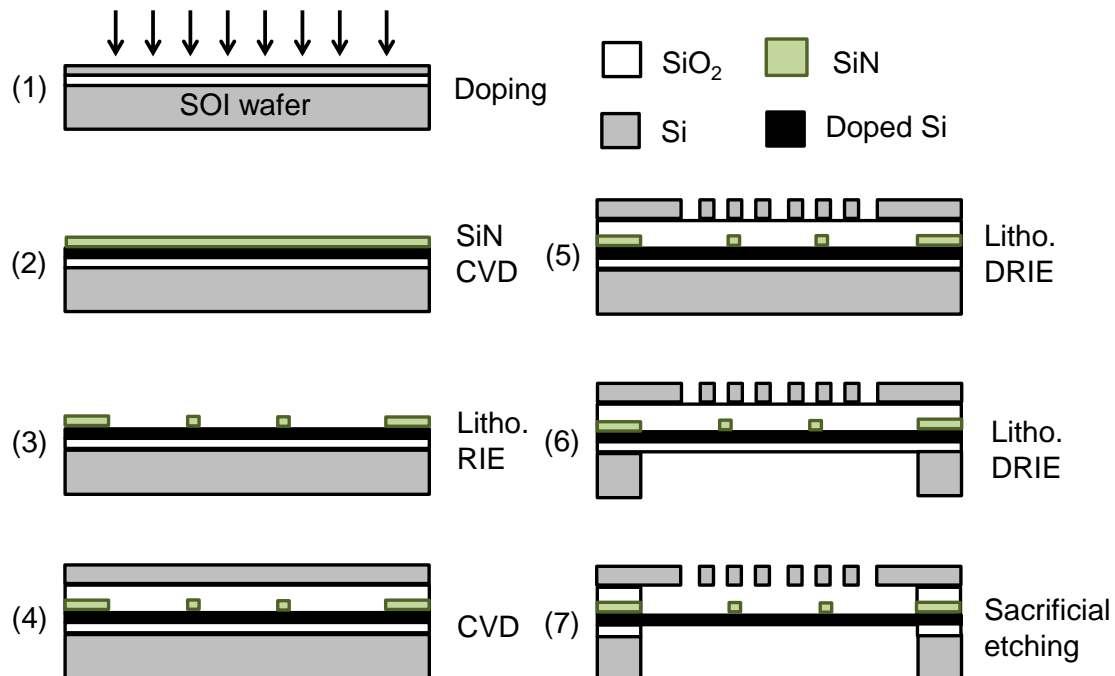


Figure 3. 22 Magnetic field at the resonance (a)  $\lambda = 15 \mu\text{m}$ ,  $40^\circ$  (b)  $\lambda = 7 \mu\text{m}$ ,  $12^\circ$ .

[57]

## 3.4.5 Possible fabrication process

A possible fabrication process of the thermal emitter based on SPP on doped Si is shown in Figure 3. 23. (1) The device layer of a silicon-on-insulator (SOI) wafer is doped by ion implantation. The wafer is thermally annealed to activate carriers. (2) A thin silicon nitride (SiN) layer is deposited by chemical vapor deposition (CVD). The thickness of the SiN layer is  $1.4 \mu\text{m}$ , which is the height of stoppers. (3) Mechanical stoppers are formed by photolithography and reactive-ion-etching (RIE). A silicon dioxide ( $\text{SiO}_2$ ) film and a polysilicon film are deposited by CVD. The respective thickness of  $3.9 \mu\text{m}$  and  $1.09 \mu\text{m}$  corresponds to the distance  $d_a$  and the thickness  $h_g$ , respectively. (5) The top silicon layer is patterned by electron beam lithography and Deep RIE so as to obtain the grating. (6) The bottom silicon layer is etched by Deep RIE. (7) The grating is released by vapor hydrogen fluoride (HF) etching of  $\text{SiO}_2$ .



**Figure 3. 23 Possible fabrication process of the thermal emitter**

**based on SPP on doped silicon slab. [57]**

## 3.4.6 Electrostatic actuation of the distance between the grating and the slab

The thermal emitter presented in Figure 3. 24 modulates thermal emission around  $9.35 \mu\text{m}$  through electrostatic actuation as shown in Figure 3. 19. Initially, the distance between the grating and the doped silicon slab is  $3.9 \mu\text{m}$ , corresponding to “ON” state. By applying sufficiently large voltage between the grating and the slab, the structure is electrostatically pulled in. The distance is determined by the height of the stopper, which is  $1.4 \mu\text{m}$ . The condition corresponds to “OFF” state.

In order to estimate the pull-in voltage, a model was built in COMSOL multiphysics. The grating area was assumed to be  $200 \mu\text{m} \times 200 \mu\text{m}$ . The grating is supported by four silicon hinges of  $200 \mu\text{m}$  long and  $10 \mu\text{m}$  width. The hinge deforms to change the distance between the grating and the slab. The simulation result is shown in Figure 3. 24 and reveals that the applied voltage of  $10 \text{ V}$  is sufficient to induce pull-in.

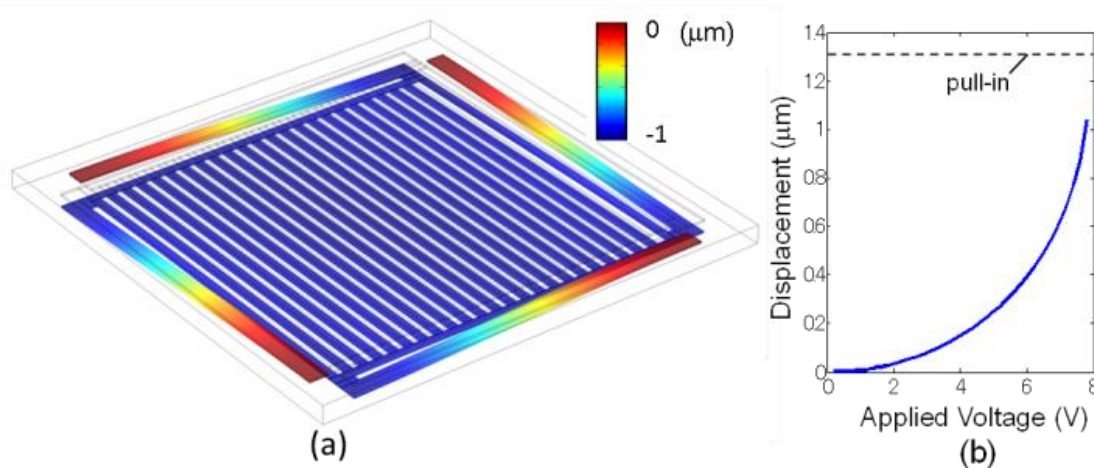


**Figure 3. 24 Electrostatic actuation of the thermal emitter simulated by COMSOL.**

**(a) Deformation in the direction perpendicular to the grating plane by the applied voltage of  $7.8 \text{ V}$ . (b) Displacement as a function of applied voltage. The displacement is measured at the center of the grating. [57]**

### 3.5 Discussion on the sharpness of the resonance

The sharpness of the resonance is affected by several factors: the material which supports the surface polariton, the thickness of the slab, the Q-factor of the resonant grating, and the evanescent decay factor in the air gap. The quantitative analysis requires another theoretical framework similar to Ref. [96] and is beyond the scope of this thesis, and thus we discuss qualitatively here.

The permittivity of the material which supports the surface polariton greatly affects the resonance Q-factor. As shown in Figure 3. 3, the permittivity of SiC is resonant and exhibits low-loss. On the contrary, the permittivity of doped silicon is lossy around the plasma frequency. Clear contrast on the sharpness is observed between the structures with SiC and doped silicon, as shown in Figure 3. 8 and Figure 3. 21 (a).

In the case that a slab is utilized as shown in Figure 3. 16, the surface polariton splits into two modes, namely symmetric and asymmetric SPPs. The symmetric mode is utilized because it is low-loss, and the imaginary part of its wavenumber decreases as the thickness of the slab decreases. The resulting sharpness of the emission is controlled by tailoring the thickness of the slab.

As shown in Figure 3. 2 and Figure 3. 17, other grating filling factor and thickness also result in the guided mode resonance, and the Q-factor of the guided mode resonance is different between parameter sets. The Q-factor of the guided mode resonance affects the sharpness of the emission.

The evanescent decay factor  $\kappa_0$  in the air gap also affects the sharpness. It is calculated from the relative lateral wavenumber  $\tilde{\beta} \equiv \beta(c/\omega)$  at the coupling point:

$$\kappa_0 = \frac{\omega}{c} \sqrt{\tilde{\beta}^2 - 1}. \quad (3.19)$$

Figure 3. 8 shows the emissivity of the grating with  $\tilde{\beta} = 1.02$ . As a comparison, we calculated the emissivity with another structure with  $\tilde{\beta} = 1.1$ . The result shown in Figure 3. 25 exhibits considerably broader emission spectra compared to Figure 3. 8. Smaller Q-factor is obtained by employing larger evanescent decay factor through taking a distance between the coupling point and light line.

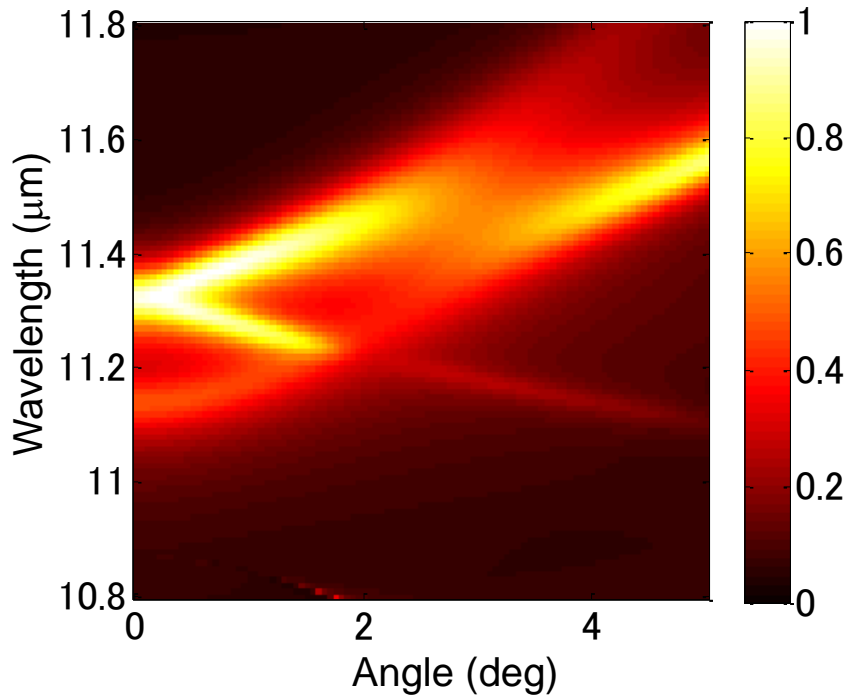


Figure 3. 25 Emissivity of the structure composed of silicon grating and SiC substrate with  $\tilde{\beta} = 1.1$ . The geometrical parameters are:  $p = 10.29 \mu\text{m}$ ,  $w = 4.94 \mu\text{m}$ ,  $h_g = 1.40 \mu\text{m}$ , and  $d_a = 10.6 \mu\text{m}$

### 3.6 Chapter summary

In this chapter, dynamic modulation of thermal radiation has been theoretically presented. The modulation is enabled by the control of the coupling between the guided mode resonance in silicon gratings and the surface polariton. Emissivity is shown to be controllable by tuning the gap distance from 36.2  $\mu\text{m}$  to 37.3  $\mu\text{m}$  or 3.9  $\mu\text{m}$  to 1.4  $\mu\text{m}$  between the thermally-transparent dielectric gratings and the interface for the surface polariton. Two types of surface polariton, namely surface phonon polariton (SPhP) on a silicon carbide (SiC) substrate and surface plasmon polariton (SPP) on a doped silicon (DSi) slab were utilized. The modulation amplitude of emissivity exceeds 90 % with the SiC emitter and 50 % with the DSi emitter. An asymmetric thermal radiation was presented with a double-grooved grating. A possible fabrication process was presented for DSi emitter. The bandwidth of the resonance is qualitatively discussed.

## Reference

- [1] J. Meléndez, A. J. de Castro, F. López, and J. Meneses, "Spectrally selective gas cell for electrooptical infrared compact multigas sensor." *Sens. Actuators A* **47**, 417 (1995).
- [2] J. Hodgkinson and R. P. Tatam, "Optical gas sensing: a review." *Meas. Sci. Technol.* **24**, 012004 (2013).
- [3] A. De Luca, M. T. Cole, A. Fasoli, S. Z. Ali, F. Udrea, and W. I. Milne, "Enhanced infra-red emission from sub-millimeter microelectromechanical systems micro hotplates via inkjet deposited carbon nanoparticles and fullerenes." *J. Appl. Phys.* **113**, 214907 (2013).
- [4] W. Weppner, "Solid-state electrochemical gas sensors." *Sens. Actuators* **12**, 107-119 (1987).
- [5] P. Krebs, and A. Grisel. "A low power integrated catalytic gas sensor." *Sens. Actuators B* **13**, 155 (1993).
- [6] C. Wang, L. Yin, L. Zhang, D. Xiang, and R. Gao. "Metal oxide gas sensors: sensitivity and influencing factors." *Sensors* **10**, 2088-2106 (2010).
- [7] Z. Han, K. Kohno, H. Fujita, K. Hirakawa, and H. Toshiyoshi. "MEMS reconfigurable metamaterial for terahertz switchable filter and modulator." *Opt. Exp.* **22**, 21326 (2014).
- [8] S. Maruyama, T. Kashiwa, H. Yugami, and M. Esashi. "Thermal radiation from two-dimensionally confined modes in microcavities." *Appl. Phys. Lett.* **79**, 1393 (2001).
- [9] H. Sai, Y. Kanamori, and H. Yugami. "High-temperature resistive surface grating for spectral control of thermal radiation." *Appl. Phys. Lett.* **82**, 1685 (2003).

- [10] K. Ikeda, H. T. Miyazaki, T. Kasaya, K. Yamamoto, Y. Inoue, K. Fujimura, T. Kanakugi, M. Okada, K. Hatade, and S. Kitagawa. "Controlled thermal emission of polarized infrared waves from arrayed plasmon nanocavities." *Appl. Phys. Lett.* **92**, 1117 (2008).
- [11] H. T. Miyazaki, T. Kasaya, M. Iwanaga, B. Choi, Y. Sugimoto, and K. Sakoda, "Dual-band infrared metasurface thermal emitter for CO<sub>2</sub> sensing", *Appl. Phys. Lett.* **105**, 121107 (2014);
- [12] C. M. Wang, Y. C. Chang, M. W. Tsai, Y. H. Ye, C. Y. Chen, Y. W. Jiang, Y. T. Chang, S. C. Lee, and D. P. Tsai. "Reflection and emission properties of an infrared emitter." *Opt. Exp.* **15**, 14673 (2007).
- [13] I. Puscasu and W. L. Schaich. "Narrow-band, tunable infrared emission from arrays of microstrip patches." *Appl. Phys. Lett.* **92**, 233102 (2008).
- [14] X. Liu, T. Tyler, T. Starr, A. F. Starr, N. M. Jokerst, and W. J. Padilla. "Taming the blackbody with infrared metamaterials as selective thermal emitters." *Phys. Rev. Lett.* **107**, 045901 (2011).
- [15] S. Y. Lin, J. G. Fleming, E. Chow, Jim Bur, K. K. Choi, and A. Goldberg. "Enhancement and suppression of thermal emission by a three-dimensional photonic crystal." *Phys. Rev. B* **62**, R2243 (2000).
- [16] M. Laroche, R. Carminati, and J-J. Greffet. "Coherent thermal antenna using a photonic crystal slab." *Phys. Rev. Lett.* **96**, 123903 (2006).
- [17] D. L. C. Chan, I. Celanovic, J. D. Joannopoulos, and M. Soljačić. "Emulating one-dimensional resonant Q-matching behavior in a two-dimensional system via Fano resonances." *Phys. Rev. A* **74**, 064901 (2006).

- [18] M. De Zoysa, T. Asano, K. Mochizuki, A. Oskooi, T. Inoue, and S. Noda. "Conversion of broadband to narrowband thermal emission through energy recycling." *Nat. Photo.* **6**, 535 (2012).
- [19] T. Inoue, M. De Zoysa, T. Asano, and S. Noda. "Single-peak narrow-bandwidth mid-infrared thermal emitters based on quantum wells and photonic crystals." *Appl. Phys. Lett.* **102**, 191110 (2013).
- [20] T. Inoue, M. De Zoysa, T. Asano, and S. Noda. "Filter-free nondispersive infrared sensing using narrow-bandwidth mid-infrared thermal emitters." *Appl. Phys. Exp.* **7**, 012103 (2014).
- [21] T. Inoue, M. De Zoysa, T. Asano, and S. Noda. "Realization of dynamic thermal emission control." *Nat. Mat.* **13**, 928 (2014).
- [22] M. U. Pralle, N. Moelders, M. P. McNeal, I. Puscasu, A. C. Greenwald, J. T. Daly, E. A. Johnson, T. George, D. S. Choi, I. El-Kady, and R. Biswas, "Photonic crystal enhanced narrow-band infrared emitters." *Appl. Phys. Lett.* **81**, 4685 (2002).
- [23] D. L. C. Chan, M. Soljacic, and J. D. Joannopoulos, "Thermal emission and design in 2D-periodic metallic photonic crystal slabs." *Opt. Express* **14**, 8785 (2006).
- [24] J. A. Schuller, T. Taubner, and M. L. Brongersma, "Optical antenna thermal emitters." *Nature Photon.* **3**, 658 (2009).
- [25] B. Neuner III, C. Wu, G. T. Eyck, M. Sinclair, I. Brener, and G. Shvets, "Efficient infrared thermal emitters based on low-albedo polaritonic meta-surfaces." *Appl. Phys. Lett.* **102**, 211111 (2013).
- [26] M. Engel, M. Steiner, A. Lombardo, A. C. Ferrari, H. V. Löhneysen, P. Avouris, and R. Krupke. "Light–matter interaction in a microcavity-controlled graphene transistor." *Nat. Comm.* **3**, 906 (2012).

- [27] M. Pu, P. Chen, Y. Wang, Z. Zhao, C. Wang, C. Huang, C. Hu, and X. Luo. "Strong enhancement of light absorption and highly directive thermal emission in graphene." *Opt. Exp.* **21**, 11618 (2013).
- [28] V. W. Brar, M. C. Sherrott, M. S. Jang, S. Kim, L. Kim, M. Choi, L. A. Sweatlock, and H. A. Atwater. "Electronic modulation of infrared radiation in graphene plasmonic resonators." *Nat. Comm.* **6** (2015).
- [29] R. Magnusson and S. S. Wang, "New principle for optical filters." *Appl. Phys. Lett.* **61**, 1022 (1992).
- [30] S. S. Wang and R. Magnusson, "Theory and applications of guided-mode resonance filters" *Appl. Opt.* **32**, 2606 (1993).
- [31] D. L. Brundrett, E. N. Glytsis, and T. K. Gaylord, "Normal-incidence guided-mode resonant grating filters: design and experimental demonstration" *Opt. Lett.* **23**, 700 (1998).
- [32] M. C. Y. Huang, Y. Zhou, and C. J. Chang-Hasnain, "A surface-emitting laser incorporating a high-index-contrast subwavelength grating." *Nat. Photon.* **1**, 119 (2007).
- [33] D. Fattal, J. Li, Z. Peng, M. Fiorentino, and R. G. Beausoleil, "Flat dielectric grating reflectors with focusing abilities" *Nat. Photon.* **4**, 466 (2010).
- [34] K. Ito and H. Iizuka, "Highly efficient-1st-order reflection in Littrow mounted dielectric double-groove grating" *AIP Adv.* **3**, 062119 (2013).
- [35] W. L. Barnes, A. Dereux, and T. W. Ebbesen. "Surface plasmon subwavelength optics." *Nature* **424**, 824 (2003).
- [36] F. H. L. Koppens, D. E. Chang, and F. J. Garcia de Abajo. "Graphene plasmonics: a platform for strong light-matter interactions." *Nano Lett.* **11**, 3370 (2011).

- [37] M. Jablan, H. Buljan, and M. Soljačić. "Plasmonics in graphene at infrared frequencies." *Phys. Rev. B* **80**, 245435 (2009).
- [38] J. Le Gall, M. Olivier, and J-J. Greffet. "Experimental and theoretical study of reflection and coherent thermal emission by a SiC grating supporting a surface-phonon polariton." *Physical Review B* **55**, no. 15 (1997): 10105.
- [39] J. J. Greffet, R. Carminati, K. Joulain, J. P. Mulet, S. Mainguy, and Y. Chen. "Coherent emission of light by thermal sources." *Nature* **416**, 61 (2002).
- [40] F. Marquier, C. Arnold, M. Laroche, J. J. Greffet, and Y. Chen, "Degree of polarization of thermal light emitted by gratings supporting surface waves." *Opt. Exp.* **16**, 5305 (2008).
- [41] C. Arnold, F. Marquier, M. Garin, F. Pardo, S. Collin, N. Bardou, J. L. Pelouard, and J. J. Greffet, "Coherent thermal infrared emission by two-dimensional silicon carbide gratings" *Phys. Rev. B* **86**, 035316 (2012).
- [42] S. Vassant, I. Moldovan Doyen, F. Marquier, F. Pardo, U. Gennser, A. Cavanna, J. L. Pelouard, and J. J. Greffet. "Electrical modulation of emissivity." *Appl. Phys. Lett.* **102**, 081125 (2013).
- [43] D. Olego and M. Cardona, "Temperature dependence of the optical phonons and transverse effective charge in 3 C-SiC." *Phys. Rev. B* **25**, 3889 (1982).
- [44] M. C. Y. Huang, Y. Zhou, and C. J. Chang-Hasnain, "A nanoelectromechanical tunable laser" *Nature Photon.* **2**, 3 (2008).
- [45] Y. Kanamori, T. Kitani, K. Hane "Control of guided resonance in a photonic crystal slab using microelectromechanical actuators." *Appl. Phys. Lett.* **90**, 031911 (2007).

- [46] W. Streyer, S. Law, G. Rooney, T. Jacobs, and D. Wasserman. "Strong absorption and selective emission from engineered metals with dielectric coatings." *Opt. Exp.* **21**, 9113-9122 (2013).
- [47] L. Li, "Formulation and comparison of two recursive matrix algorithms for modeling layered diffraction gratings." *JOSA A* **13**, 1024 (1996).
- [48] P. Sheng, R. S. Stepleman, and P. N. Sanda. "Exact eigenfunctions for square-wave gratings: Application to diffraction and surface-plasmon calculations." *Phys. Rev. B* **26**, 2907 (1982).
- [49] L. Li, "A modal analysis of lamellar diffraction gratings in conical mountings." *J. Mod. Opt.* **40**, 553 (1993).
- [50] T. Clausnitzer, T. Kämpfe, E-B. Kley, A. Tünnermann, U. Peschel, A. V. Tishchenko, and O. Parriaux. "An intelligible explanation of highly-efficient diffraction in deep dielectric rectangular transmission gratings." *Opt. Express* **13**, 10448 (2005).
- [51] H. Iizuka, N. Engheta, H. Fujikawa, K. Sato, and Y. Takeda, "Role of propagating modes in a double-groove grating with a+ 1st-order diffraction angle larger than the substrate-air critical angle." *Opt. Lett.* **35**, 3973 (2010).
- [52] J. J. Greffet and M. Nieto-Vesperinas. "Field theory for generalized bidirectional reflectivity: derivation of Helmholtz's reciprocity principle and Kirchhoff's law." *J. Opt. Soc. Am. A* **15**, 2735 (1998).
- [53] CST Microwave Studio, 2013, <http://www.cst.com>.
- [54] Fu, C. J., and Z. M. Zhang. "Nanoscale radiation heat transfer for silicon at different doping levels." *Int. J. Heat Mass Trans.* **49**, 1703 (2006).

- [55] D. Chan, I. Celanovic, J. Joannopoulos, and M. Soljačić. "Emulating one-dimensional resonant Q-matching behavior in a two-dimensional system via Fano resonances." *Phys. Rev. A* **74**, 064901 (2006).
- [56] Reprinted from *Applied Physics Letters*, Vol. **104** (2014), 051127, K. Ito, T. Matsui, and H. Iizuka, © 2014 AIP, with permission from AIP Publishing LLC.
- [57] Reprinted from *IEEJ Transactions on Sensors and Micromachines*, Vol. **135** (2015), 184-190, K. Ito, T. Matsui, H. Iizuka, and H. Toshiyoshi, 電気学会 E 部門誌.

## *Chapter 4 Monochromatic thermal emitter*

This chapter demonstrates the control of parasitic electromagnetic modes excited in metal-insulator-metal metamaterials. The suppression of these modes enables quasi-monochromatic thermal emission. The suppression is performed partially owing to the frequency shift of the second-order resonance, which is realized by arranging the rectangular resonators in a diagonal manner or by densely placing square resonators. Both arrangements of resonators utilize proximity interaction between resonators. Other parasitic modes observed in conventional square resonators are successfully suppressed by dense placement, and the integrated parasitic heat flux decreases from  $11.8 \text{ Wsr}^{-1}\text{m}^{-2}$  to  $4.0 \text{ Wsr}^{-1}\text{m}^{-2}$  at an angle of  $60^\circ$ . The metamaterials are fabricated, and their reflection or thermal emission spectra are measured by Fourier-transformed infrared spectrometer. The measured spectra are supported by numerical simulations.

## 4.1 Introduction

### 4.1.1 Motivation

In the field of automotive engineering, various types of gas should be measured for the monitoring of the exhaust and the cabin ambient. Nondispersive infrared (NDIR) sensing [1]-[3], where the gas concentration is derived from the absorption of infrared light, has advantages of high reliability and selectivity compared to electrochemical [4], catalytic [5] or metal-oxide gas sensors [6]. Each gas has a characteristic absorption spectrum, thus the spectroscopic analysis gives us not only the concentration but also the composition of the gas. In this field, thermal emitter is generally utilized as a light source. Broadband thermal radiation from a blackbody-like emitter is filtered to produce monochromatic light.

Alternatively, monochromatic thermal emitter is pursued in order to reduce number of components and to improve energy efficiency. Subwavelength structures induce resonances at certain frequencies, resulting in monochromatic thermal emissions. Such tailoring of thermal emission by subwavelength structures has been already reviewed in the previous chapter. In this chapter, we focus on the metamaterial that consists of metal-insulator-metal trilayers.

### 4.1.2 Metal-insulator-metal (MIM) metamaterial

Metal-insulator-metal (MIM) metamaterials have been widely investigated [7]-[43] because of their omnidirectional electromagnetic response and ease of fabrication. In these structures, trilayers are deposited on a substrate, and the top metal layer is perforated to form resonators. Incident light at the resonant frequency excites strong magnetic field in the insulator layer and antiparallel currents in the two metal layers,

resulting in total absorption through loss in the metal and/or the insulator. This resonant absorption in the planar trilayer structure is called localized surface plasmon polariton [14], magnetic polariton [9], and optical nanoantenna [41]. The spectral range of MIM emitters spans from visible to terahertz, and their fundamental resonant frequency  $f_r$  satisfies

$$f_r = \frac{c}{2wn_{\text{eff}}}, \quad (4.1)$$

where  $c$  is the speed of light,  $w$  is the width of the cavity resonator,  $n_{\text{eff}}$  is the effective refractive index in the cavity resonator. Thus, we can design the fundamental frequency by properly choosing the width of the cavity.

As the metal layer, gold, silver, and aluminum have been frequently utilized because of their low loss in the infrared range. Aluminum oxide is common for the insulating layer. In this work, aluminum is employed as the metal because of their CMOS compatibility. Silicon is adopted as the insulator because of high permittivity.

Several types of structures have been utilized as resonant cavities. One-dimensional gratings have been adopted to achieve emission in p-polarization [7]-[13]. The magnetic field of s-polarized light is perpendicular to the resonant cavity, thus s-polarized light does not excite resonances. Circular resonators [14][22][23] have been investigated because they are completely symmetric about the rotation in the azimuth direction. Polarization-independent emissivity is obtained even at oblique angles. Recently, sphere lithography has been introduced for such circular resonators in order to skip electron-beam lithography [26]. Rectangular resonators have been widely investigated [27]-[41], and we focus on them to control parasitic modes.

The conventional rectangular resonators with silicon as the insulator and aluminum as the metal are shown in Figure 4. 1. In a certain condition, complete

omnidirectionality against azimuth rotation is achieved. Furthermore, the Q-factor is controlled by the aspect ratio of the rectangle [30].

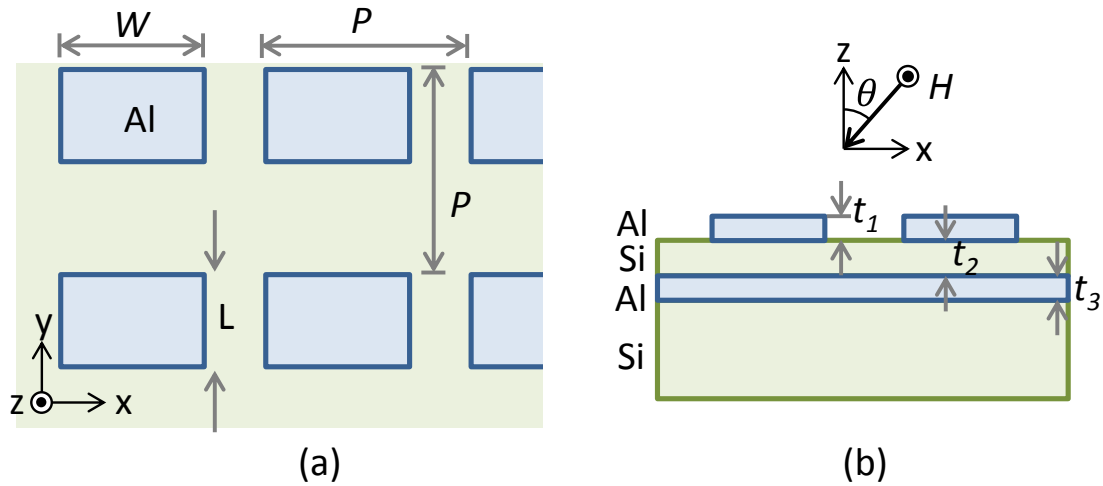


**Figure 4. 1 MIM metamaterial thermal emitter. [46]**

#### 4.1.3 Fundamental and parasitic mode

The spectral reflectivity of a typical MIM metamaterial with a period of  $P = 2.0 \mu\text{m}$ , a width of  $W = 1.4 \mu\text{m}$ , and a length of  $L = 0.95 \mu\text{m}$  is shown in Figure 4. 2. Throughout this section, spectra were simulated by CST microwave studio. The thickness of the three layers  $t_1$ ,  $t_2$ , and  $t_3$ , are set to be  $0.1 \mu\text{m}$ ,  $0.15 \mu\text{m}$ , and  $0.1 \mu\text{m}$ , respectively. For simplicity, the incidence in  $xz$ -plane is considered in this study. The fundamental and the higher modes are excited in such an MIM metamaterial. The reflectivity dips are observed in all cases at 28 THz. This dip corresponds to the fundamental mode, and total absorption is obtained at normal incidence. The absorption corresponding to the second-order mode is observed at 55 THz, in the case of the oblique incidence in p-polarization. As expected, the ratio of the second-order to the fundamental frequencies is almost two-fold. At normal incidence or in s-polarization, the second-order mode is

not excited with sufficient amplitude, because the z-component of the electric field in the incident light is indispensable in order to excite the second-order mode [31].

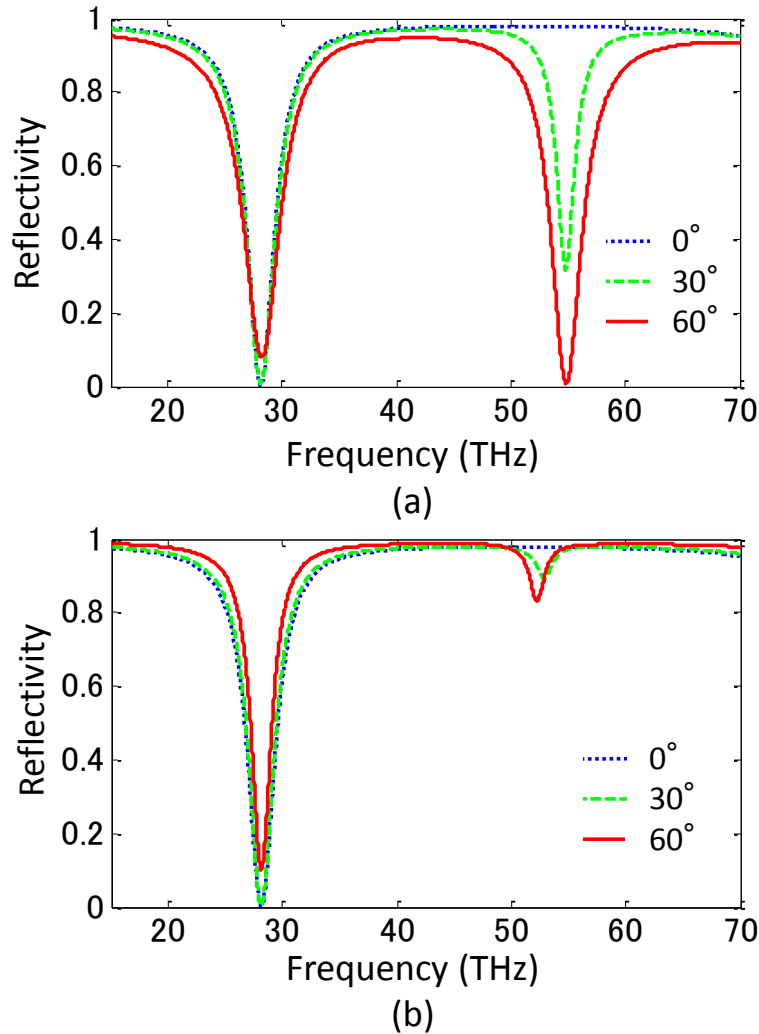


**Figure 4. 2 Reflectivity of the conventional emitter.**

**(a) p-polarization (b) s-polarization. [46]**

The magnetic fields at the resonances are shown in Table 4. 1. Since the incidence is p-polarized, the x- and z-components of magnetic field are zero. The snapshot of the y-component of magnetic field across two neighboring periods is shown so as to reveal the amplitude and the phase relationship across neighboring periods. The field is almost

uniform in the  $y$ - and the  $z$ -directions in the insulating layer of the rectangular resonators. In the  $x$ -direction, the field is zero on the edge of the rectangle. The field takes the maximum amplitude at the center of the rectangle at the fundamental frequency. At the second-order frequency, the field is zero at the center of the rectangle, and the fields in the left-hand side and the right-hand side are antiparallel.

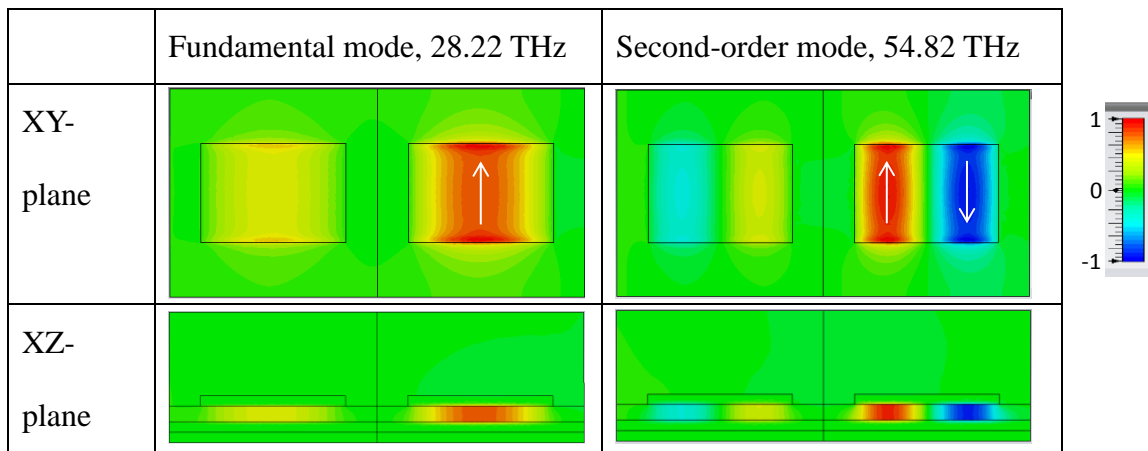


**Table 4. 1** Magnetic field  $H_y$  in the conventional emitter at an angle of  $60^\circ$ . [46]

Thermal radiation spectra from square resonator arrays are shown in Figure 4. 3. The geometrical parameters are:  $P = 1.96 \mu\text{m}$ ,  $W = L = 1.26 \mu\text{m}$ ,  $t_1 = t_3 = 0.1 \mu\text{m}$ , and  $t_2 = 0.13 \mu\text{m}$ . The selective emission is observed at a wavelength of  $10 \mu\text{m}$ . Meanwhile, there are several parasitic peaks at shorter wavelengths. The peak at  $5 \mu\text{m}$  corresponds to the second-order resonance. All the parasitic modes including the mode at  $5 \mu\text{m}$  and others degrade the performance of the thermal emitter.

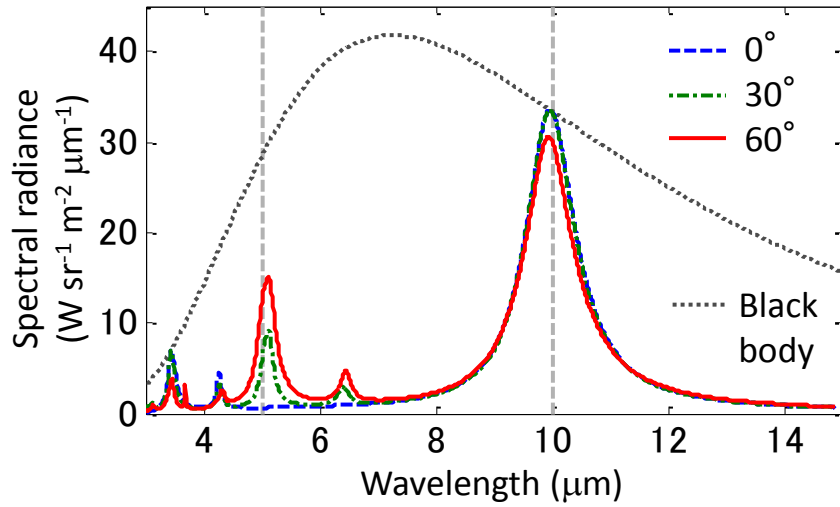


**Figure 4. 3 Thermal radiation spectra from the conventional emitter with square resonators. The emitter temperature is 400 K. [47]**

#### 4.1.4 Focus of this chapter

As already shown, the ratio of the second-order to the fundamental frequencies is fixed to be two-fold in the conventional MIM thermal emitter albeit the control of the ratio is required. Furthermore, several other parasitic modes are excited in square resonators. The thermal emission originating from these parasitic modes reduces the signal-to-background ratio of the system employing such an emitter. The control of these parasitic modes independent of the fundamental frequency allows us to avoid the false-detection through the parasitic modes. In this chapter, we focus on the control of the parasitic modes. In Section 4.2, diagonally arranged rectangular resonators are used to control the frequency interval between the fundamental and the second-order modes. In Section 4.3, densely-placed square resonators are investigated toward quasi-monochromatic emission. Both geometries utilize proximity interaction between neighboring resonators.

## 4.2 Second-order control by a diagonal arrangement

## 4.2.1 Geometry

The geometry of the presented MIM metamaterial is shown in Figure 4. 4. Two rectangular resonators are placed in one period. The shift  $S$  in the  $x$ -direction between two resonators plays a key role in the frequency interval control. The gap  $G$  between resonators in the  $y$ -direction determines the strength of the proximity coupling. The period  $P$  is fixed at  $2.0 \mu\text{m}$  throughout this section, such that the diffracted reflections are evanescent waves at the frequency lower than  $75 \text{ THz}$  in any angle of incidence. The width of the rectangle and the thicknesses are the same as those of the conventional rectangular resonators:  $W = 1.4 \mu\text{m}$ ,  $t_1 = 0.1 \mu\text{m}$ ,  $t_2 = 0.15 \mu\text{m}$ , and  $t_3 = 0.1 \mu\text{m}$ , respectively. The gap  $G$  is set at  $0.05 \mu\text{m}$  so as to enhance the proximity coupling. The symmetric, diagonal arrangement is attained by the half-shift ( $S = 1.0 \mu\text{m}$ ). As shown later, the frequency interval between the fundamental and the second-order mode is maximized at this condition, through the proximity coupling between resonators.

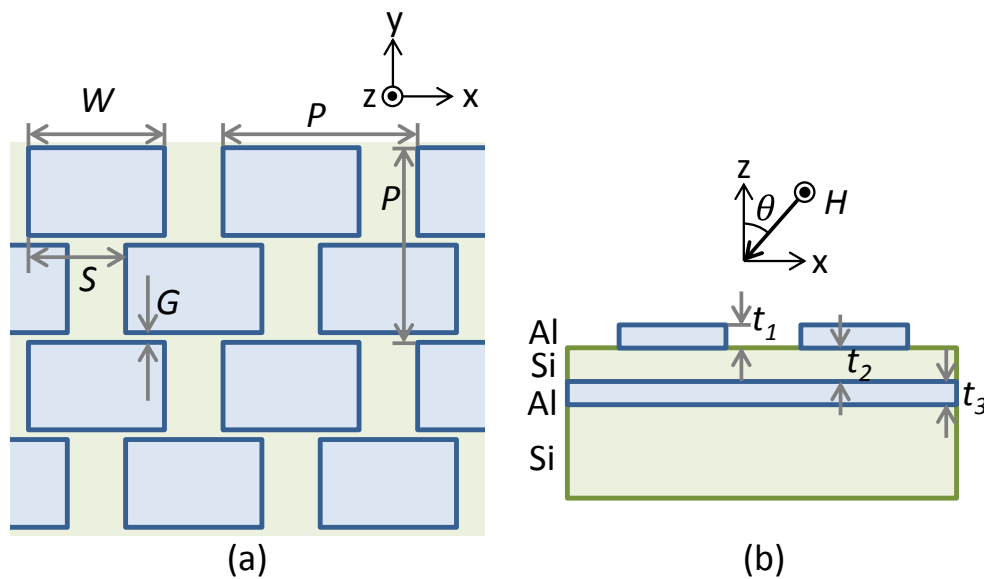


**Figure 4. 4 Diagonally arranged rectangular resonators. [46]**

## 4.2.2 Second-order resonance control

The resonant frequency of the half-shifted MIM metamaterial is shown in Figure 4. 5 (a). The second-order frequencies are sufficiently higher than twice the fundamental frequencies at all the incident angles. The ratio between the second-order and the fundamental frequencies is qualitatively shown in Figure 4. 5 (c). The ratio exceeds 2.5 at incident angles smaller than  $20^\circ$ . The ratio decreases as the incident angle increases. The enhancement of the frequency interval is not observed in the metamaterial without shift, as shown in Figure 4. 5 (b) and (d).

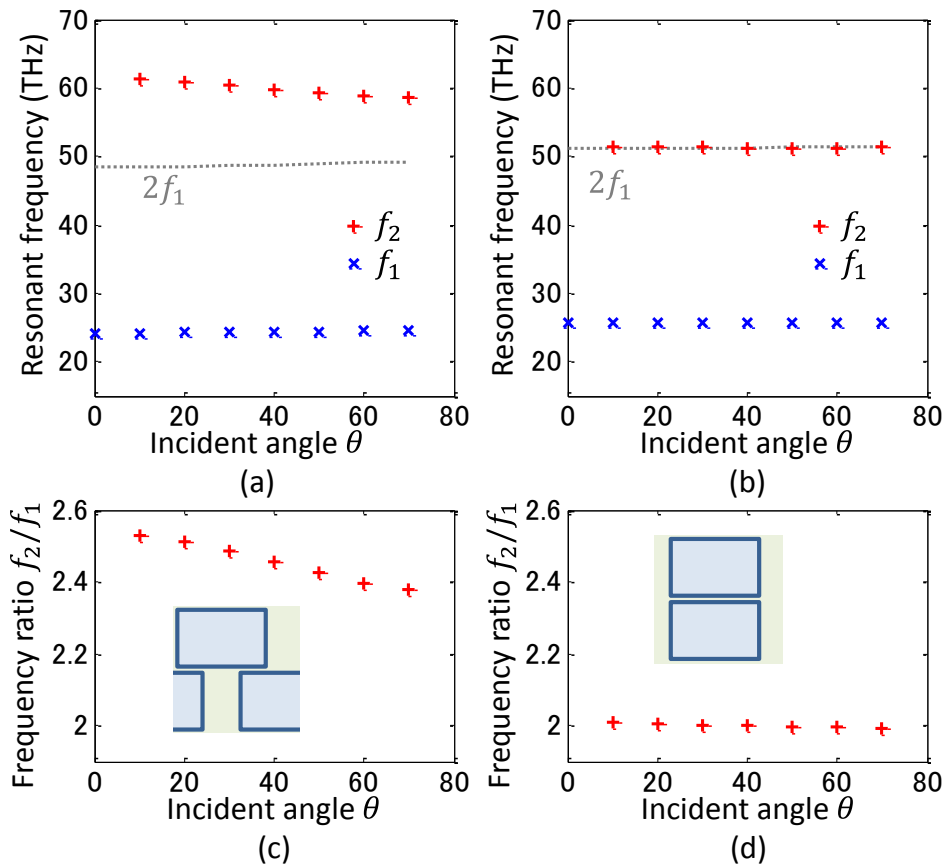


**Figure 4. 5 Resonant frequencies as a function of incident angle.**

**(a)(c) Half-shifted,  $S = 1.0 \mu\text{m}$ . (b)(d) No shift,  $S = 0.0 \mu\text{m}$ .**

**(c)(d) Ratio between the second-order and the fundamental frequencies. [46]**

The  $y$ -components of the magnetic fields at the resonances are shown in Table 4. 2. The neighboring resonators are almost in-phase at the fundamental frequency. At the second-order frequency, the neighboring magnetic fields are antiparallel. For example, the magnetic field in the left-hand side of resonator A is upward, whereas the field in the right-hand side of resonator B is downward. Thus, the interaction between neighboring resonators shortens the effective width for the second-order mode. The shortening is larger as the incident angle is smaller, because the phase difference between the magnetic fields is close to  $\pi$  in such cases. Such a trend is already observed in Figure 4. 5 (a).

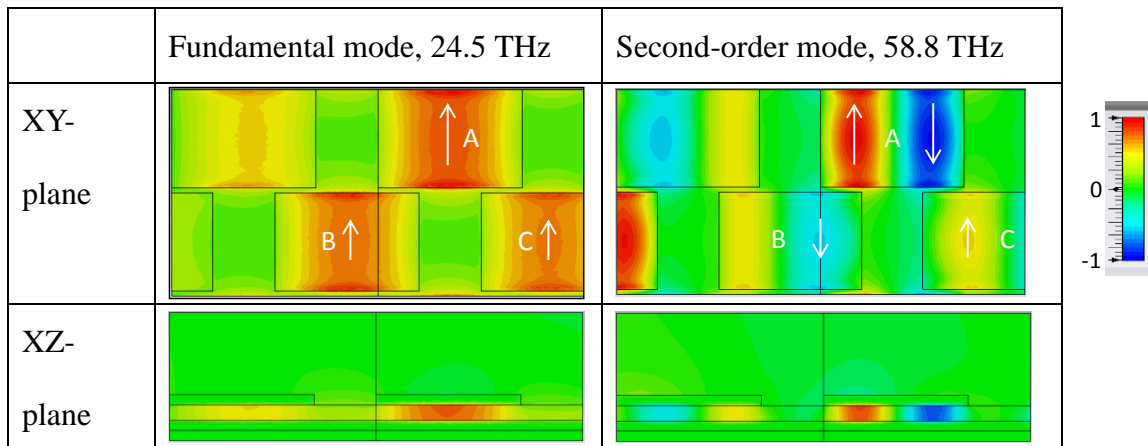


**Table 4. 2 Magnetic field  $H_y$  at the resonant frequencies at an angle of  $60^\circ$ . [46]**

Next we investigate how the geometrical parameter affects the frequency interval. Firstly, the gap value is varied from  $0.05 \mu\text{m}$  to  $0.50 \mu\text{m}$ . As shown in Figure 4. 6 (a) and (c), the ratio between the second-order and the fundamental frequencies is maximized when the gap  $G$  is minimized. This illustrates that the interval control is possible though the proximity interaction. The shift of the fundamental frequency is caused by the variation of the length of the rectangle. Secondary, the shift value  $S$  is varied from  $0.0 \mu\text{m}$  to  $1.0 \mu\text{m}$ . The ratio is maximized when the shift is large, as shown

in Figure 4. 6 (b) and (d). Interestingly, two other modes are excited in asymmetrically shifted metamaterials. In particular, the higher mode  $f_{ph}$  splits from the second-order resonance. The mode is discussed in detail in the next section.

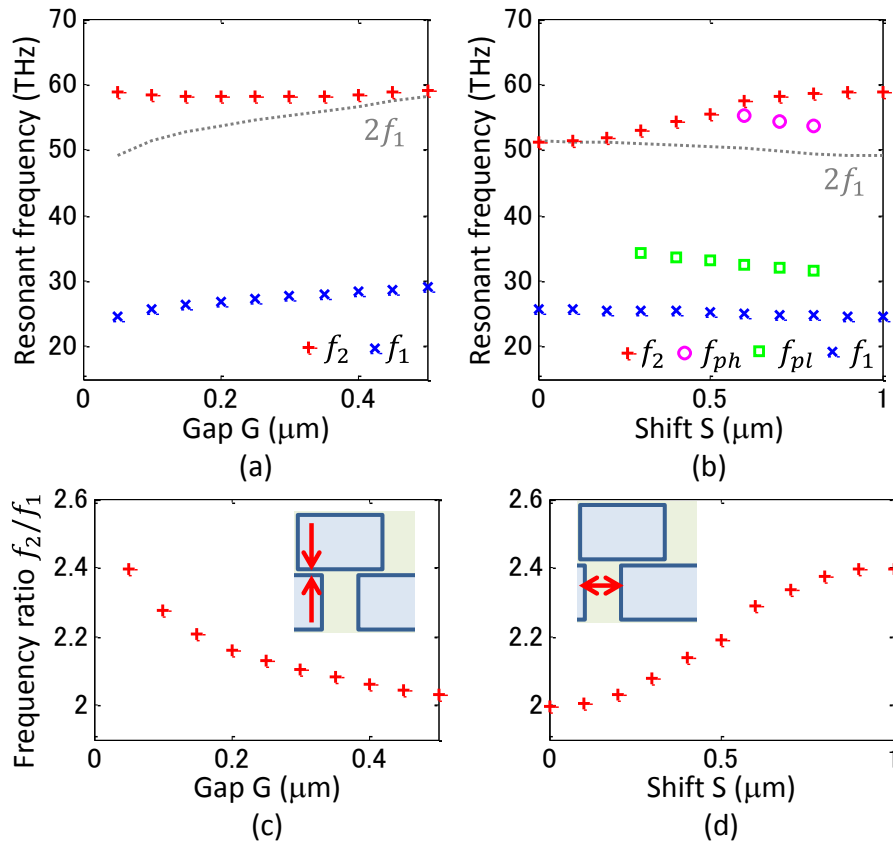


**Figure 4. 6 Resonant frequencies at an angle of  $60^\circ$ .**

**(a)(c) As a function of gap. (b)(d) As a function of shift.**

**(c)(d) Ratio between the second-order and the fundamental frequencies. [46]**

## 4.2.3 Asymmetrically-shifted resonators

The metamaterial with a shift of  $0.7 \mu\text{m}$  is investigated in order to understand the split mode. Figure 4. 7 shows the reflectance of the metamaterial with  $t_3 = 0.25 \mu\text{m}$ , which is chosen so as to maximize the absorption at the split mode. Interestingly, the split mode is excited in the normal incidence at a frequency of  $50.65 \text{ THz}$  (i). The magnetic field is shown in Figure 4. 8 (a). The field in the left-hand side of resonator A and that in the right-hand side of resonator B interact to each other, and the fields are in the same direction, i.e. constructive interaction. The field in the right-hand side of resonator A and that in the left-hand side of resonator C are also in the same direction. The same relationship of the fields is also observed at an oblique incidence as shown in Figure 4. 8 (b) (ii). Because of such a relationship between the fields, the split mode frequency is lower than the second-order frequency (iii), where the magnetic fields between resonators are antiparallel as shown in Figure 4. 8 (c).

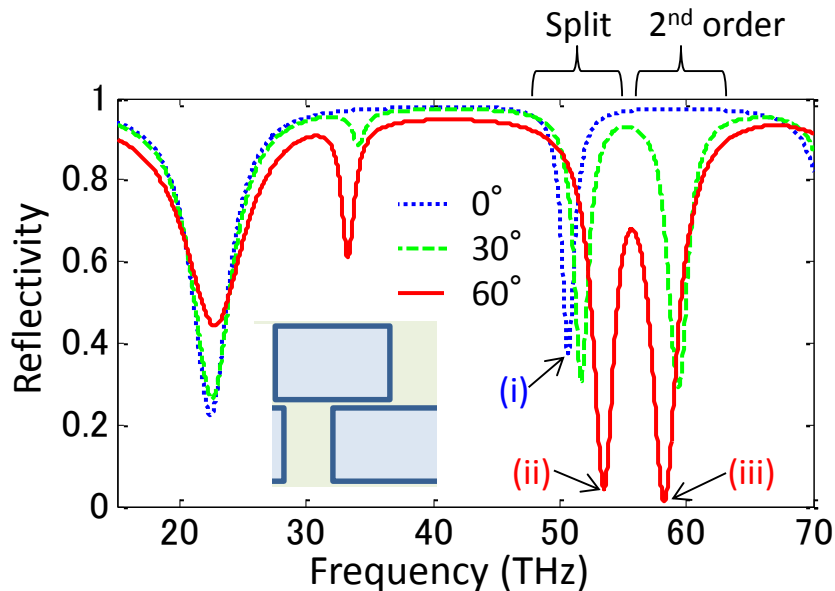


**Figure 4. 7 Reflection spectra of the asymmetrically shifted MIM resonator [46]**

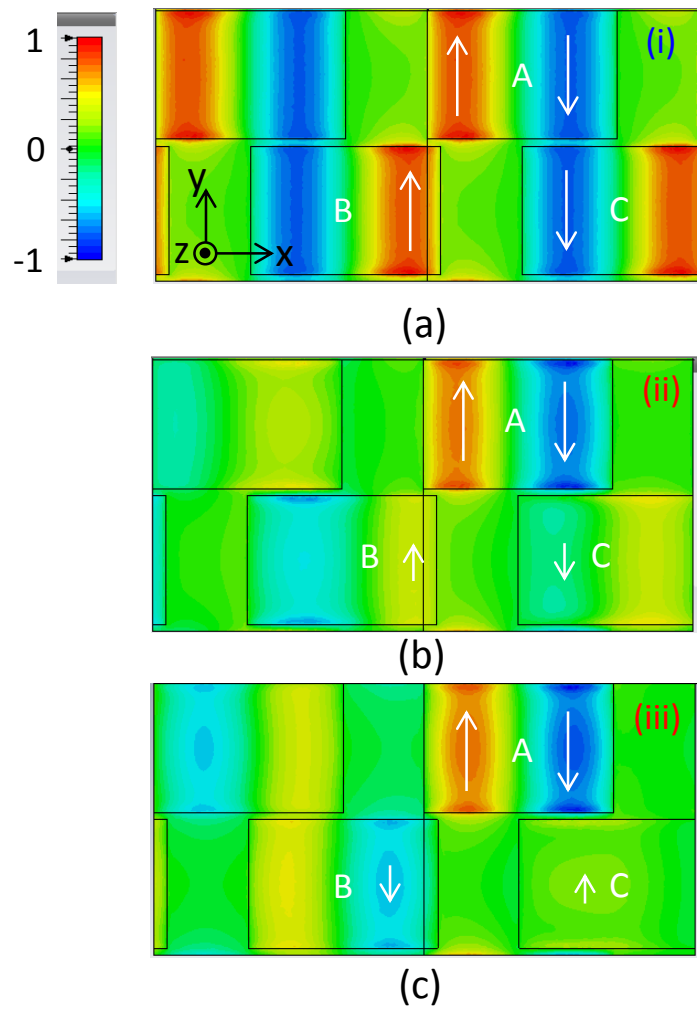


**Figure 4. 8 Magnetic fields  $H_y$  in the asymmetrically shifted resonators.**

**(a) Split mode, normal (b) Split mode,  $60^\circ$  (c) Second-order mode,  $60^\circ$  [46]**

### 4.3 Densely placed square resonators

#### 4.3.1 Geometry

Figure 4. 9 shows the schematics of the densely-placed square resonators. The geometrical parameters are  $P = 0.89 \mu\text{m}$ ,  $W = L = 0.87 \mu\text{m}$ ,  $t_1 = t_3 = 0.1 \mu\text{m}$  and  $t_2 = 0.09 \mu\text{m}$ . The gap between resonators is  $0.02 \mu\text{m}$ , and it enables the strong interaction between resonators.

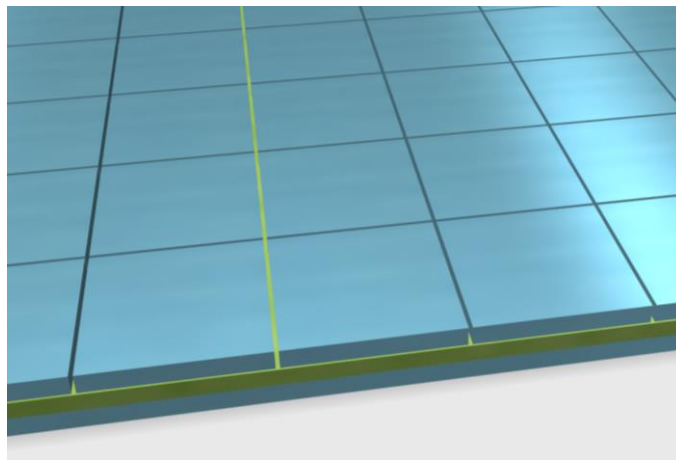


**Figure 4. 9 Schematics of the densely-placed metamaterial [47]**

#### 4.3.2 Parasitic control toward monochromatic emission

Thermal radiation spectra from the densely-placed metamaterial at a temperature of 400 K are shown in Figure 4. 10. The selective emission is observed at a wavelength of  $10 \mu\text{m}$ . The parasitic emission is significantly suppressed compared to the radiation from the conventional emitter shown in Figure 4. 3. There is only one parasitic peak around a wavelength of  $4 \mu\text{m}$ , and it corresponds to the second-order mode. Other peaks observed in Figure 4. 3 disappear due to the densely-placed geometry. The parasitic heat flux, which is defined as the integrated spectra from  $3$  to  $7 \mu\text{m}$ , is suppressed from  $11.8 \text{ Wsr}^{-1}\text{m}^{-2}$  to  $4.0 \text{ Wsr}^{-1}\text{m}^{-2}$  at an angle of  $60^\circ$ .

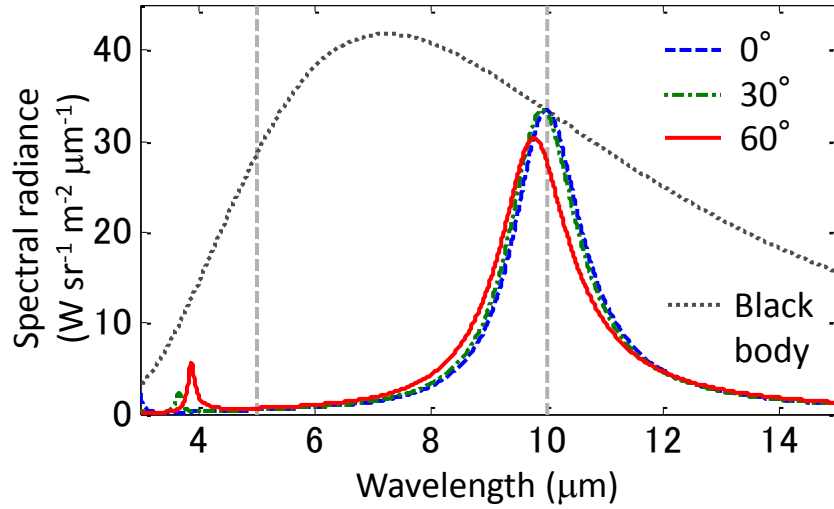


**Figure 4. 10 Thermal radiation spectra of the densely-placed MIM metamaterial**

[47]

The emissivity profiles are investigated in detail, in order to explain the suppression mechanism. The emissivity of the conventional and the densely-packed emitters in both polarizations are shown as a function of angles in Figure 4. 11 and Figure 4. 12. In the conventional thermal emitter, the second-order mode is excited in p-polarization at half the wavelength of the fundamental mode. Additionally, the third-order mode is excited at one third of the fundamental wavelength. Resonance originating from the propagating surface plasmon polariton exhibits the dependence on the angle. There are other parasitic peaks named mode A and mode B. Mode A is excited in both polarizations, while mode B is excited only in the s-polarization. On the contrary, these parasitic modes are suppressed except the second-order mode in the densely-placed emitter. The wavelength of the second-order mode is successfully shifted toward shorter wavelength.

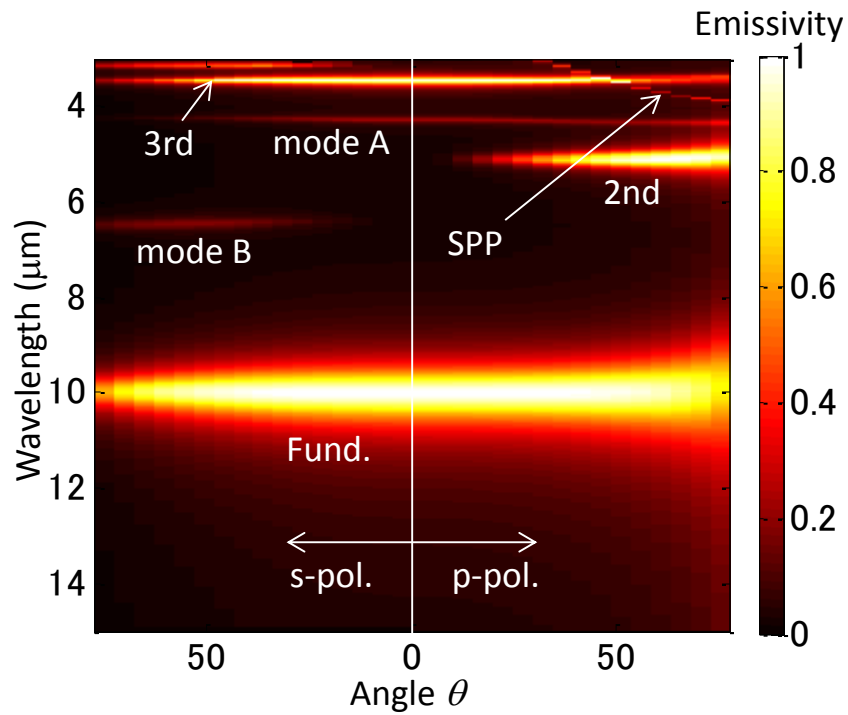


Figure 4. 11 Emissivity profile of the conventional emitter. [47]

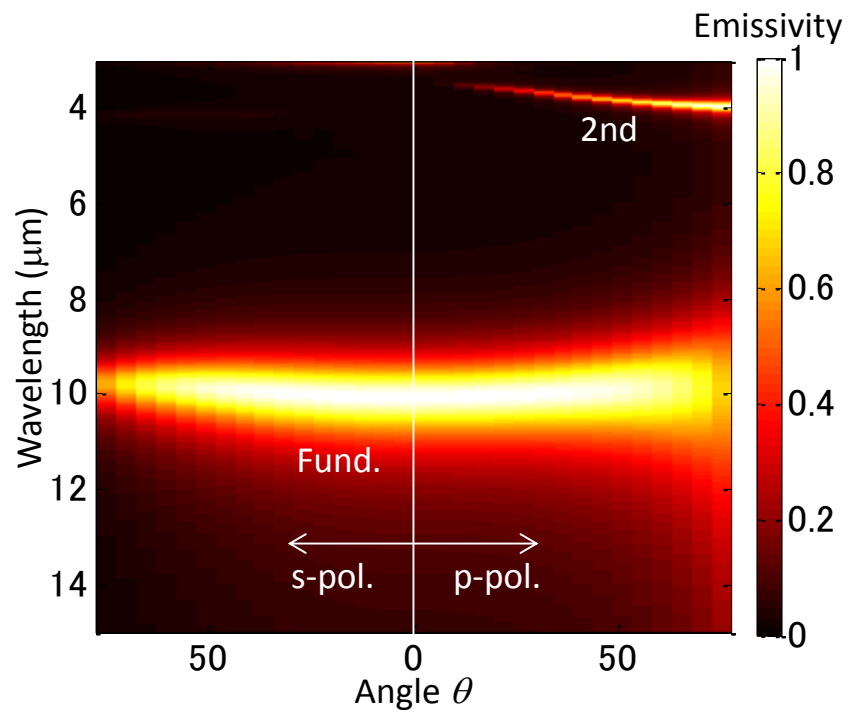
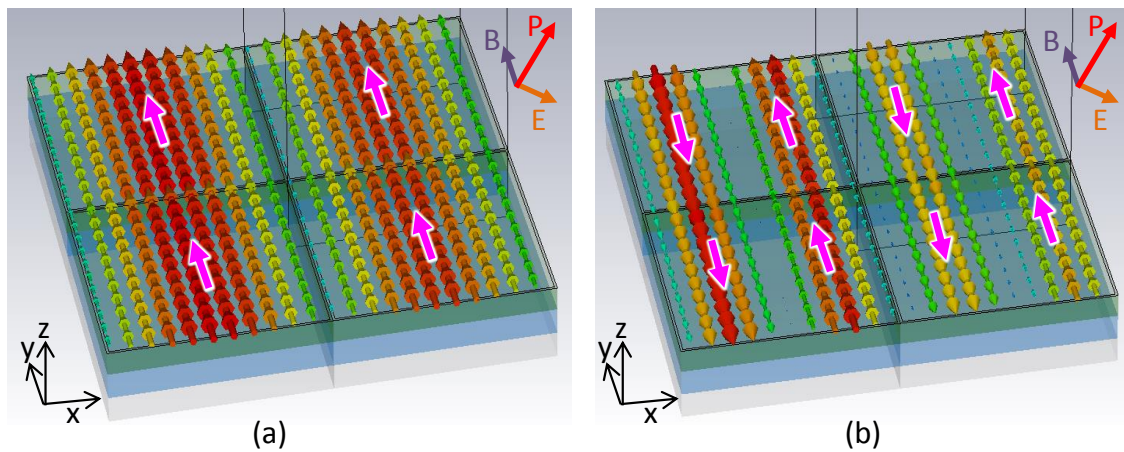


Figure 4. 12 Emissivity profile of the densely-packed emitter. [47]

Figure 4. 13 explains the reason why the ratio between the second-order and the fundamental wavelengths are larger than twofold. In the densely-placed emitter, the fields in neighboring resonators interact to each other. Because the magnetic fields at the fundamental wavelength have almost the same phase, the effective width of the resonator becomes wider. On the other hand, the fields at the second-order wavelength are antiparallel, thus the effective width is almost constant.



**Figure 4. 13 Magnetic field profiles in the densely-placed emitter at an emission angle of  $30^\circ$  in p-polarization.**

**(a) Fundamental mode (b) Second-order mode [47]**

Figure 4. 14 shows the fields of mode A and mode B in the conventional resonators. Considering the magnetic field of mode A, the field at position  $\alpha$  is in the positive x-direction, whereas that at position  $\beta$  is in the negative x-direction. These magnetic fields connect to the far-field emission through the area where top aluminum does not exist, so as to satisfy the Gauss's law for magnetism. The area decreases as the gap becomes smaller, and the Gauss's law for magnetism is not more satisfied because the field at position  $\alpha$  and that at position  $\beta$  of the neighboring resonator interact destructively. Thus, mode A is not excited in the densely-placed resonators. The same condition applies to mode B.

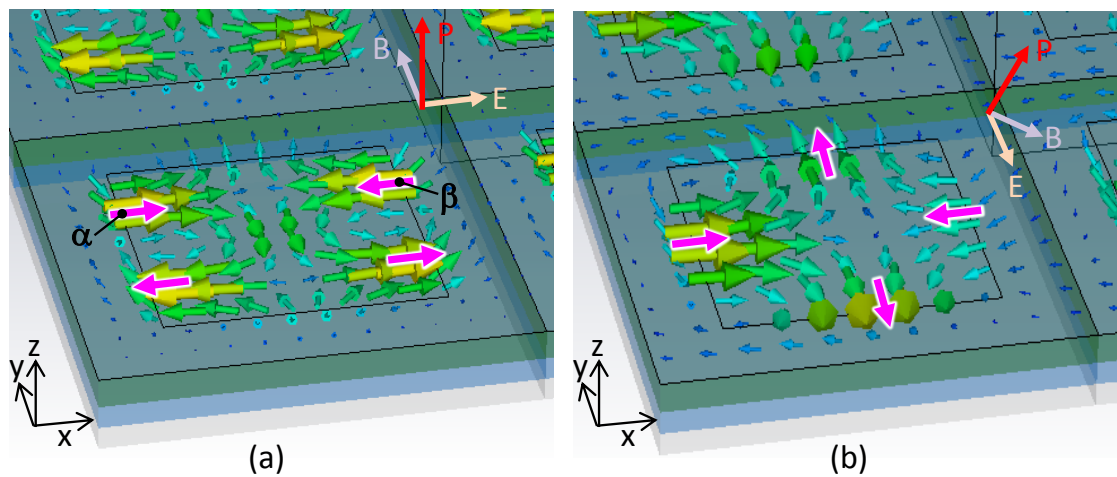


**Figure 4. 14 Magnetic field profiles in the conventional emitter.**

**(a) mode A, 4.27  $\mu\text{m}$ , 0°, p-polarization. (b) Mode B, 6.40  $\mu\text{m}$ , 30°, s-polarization.**

[47]

## 4.3.3 Gap dependence

Figure 4. 15 shows how the resonant emission is modified according to the gap values. Changing parameters are (a) the gap  $g_x$  in the x-direction, (b) the gap  $g_y$  in the y-direction, and (c) both gaps simultaneously from  $0.02 \mu\text{m}$  to  $0.2 \mu\text{m}$ . In all three case, the amplitude of mode A decreases as the gap decreases. The wavelength ratio between the fundamental and the second-order modes are larger than twofold in Figure 4. 15 (a) and (c). This means that the proximity interaction in the x-direction plays the key role in the control of the second-order harmonics, i.e., the effective width of the fundamental mode is enlarged by the interaction, while that of the second-order mode is unchanged. On the other hand, the proximity interaction in the y-direction shifts both the second-order and the fundamental wavelengths, i.e., the effective lengths of both modes are almost the same. Surface plasmon polariton (SPP) vanishes from this wavelength range by the small period in the x-direction, because SPP is excited at the wavelength where the first order diffraction becomes evanescent.

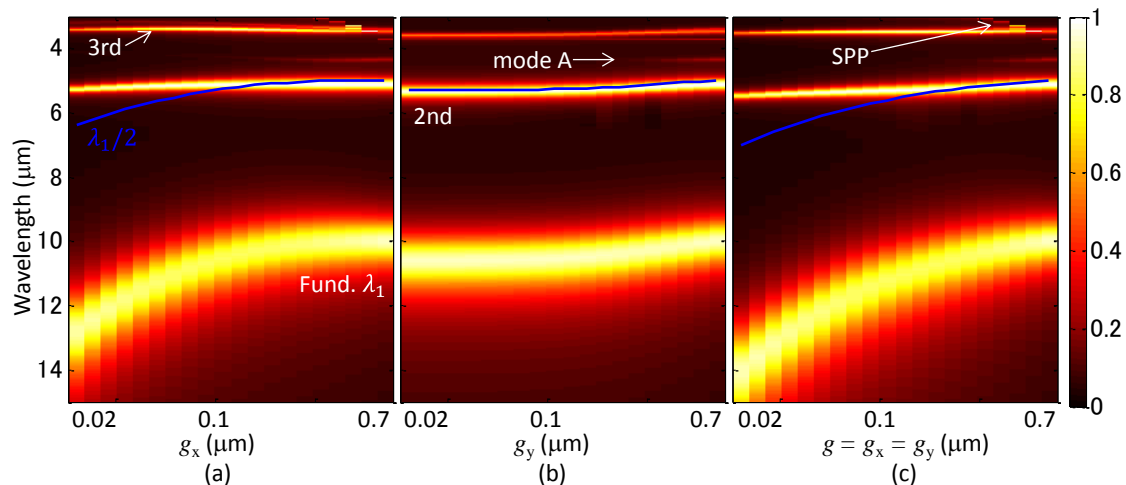


**Figure 4. 15 Emissivity at an angle of  $60^\circ$  in p-polarization as a function of (a)  $g_x$ , (b)  $g_y$ , and (c)  $g = g_x = g_y$ . [47]**

#### 4.4 Experimental investigations

##### 4.4.1 Fabrication of the metamaterials

The presented MIM metamaterials were fabricated by electron-beam lithography and reactive-ion-etching. Firstly, the trilayer were deposited by magnetron sputtering on a 4-inch silicon substrate with a standard thickness of 525  $\mu\text{m}$ . An electron-beam resist (ZEP 520A, Nippon Zeon) was spin-coated onto the wafer with a rotation speed of 4000 rpm, and was baked on a hotplate at 180  $^{\circ}\text{C}$  for 5 min. Electron beam was irradiated to the wafer by an electron-beam writer with a variable-shaped beam capability (F5112 + VD01, Advantest) [48]. The metamaterial with an area of 11 mm  $\times$  10.5 mm was written in 15 min with a dose of 110  $\mu\text{C}/\text{cm}^2$ . The resist was developed by n-amyl acetate (ZED-N50) for 120 sec, and was rinsed by the mixture of methyl isobutyl keton and isopropyl alcohol (ZMD-B). The resist pattern was transferred to the top aluminum layer by reaction-ion-etching. The fabricated metamaterials with the diagonal arrangements were shown in Figure 4. 16.

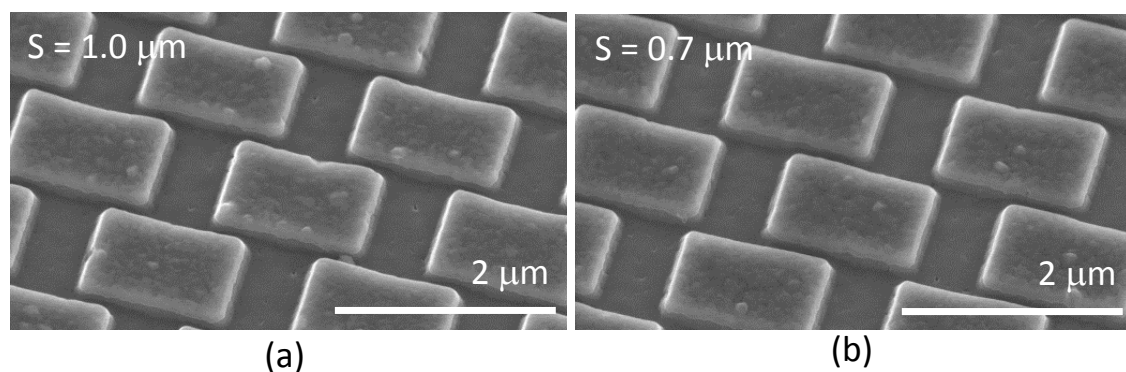


**Figure 4. 16 SEM of the fabricated metamaterials with the diagonal arrangements.**

**(a) Half-shifted resonators. (b) Asymmetrically shifted resonators. [46]**

## 4.4.2 Reflection spectra of diagonally arranged metamaterials

The reflectivity spectra of MIM metamaterial were measured by FT-IR. The ratio of the second-order to the fundamental frequencies is sufficiently larger than two-fold in the half-shifted metamaterial as shown in Figure 4. 17. As discussed, the second-order frequency becomes higher as the incident angle decreases. Two parasitic modes are observed in the asymmetrically-shifted absorber as shown in Figure 4. 18. The frequencies of these two modes are close to the fundamental or the second-order modes, respectively, as investigated in Subsection 4.2.3.

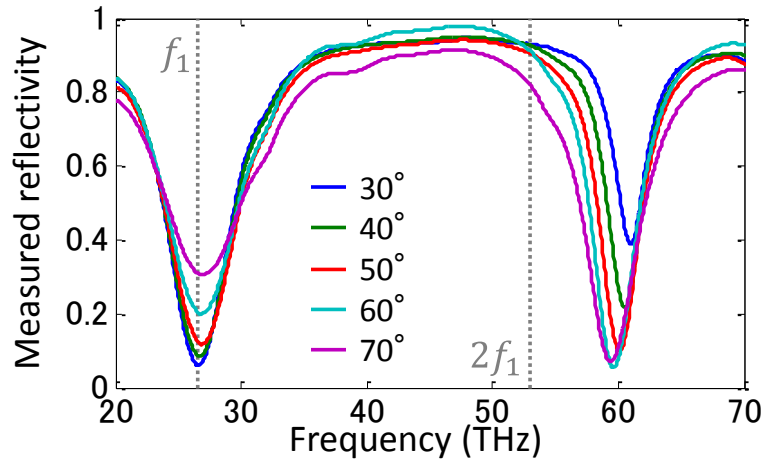


Figure 4. 17 Measured reflectivity of the half-shifted resonators. [46]

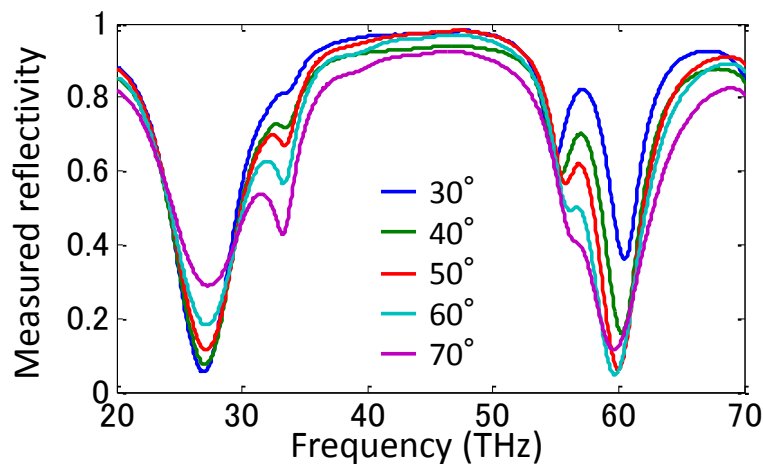
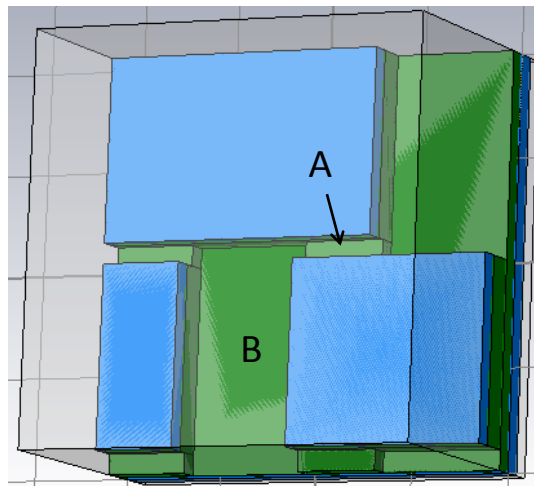


Figure 4. 18 Measured reflectivity of the asymmetrically shifted resonators. [46]

The model shown in Figure 4. 19 was utilized for the numerical simulation in order to support the measured spectra, Here, the depth of the overetch at position A (narrow gap between rectangles) was set to be  $0.05 \mu\text{m}$ , whereas the depth at position B (other positions) was set to be  $0.15 \mu\text{m}$ . Such position-dependent depth of overetch is attributed to the etch-rate of RIE process, which is dependent on the opening width of the resist mask. The permittivity of amorphous silicon  $\epsilon_{\alpha Si}$  is expressed by a Drude model:

$$\epsilon_{\alpha Si} = \epsilon_{\infty} - \frac{f_p^2}{f(f + i\gamma)}, \quad (4.2)$$

where the selected parameters  $\epsilon_{\infty} = 3.85^2$ ,  $f_p = 54.59 \text{ THz}$ , and  $\gamma = 9.024 \text{ THz}$  are consistent with Ref. [44][45]. The numerically calculated spectra are shown in Figure 4. 20 and Figure 4. 21. They agree with the measured reflectivity well. As shown in Figure 4. 22, the numerical calculation without overetch (OE) also exhibits the enhanced frequency ratio and follows the measured spectra qualitatively, while the calculation with OE quantitatively reproduces the resonant wavelengths.



**Figure 4. 19 Model utilized for the numerical simulation.**

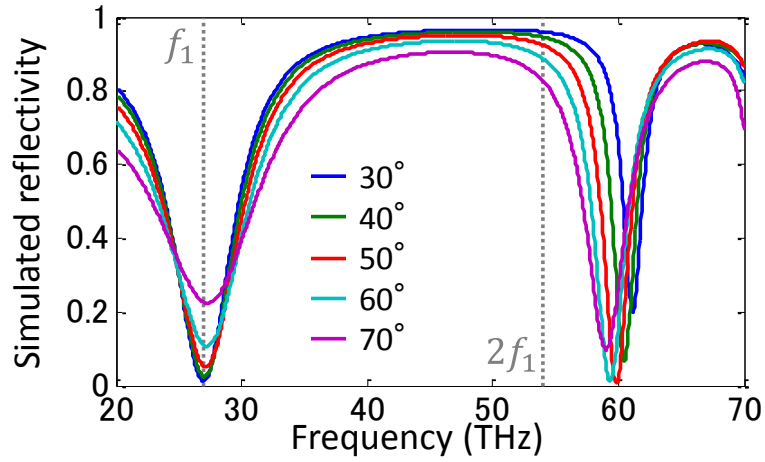


Figure 4. 20 Simulated reflectivity of the half-shifted resonators. [46]

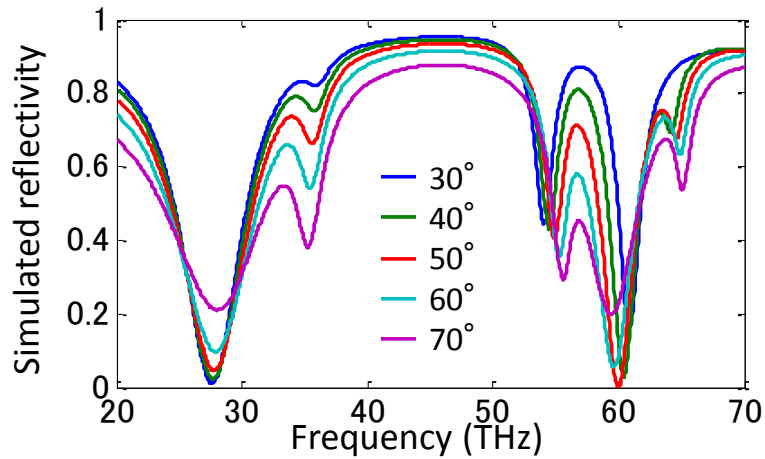


Figure 4. 21 Simulated reflectivity of the asymmetrically shifted resonators. [46]

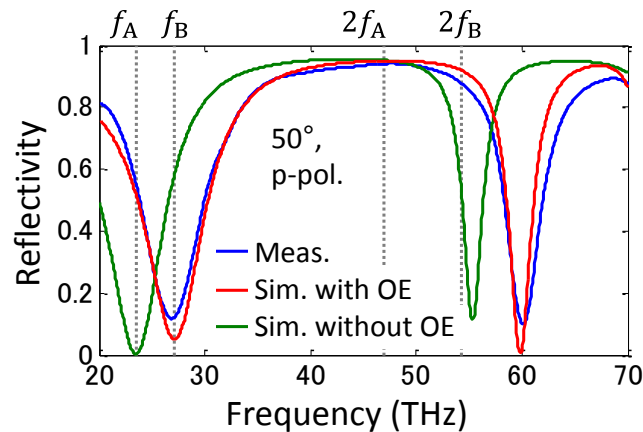
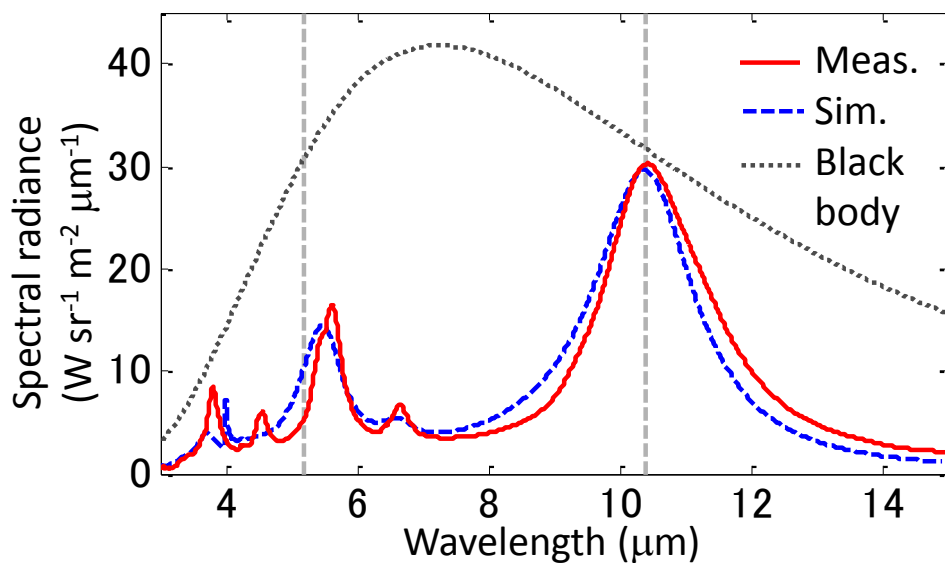


Figure 4. 22 Reflectivity of the half-shifted resonators at  $50^\circ$  in p-pol. Reflectivity measured, simulated with overetch (OE), and simulated without OE are shown.

## 4.4.3 Thermal radiation and reflection spectra of densely-placed square emitters

Thermal radiation spectra from the square emitters were measured by Fourier-transformed infrared spectrometer with an accessory for emission measurement. The measurement was outsourced, and the measured blackbody spectrum agrees well with the Planck equation. This validates the quality of the calibration at the outsourced company. The measured spectra of the conventional emitter are shown in Figure 4. 23. Several parasitic peaks are observed at the wavelength shorter than 7  $\mu\text{m}$ . Such parasitic modes are successfully eliminated or shifted to a shorter wavelength in the densely-placed emitter as shown in Figure 4. 24.



**Figure 4. 23 Thermal radiation spectra of the conventional emitter. [47]**

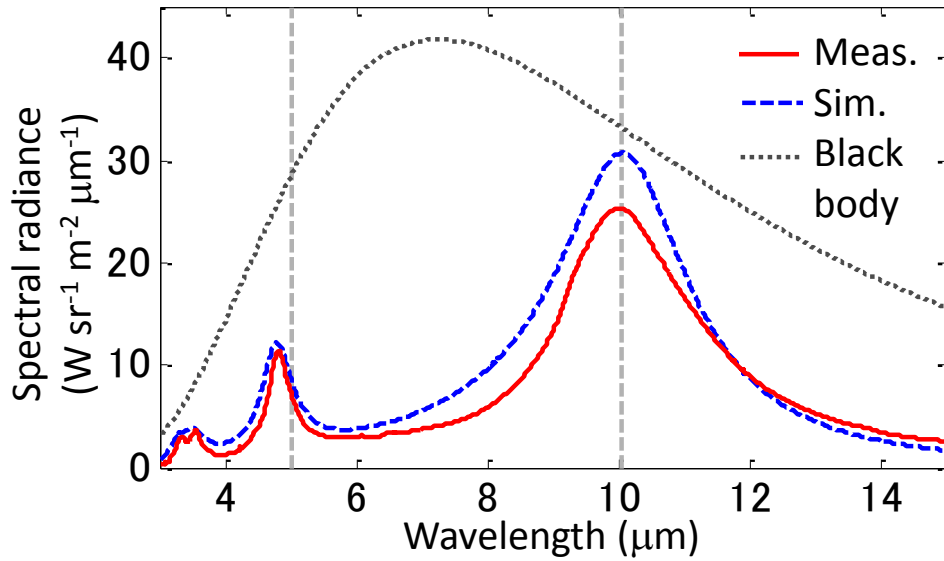
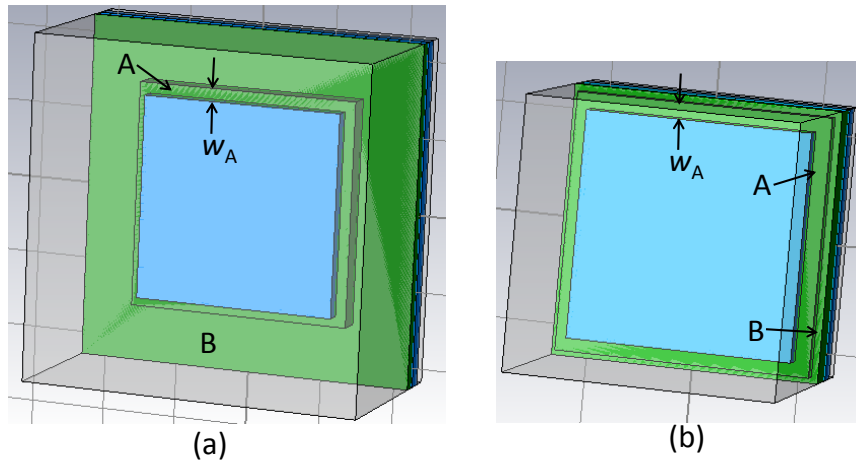


Figure 4. 24 Thermal radiation spectra of the densely-placed emitter. [47]

Spectra were numerically simulated by the model shown in Figure 4. 25. Here, the depth of the overetch at area B was set to be  $0.15 \mu\text{m}$  and  $0.07 \mu\text{m}$  for the conventional and the densely-placed resonators, respectively. We assume an intact area A around the metallic square, where the depth of the overetch is zero. The width  $w_A$  of area A is set to be  $0.07 \mu\text{m}$  for both resonators. The permittivity of amorphous silicon  $\epsilon_{\alpha Si}$  was set to be a constant value of  $13 + 1i$ . The numerically simulated spectra are also shown in Figure 4. 23 and Figure 4. 24, and they agree well with the measured spectra.



**Figure 4. 25 Model for the numerical simulation.**

**(a) Conventional resonator. (b) Densely-placed resonator.**

The peak of the measured spectra differs from that of the measured spectra. This is because the densely-placed resonator is sensitive to the fluctuation of the gap originating from the fabrication error. Although the peak emissivity at the fundamental mode is lower than the numerical simulation, the red-shift of the second-order wavelength and the elimination of mode A and mode B are experimentally validated.

The relationship between the resonant wavelengths and the gap size was experimentally studied based on microscopic reflection spectroscopy. The observation angle was set around  $30^\circ$ . The gap size was varied between  $0.1 \mu\text{m}$  to  $0.5 \mu\text{m}$  in the GDS file, while the width of the metallic square was set to be  $0.85 \mu\text{m}$ . The observed resonant wavelengths are shown in Figure 4. 26. The fundamental wavelength is almost twice the second-order wavelength when the gap is large. The ratio becomes higher as the gap becomes smaller, through the increase of the fundamental wavelength. On the contrary, the second-order wavelength is kept almost constant in this parametric study. This tendency follows the simulated results shown in Figure 4. 15 (c).

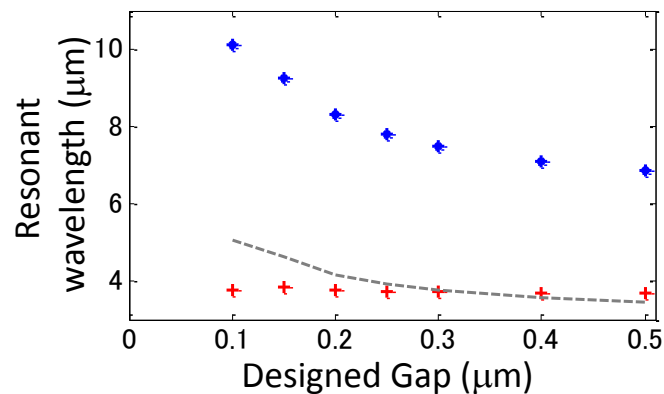


**Figure 4. 26 Resonant wavelengths as a function of the designed gap. The blue dots denote the fundamental wavelengths, and the red crosses denote the second-order wavelengths. The gray dashed curve denotes the half the fundamental wavelengths.**

[47]

#### 4.5 Chapter summary

A quasi-monochromatic thermal emitter has been realized by utilizing the proximity interaction between metal-insulator-metal resonators. The frequency interval between the fundamental and the second-order modes is enlarged by diagonally arranging rectangular resonators or densely placing square resonators. A ratio larger than 2.5 is observed in both configurations. Other parasitic modes are eliminated in the densely-placed resonators. The integrated parasitic heat flux in the densely-placed resonators are suppressed from  $11.8 \text{ Wsr}^{-1}\text{m}^{-2}$  to  $4.0 \text{ Wsr}^{-1}\text{m}^{-2}$  at an angle of  $60^\circ$ . The presented metamaterial absorbers or thermal emitters were fabricated by electron-beam lithography. The fabricated metamaterials were evaluated by Fourier-transform infrared spectrometer, and the measured spectra agree well with numerical simulations.

**Reference**

- [1] J. Meléndez, A. J. de Castro, F. López, and J. Meneses, “Spectrally selective gas cell for electrooptical infrared compact multigas sensor.” *Sens. Actuators A* **47**, 417 (1995).
- [2] J. Hodgkinson and R. P. Tatam, “Optical gas sensing: a review.” *Meas. Sci. Technol.* **24**, 012004 (2013).
- [3] A. De Luca, M. T. Cole, A. Fasoli, S. Z. Ali, F. Udrea, and W. I. Milne, “Enhanced infra-red emission from sub-millimeter microelectromechanical systems micro hotplates via inkjet deposited carbon nanoparticles and fullerenes.” *J. Appl. Phys.* **113**, 214907 (2013).
- [4] W. Weppner, "Solid-state electrochemical gas sensors." *Sens. Actuators* **12**, 107-119 (1987).
- [5] P. Krebs, and A. Grisel. "A low power integrated catalytic gas sensor." *Sens. Actuators B* **13**, 155 (1993).
- [6] C. Wang, L. Yin, L. Zhang, D. Xiang, and R. Gao. "Metal oxide gas sensors: sensitivity and influencing factors." *Sensors* **10**, 2088-2106 (2010).
- [7] C. M. Wang, Y. C. Chang, M. W. Tsai, Y. H. Ye, C. Y. Chen, Y. W. Jiang, Y. T. Chang, S. C. Lee, and D. P. Tsai. "Reflection and emission properties of an infrared emitter." *Opt. Exp.* **15**, 14673 (2007).
- [8] Y. H. Ye, Y. W. Jiang, M. W. Tsai, Y. T. Chang, C. Y. Chen, D. C. Tzuang, Y. T. Wu, and S. C. Lee, “Localized surface plasmon polaritons in Ag/SiO<sub>2</sub>/Ag plasmonic thermal emitter” *Appl. Phys. Lett.* **93**, 033113 (2008)

- [9] B. J. Lee, L. P. Wang, and Z. M. Zhang. "Coherent thermal emission by excitation of magnetic polaritons between periodic strips and a metallic film." *Opt. Exp.* **16**, 11328 (2008).
- [10] M. Diem, T. Koschny, and C. M. Soukoulis. "Wide-angle perfect absorber/thermal emitter in the terahertz regime." *Phys. Rev. B* **79**, 033101 (2009).
- [11] J. A. Mason, S. Smith, and D. Wasserman, "Strong absorption and selective thermal emission from a midinfrared metamaterial" *Appl. Phys. Lett.* **98**, 241105 (2011).
- [12] C. Koechlin, P. Bouchon, F. Pardo, J. Jaeck, X. Lafosse, J. L. Pelouard, and R. Häïdar. "Total routing and absorption of photons in dual color plasmonic antennas." *Appl. Phys. Lett.* **99**, 241104 (2011).
- [13] L. P. Wang, and Z. M. Zhang. "Wavelength-selective and diffuse emitter enhanced by magnetic polaritons for thermophotovoltaics." *Appl. Phys. Lett.* **100**, 063902 (2012).
- [14] I. Puscasu and W. L. Schaich. "Narrow-band, tunable infrared emission from arrays of microstrip patches." *Appl. Phys. Lett.* **92**, 233102 (2008).
- [15] X. Liu, T. Starr, A. F. Starr, and W. J. Padilla, "Infrared spatial and frequency selective metamaterial with near-unity absorbance," *Phys. Rev. Lett.* **104**, 207403 (2010).
- [16] N. Liu, M. Mesch, T. Weiss, M. Hentschel, and H. Giessen. "Infrared perfect absorber and its application as plasmonic sensor." *Nano Lett.* **10**, 2342 (2010).
- [17] K. Aydin, V. E. Ferry, R. M. Briggs, and H. A. Atwater, "Broadband polarization-independent resonant light absorption using ultrathin plasmonic super absorbers," *Nat. Commun.* **2**, 517 (2011).

- [18] X. Liu, T. Tyler, T. Starr, A. F. Starr, N. M. Jokerst, and W. J. Padilla. "Taming the blackbody with infrared metamaterials as selective thermal emitters." *Phys. Rev. Lett.* **107**, 045901 (2011).
- [19] K. B. Alici, A. B. Turhan, C. M. Soukoulis, and E. Ozbay. "Optically thin composite resonant absorber at the near-infrared band: a polarization independent and spectrally broadband configuration." *Opt. Exp.* **19**, 14260 (2011).
- [20] B. Zhang, Y. Zhao, Q. Hao, B. Kiraly, I. C. Khoo, S. Chen, and T. J. Huang. "Polarization-independent dual-band infrared perfect absorber based on a metal-dielectric-metal elliptical nanodisk array." *Opt. Exp.* **19**, 15221 (2011).
- [21] Z. H. Jiang, S. Yun, F. Toor, D. H. Werner, and T. S. Mayer. "Conformal dual-band near-perfectly absorbing mid-infrared metamaterial coating." *ACS nano* **5**, 4641 (2011).
- [22] C. W. Cheng, M. N. Abbas, C. W. Chiu, K. T. Lai, M. H. Shih, and Y. C. Chang. "Wide-angle polarization independent infrared broadband absorbers based on metallic multi-sized disk arrays." *Opt. Exp.* **20**, 10376 (2012).
- [23] M. G. Nielsen, A. Pors, O. Albrektsen, and S. I. Bozhevolnyi. "Efficient absorption of visible radiation by gap plasmon resonators." *Opt. Exp.* **20**, 13311 (2012).
- [24] K. Chen, R. Adato, and H. Altug. "Dual-band perfect absorber for multispectral plasmon-enhanced infrared spectroscopy." *Acs Nano* **6**, 7998 (2012).
- [25] J. A. Bossard, L. Lin, S. Yun, L. Liu, D. H. Werner, and T. S. Mayer. "Near-ideal optical metamaterial absorbers with super-octave bandwidth." *ACS nano* **8**, 1517 (2014).

- [26] T. D. Dao, K. Chen, S. Ishii, A. Ohi, T. Nabatame, M. Kitajima, and T. Nagao. "Infrared Perfect Absorbers Fabricated by Colloidal Mask Etching of Al–Al<sub>2</sub>O<sub>3</sub>–Al Trilayers." *ACS Photonics* 2, no. 7 (2015): 964-970.
- [27] H. Wang, V. P. Sivan, A. Mitchell, G. Rosengarten, P. Phelan, and L. Wang. "Highly efficient selective metamaterial absorber for high-temperature solar thermal energy harvesting." *Sol. Energy Mater. Sol. Cell.* **137**, 235 (2015).
- [28] P. E. Chang, Y. W. Jiang, H. H. Chen, Y. T. Chang, Y. T. Wu, L. D. Tzuang, Y. H. Ye, and S. C. Lee. "Wavelength selective plasmonic thermal emitter by polarization utilizing Fabry-Pérot type resonances." *Appl. Phys. Lett.* **98**, 073111 (2011).
- [29] C. Wu, B. Neuner III, G. Shvets, J. John, A. Milder, B. Zollars, and S. Savoy. "Large-area wide-angle spectrally selective plasmonic absorber." *Phys. Rev. B* **84**, 075102 (2011).
- [30] A. Sakurai, B. Zhao, and Z. M. Zhang. "Resonant frequency and bandwidth of metamaterial emitters and absorbers predicted by an RLC circuit model." *J. Quant. Spec. Rad. Trans.* **149**, 33 (2014).
- [31] J. Hao, L. Zhou, and M. Qiu. "Nearly total absorption of light and heat generation by plasmonic metamaterials." *Phys. Rev. B* **83**, 165107 (2011).
- [32] D. Costantini, A. Lefebvre, A-L. Coutrot, I. Moldovan-Doyen, J-P. Hugonin, S. Boutami, F. Marquier, H. Benisty, and J-J. Greffet. "Plasmonic Metasurface for Directional and Frequency-Selective Thermal Emission." *Phys. Rev. Appl.* **4**, 014023 (2015).
- [33] J. Hao, J. Wang, X. Liu, W. J. Padilla, L. Zhou, and M. Qiu. "High performance optical absorber based on a plasmonic metamaterial." *Appl. Phys. Lett.* **96**, 251104 (2010).

- [34] P. Bouchon, C. Koechlin, F. Pardo, R. Haïdar, and J. L. Pelouard. "Wideband omnidirectional infrared absorber with a patchwork of plasmonic nanoantennas." *Opt. Lett.* **37**, 1038 (2012).
- [35] J. Hendrickson, J. Guo, B. Zhang, W. Buchwald, and R. Soref. "Wideband perfect light absorber at midwave infrared using multiplexed metal structures." *Opt. Lett.* **37**, 371 (2012).
- [36] T. Maier, and H. Brueckl. "Multispectral microbolometers for the midinfrared." *Opt. Lett.* **35**, 3766 (2010).
- [37] H. Wang and L. Wang. "Perfect selective metamaterial solar absorbers." *Opt. Exp.* **21**, A1078 (2013).
- [38] H. T. Miyazaki, T. Kasaya, M. Iwanaga, B. Choi, Y. Sugimoto, and K. Sakoda, "Dual-band infrared metasurface thermal emitter for CO<sub>2</sub> sensing", *Appl. Phys. Lett.* **105**, 121107 (2014);
- [39] W. Streyer, K. Feng, Y. Zhong, A. J. Hoffman, and D. Wasserman. "Selective absorbers and thermal emitters for far-infrared wavelengths." *Appl. Phys. Lett.* **107**, 081105 (2015).
- [40] M. Makhsiyani, P. Bouchon, J. Jaeck, J. L. Pelouard, and R. Haïdar, "Shaping the spatial and spectral emissivity at the diffraction limit," *Appl. Phys. Lett.* **107**, 251103 (2015).
- [41] C. Ciraci, J. B. Lassiter, A. Moreau, and D. R. Smith, "Quasi-analytic study of scattering from optical plasmonic patch antennas," *J. Appl. Phys.*, **114**, 163108 (2013).
- [42] H. T. Chen, "Interference theory of metamaterial perfect absorbers," *Opt. express*, **20**, 7165-7172 (2012).

- [43] J. Nath, S. Modak, I. Rezadad, D. Panjwani, F. Rezaie, J. W. Cleary, and R. E. Peale, "Far-infrared absorber based on standing-wave resonances in metal-dielectric-metal cavity," *Opt. Express* **23**, 20366 (2015).
- [44] J. E. Fredrickson, C. N. Waddell, W. G. Spitzer, and G. K. Hubler. "Effects of thermal annealing on the refractive index of amorphous silicon produced by ion implantation." *Appl. Phys. Lett.* **40**, 172 (1982).
- [45] S. Basu, B. J. Lee, and Z. M. Zhang. "Infrared radiative properties of heavily doped silicon at room temperature." *J. Heat Trans.* **132**, 023301 (2010).
- [46] Reprinted from *Journal of Applied Physics*, Vol. **119** (2016), 063101, K. Ito, H. Toshiyoshi, and H. Iizuka, © 2016 AIP, with permission from AIP Publishing LLC.
- [47] Reprinted from *Optics Express*, Vol. **24** (2016), 12803-12811, K. Ito, H. Toshiyoshi, and H. Iizuka, © 2016 Optical Society of America.
- [48] The samples were fabricated using an electron-beam (EB) lithography apparatus (F5112 + VD01) donated by the Advantest Corporation at the VLSI Design and Education Center (VDEC) of the University of Tokyo, through MEXT Nanotechnology Platform Project.

## *Chapter 5 Thermal rectification*

This chapter demonstrates thermal rectification utilizing thermal radiation from a phase-change material. Vanadium dioxide ( $\text{VO}_2$ ), which exhibits metal-insulator transition around 340 K, is employed to achieve a thermal rectification contrast ratio of 2, which is the largest value ever measured around room temperature. The sputter-deposited  $\text{VO}_2$  film is characterized by an infrared spectrometer to obtain the mid-infrared permittivity. A theoretical model based on fluctuation electrodynamics is developed to predict the heat flux across the rectifier. The measured heat flux agrees well with the model. Tuning of operation temperature range from 300-350 K to 275-325 K is also demonstrated.

### 5.1. Introduction

Thermal management without consuming power is of crucial importance in highly integrated systems or mobile systems. Conventionally, heat is mainly managed by placing thermal path made of materials with high conductivity, and/or connecting to heat sink which is cooled by convection. More intelligent thermal devices such as thermal rectifier or thermal diode is long expected.

Thermal rectifier is a two-terminal device whose heat transfer coefficient is dependent on the direction of heat flow. One of the main performance parameters of thermal rectifiers is thermal rectification contrast ratio:

$$R_T \equiv (\Phi_F - \Phi_R)/\Phi_R, \quad (5.1)$$

where  $\Phi_F$  and  $\Phi_R$  respectively denote the heat flux amounts in the forward and the reverse temperature biased scenarios. Considerable numbers of studies have been done to realize solid-state thermal rectifier since the first observation by Starr [1]. He observed thermal conductance of the interface between the copper and the cuprous oxide. The physical mechanism of the rectification is explained as the direction-dependent energy transport rate between electron and phonons. There are growing interests in the rectification utilizing nanostructured material around the turn of millennium. Teranneo and his colleagues theoretically predicted the rectification on one-dimensional nonlinear chains [2]. Chang measured heat transfer across asymmetrically loaded nanotubes to achieve rectification ratio of 0.07 [3]. Alternatively, several groups have investigated rectifiers consisting of two materials which have different temperature dependence of thermal conductivity [4]-[7]. Other mechanisms have been introduced for the solid-state thermal rectifier [8]-[10], but experimentally validated rectification ratios have been relatively small except the case of the

temperature below 1 K [11].

To achieve high rectification contrast, we focus on the radiative path [12]-[19] rather than diffusive conductive path. The high tunability of radiation compared to conduction adds more flexibility on the design of thermal rectifiers. The abrupt change of the infrared response found in a phase-change material is utilized in this work.

## 5.2. Phase-change material

Phase-change materials change their physical properties according to external stimuli including temperature, electric field, and magnetic field. The most famous examples are germanium-antimony-tellurium (GST) for rewritable digital versatile disc (DVD) and phase-change memory (PCM) [20]. Another examples is the storage of latent heat, which is released according to melting and solidifying. In this work, we utilize vanadium dioxide ( $\text{VO}_2$ ), which is classified as a Mott-insulator. Its crystal structure changes from monoclinic to tetragonal around 340 K as shown in the inset of Figure 5. 1, simultaneously inducing metal-insulator transition (MIT). With MIT, the electrical resistance of  $\text{VO}_2$  drops around three orders of magnitude as plotted in Figure 5. 1.

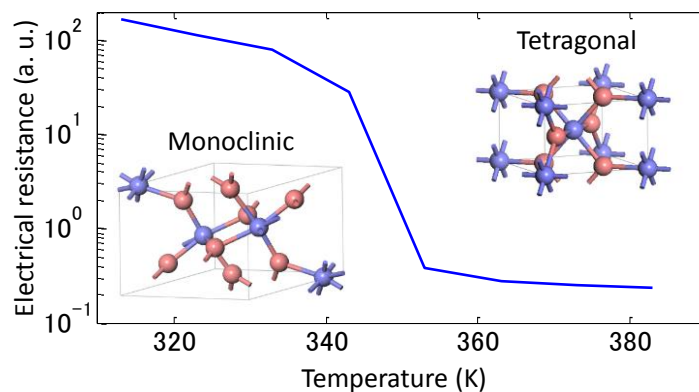


**Figure 5. 1 Electrical resistance of  $\text{VO}_2$  as a function of temperature.**

**(Inset) Crystal structures in the insulating state and the metallic state.**

The optical constant of VO<sub>2</sub> was reported to change drastically due to the excited free electrons in the metallic state around half a century ago [21]. In the insulating state, the permittivity  $\epsilon(\omega)$  is governed by optical phonons, and is expressed by Lorentz model:

$$\epsilon(\omega) = \epsilon_{\infty} + \sum_{j=1}^N \frac{S_j \omega_j^2}{\omega_j^2 - i\gamma_j \omega - \omega^2}, \quad (5.2)$$

where  $\epsilon_{\infty}$  is the permittivity at the infinite frequency,  $N$  the number of oscillators,  $S_j$  the amplitude of the oscillator,  $\omega_j$  the phonon vibration frequency,  $\gamma_j$  the scattering rate, and  $\omega$  the angular frequency. The permittivities parallel and perpendicular to the optical axis,  $\epsilon_{\parallel}$  and  $\epsilon_{\perp}$ , respectively, have different Lorentz parameters. For polycrystalline film of such a uniaxial material, the effective permittivity  $\epsilon_e$  is

isotropic and calculated as [22][23] 
$$\epsilon_e = \frac{\epsilon_{\perp} \pm \sqrt{\epsilon_{\perp}^2 + 8\epsilon_{\perp}\epsilon_{\parallel}}}{4}.$$

On the contrary, the permittivity of metallic VO<sub>2</sub> is governed by induced free electrons and is expressed by the Drude model:

$$\epsilon(\omega) = -\frac{\omega_p^2 \epsilon_{\infty}}{\omega^2 + i\omega\gamma_p}, \quad (5.3)$$

where  $\omega_p$  and  $\gamma_p$  are the plasma frequency and the scattering rate, respectively.

Although the metal-insulator transition of VO<sub>2</sub> is reported to change mid-infrared response [24]-[30], radiative thermal rectifiers based on phase-change materials have not been experimentally demonstrated.

5.3. Proposal of the thermal rectifier based on the phase-change of VO<sub>2</sub>

The sketch of the proposed thermal rectifier is shown in Figure 5. 2. It utilizes thermal radiation, which is largely modulated due to the metal-insulator transition of VO<sub>2</sub>. The emitter temperature  $T_H$  and the receiver temperature  $T_L$  are set so as to satisfy  $T_L < 340$  K  $< T_H$ . In the forward scenario, the VO<sub>2</sub> film is in the insulating state, thus the radiative flux from the fused quartz substrate is accepted by the underlying silicon substrate through the quasi-transparent VO<sub>2</sub> film. In the reverse scenario, the VO<sub>2</sub> film in the metallic state reflects back the thermal radiation from the silicon substrate, resulting in a small radiative heat flux toward the fused quartz substrate. Note that VO<sub>2</sub> in the metallic state is far from perfect electric conductor, thus finite amount of thermal emission is transferred to the emitter.

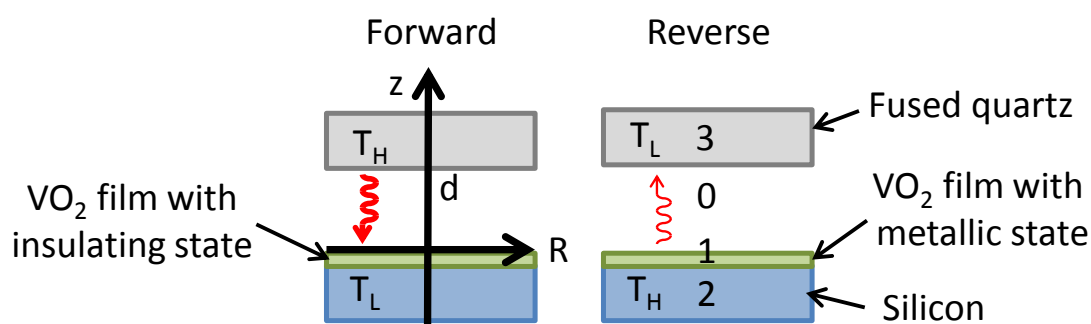


**Figure 5. 2 Sketch of the thermal rectifier based on the phase-change of VO<sub>2</sub> [34]**

#### 5.4. Deposition of the VO<sub>2</sub> film

A vanadium target was sputtered to deposit a metallic vanadium film. The film was thermally annealed in an oxygen flow at a temperature of 600 °C. The SEM image from the top and the side are shown in Figure 5. 3. From an optical point of view, the granular film is treated as homogenous because the size of grains (200 nm) is considerably smaller than the wavelength of the interest (2 μm). The X-ray diffraction (XRD) spectrum is shown in Figure 5. 4, and clearly indicates that the VO<sub>2</sub> film is stoichiometric.

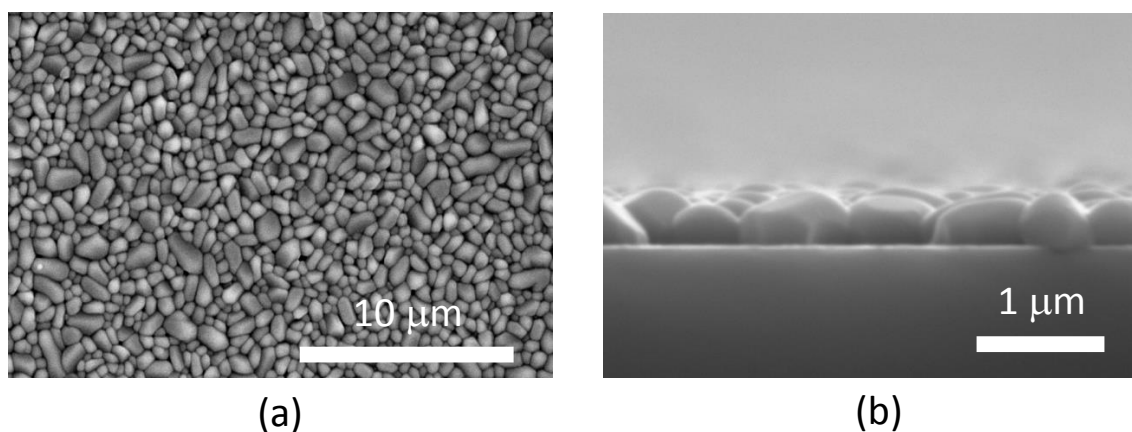


Figure 5. 3 SEM images of the VO<sub>2</sub> film [34]

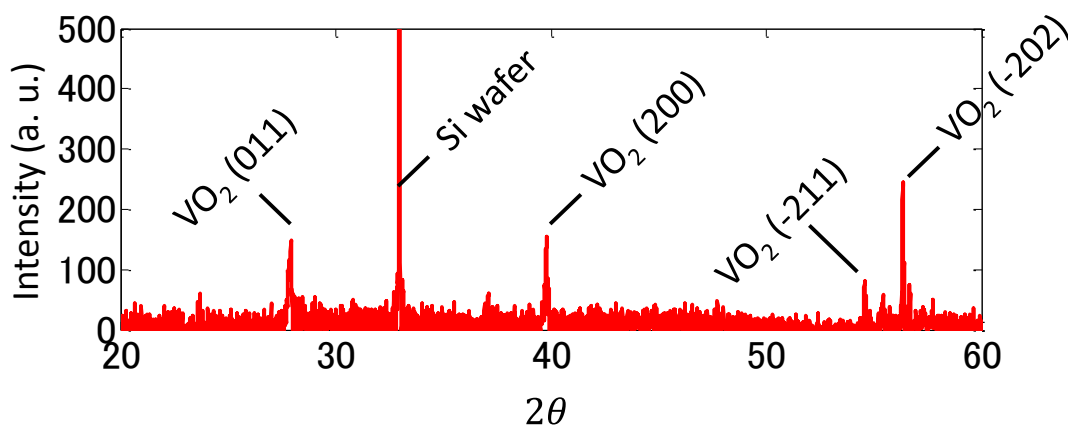


Figure 5. 4 X-ray diffraction spectrum of the VO<sub>2</sub> film [34]

## 5.5. Analysis of infrared response

The infrared response of the deposited film on the silicon substrate was measured by a Fourier transform infrared spectrometer (FT-IR). A FT-IR attachment which enables reflection measurement was utilized and the incident angle was set to be  $30^\circ$  and  $60^\circ$  from the normal. The reflectance was measured by comparing the intensity of the  $\text{VO}_2$  and that of a gold film. The reflectance  $R_{\text{VO}_2}$  of the  $\text{VO}_2$  film was calculated as:

$$R_{\text{VO}_2} = \frac{I_{\text{VO}_2, \text{M}} - I_{\text{BG, M}}}{I_{\text{Au, M}} - I_{\text{BG, M}}} R_{\text{Au, S}}, \quad (5.4)$$

where  $I_{\text{VO}_2, \text{M}}$ ,  $I_{\text{Au, M}}$ , and  $I_{\text{BG, M}}$  are the measured intensity of the  $\text{VO}_2$ , the gold film, and background, respectively.  $R_{\text{Au, S}}$  is the reflectance of the gold film calculated by Fresnel's equation and the permittivity of gold. The measured reflectance of the  $\text{VO}_2$  film at 300 K and 400 K is shown in Figure 5. 5.

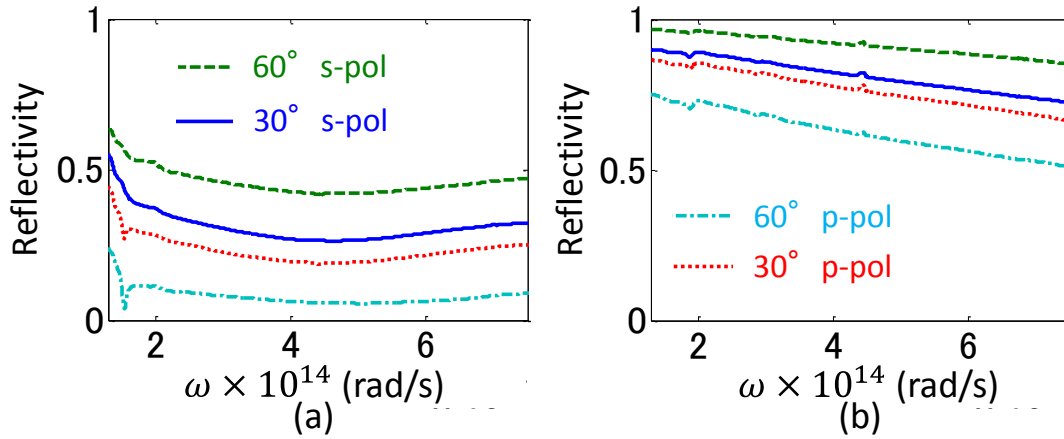


**Figure 5. 5 Measured reflectance of the (a) insulating and the (b) metallic  $\text{VO}_2$  film.**

**Green dashed line: 60 s-pol. Blue solid line: 30 s-pol. Red dotted line: 30 p-pol.**

**Cyan dash-dotted line: 60 p-pol. [34]**

By utilizing the measured reflectance, we estimated the permittivity of the deposited VO<sub>2</sub> film. The reflectivity of the insulating film was calculated by the transmission matrix method, using the Lorentz parameters reported in Ref. [21] as shown in Figure 5.6 (a). The calculated reflectivity reproduces the measured spectra, indicating that the reported Lorentz parameters is applicable to the insulating state. On the contrary, the reflectivity of the metallic film calculated using the reported Drude parameters ( $\omega_p = 8000 \text{ cm}^{-1}$  and  $\gamma_p = 10000 \text{ cm}^{-1}$ ) [21] deviates from the measured spectra as shown in Figure 5.6 (b). Thus, the Drude parameters are fitted to be  $\omega_p = 14000 \text{ cm}^{-1}$  and  $\gamma_p = 10000 \text{ cm}^{-1}$  and the recalculated spectra are shown in Figure 5.7. The recalculated Drude parameters indicate that the carrier density of the deposited film is higher than that of the reported VO<sub>2</sub> [21]. The carrier scattering also seems to be weaker than the reported film. These differences on electronic property might be explained by the granularity of the deposited film.

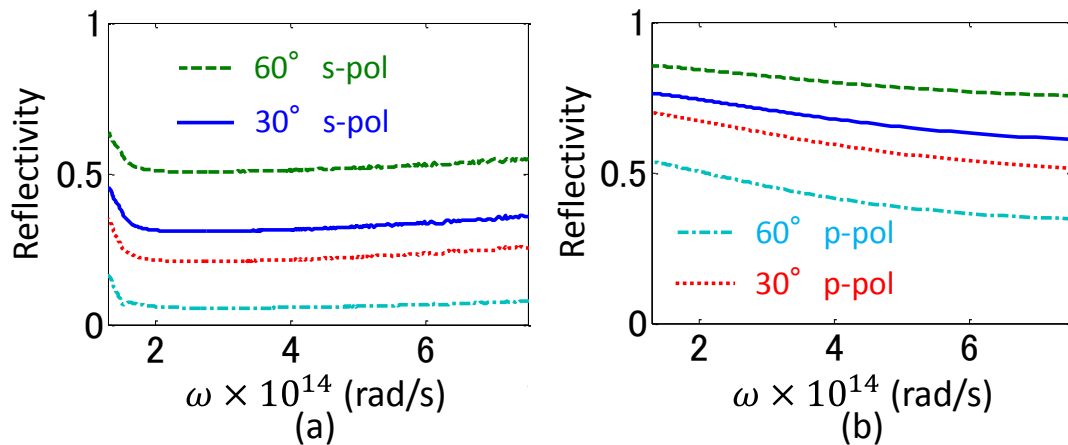


**Figure 5.6** Calculated reflectance of the (a) insulating and the (b) metallic VO<sub>2</sub> film utilizing the parameters reported in [21]. [34]

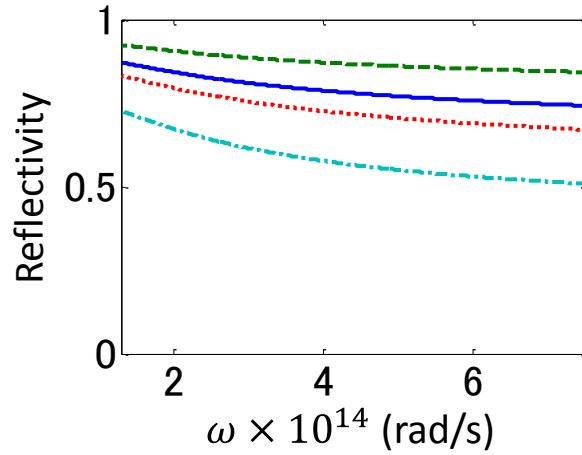


**Figure 5. 7 Fitted reflectance of the metallic VO<sub>2</sub> film [34]. The graph legend is the same as that in Figure 5. 5.**

### 5.6. Numerical prediction of heat flux

The heat flux across the thermal rectifier was estimated by fluctuational electrodynamics. Here, near-field components are ignored because the gap between the emitter and the receiver surface is 1 mm, which is considerably larger than the Wien's peak wavelength at 400 K (7.2 μm). Thus the heat flux  $\phi$  is written as:

$$\phi = \frac{1}{\pi^2} \int_0^{+\infty} d\omega [\theta(\omega, T_H) - \theta(\omega, T_L)] \sum_{j=s,p} \int_0^{\frac{\omega}{c}} Z(\omega, \beta, j) \beta d\beta. \quad (5.5)$$

where

$$\theta(\omega, T) = \frac{\hbar\omega}{\exp(\hbar\omega/k_B T) - 1}, \quad (5.6)$$

$$Z(\omega, \beta, j) = \frac{(1 - |r_{01}|^2)(1 - |r_{02}|^2)}{4|1 - r_{01}r_{02}e^{2i\gamma_0 d_g}|^2}. \quad (5.7)$$

$\omega$  is the angular frequency,  $c$  is the speed of light,  $\beta$  is the lateral wavenumber,  $j$  is the polarization,  $\hbar$  is the reduced Planck's constant,  $k_B$  is the Boltzmann constant,  $r_{01}$

and  $r_{02}$  are the reflection coefficient of the fused quartz and the VO<sub>2</sub>,  $\gamma_0$  is the vertical wavenumber in the gap, and  $d_g$  is the gap width.

The steps of  $\omega$  and  $\beta$  was determined for the numerical integration in Eq. (5.5) such that the calculated results converge. As an example, the calculated exchange function  $Z(\omega, \beta, j)$  with various steps of wavenumber is shown in Figure 5. 8. The results are shown with normalized wavenumber  $\tilde{\beta} = \beta c / \omega$ . The selected frequency range is shown to compare the difference. In case that the step of wavenumber or that of frequency is large, the exchange function significantly differs from others. The wavenumber step of  $\Delta\tilde{\beta} = 2.5 \times 10^{-4}$  and the frequency step of  $2 \times 10^{11}$  rad/s were chosen for the numerical integration.

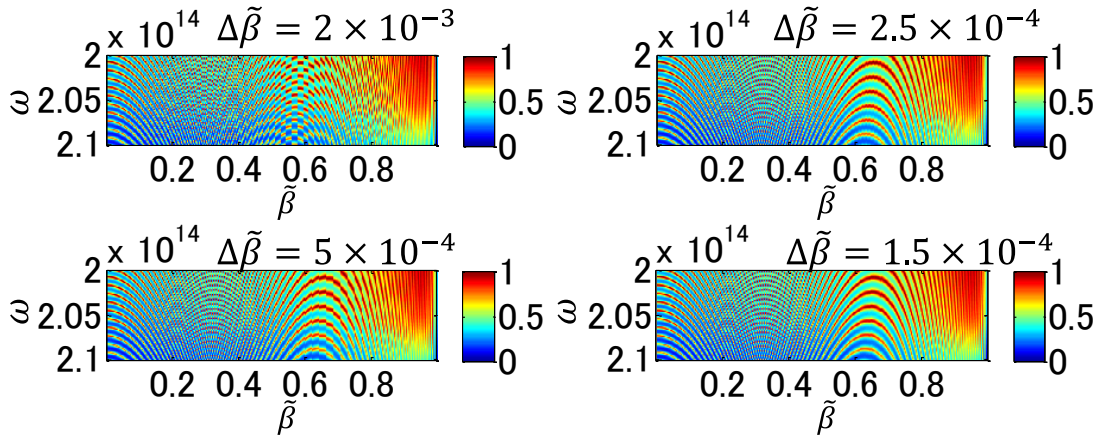


**Figure 5. 8** Calculated  $Z(\omega, \beta, j)$  with various steps of  $\tilde{\beta} = \beta c / \omega$ .

Figure 5. 9 (a) shows the numerically calculated exchange function profile in the forward scenario in p-polarization. The optical constants of fused quartz reported in Ref. [32] are employed. There are several spectral bands where the exchange functions are smaller than 0.5. These bands correspond to the Reststrahlen region of SiO<sub>2</sub> or VO<sub>2</sub>. The exchange function is integrated with respect to the wavenumber, and is multiplied by

Planck's distribution, in order to derive the spectral heat flux as shown in Figure 5.9 (b).

High heat flux contrast between two scenarios is clearly observed.

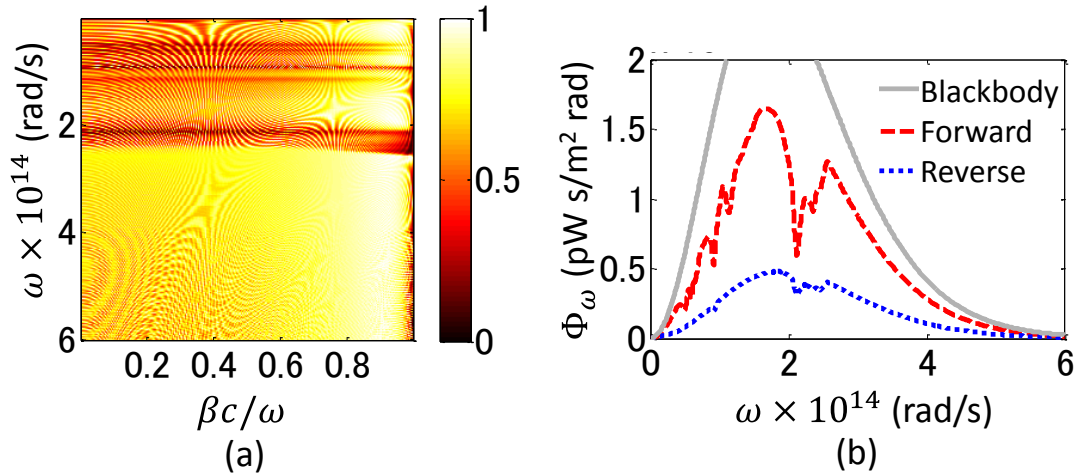


**Figure 5.9 Numerically calculated heat flux. (a) Exchange function  $Z(\omega, \beta, j)$  in the forward scenario in p-polarization. (b) Spectral net heat flux transferred from hot body (370 K) to cold body (300 K). [34]**

### 5.7. Heat flux measurement

The heat flux across the thermal rectifier was measured in steady-state conditions, which have been widely utilized to measure thermal conductivity of materials. The receiver temperature is fixed at 300 K, and the apparatus explained in Chapter 2 is utilized. The heat flux was measured twice with inverting the direction of the thermal rectifier, which is required because the measurement apparatus cannot be applied to upward heat flux. Such an inversion of the direction allows us to evaluate the forward and the reverse scenario. The measured heat flux is shown in Figure 5.10. In the forward scenario, the heat flux increases with the increase of the emitter temperature. In the reverse scenario, the heat flux decreases in the range from 340 K to 350 K due to the

phase change of  $\text{VO}_2$  from the insulating state to the metallic state. During cooling, the heat flux get back to the high values through the phase change from the metallic state to the insulating state. The transition temperature differs between heating and cooling, and the hysteresis is due to first-order phase transition of  $\text{VO}_2$ . Such a hysteresis was also reported in literatures [29].

The high contrast between the forward scenario and the reverse scenario is observed above 350 K. The thermal rectification contrast ratio reaches almost 2, which is the highest value ever reported in solid-state rectifiers working around room temperature.

The numerically predicted heat flux explained in the last section is plotted as lines in Figure 5. 10. The numerical calculation and the measured data agree well, indicating that both the numerical prediction and the measurement are done in a proper manner.

Note that the heat flux is measured at a pressure lower than  $5 \times 10^{-3}$  Pa. In the case that the pressure is around 10 Pa, the heat flux is considerably higher and the rectification vanishes due to heat conduction through air.

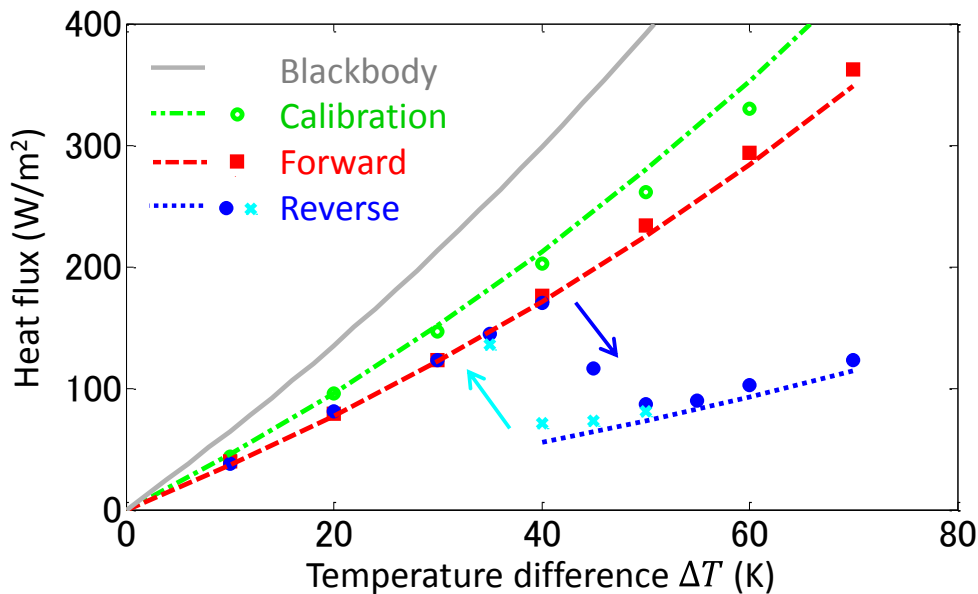
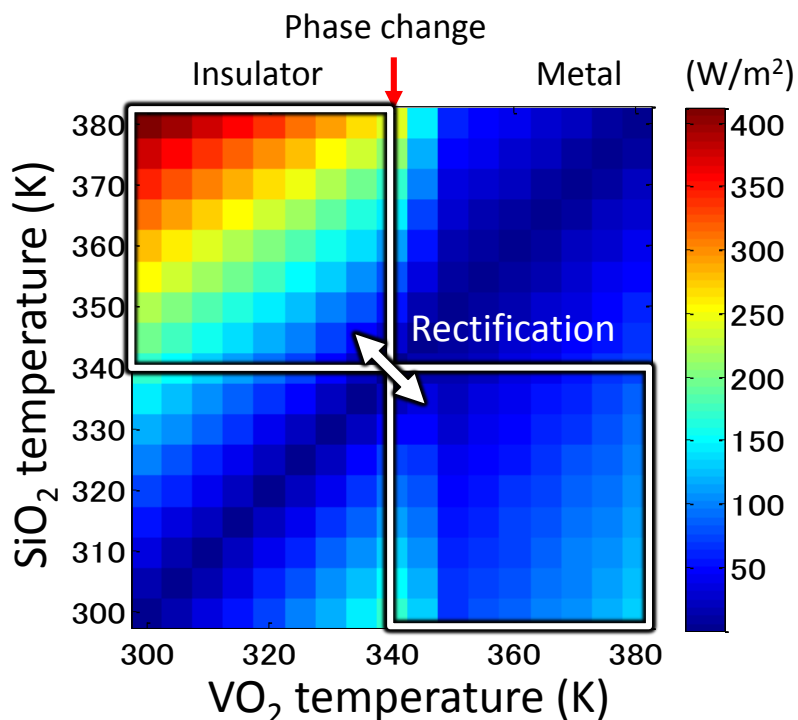


Figure 5. 10 Heat flux across the thermal rectifier. [34]



**Figure 5. 11 Estimated heat flux as a function of temperatures of SiO<sub>2</sub> and VO<sub>2</sub>.**

**The square regions indicate the area where thermal rectification occurs.**

Figure 5. 11 presents the heat flux across the thermal rectifier in a different way. The heat flux was numerically estimated by varying the emitter temperature and the receiver temperature. The exchange function was derived from the measured heat flux during heating. The heat flux is significantly different across the VO<sub>2</sub> temperature of 340 K. Thermal rectification is observed between the right-bottom and the left-top square regions. If the temperature condition is outside these two squares, heat flux is not rectified. We call it a thermal rectifier even though the absolute temperature range is limited. Note that the rectification in electrical semiconductor diode does not occur in the case the bias voltage is smaller than the built-in potential or larger than the breakdown voltage.

### 5.8. Tailoring the operation temperature range

Until now, the emitter temperature was set to be higher than 340 K, and the receiver temperature was set to be lower than 340 K. The control of the transition temperature allows us to apply the thermal rectifier to other operation temperature ranges.

Tungsten was doped into the VO<sub>2</sub> film to control the transition temperature. Tungsten doping induces strain in the VO<sub>2</sub> film, which lowers the transition temperature. The alloy of tungsten and vanadium with the atomic ratio of 0.01 was used as sputtering target for the deposition of the film.

The heat flux across the thermal rectifier with modified transition temperature was measured with the receiver temperature of 275 K. The result is shown in Figure 5. 12. In the forward scenario, the heat flux increases as the emitter temperature rises. In the reverse scenario, the heat flux decreases in the range from 310 K to 330 K due to the metal-insulator transition. The transition temperature is estimated to be tuned from 340 K to 315 K. The reduction rate of transition temperature is consistent with the reported value of 19.5 K/at% in Ref. [33]. The rectification contrast ratio is shown in Figure 5. 12 (b). We see that the high rectification ratio of 2 is maintained while tuning the transition temperature. The operation temperatures were successfully tuned from 350 K and 300 K to 325 K and 275 K.

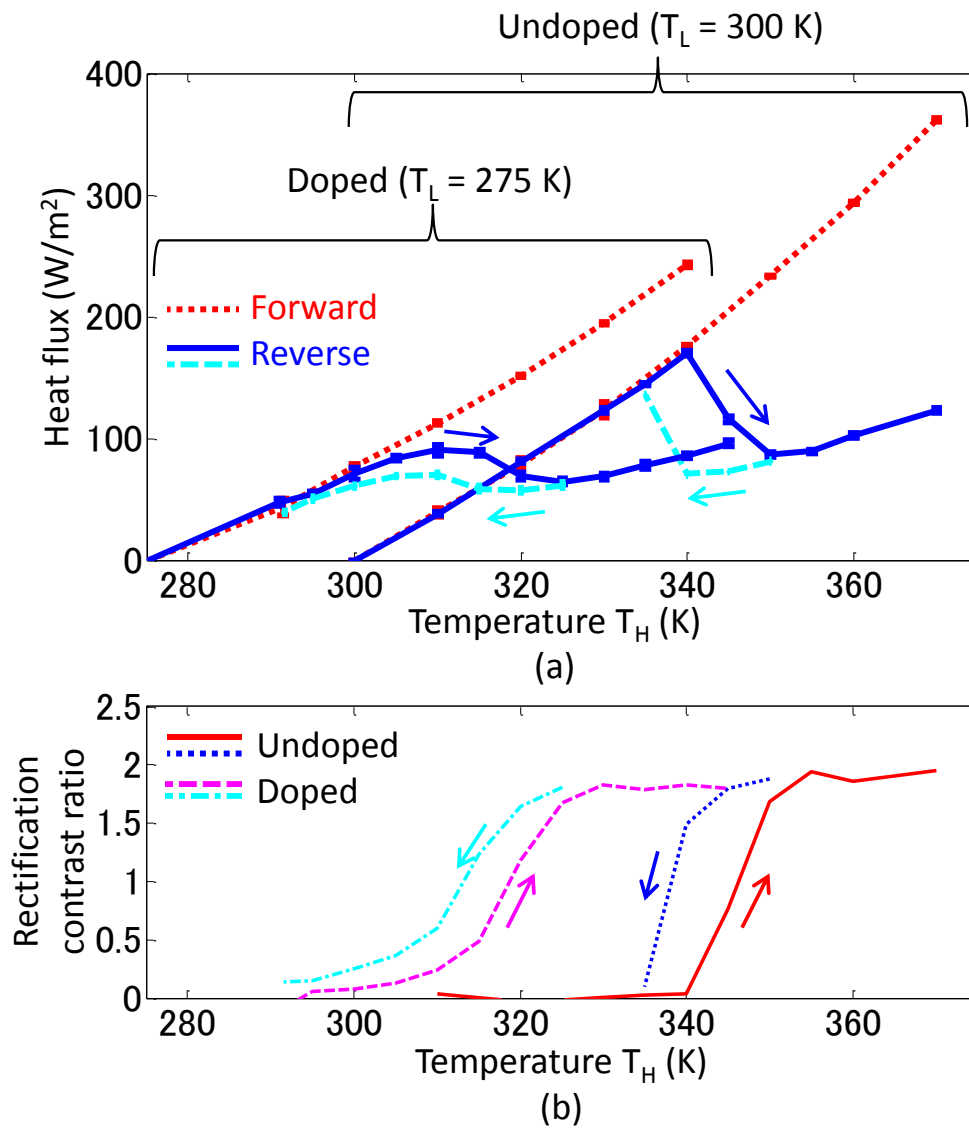


Figure 5.12 Thermal rectifiers with / without the tungsten doping.

(a) Heat flux. (b) Thermal rectification contrast ratio. [34]

### 5.9. Chapter summary

In this chapter, radiative thermal rectifiers with a phase-change material have been successfully demonstrated. The metal-insulator transition of vanadium oxide allows us to obtain a high thermal rectification contrast ratio of 2. The emitter and the receiver were optically characterized by an infrared spectrometer to model the rectifier by fluctuation electrodynamics. The modeled heat flux captures the measured values, validating the theoretical and the experimental procedure employed in this work. The operation temperature range was successfully tuned from 300-350 K to 275-325 K by tungsten doping with an atomic ratio of 0.01 into the vanadium dioxide film.

**Reference**

- [1] C. Starr, "The copper oxide rectifier." *J. Appl. Phys.* **7**, 15 (1936).
- [2] M. Terraneo, M. Peyrard, and G. Casati. "Controlling the energy flow in nonlinear lattices: a model for a thermal rectifier." *Phys. Rev. Lett.* **88**, 094302 (2002).
- [3] C. W. Chang, D. Okawa, A. Majumdar, and A. Zettl, Solid-state thermal rectifier. *Science*, **314**, 1121 (2006).
- [4] W. Kobayashi, Y. Teraoka, and I. Terasaki, An oxide thermal rectifier. *Appl. Phys. Lett.* **95**, 171905 (2009).
- [5] D. Sawaki, W. Kobayashi, Y. Morimoto, and I. Terasaki, "Thermal rectification in bulk materials with asymmetric shape" *Appl. Phys. Lett.* **98**, 081915 (2011).
- [6] T. Takeuchi, H. Goto, R. Nakayama, Y. Terazawa, K. Ogawa, A. Yamamoto, T. Itoh, and M. Mikami. "Improvement in rectification ratio of an Al-based bulk thermal rectifier working at high temperatures." *J. Appl. Phys.* **111**, 093517 (2012).
- [7] R. Nakayama, T. Takeuchi, "Thermal Rectification in Bulk Material Through Unusual Behavior of Electron Thermal Conductivity of Al-Cu-Fe Icosahedral Quasicrystal" *J. Electronic Materials*,
- [8] H. Tian, D. Xie, Y. Yang, T. L. Ren, G. Zhang, Y. F. Wang, C. J. Zhou, P. G. Peng, L. G. Wang, and L. T. Liu. "A novel solid-state thermal rectifier based on reduced graphene oxide." *Sci. rep.* **2** (2012).
- [9] J. Zhu, K. Hippalgaonkar, S. Shen, K. Wang, Y. Abate, S. Lee, J. Wu, X. Yin, A. Majumdar, and X. Zhang. "Temperature-Gated Thermal Rectifier for Active Heat Flow Control." *Nano Lett.* **14**, 4867 (2014).

- [10] R. Scheibner, M. König, D. Reuter, A. D. Wieck, C. Gould, H. Buhmann, and L. W. Molenkamp. "Quantum dot as thermal rectifier." *New J. Phys.* **10**, 083016 (2008).
- [11] M. J. Martínez-Pérez, A. Fornieri, and F. Giazotto. "Rectification of electronic heat current by a hybrid thermal diode." *Nat. Nano.* **10**, 303 (2015).
- [12] C. R. Otey, W. T. Lau, and S. Fan, Thermal rectification through vacuum. *Phys. Rev. Lett.* **104**, 154301 (2012).
- [13] H. Iizuka, and S. Fan, Rectification of evanescent heat transfer between dielectric-coated and uncoated silicon carbide plates. *J. Appl. Phys.* **112**, 024304 (2012).
- [14] S. Basu, and Francoeur M. Near-field radiative transfer based thermal rectification using doped silicon. *Appl. Phys. Lett.* **98**, 113106 (2011).
- [15] L. P. Wang, and Z. M. Zhang, Thermal rectification enabled by near-field radiative heat transfer between intrinsic silicon and a dissimilar material. *Nanosc. Microsc. Thermophys. Eng.* **17**, 337 (2013).
- [16] H. Iizuka, and S. Fan, Consideration of enhancement of thermal rectification using metamaterial models, *J. Quant. Spec. Rad. Trans.* **148**, 156 (2014)
- [17] Y. Yang, S. Basu, and L. Wang, Radiation-based near-field thermal rectification with phase transition materials, *Appl. Phys. Lett.* **103**, 163101 (2013).
- [18] P. Ben-Abdallah, and S. A. Biehs, Phase-change radiative thermal diode. *Appl. Phys. Lett.* **103**, 191907 (2013).
- [19] Z. Chen, C. Wong, S. Lubner, S. Yee, J. Miller, W. Jang, C. Hardin, A. Fong, J. E. Garay, and C. Dames. "A photon thermal diode." *Nat. comm.* **5** (2014).

- [20] H. Horii, J. H. Yi, J. H. Park, Y. H. Ha, I. G. Baek, S. O. Park, Y. N. Hwang et al. "A novel cell technology using N-doped GeSbTe films for phase change RAM." IEEE Proc. VLSI Tech. Symp. 177 (2003).
- [21] A. S. Barker, H. W. Verleur, and H. J. Guggenheim, Infrared optical properties of vanadium dioxide above and below the transition temperature, Phys. Rev. Lett. **17**, 1286 (1966).
- [22] I. Fedorov, J. Petzelt, V. Zelezny, G. A. Komandin, A. A. Volkov, K. Brooks, Y. Huang, and N. Setter. "Far-infrared dielectric response of PbTiO<sub>3</sub> and PbZr<sub>1-x</sub>Ti<sub>x</sub>O<sub>3</sub> thin ferroelectric films." J. Phys. Condens. Mat. **7**, 4313 (1995).
- [23] O. Levy, and D. Stroud. "Maxwell Garnett theory for mixtures of anisotropic inclusions: Application to conducting polymers." Phys. Rev. B, **56**, 8035 (1997).
- [24] M. M. Qazilbash, M. Brehm, B.G. Chae, P.C. Ho, G. O. Andreev, B.J. Kim, S. J. Yun, A. V. Balatsky, M. B. Maple, F. Keilmann, H. T. Kim, and D. N. Basov. "Mott transition in VO<sub>2</sub> revealed by infrared spectroscopy and nano-imaging." Science **318**, 1750 (2007).
- [25] P. J. van Zwol, K. Joulain, P. Ben-Abdallah, and J. Chevrier, Phonon polaritons enhance near-field thermal transfer across the phase transition of VO<sub>2</sub>, Phys. Rev. B, **84**, 161413 (2011).
- [26] P. J. van Zwol, L. Ranno, and J. Chevrier, Tuning Near Field Radiative Heat Flux through Surface Excitations with a Metal Insulator Transition, Phys. Rev. Lett. **108**, 234301 (2012).
- [27] F. Guinneton, L. Squques, J. C. Valmalette, F. Cros, and J. R. Garvarri, Comparative study between nanocrystalline powder and thin film of vanadium

- dioxide VO<sub>2</sub> : electrical and infrared properties, *J. Phys. Chem. Solids*, **62**, 1229 (2001).
- [28] P. J. van Zwol, L. Ranno, and J. Chevrier, Emissivity measurements with an atomic force microscope, *J. Appl. Phys.* **111**, 063110 (2012).
- [29] M. A. Kats, D. Sharma, J. Lin, P. Genevet, R. Blanchard, Z. Yang, M. M. Qazilbash, D. N. Basov, S. Ramanathan, and F. Capasso. "Ultra-thin perfect absorber employing a tunable phase change material." *Appl. Phys. Lett.* **101**, 221101 (2012).
- [30] M. A. Kats, R. Blanchard, S. Zhang, P. Genevet, C. Ko, S. Ramanathan, and F. Capasso. " Vanadium dioxide as a natural disordered metamaterial: perfect thermal emission and large broadband negative differential thermal emittance." *Phys. Rev. X* **3**, 041004 (2013).
- [31] G. J. Kovács, D. Bürger, I. Skorupa, H. Reuther, R. Heller, and H. Schmidt, Effect of the substrate on the insulator–metal transition of vanadium dioxide films, *J. Appl. Phys.* **109**, 063708 (2011).
- [32] R. Kitamura, L. Pilon, and M. Jonasz. "Optical constants of silica glass from extreme ultraviolet to far infrared at near room temperature." *Appl. Opt.* **46**, 8118 (2007).
- [33] H. Takami, T. Kanki, S. Ueda, K. Kobayashi, and H. Tanaka. "Filling-controlled Mott transition in W-doped VO<sub>2</sub>." *Phys. Rev. B*, **85**, 205111 (2012).
- [34] Reprinted from *Applied Physics Letters*, Vol. 105 (2014), 253503, K. Ito et al., © 2014 AIP, with permission from AIP Publishing LLC.

## *Chapter 6 Near-field radiative heat transfer*

This chapter demonstrates a submicron gap formation methodology for near-field radiative heat transfer. Spacer pillars are micromachined on fused quartz chips, which are placed face-to-face to form a uniform submicron gap. A pressure as high as 6 kPa is applied toward the gap with the width of 0.5  $\mu\text{m}$ , 1  $\mu\text{m}$ , or 2  $\mu\text{m}$ , in order to compensate the intrinsic deflection of the chips. The uniformity of the submicron gap is evaluated by inspecting the optical interferometric spectra attained at the four corners of the chip stack with the area of  $19 \times 8.6$  mm. The measured heat flux across the gap is found to be twice as smaller than the electromagnetic heat transfer predicted by fluctuation electrodynamics, indicating that the parasitic heat conduction through the spacers is successfully suppressed to be smaller than the electromagnetic transfer. The heat flux across the gap is modelled by an equivalent thermal circuit model.

### 6.1. Introduction

The amount of the radiative heat transfer is limited by Stefan-Boltzmann's law in the far-field regime, where the distance between the hot body and the cold body is sufficiently larger than the Wien's peak wavelength. On the other hand, the radiative transfer between two materials placed in proximity is no more explained by Planck's law or the concept of emissivity [1]. In some conditions, it is larger than the blackbody radiation calculated by Stefan-Boltzmann's law. This heat flux enhancement due to near-field coupling is called near-field radiative heat transfer or near-field thermal radiation.

As discussed in section 2.2.4, near-field radiative heat transfer from a hot semi-infinite plate with a temperature  $T_H$  to a cold plate semi-infinite plate with a temperature  $T_L$  across a planar gap  $d$  is calculated as follows:

$$\phi = \frac{1}{\pi^2} \int_0^{+\infty} d\omega [\theta(\omega, T_H) - \theta(\omega, T_L)] \sum_{j=s,p} \int_0^{+\infty} Z(\omega, \beta, j) \beta d\beta, \quad (6.1)$$

where exchange function  $Z(\omega, \beta, j)$  is

$$\int_0^{+\infty} Z(\omega, \beta, j) \beta d\beta = \int_0^{\omega/c} \frac{(1 - |r_j|^2)^2}{4|1 - r_j^2 e^{2i\gamma_0 d}|^2} \beta d\beta + \int_{\omega/c}^{+\infty} \frac{\text{Im}(r_j)^2 e^{-2\text{Im}(\gamma_0) d}}{|1 - r_j^2 e^{-2\text{Im}(\gamma_0) d}|^2} \beta d\beta, \quad (6.2)$$

where  $\omega$  is the frequency,  $c$  is the speed of light,  $\beta$  is the lateral wavenumber,  $j$  is the polarization,  $\theta(\omega, T) = \hbar\omega / (\exp(\hbar\omega/k_B T) - 1)$  is the mean energy of the Planck oscillator at the temperature  $T$ ,  $k_B$  is the Boltzmann constant,  $\hbar$  is the reduced Planck constant,  $r_j$  is the Fresnel reflection coefficient incident from the vacuum to the plate in  $j$ -polarization, and  $\gamma_0$  is the wavenumber perpendicular to the plate surface in the gap. The electromagnetic heat fluxes between silicon carbide (SiC) plates and between silicon dioxide (SiO<sub>2</sub>) plates were calculated utilizing Eq. (6.1), and is plotted in

Figure 6. 1 as a function of the gap.

Around 1970, two research groups experimentally investigated near-field radiative heat transfer between two metallic plates [2][3]. They observed the enhancement of heat flux according to the decrease of the distance between plates but the amount of the flux was still smaller than the blackbody radiation. At almost the same time, the theoretical treatment of near-field thermal radiation was investigated in a rigorous manner [4]-[6]. The framework of the calculation is called fluctuation dissipation theorem, and is explained in section 2.2.4 of this thesis. The calculation of the heat transfer have been developed so as to calculate that between multilayers [7], spheres [8], sphere and plates [9], and arbitral shaped objects [10], as summarized in a review [11].

By utilizing the fluctuation dissipation theorem applied to the multilayered systems, theorists have explored applications based on near-field radiative heat transfer [12]-[25]. Thermophotovoltaics, where radiative heat is converted to the electricity, is improved in terms of the output power due to the heat flux enhancement. Narayanaswamy and his colleagues presented that surface modes could tune the spectral characteristic of the heat transfer [12]. Laroche calculated the energy conversion efficiency of the system by introducing photovoltaic cell model [13]. Park introduced a more detailed photovoltaic cell model including carrier transport inside semiconductors [14]. Francoeur presented that the temperature rise inside photovoltaic cell impacts the conversion efficiency [15].

Heat transfer control is another important application of near-field thermal radiation. In this context, thermal rectification [16]-[21], thermal modulation [22]-[24], and thermal transistor [25] have been proposed.

On the experimental side, significant reduction of the gap across which radiative heat flux is transferred have been achieved by employing the cantilever of atomic force

microscope [26][27] or the sphere-plate configuration [28]-[37]. On the contrary to the parallel-plate geometry, the alignment of two bodies is simpler in these configurations. The minimum gap width less than 5 nm was successfully achieved in the sphere-plate configuration, with the reasonable agreement with the theoretical calculation [37].

Although submicron gaps have been achieved by utilizing the sphere-plate configuration, the heat transfer across these gaps is relatively small compared to the parallel-plate configuration. Figure 6. 1 plots the measured heat transfer coefficients reported in Ref. [30] as blue circles. The sphere area projected to a plate is utilized to normalize the transferred flux. It is clear that these points in the deep submicron regime are more than one order of magnitude smaller than the heat transfer between SiO<sub>2</sub> plates calculated by fluctuation dissipation theorem. This is because the area of the submicron gap is a small fraction compared with the total area.

Recently, the parallel-plate configuration has been revisited by experimentalists. They utilized positioners with the precision finer than 1  $\mu\text{m}$  to control the angle and the distance between plates. Ottens achieved a minimum gap of 2  $\mu\text{m}$  while monitoring the gap by capacitance measurement [38]. Kralik applied the methodology to the cryogenic condition to achieve 4 orders of magnitude enhancement [40]. Ijiro achieved a minimum gap value of 1  $\mu\text{m}$  [41].

One of the reasons why a submicron gap has not been achieved by positioners is the non-ideality of flat surfaces. For instance, the modern polishing technology cannot achieve atomically flat surface, and the deviation of the semiconductor wafers is characterized by bow and warp. As another example, all materials deform their shapes with the variation of temperatures due to thermal expansion. For another instance, if one deposits a film onto a substrate, the difference of the thermal expansion coefficients

causes residual stress to deflect the substrate because the deposition temperature is generally higher than room temperature.

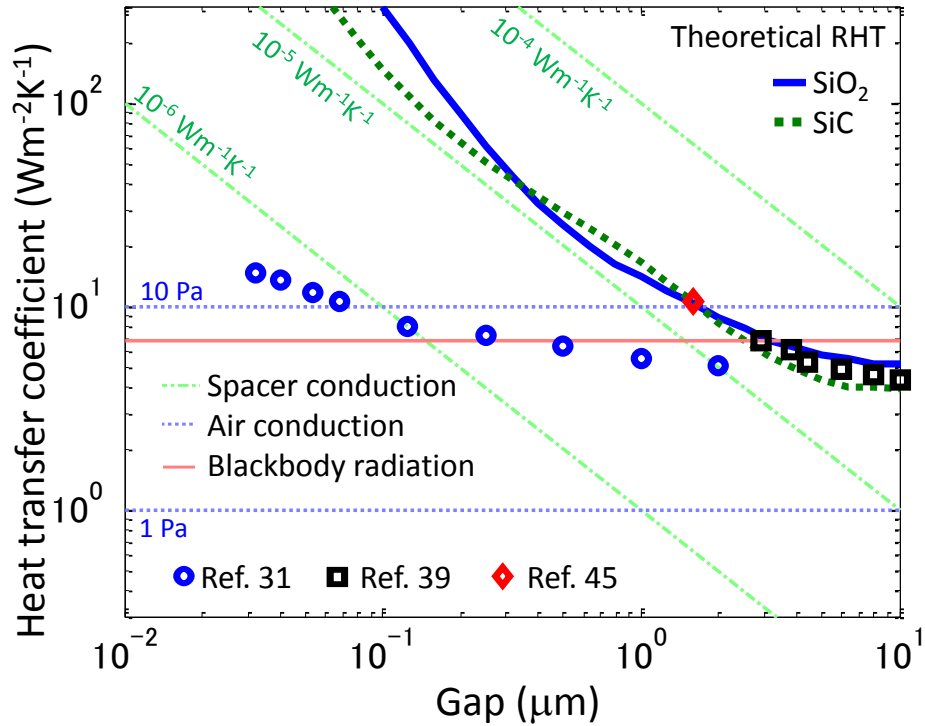


**Figure 6. 1 Heat transfer coefficient across gaps. Thermal conduction through homogenous spacer layer with thermal conductivities of  $10^{-4}$ ,  $10^{-5}$ , and  $10^{-6}$   $\text{Wm}^{-1}\text{K}^{-1}$  are shown as green dash dotted lines. Conductive heat flux through air with pressures of 10 and 1 Pa are shown in horizontal blue dotted lines. [47]**

## 6.2. Gap formation methodology

### 6.2.1. Analysis of heat transfer

In this work, submicron spacers are utilized to position two surfaces across a narrow gap. The gap width is equal to the height of the spacers. In order to compensate the non-ideality of flat surfaces, a pressure is applied across the gap. Several researchers have tried to form a gap by utilizing spacers [42]-[44] but the gap uniformity was not monitored or discussed in these works.

Fused quartz was chosen as the hot body and the cold body for the large heat flux enhancement owing to the excitation of surface phonon polariton. As shown in Figure 6. 1, the electromagnetic transfer between fused quartz substrates increases as the gap  $d$  becomes smaller, and the curve mostly follows  $1/d^2$  trend. Figure 6. 1 also shows the heat transfer coefficients of the parasitic thermal conduction through homogeneous spacer layer with low thermal conductivity. The thermal conduction also follows the  $1/d^2$  trend by definition, and the parasitic conduction through a material with a thermal conductivity of  $10^{-5}$  W/mK is the same order of magnitude as the thermal radiation.

Pillar structures are utilized as the spacer layer for low effective thermal conductivity. If a material with a thermal conductivity of 1 W/mK is employed, spacers with a size of  $3 \times 3 \mu\text{m}$  placed with a density of  $1 \text{ mm}^{-2}$  gives the same amount of conductive heat transfer as that of electromagnetic transfer.

## 6.2.2. Evaluation of the wafer surface

The non-ideality of substrates discussed in Section 6.1 is compensated by the exertion of force as shown in Figure 6. 2. A uniform gap whose width is equal to the spacer height is achieved. Both chips have spacers, and thus the spacer density is  $2 \text{ mm}^{-2}$ .

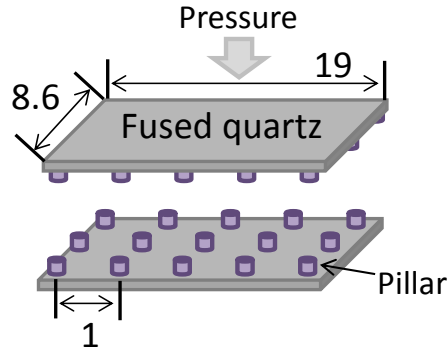


**Figure 6. 2 Gap formation (Unit:  $\mu\text{m}$ ) [47]**

For the estimation of the pressure required to compensate the non-ideality, the chip surface was monitored by a 3D optical surface profiler (Zygo, NewView 5022). Figure 6. 3 shows the height profile of fused quartz chip surface. We see that the surface is locally smooth enough for a 500 nm gap. On the other hand, the surface is globally deflecting by 100 nm peak-to-valley. Such deflection should be compensated for submicron gap formation.

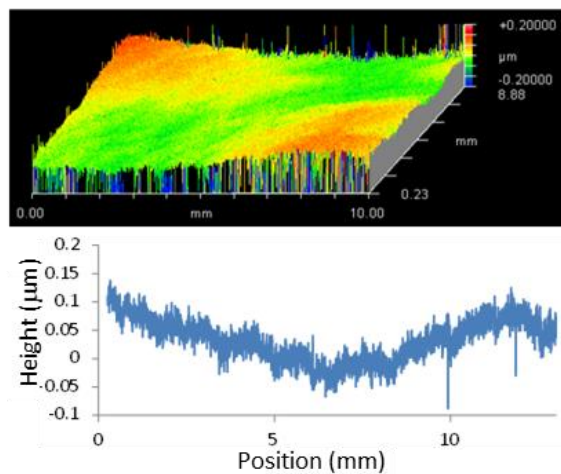


**Figure 6. 3 Surface of fused quartz chip**

The mechanical deformation of the fused quartz chip by the exerted force was simulated by COMSOL Multiphysics. The length and the thickness of the fused quartz chip were set to be 19 mm and 600  $\mu\text{m}$ , respectively, which reflect the actual chip size. On the other hand, infinite width was chosen by setting periodic boundary condition, in order to avoid the convergence problem. The half of the chip is placed on a fixed plane. Then a 1 N force is exerted to the whole chip as a uniform pressure, and the deformation is monitored as shown in Figure 6. 4. Maximum deformation of 6  $\mu\text{m}$  is observed at the edge of the chip. This simulation result indicates that a 1 N force is enough to compensate the intrinsic bending of the chip, whose amplitude is in the order of 100 nm.

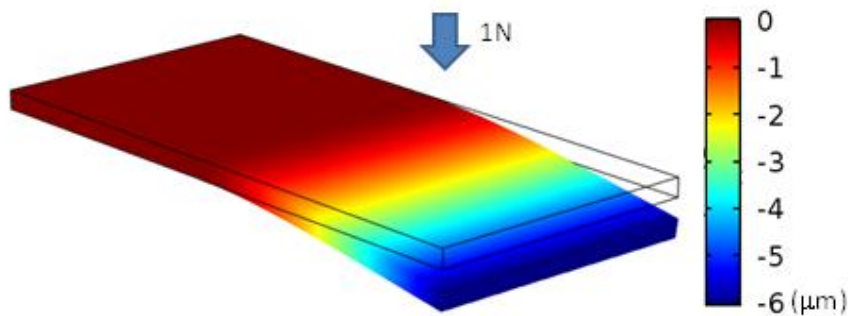


**Figure 6. 4 Simulated mechanical deflection of the chip**

The local deformation between spacers was simulated as shown in Figure 6. 5. A rectangular solid of fused quartz with a size of  $1\text{ mm} \times 1\text{ mm} \times 0.6\text{ mm}$  was simulated with the periodic boundary condition in the x- and the y-direction. The bottom corners of the solid are fixed against the exertion of the pressure. A pressure of 6 kPa, which corresponds to a force of 1 N over the chip, is applied in the z-direction from the top of the solid. The deformation in the z-direction is shown in Figure 6. 5. The maximum deformation owing to the force is smaller than 10 nm at the bottom of the solid. The local deformation between spacers is negligibly small compared to the gap width and the global bending of the chip.

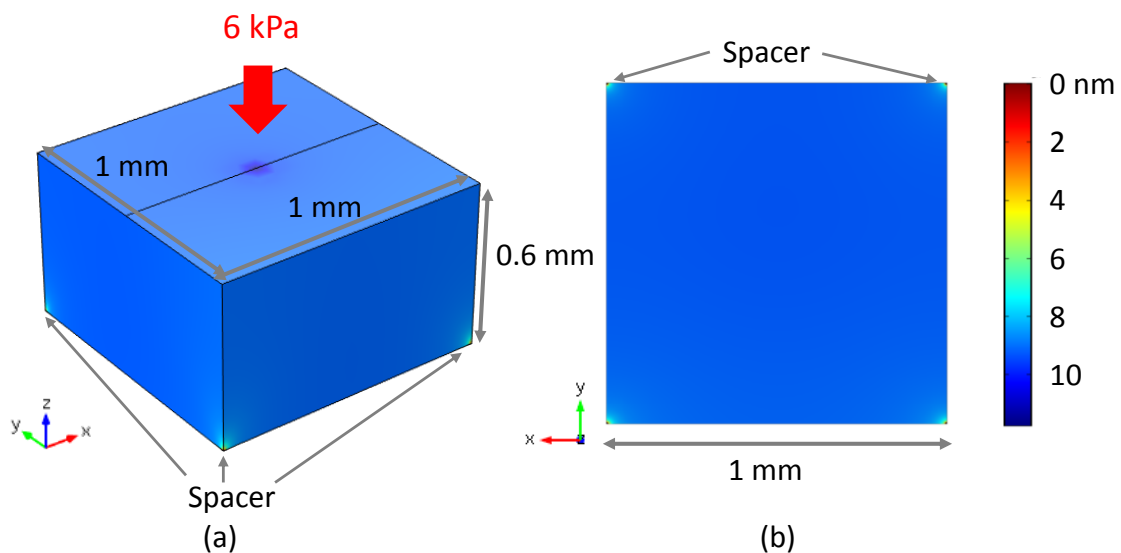


**Figure 6. 5 Simulated local deformation between spacers**

**(a) Bird's-eye view (b) Bottom view**

### 6.2.3. Selection of spacer material

The spacer material should be chosen so as to satisfy two requirements, namely low thermal conductivity and tolerance to the exerted pressure. As discussed in section 6.2.1, the thermal conductivity of the spacer material, the density of the spacer, and the top area of the spacer determine the amount of the parasitic thermal conduction. As discussed in section 6.2.2, a pressure is exerted to compensate the non-ideality of the chip surface, and thus the spacer should possess sufficient mechanical tolerance. Fused quartz satisfies these two requirements: its thermal conductivity is  $1.3 \text{ Wm}^{-1}\text{K}^{-1}$ , and its compressive strength is 1.1 GPa.

When spacers with a top area of  $2 \times 2 \text{ }\mu\text{m}$  are placed with a density of  $2 \text{ mm}^{-2}$ , the parasitic thermal conduction across the  $1 \text{ }\mu\text{m}$  gap is calculated to be  $10.4 \text{ Wm}^{-2}\text{K}^{-1}$ . This value is slightly smaller than the electromagnetic transfer predicted by fluctuation electrodynamics. When a force of 1 N is applied over the chip, the pressure applied to the top of the spacer is calculated to be 760 MPa. The value is smaller than the compressive strength of fused quartz.

#### 6.2.4. Microfabrication of spacers

The spacers were fabricated by the standard microfabrication process. Two processes, namely deep-ultraviolet contact lithography and buffered hydrofluoric acid (BHF) etching were utilized for the fabrication.

Deep-ultraviolet contact lithography was utilized to transfer the spacer pattern from the photomask shown in Figure 6. 6 to the photoresist on a fused quartz substrate. Positive photoresist iP3100 (TOK) and developer NMD-3 (TOK) were employed. In the contact lithography, sticking between the photomask and a fused quartz substrate was sometime observed. This is due to the lack of asperity on the photomask; the most part of chromium on the photomask is etched because the density of spacers is low as shown in Figure 6. 6. The adhesion was avoided by the optimization of the pre-bake temperature and time. One might avoid the adhesion by using projection exposure or electron-beam lithography.

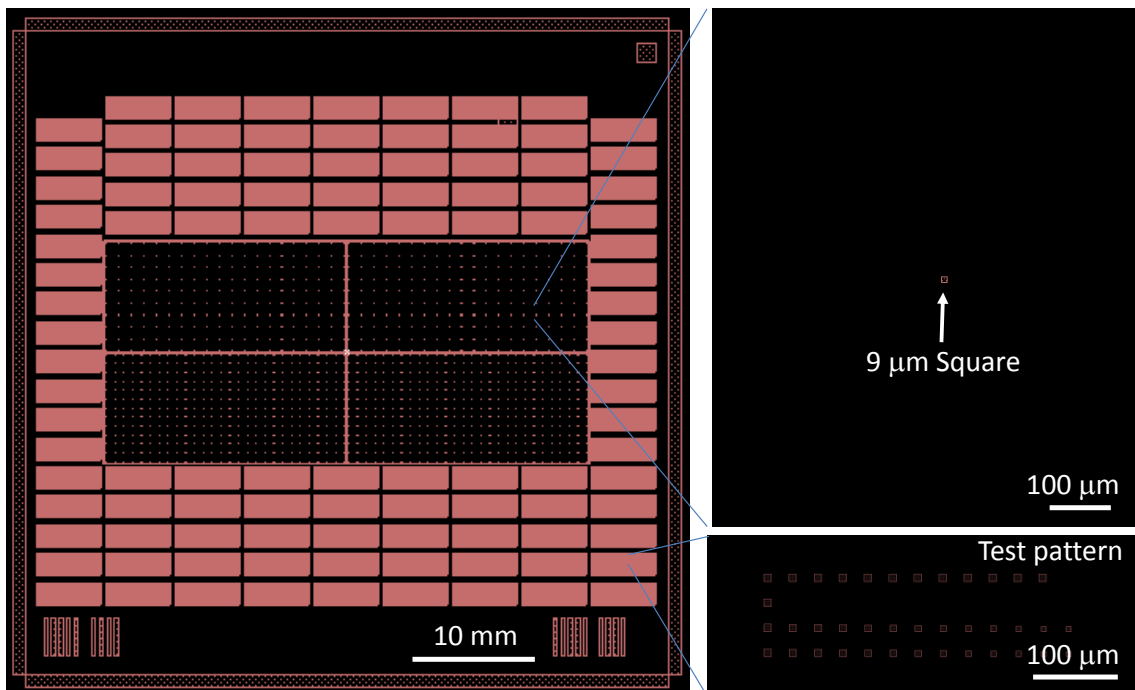


**Figure 6. 6 GDS data of the photomask for 2 μm gap**

The resist pattern was transferred to the fused quartz substrate by wet-etching using BHF. The substrate was etched in a thermostated bath with a temperature of 23 °C. The etch-rate was measured to be 70 nm/min. Etching durations of 7 min, 14 min, and 28 min were adopted for spacers with heights of 0.5  $\mu\text{m}$ , 1  $\mu\text{m}$ , and 2  $\mu\text{m}$ , respectively.

Undercut is observed because of the isotropic nature of wet-etching. Such undercut should be monitored and compensated to fabricate the spacers with designated top area. Figure 6. 7 shows the SEM image of the fabricated spacer with a height of 2  $\mu\text{m}$ , observed at the top. Although BHF etching of fused quartz is isotropic process, the ratio of the horizontal to the vertical etch rate is around 1.5, which is attributed to the non-ideal adhesion between the fused quartz and the photoresist. During wet-etching, BHF soak into the interface between the photoresist and the fused quartz, which causes the enhanced etch-rate in the horizontal direction.

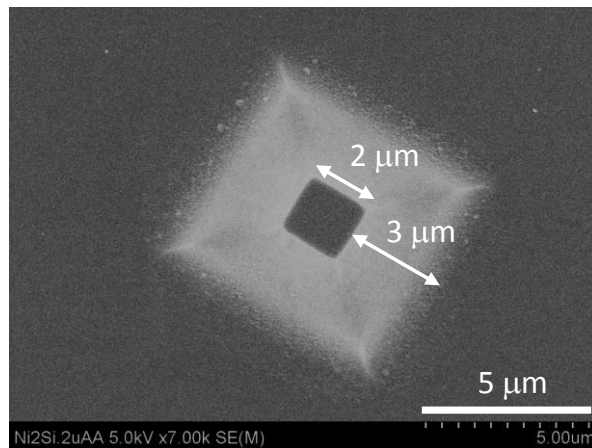


**Figure 6. 7 SEM of the manufactured spacer with a height of 2  $\mu\text{m}$ . The spacer is observed at the top. For SEM observation, platinum is sputtered on the surface with a thickness of a few tens of nanometers.**

Different photomasks were designed for the spacers with different heights. The sizes of rectangles on the photomask are  $6\ \mu\text{m}$ ,  $7\ \mu\text{m}$ , and  $9\ \mu\text{m}$ , for the spacers with heights of  $0.5\ \mu\text{m}$ ,  $1\ \mu\text{m}$ , and  $2\ \mu\text{m}$ , respectively. The SEM images of the fabricated spacers are shown in Figure 6. 8. The substrate was diced into chips with a size of  $19\ \text{mm} \times 8.6\ \text{mm}$  after the fabrication of the spacers.

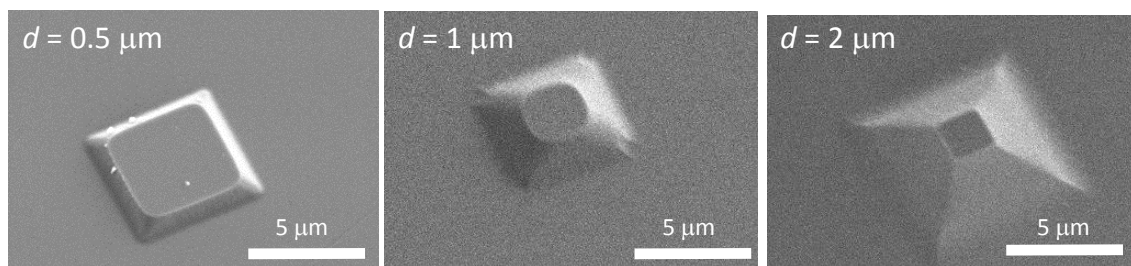


**Figure 6. 8 Bird's eye view SEM of manufactured spacers. [47]**

### 6.2.5. Mechanical tolerance of spacers

As discussed in 6.2.3, high pressure was exerted to the top of spacers. In order to validate that the spacers are mechanically tolerant to the exerted pressure, the spacers was observed after the gap formation, as shown in Figure 6. 9. As expected, the spacer with a size of  $2 \times 2 \mu\text{m}$  placed with a density of  $2 \text{ mm}^{-2}$  maintains its shape after the gap formation, with a slight damage on the top of the spacer.

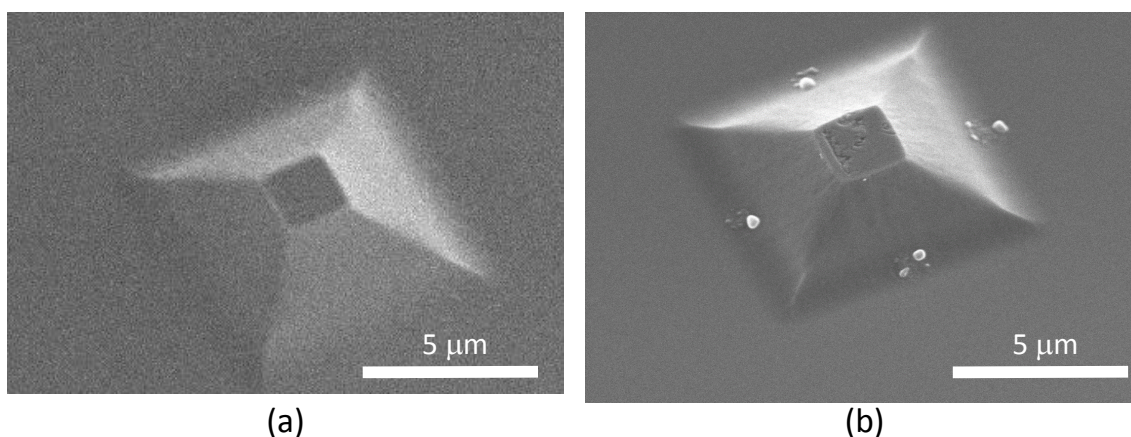


**Figure 6. 9 SEM of a spacer with a density of  $2 \text{ mm}^{-2}$ .**

**(a) Before the gap formation. (b) After the gap formation. [47]**

On the contrary, spacers with a density of  $1 \text{ mm}^{-2}$  were found to have fractured as shown in Figure 6. 10. This is because of the high pressure exceeding the compressive strength of fused quartz.

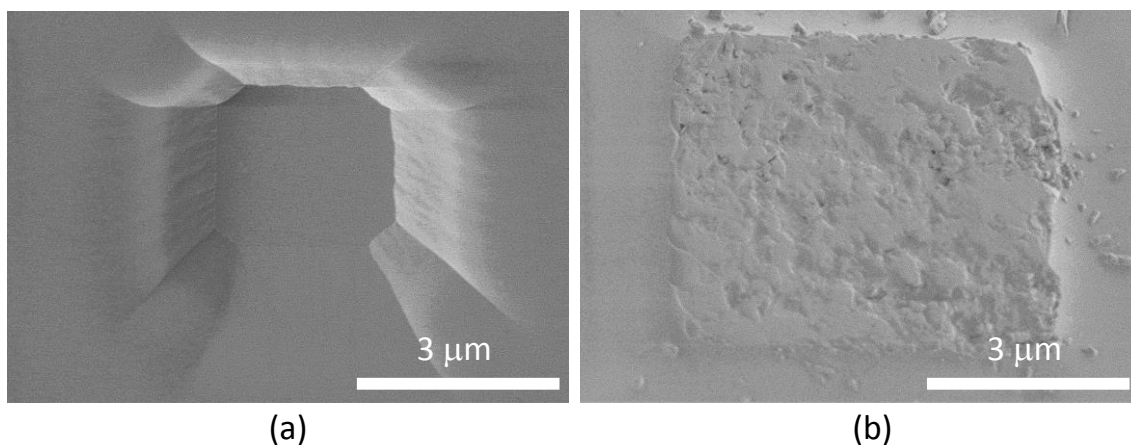


**Figure 6. 10 SEM of a spacer with a density of  $1 \text{ mm}^{-2}$ .**

### 6.3. Evaluation of the gap

The gap width and the gap uniformity were optically evaluated. Such an evaluation assures the uniformity of the gap.

#### 6.3.1. Optical setup

An optical setup shown in Figure 6. 11 was developed for the optical measurement. The light from the white light source is transformed to be a parallel beam by Lens A, and is reflected by the beam splitter. Then the light is focused onto the end of Fiber B by Lens B. The light is transmitted to a thin (a diameter of 0.9 mm) optical fiber whose sleeve is stainless steel (Ocean Optics, FL-400). The light illuminates the chip stack and interferes with itself due to the gap. The reflected light passes through the thin fiber again, and couples to the end of Fiber C through the beam splitter. The interference is analyzed by the spectrometer. The numerical aperture of the fibers is 0.22, which corresponds to a divergence angle of  $\pm 12.7^\circ$ .

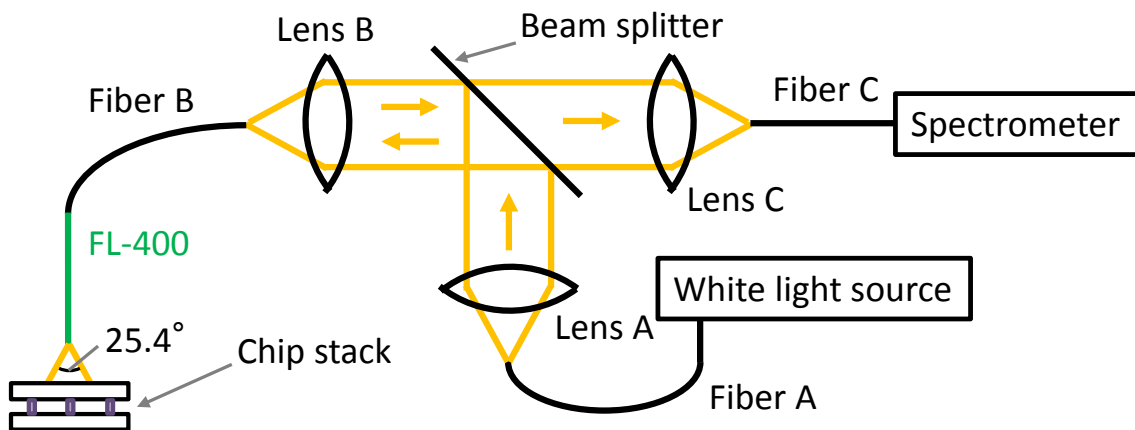


**Figure 6. 11 Schematics of the optics for the gap evaluation**

## 6.3.2. Interferometric optical spectra

Theoretically, the reflectance spectrum  $R$  at normal incidence is calculated as follows:

$$R = R_0 + \left| r_{SV} + \frac{t_{SV}r_{VS}t_{VS}e^{4\pi id/\lambda}}{1 - r_{VS}^2e^{4\pi id/\lambda}} \right|^2, \quad (6.3)$$

where  $R_0$  is the background reflection from the top and the bottom of the substrates,  $r_{SV}$  and  $t_{SV}$  are respectively the reflection and transmission coefficient incident from the fused quartz,  $r_{VS}$  and  $t_{VS}$  are respectively the reflection and transmission coefficient incident from vacuum, and  $\lambda$  is the wavelength. In Eq. (6.3), the background reflection is assumed to be incoherent with the reflection from the gap. This assumption is justified because the substrate is thick (600  $\mu\text{m}$ ) compared to the wavelength ( $< 1 \mu\text{m}$ ), and the divergence angle from the optical fiber is large enough ( $\pm 12.7^\circ$ ). According to Eq. (6.3), the reflectivity spectrum has dips when  $\lambda = 2d/n$  and has peaks when  $\lambda = 2d/(n + 0.5)$ , where  $n$  is an integer.

The measured reflectance spectra are plotted in Figure 6. 12 as black lines. The envelope of the measured reflectance agrees well with the theoretical reflectance. The observed fluctuation is attributed to the multiple reflections within the developed optics.

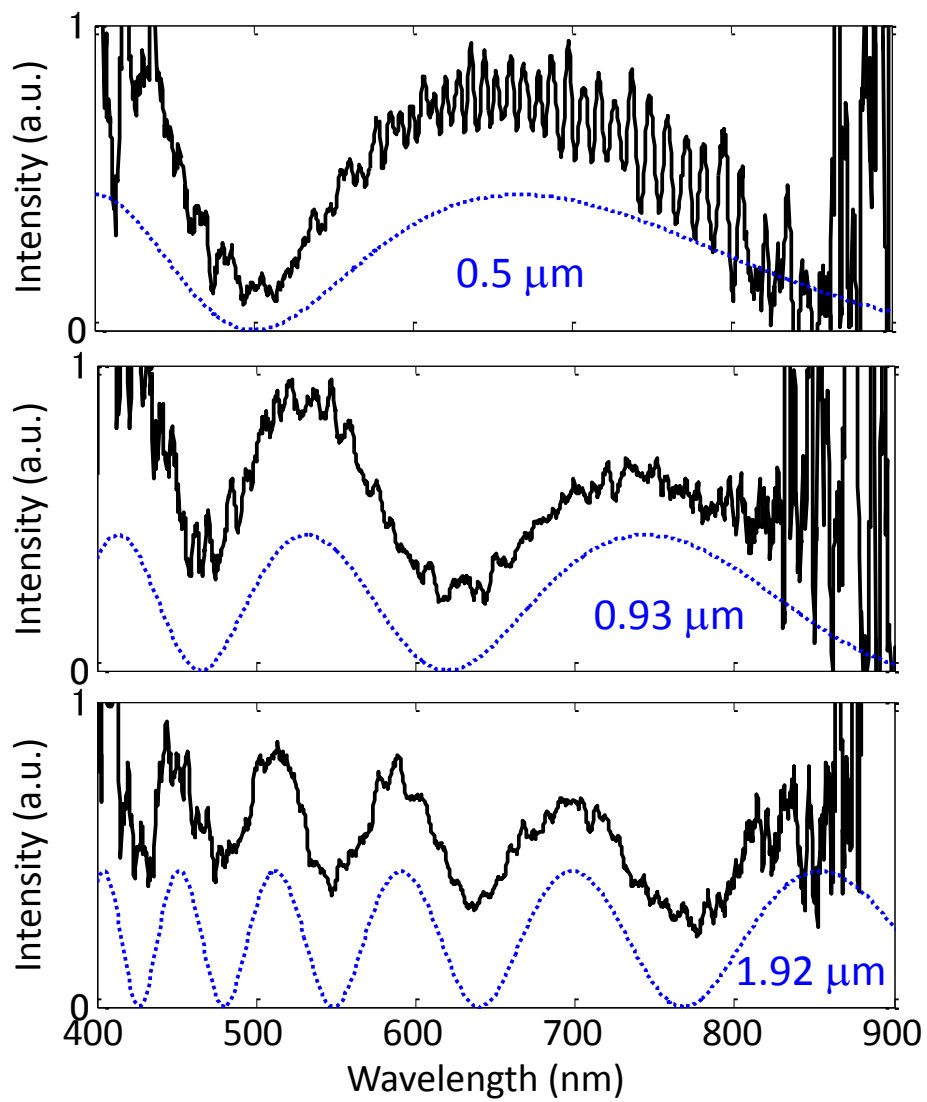


**Figure 6. 12** Measured spectra for gaps with nominal sizes of 0.5  $\mu\text{m}$ , 1  $\mu\text{m}$ , 2  $\mu\text{m}$  (black lines). Calculated reflection spectra (blue dotted lines) [47]

## 6.4. Developed apparatus

An apparatus shown in Figure 6. 13 was developed in order to achieve three functionalities required for this work, namely the exertion of the force, the evaluation of the gap uniformity, and the measurement of the heat transfer. The apparatus is based on the heat flux measurement system discussed in Section 2.4.2. For the exertion of the force, the copper heat spreader is connected to the compression spring through ceramic posts. The compression spring has a small spring constant of 1.0 N/mm, which enables the precise control of the applied force. For a soft gap formation, two extension springs with a smaller spring constant of 0.06 N/m are connected in parallel to the compression spring. In order to allow the thin fiber to access the chips, the copper heat spreader is perforated at four points, as shown in Figure 6. 14. All the plates positioned above the spreader are perforated at the same positions. Likewise, the upper thermal gap pad is cut at the four points. After the gap formation, the optical fiber is inserted to each hole sequentially for the reflectance measurement.

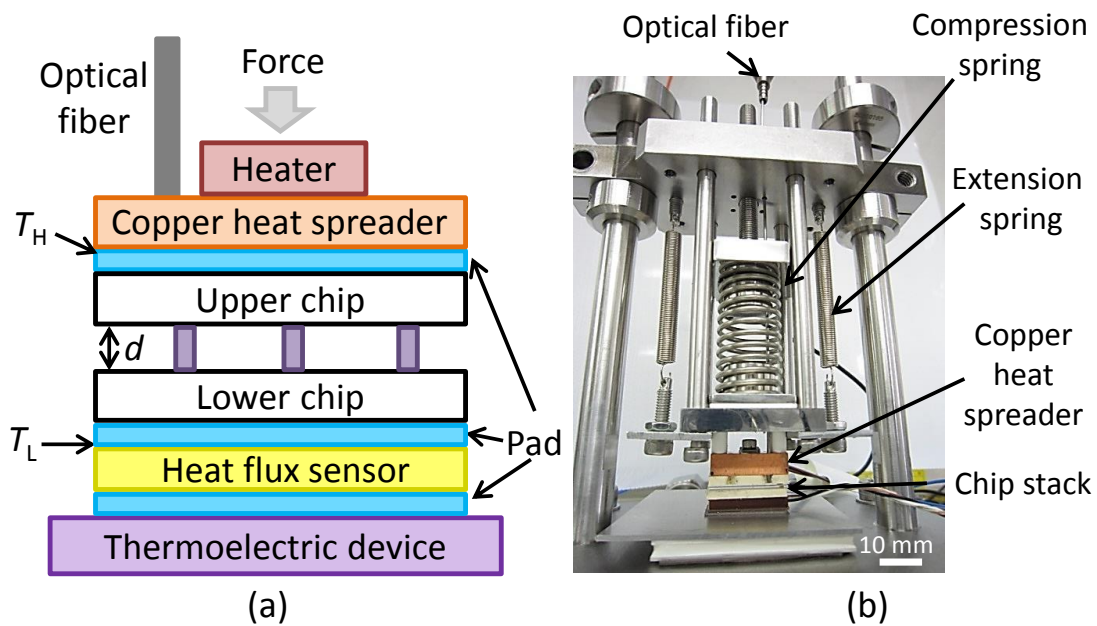


**Figure 6. 13 Developed apparatus. (a) Schematics. (b) Photograph. [47]**

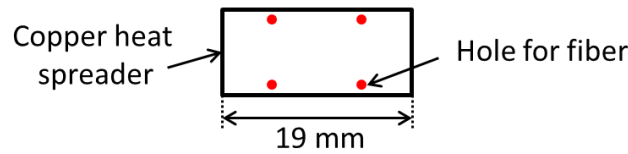


**Figure 6. 14 Position of the perforated holes for optical measurement. [47]**

### 6.5. Measurement of the heat flux across the gap

#### 6.5.1. Calibration of the thermal series resistance ( $R_S$ )

We estimated the temperature drop between the thermocouple and the chip surface in order to accurately determine the heat flux by utilizing the developed apparatus (Figure 6. 15). The temperature drop is represented by the thermal series resistance  $R_S$  in the equivalent thermal circuit model shown in Figure 6. 15 (b). For the estimation of  $R_S$ , the heat transfer across a single chip was measured by the setup shown in Figure 6. 16. The measured heat flux is shown in Figure 6. 17, and the thermal resistance  $R_{\text{Calib}}$  is derived from the slope. The thermal resistance  $R_S$  is derived as the sum of  $R_{\text{Calib}}$  and the thermal resistance of a single chip, and it is calculated as  $R_S = 4 \times 10^{-3} \text{ m}^2 \text{KW}^{-1}$ .

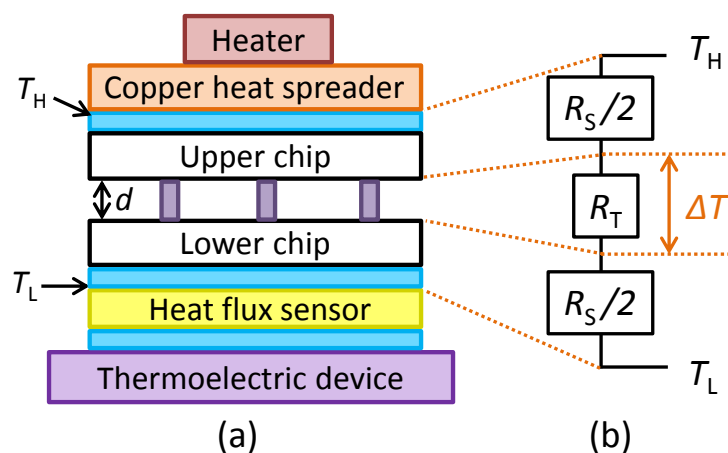


**Figure 6. 15 (a) Developed apparatus shown in Figure 6. 13. Components related to the heat flux measurement are illustrated. (b) Equivalent thermal circuit model.**

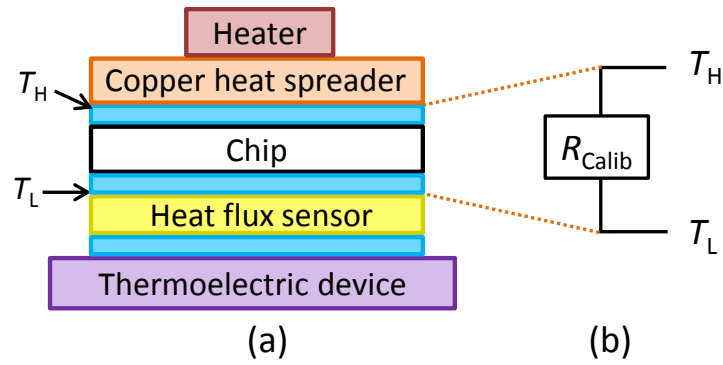


Figure 6.16 (a) Setup for the calibration of  $R_S$ .

(b) Equivalent thermal circuit model.

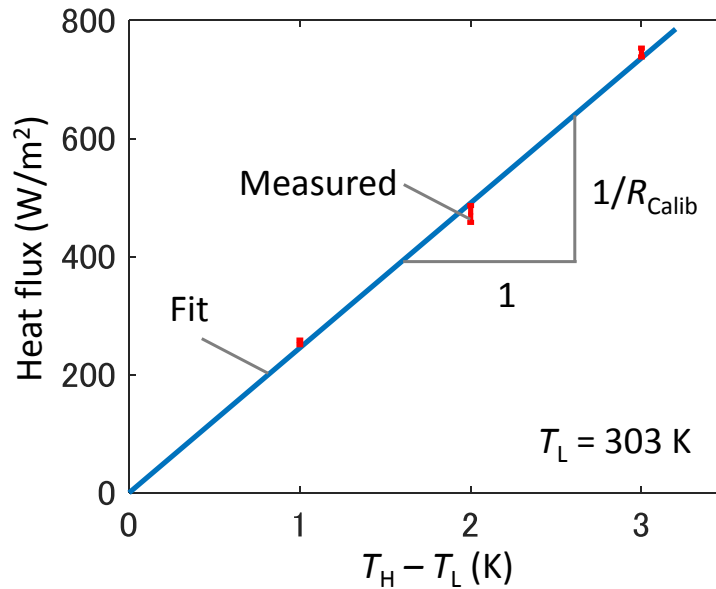


Figure 6.17 Heat flux measured in the calibration of  $R_S$ .

The thermal resistance  $R_T$  between the two chip surfaces is the measurement target in this study. The resistance  $R_T$  is evaluated by the thermal series resistance  $R_S$  and the measured heat flux  $\Phi$  as written in below:

$$R_T = \frac{T_H - T_L}{\Phi} - R_S. \quad (6.4)$$

## 6.5.2. Heat flux as a function of temperature difference

The measured heat flux in the setup shown in Figure 6. 15 (a) is shown in Figure 6. 18. The temperature  $T_L$  was maintained at 293 K. The flux is plotted as a function of calculated temperature difference between the two chip surfaces  $\Delta T$ . Figure 6. 18 also shows theoretical electromagnetic heat flux calculated by fluctuation dissipation theorem as reference. The measured heat flux is larger than the theoretical prediction, and the difference is attributed to the parasitic heat conduction through spacers.

In the temperature range, the measured and the calculated heat fluxes are linear to the temperature difference because the temperature difference (20 K) is sufficiently smaller than the absolute temperature (293 K). The slope is regarded as the heat transfer coefficient of the gap in this study.

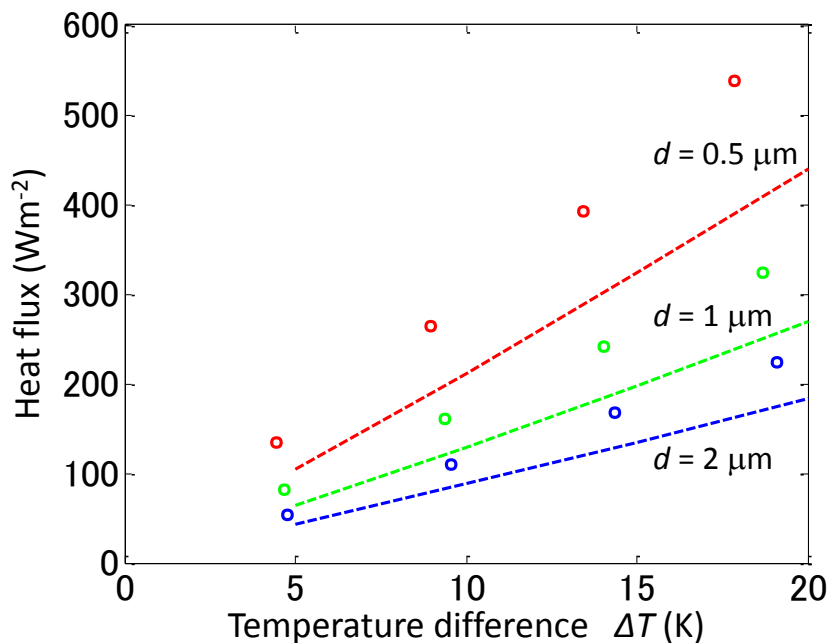


**Figure 6. 18 Measured heat fluxes. Lines are theoretical electromagnetic fluxes.**

[47]

## 6.5.3. Heat transfer coefficient

The gap formation and the heat transfer measurement were repeated four times for each nominal gap of 0.5  $\mu\text{m}$ , 1.0  $\mu\text{m}$ , and 2.0  $\mu\text{m}$ . The measured heat transfer coefficients are shown in Figure 6. 19. The standard deviation of the optical interferometry at the four points is shown as the errorbar in the x-direction, and that of the heat flux measurement is in the y-direction. The theoretically calculated radiative heat transfer is plotted as solid lines. Twice the theoretical heat flux is plotted as dashed lines.

It is clear that the measured flux is equal to or smaller than twice the theoretical flux. This means that the parasitic heat conduction through spacers was successfully suppressed to be equal to or smaller than the electromagnetic heat transfer. The suppression is achieved by the presented gap formation methodology with the proper spacer design.

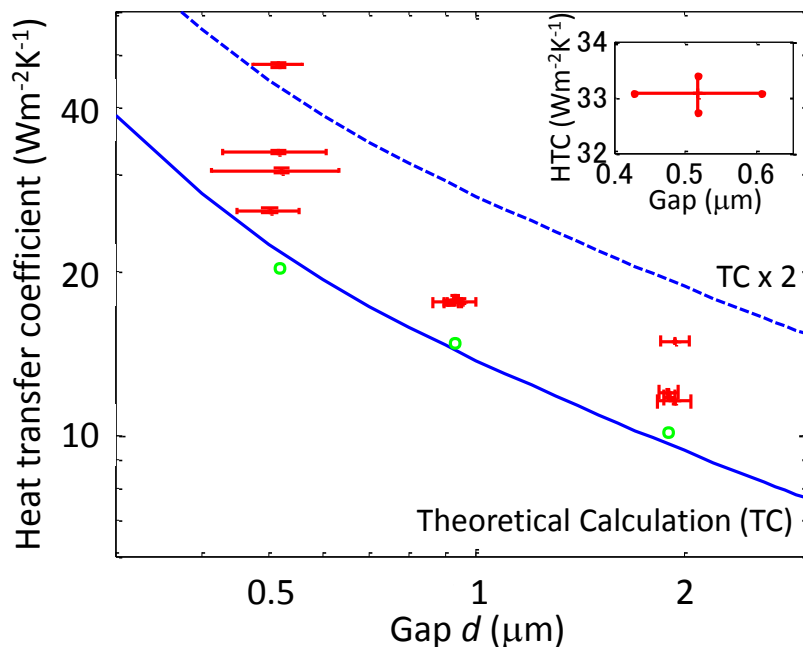


**Figure 6. 19 Measured heat transfer coefficients [47]**

## 6.6. Discussion

The measured heat transfer across the gap is modeled by using the equivalent thermal circuit model shown in Figure 6. 20 (a). The electromagnetic heat transfer is represented by the thermal resistance  $R_R$ . The parasitic thermal conduction through spacers is represented as the series of thermal resistances  $R_C$  and  $R_G$ ; these are the contact resistance between the spacer top and the opposing chip surface and the thermal resistance of the spacer body, respectively. The resistance  $R_G$  is simulated by COMSOL with the model shown in Figure 6. 20 (b). In Figure 6. 20 (b), the spacer is colored so as to indicate the corresponding thermal resistance  $R_C$  and  $R_G$ .

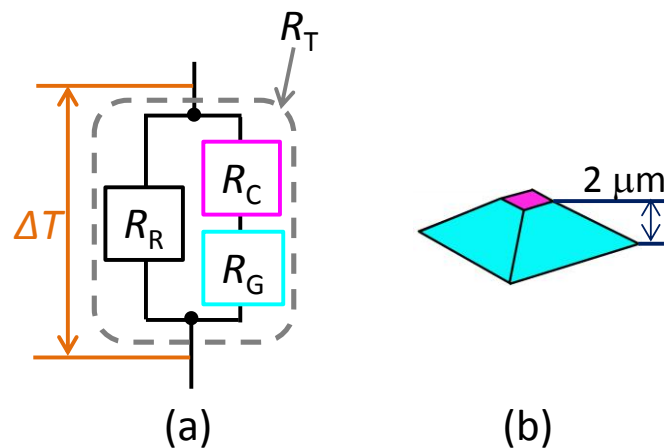


**Figure 6. 20 Equivalent thermal circuit model of the gap (a) Circuit model.**

**(b) Spacer model for the simulation of  $R_G$ . [47]**

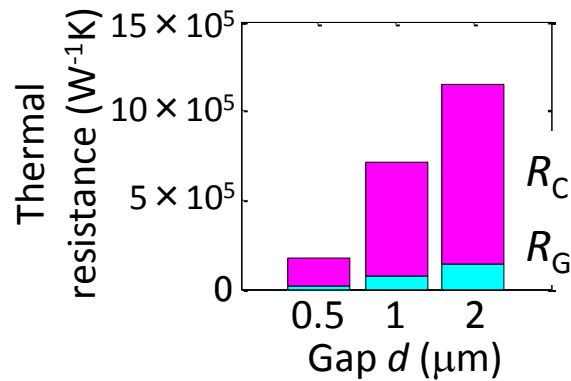


**Figure 6. 21 Modelled thermal resistance of one spacer. [47]**

The contact resistance between bodies is dependent on numbers of factors including materials and surface roughness [42]. Thus, the contact resistance  $R_C$  is utilized as a fitting parameter so as to explain the heat transfer across the gap. The determined thermal contact resistance per area is  $4 \times 10^{-6} \text{ m}^2\text{KW}^{-1}$ . The value is in the same order of magnitude as the reported value in Ref. [46], in which the heat transfer across a polysilicon/nitride interface is evaluated. The fitted contact thermal resistance  $R_C$  and the simulated thermal resistance of the spacer body  $R_G$  per one spacer are shown in Figure 6. 21. The result indicates that the contact resistance  $R_C$  plays a key role in the suppression of the parasitic thermal conduction through spacers.

The radiative thermal resistance  $R_R$  is calculated by using the determined  $R_C$  and the simulated  $R_G$ . The inverse of  $R_R$ , which has the dimension of the heat transfer coefficient, is plotted in Figure 6. 19 as green dots. The modeled heat transfer coefficient and theoretical electromagnetic transfer agree well with the single fitting parameter of thermal contact resistance per area.

### 6.7. Chapter summary

In this chapter, a methodology to form and to validate a submicron gap for near-field radiative heat transfer has been presented for the first time. The parallel-plate configuration, which enables large heat flux enhancement per area, was employed in this study. The micromachined spacers with a height of 0.5  $\mu\text{m}$ , 1  $\mu\text{m}$ , and 2  $\mu\text{m}$  were utilized to determine the gap width. A pressure as high as 6 kPa was applied to the chip stack with an area of 19 mm  $\times$  8.6 mm to make a uniform gap, which was validated by the optical interferometry at the four corners. The heat transfer across the gap was measured to be smaller than twice the calculated radiative heat transfer, which means that the parasitic heat transfer was successfully suppressed smaller than the radiative heat transfer. The heat transfer was modelled by an equivalent thermal circuit model, which suggests that the suppression of the parasitic conduction is dominated by the thermal contact resistance between the top of spacers and the opposing chip.

**Reference**

- [1] J. R. Howell, R. Siegel, and M. P. Menguc. Thermal radiation heat transfer. CRC press, 2010.
- [2] C. M. Hargreaves, "Anomalous radiative transfer between closely-spaced bodies." *Phys. Lett. A* **30**, 491 (1969).
- [3] G. A. Domoto, R. F. Boehm, and C. L. Tien. "Experimental investigation of radiative transfer between metallic surfaces at cryogenic temperatures." *J. Heat Transf.* **92**, 412 (1970).
- [4] E. G. Cravalho, C. L. Tien, and R. P. Caren. "Effect of small spacings on radiative transfer between two dielectrics." *J. Heat Transf.* **89**, 351 (1967).
- [5] D. Polder and M. Van Hove, Theory of radiative heat transfer between closely spaced bodies , *Phys. Rev. B* **4**, 3303 (1971).
- [6] S. M. Rytov, Y. A. Kravtsov, and V. I. Tatarskii. "Principles of statistical radiophysics 2." (1988).
- [7] M. Francoeur, M. P. Mengüç, and R. Vaillon. "Solution of near-field thermal radiation in one-dimensional layered media using dyadic Green's functions and the scattering matrix method." *J. Quant. Spec. Rad. Transfer* **110**, 2002 (2009).
- [8] A. Narayanaswamy, and G. Chen. "Thermal near-field radiative transfer between two spheres." *Phys. Rev. B* **77**, 075125 (2008).
- [9] C. Otey, and S. Fan. "Numerically exact calculation of electromagnetic heat transfer between a dielectric sphere and plate." *Phys. Rev. B* **84**, 245431 (2011).
- [10] A. W. Rodriguez, M. T. H. Reid, and S. G. Johnson. "Fluctuating-surface-current formulation of radiative heat transfer for arbitrary geometries." *Phys. Rev. B* **86**, 220302 (2012).

- [11] C. R. Otey, L. Zhu, S. Sandhu, and S. Fan. "Fluctuational electrodynamics calculations of near-field heat transfer in non-planar geometries: a brief overview." *J. Quant. Spec. Rad. Transfer* **132**, 3 (2014).
- [12] A. Narayanaswamy, and G. Chen. "Surface modes for near field thermophotovoltaics." *Appl. Phys. Lett.* **82**, 3544 (2003).
- [13] M. Laroche, R. Carminati, and J. J. Greffet. "Near-field thermophotovoltaic energy conversion." *J. Appl. Phys.* **100**, 063704 (2006).
- [14] K. Park, S. Basu, W. P. King, and Z. M. Zhang. "Performance analysis of near-field thermophotovoltaic devices considering absorption distribution." *J. Quant. Spec. Rad. Transfer* **109**, 305 (2008).
- [15] M. Francoeur, R. Vaillon, and M. Pinar Mengüç. "Thermal impacts on the performance of nanoscale-gap thermophotovoltaic power generators." *IEEE Trans. Energy Conv.* **26**, 686 (2011).
- [16] C. R. Otey, W. T. Lau, and S. Fan, Thermal rectification through vacuum. *Phys. Rev. Lett.* **104**, 154301 (2010).
- [17] S. Basu, and M. Francoeur "Near-field radiative transfer based thermal rectification using doped silicon." *Appl. Phys. Lett.* **98**, 113106 (2011).
- [18] H. Iizuka, and S. Fan, Rectification of evanescent heat transfer between dielectric-coated and uncoated silicon carbide plates. *J. Appl. Phys.* **112**, 024304 (2012).
- [19] L. P. Wang, and Z. M. Zhang, Thermal rectification enabled by near-field radiative heat transfer between intrinsic silicon and a dissimilar material. *Nanosc. Microsc. Thermophys. Eng.* **17**, 337 (2013).

- [20] Y. Yang, S. Basu, and L. Wang, Radiation-based near-field thermal rectification with phase transition materials, *Appl. Phys. Lett.* **103**, 163101 (2013).
- [21] H. Iizuka, and S. Fan, Consideration of enhancement of thermal rectification using metamaterial models, *J. Quant. Spec. Rad. Trans.* **148**, 156-164 (2014)
- [22] L. Zhu, C. R. Otey, and S. Fan. "Negative differential thermal conductance through vacuum." *Appl. Phys. Lett.* **100**, 044104 (2012).
- [23] S. A. Biehs, F. S. S. Rosa, and P. Ben-Abdallah. "Modulation of near-field heat transfer between two gratings." *Appl. Phys. Lett.* **98**, 243102 (2011).
- [24] L. Cui, Y. Huang, J. Wang, and K. Y. Zhu. "Ultrafast modulation of near-field heat transfer with tunable metamaterials." *Appl. Phys. Lett.* **102**, 053106 (2013).
- [25] P. Ben-Abdallah, and S. A. Biehs, Near-Field thermal transistor, *Phys. Rev. Lett.* **112**, 044301 (2014).
- [26] A. Kittel, W. Müller-Hirsch, J. Parisi, S. A. Biehs, D. Reddig, and M. Holthaus. "Near-field heat transfer in a scanning thermal microscope." *Phys. Rev. Lett.* **95**, 224301 (2005).
- [27] Y. De Wilde, F. Formanek, R. Carminati, B. Gralak, P. A. Lemoine, K. Joulain, J. P. Mulet, Y. Chen, and J. J. Greffet. "Thermal radiation scanning tunnelling microscopy." *Nature* **444**, 740 (2006).
- [28] A. Narayanaswamy, S. Shen, and G. Chen. "Near-field radiative heat transfer between a sphere and a substrate." *Phys. Rev. B* **78**, 115303 (2008).
- [29] S. Shen, A. Narayanaswamy, and G. Chen. "Surface phonon polaritons mediated energy transfer between nanoscale gaps." *Nano Lett.* **9**, 2909 (2009).
- [30] E. Rousseau, A. Siria, G. Jourdan, S. Volz, F. Comin, J. Chevrier, and J. J. Greffet. "Radiative heat transfer at the nanoscale." *Nat. Photo.* **3**, 514 (2009).

- [31] P. J. van Zwol, L. Ranno, and J. Chevrier, "Tuning near field radiative heat flux through surface excitations with a metal insulator transition." *Phys. Rev. Lett.* **108**, 234301 (2012).
- [32] P. J. van Zwol, S. Thiele, C. Berger, W. A. De Heer, and J. Chevrier. "Nanoscale radiative heat flow due to surface plasmons in graphene and doped silicon." *Phys. Rev. Lett.* **109**, 264301 (2012).
- [33] B. Guha, C. Otey, C. B. Poitras, S. Fan, and M. Lipson, "Near-field radiative cooling of nanostructures." *Nano Lett.* **12**, 4546 (2012).
- [34] J. Shi, P. Li, B. Liu, and S. Shen, "Tuning near field radiation by doped silicon." *Appl. Phys. Lett.* **102**, 183114 (2013).
- [35] J. Shi, B. Liu, P. Li, L. Y. Ng, and S. Shen, "Near-Field Energy Extraction with Hyperbolic Metamaterials." *Nano Lett.* **15**, 1217 (2015).
- [36] B. Song, Y. Ganjeh, S. Sadat, D. Thompson, A. Fiorino, V. Fernández-Hurtado, J. Feist, F. J. Garcia-Vidal, J. C. Cuevas, P. Reddy, E. Meyhofer, "Enhancement of near-field radiative heat transfer using polar dielectric thin films." *Nat. Nano.* **10**, 253 (2015).
- [37] K. Kim, B. Song, V. Fernández-Hurtado, W. Lee, W. Jeong, L. Cui, D. Thompson, J. Feist, M. H. Reid, F. J. García-Vidal, and J. C. Cuevas, "Radiative heat transfer in the extreme near field." *Nature* **528**, 387 (2015).
- [38] R. S. Ottens, V. Quetschke, S. Wise, A. A. Alemi, R. Lundock, G. Mueller, D. H. Reitze, D. B. Tanner, and B. F. Whiting. "Near-field radiative heat transfer between macroscopic planar surfaces." *Phys. Rev. Lett.* **107**, 014301 (2011).
- [39] T. Kralik, P. Hanzelka, V. Musilova, A. Srnka, and M. Zobac. "Cryogenic apparatus for study of near-field heat transfer." *Rev. Sci. Inst.* **82**, 055106 (2011).

- [40] T. Kralik, P. Hanzelka, M. Zobac, V. Musilova, T. Fort, and M. Horak. "Strong near-field enhancement of radiative heat transfer between metallic surfaces." *Phys. Rev. Lett.* **109**, 224302 (2012).
- [41] T. Ijro, and N. Yamada. "Near-field radiative heat transfer between two parallel SiO<sub>2</sub> plates with and without microcavities." *Appl. Phys. Lett.* **106**, 023103 (2015).
- [42] R. S. DiMatteo, P. Greiff, S. L. Finberg, K. Young-Waithe, H. K. H. Choy, M. M. Masaki, and C. G. Fonstad, "Enhanced photogeneration of carriers in a semiconductor via coupling across a nonisothermal nanoscale vacuum gap." *Appl. Phys. Lett.* **79**, 1894 (2001).
- [43] R. DiMatteo, P. Greiff, D. Seltzer, D. Meulenberg, E. Brown, E. Carlen, K. Kaiser, S. Finberg, H. Nguyen, J. Azarkevich, P. Baldasaro, J. Beausang, L. Danielson, M. Dashiell, D. DePoy, H. Ehsani, W. Topper, K. Rahner, and R. Siergiej, "Micron-gap thermophotovoltaics" *AIP Conf. Proc.* **232** (2003).
- [44] L. Hu, A. Narayanaswamy, X. Chen, and G. Chen, "Near-field thermal radiation between two closely spaced glass plates exceeding Planck's blackbody radiation law." *Appl. Phys. Lett.* **92**, 133106 (2008).
- [45] E. G. Wolff, and D. A. Schneider, "Prediction of thermal contact resistance between polished surfaces." *Int. J. Heat Mass Trans.* **41**, 3469 (1998).
- [46] W. B. Song, M. S. Sutton, and J. J. Talghader, "Thermal contact conductance of actuated interfaces." *Appl. Phys. Lett.* **81**, 1216 (2002).
- [47] Reprinted from *Applied Physics Letters*, Vol. 106 (2015), 083504, K. Ito et al., © 2015 AIP, with permission from AIP Publishing LLC.

## *Chapter 7 Discussion and Conclusion*

This chapter discusses the results obtained in this study. Firstly, each preceding chapter is summarized. Secondary, the achievements are quantitatively compared with other reported works. Thirdly, the relationship between the fabrication error and the performance of the radiation control is examined. Fourthly, the significant implication of the achievements toward mid-infrared light source for non-dispersive infrared sensing and thermal management in artificial satellites is discussed. Finally, this study is concluded.

### 7.1 Summary of this work

Chapter 1 has introduced the backgrounds of this work. The applications of thermal radiation were briefly reviewed. Then, four vital types of thermal radiation control, namely dynamic control, monochromatic emission, thermal rectification, and near-field effects were explained, toward mid-infrared light source for non-dispersive infrared sensing (NDIR) and thermal management in artificial satellites. The organization of the thesis was described.

Chapter 2 has introduced the theory of thermal radiation and the methodologies employed in this work. The Maxwell's equation, spectral intensity, emissivity, and view factor were explained for the discussion in the subsequent chapters. Electromagnetic simulation techniques were described for the design and modelling of thermal radiation devices. Fabrication methodologies were explained for the experimental demonstration of microstructured thermal devices. Evaluation methodologies including Fourier-transform infrared spectrometer and heat flux measurement system were also described.

Chapter 3 has theoretically presented the dynamic modulation of thermal radiation. The modulation is enabled by the control of the coupling between the guided mode resonance in silicon gratings and the surface polariton. Emissivity is shown to be controllable by tuning the gap distance between the thermally-transparent dielectric gratings and the interface for the surface polariton. Two types of surface polaritons, namely the surface phonon polariton (SPhP) on a silicon carbide (SiC) substrate and the surface plasmon polariton (SPP) on a doped silicon (DSi) slab were utilized. The modulation amplitude of emissivity exceeds 90 % with the SiC emitter and 50 % with the DSi emitter. An asymmetric thermal radiation was presented with a double-grooved

grating. A possible fabrication process was presented for the DSi emitter.

Chapter 4 has demonstrated a quasi-monochromatic thermal emitter by utilizing the proximity interaction between metal-insulator-metal resonators. The frequency interval between the fundamental and the second-order modes is enlarged by diagonally arranging rectangular resonators or densely placing square resonators. Other parasitic modes are eliminated in the densely-placed resonators, and the integrated parasitic heat flux is suppressed from  $11.8 \text{ Wsr}^{-1}\text{m}^{-2}$  to  $4.0 \text{ Wsr}^{-1}\text{m}^{-2}$  at an angle of  $60^\circ$ . The presented metamaterial absorbers or thermal emitters were fabricated by electron-beam lithography. The fabricated metamaterials were evaluated by Fourier-transform infrared spectrometer, and the measured spectra agree well with numerical simulations.

Chapter 5 has demonstrated radiative thermal rectifiers with a phase-change material. The metal-insulator transition of vanadium oxide ( $\text{VO}_2$ ) allows us to obtain a high thermal rectification contrast ratio of 2. The emitter and the receiver were optically characterized by an infrared spectrometer to model the rectifier by fluctuation electrodynamics. The modeled heat flux captures the measured values, validating the theoretical and the experimental procedure employed in this work. The operation temperature range was successfully tuned by tungsten doping into the  $\text{VO}_2$  film.

Chapter 6 has developed a methodology to form and to validate a submicron gap for near-field radiative heat transfer, which has never been proposed before this study. The parallel-plate configuration, which enables large heat flux enhancement per area, was employed in this study. The micromachined spacers were utilized to determine the gap width, and a pressure was applied to the chip stack to make a uniform gap, which was validated by the optical interferometry at the four corners. The heat transfer across the gap was measured to be smaller than twice the calculated radiative heat transfer, which

means that the parasitic heat transfer was successfully suppressed smaller than the radiative heat transfer. The heat transfer was modelled by an equivalent thermal circuit model, which suggests that the suppression of the parasitic conduction is dominated by the thermal contact resistance between the top of spacers and the opposing chip.

## 7.2 Comparison with other works

In Chapter 3, the dynamic modulation of thermal radiation has been theoretically demonstrated. The modulation amplitude of emissivity exceeds 90 % in the SiC emitter, which is larger than the highest value ever reported (69 %) [1] by utilizing a photonic crystal composed of quantum wells. Furthermore, the emitters consist of silicon, doped silicon, and silicon carbide, which are materials with relatively low cost. The materials utilized in the preceding works, quantum well [1]-[2] or high-quality graphene [3], are still expensive compared to the material used in this work.

In Chapter 4, parasitic modes of metal-insulator-metal (MIM) thermal emitters have shown to be suppressed by the arrangement of patch resonators. Although numbers of researchers have reported the control of the fundamental mode of the MIM metamaterial thermal emitter, a limited number of works investigated [4][5] or targeted on [6] higher-order modes. However, the control of parasitic modes while keeping the fundamental frequency constant has never been discussed before this study. This work has utilized the proximity interaction between resonators in order to suppress the parasitic modes including the second-order mode and others, and the proposed method was successfully validated by the numerical simulation and the experiment. For mid-infrared light source, another requirement other than the parasitic suppression is the line-width of the emission. Because absorption spectra of various chemical compound

are narrow, Inoue and his colleagues developed a photonic crystal emitter composed of quantum wells, and they achieved a Q-factor larger than 100 [7]. Although the Q-factor of the presented MIM emitter is low ( $Q < 10$ ) and the densely-tiling slightly lowers Q-factor [8], the Q-factor of MIM emitters is improved by utilizing cross-shaped resonators [9][10]. Note that there might be some applications which do not need high Q-factor but the parasitic suppression, such as infrared drying.

In Chapter 5, thermal rectification has experimentally investigated by employing the radiative property of a phase-change material. For conductive thermal rectifiers, various physical phenomena have been utilized for the experimental demonstration [11]-[13]. However, the measured rectification contrast ratios remain relatively small values; e.g., Ref. [13] reported rectification contrast ratio of 0.6 by utilizing temperature dependent thermal conductivity of a quasicrystal. For radiative thermal rectifiers, several theoretical works have utilized the temperature dependence of the optical constants [14]-[18]. However, the experimental implementation of the radiative thermal rectifier was rare and showed low contrast ratio [19] before this study. Owing to the metal-insulator transition of  $\text{VO}_2$ , the presented thermal rectifier exhibits a large contrast ratio of 2 experimentally. An alternative thermal diode based on mechanical switches and shape memory alloy was recently demonstrated [20]. A high contrast ratio of 90 was achieved with the cost of bulky mechanical components. A detailed comparison requires further optimization and specifications from applications. Note that the radiative heat transfer between  $\text{VO}_2$  and other materials is also a platform of functionalities other than thermal rectification [21]-[24]. Furthermore,  $\text{VO}_2$  can be employed to tune thermal conduction [25] and the optical response in the visible spectrum [26].

In Chapter 6, a methodology to form submicron gaps has been presented. Submicron gaps for near-field radiative heat transfer have been realized by the sphere-plate geometry [27]-[29]. The smallest gap width of 2 nm was recently reported [29]. Meanwhile, the heat flux enhancement is smaller than that in the parallel-plate configuration. The smallest gap achieved using the parallel-plate configuration has remained 1  $\mu\text{m}$  [30]-[32] before this study, because the alignment of two parallel plates is extremely difficult due to the deviation of the real surface from the ideal flat surface. The presented methodology successfully compensates the intrinsic deflection of substrates and achieves submicron gap with an area exceeding 1  $\text{cm}^2$ . Recently, several research groups also achieved a submicron gap in the parallel-plate configuration by utilizing large mechanical support [33]-[35]. Lim and her colleagues achieved 400 nm by using wafer bonding [33]. St-Gelais and his colleagues achieved 40 nm between integrated SiC nanobeams [34]. Song and his colleagues achieved 60 nm with an area of 50  $\mu\text{m} \times 50 \mu\text{m}$  by utilizing a complexed alignment system [35]. Since our method utilizes tiny spacers to support the gap, the area of our gap is scalable.

### 7.3 Discussion on the fabrication error

Chapter 3 and Chapter 4 discuss the electromagnetic resonances in the microstructures. Such resonances are sensitive to the fluctuation of geometries originating from the fabrication error as reported in Section 4.4.3. This section discusses the fabrication error by simulating the electromagnetic response of the structure presented in Chapter 3.

The guided mode resonance in grating structures is sensitive to the grating geometries. The grating height, which is one of the grating geometries, is determined by the deposition process. Since the area of the structure should exceed 1  $\text{cm}^2$  in order to

obtain enough amount of thermal radiation, the uniformity of the deposition process potentially affects the performance of the thermal emitter. Figure 7. 1 shows the emissivity of the structure with SiC, when the height  $h_g$  of the grating is varied from  $0.95 \mu\text{m}$  to  $1.07 \mu\text{m}$  with a step of  $20 \text{ nm}$ . Small fluctuation (4 %) of the grating height degrades the peak emissivity from near unity to a value lower than 0.5. Figure 7. 2 shows the emissivity of the structure with doped silicon when  $h_g$  is varied from  $1.03 \mu\text{m}$  to  $1.15 \mu\text{m}$ . The peak emissivity remains almost constant.

The clear contrast between Figure 7. 1 and Figure 7. 2 originates from the sharpness of the resonance. The electromagnetic response is sensitive to the fluctuation of geometries in the case that the Q-factor is high. Thus, it is better to acquire information related to the fabrication error before designing the Q-factor of the structure. Otherwise, one should repeat the trials and errors before finally designing the Q-factor, as shown in Figure 7. 3. Of course, it is better to take care of not only the uniformity in a wafer but also the repeatability between wafers and runs.

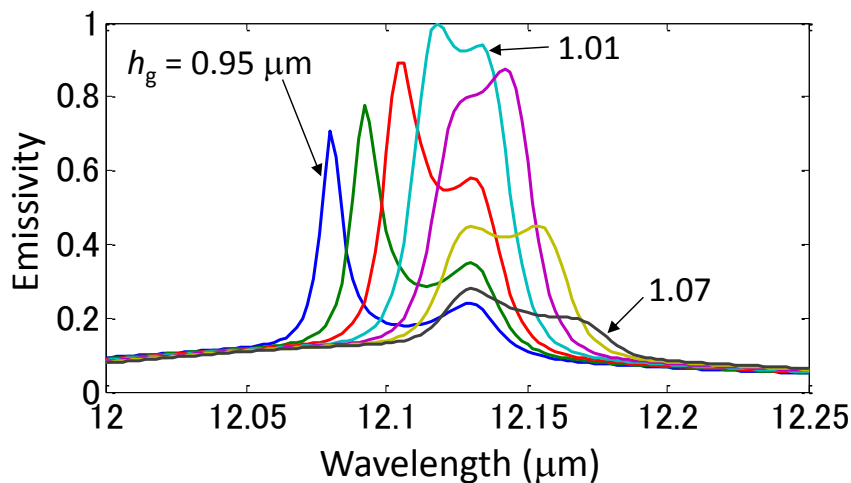


**Figure 7. 1 Emissivity of the structure with SiC substrate. The height  $h_g$  of the grating is varied with a step of  $20 \text{ nm}$ .**

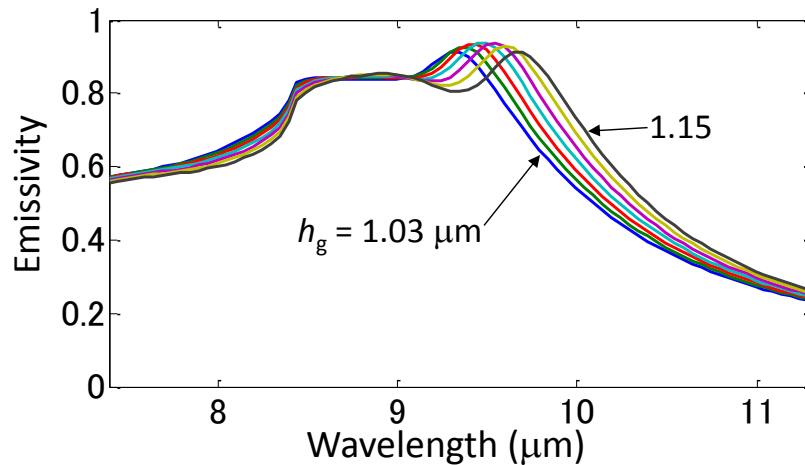


**Figure 7. 2 Emissivity of the structure with doped silicon slab. The height  $h_g$  of the grating is varied with a step of 20 nm.**

The same scenario is applied to the MIM emitters presented in Chapter 4. The ratio of the fundamental to the second-order wavelength is enhanced when the gap between resonators becomes smaller, as shown in Figure 4.15. When the gap is small, the fluctuation of the gap worsens the response such that the emissivity peak does not reach near unity, as discussed in Section 4.4.3. Thus, it is better to iterate the fabrication in order to optimize the gap size and wavelength ratio considering fabrication error, as shown in Figure 7. 3.

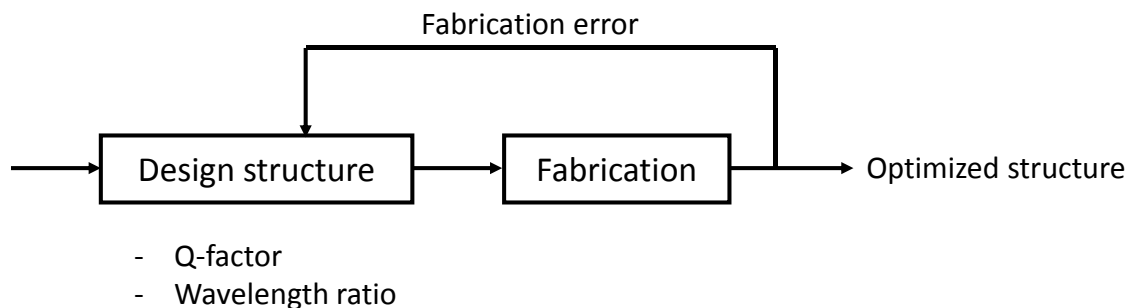


**Figure 7. 3 Flowchart of the design and fabrication iteration.**

#### 7.4 Significant implication of this work and future research directions

The achievements in this work can be applied to two scenes of thermal radiation control, namely, mid-infrared light source for non-dispersive infrared sensing (NDIR) and thermal management in artificial satellites.

##### 7.4.1 Mid-infrared light source for NDIR

Mid-infrared light source for NDIR requires two functionalities: dynamic modulation and monochromaticity. The direct modulation of thermal emissivity has been theoretically realized by coupling guided mode resonance and surface polaritons. The modulation enables the high-frequency infrared light while maintaining the emitter temperature constant. The background noise in NDIR system is eliminated by synchronizing the thermal emitter and the detector. Higher modulation frequency allows us to reduce the noise with a  $1/f$  spectrum. The amplitude of the modulation was theoretically predicted to exceed 90 %. This large modulation amplitude will contribute to suppress background efficiently.

A quasi-monochromatic thermal emitter has been realized by suppressing parasitic modes of metal-insulator-metal (MIM) thermal emitters. The second-order mode is shifted toward higher frequencies, and other parasitic modes are eliminated. The control of the parasitic modes is enabled by the geometrical design of the resonators, and the detailed investigation on the geometrical parameters enables the further design optimization to a specific constrain. The infrared light from MIM emitters is purified, and the power efficiency of such emitters is improved. The spurious detection in NDIR sensing is avoided by the control of parasitic modes.

In this thesis, these two functionalities have been realized by utilizing different types

of electromagnetic resonance. In future, these two functionalities will be merged into one device, such as an MIM emitter with electrostatically movable top aluminum patterns. Such a device is readily manufacturable with the current MEMS technologies, and the device is going to be optimized to detect specific molecules in NDIR systems.

#### 7.4.2 Thermal management in artificial satellites

Artificial satellites requires intelligent thermal management based on thermal conduction and radiation, because the environment is vacuum. The tough constrain on payload also limits the components for thermal management, e.g. controllers and sensors.

A thermal rectifier working in vacuum has been experimentally presented by utilizing thermal radiation. A high contrast ratio of 2 is achieved by the metal-insulator transition of VO<sub>2</sub>. The heat flux across thermal rectifiers is modulated according to the direction of temperature gradient, and thus they will be utilized as autonomous temperature regulation systems in artificial satellites.

The heat flux of thermal rectifier is enhanced by the near-field radiative heat transfer. In this thesis, a methodology to form submicron gaps has been presented for near-field radiative heat transfer. The gap uniformity is validated by observing optical interferometric spectra. Such validation will contribute to assure the quality of thermal management systems utilizing near-field thermal radiation. The presented methodology allows us to suppress the parasitic heat conduction by low-density pillars and to compensate the intrinsic bending of wafers simultaneously.

In the case that near-field thermal rectifier is realized, the modulation amplitude is enhanced. The contrast between the forward and the reverse scenarios will be kept large

by suppressing the parasitic heat conduction through the spacers. Such a suppression will be enabled based on the presented design strategy of spacers based on the physical constants of fused quartz and equivalent thermal circuit model.

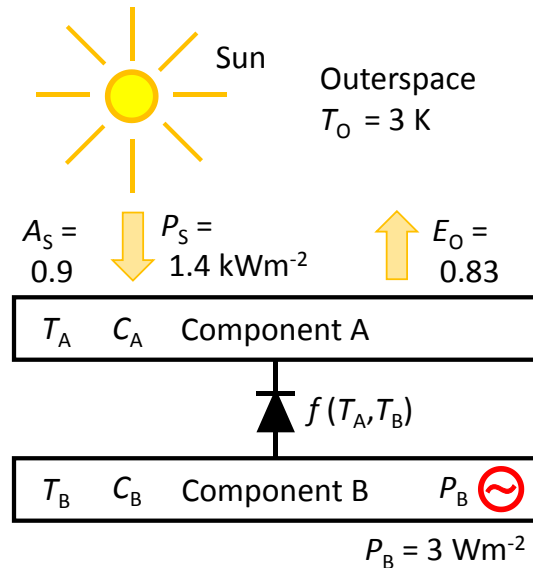


**Figure 7. 4 Situation in an artificial satellite, where the heat flux is managed by a thermal rectifier. A one-dimensional problem is considered, and the heat flux is normalized per area.**

In order to discuss more quantitatively, we consider a situation shown in Figure 7. 4. Component A and B are installed in an artificial satellite, and component A is exposed to outerspace. The satellite is rotating around the earth with a period of 90 min. Component A is exposed to the sunlight with a power  $P_S = 1.4 \text{ kWm}^{-2}$  during half the period, and absorbs it with an absorptivity  $A_S$  of 0.9, and it radiates to outerspace with an emissivity  $E_O$  of 0.83. Component B is thermally connected to component A through a thermal rectifier, and generates heat internally with a rate  $P_B$  of  $3 \text{ Wm}^{-2}$ . The generated heat is wasted through the thermal rectifier and component A toward outerspace, and the increase of the temperature  $T_B$  of component B is assumed to decrease the lifetime of the satellite. The temperature of component A and component B follows the equations

below:

$$C_A \frac{dT_A}{dt} = DA_S P_S - \sigma E_O (T_A^4 - T_O^4) + Nf(T_A, T_B), \quad (7.1)$$

$$C_B \frac{dT_B}{dt} = P_B - Nf(T_A, T_B), \quad (7.2)$$

where  $C_A = 10^6 \text{ JK}^{-1}\text{m}^{-2}$  and  $C_B = 5 \times 10^4 \text{ JK}^{-1}\text{m}^{-2}$  denote the thermal capacity of component A and B, respectively,  $D$  is equal to unity or zero when the sunlight illuminates or does not illuminate, respectively, and  $\sigma$  is the Stefan-Boltzmann constant. The transfer function  $f$  of the thermal rectifier is assumed to be:

$$f = \begin{cases} 0.6\sigma(T_B^4 - T_A^4) & (T_A < 340 \text{ K}) \\ 0.2\sigma(T_B^4 - T_A^4) & (T_A \geq 340 \text{ K}) \end{cases}, \quad (7.3)$$

following Figure 5.11. The heat flux enhancement factor  $N$  is set to be 5 in order to include the near-field coupling across a submicron gap. The calculated transient temperature is shown in Figure 7. 5. The periodic temperature history converges after 1500 min, and the duration between 1830 min and 1950 min is shown. Thermal rectification is observed around the 1865 min and 1915 min, and the rectification due to  $\text{VO}_2$  slows down the heating while it boosts the cooling. The temperature reduction is clearer with an ideal rectifier with a contrast ratio of 98. For the comparison, thermal rectifier is replaced with a conductive or a radiative path. With the conductive path,  $T_B$  almost follows  $T_A$  because of the large heat transfer coefficient of  $80 \text{ WK}^{-1}\text{m}^{-2}$ , and thus the maximum temperature of  $T_B$  is as high as that of  $T_A$ . With the radiative path,  $f = 0.05\sigma(T_B^4 - T_A^4)$  and  $N = 1$  are assumed, and  $T_B$  is kept at high because the internally generated heat does not dissipate enough through the almost insulating radiative path. The unique transfer function including the rectification lowers both the maximum and the average temperatures. Note that the aging of the phase transition should be investigated before implementations.

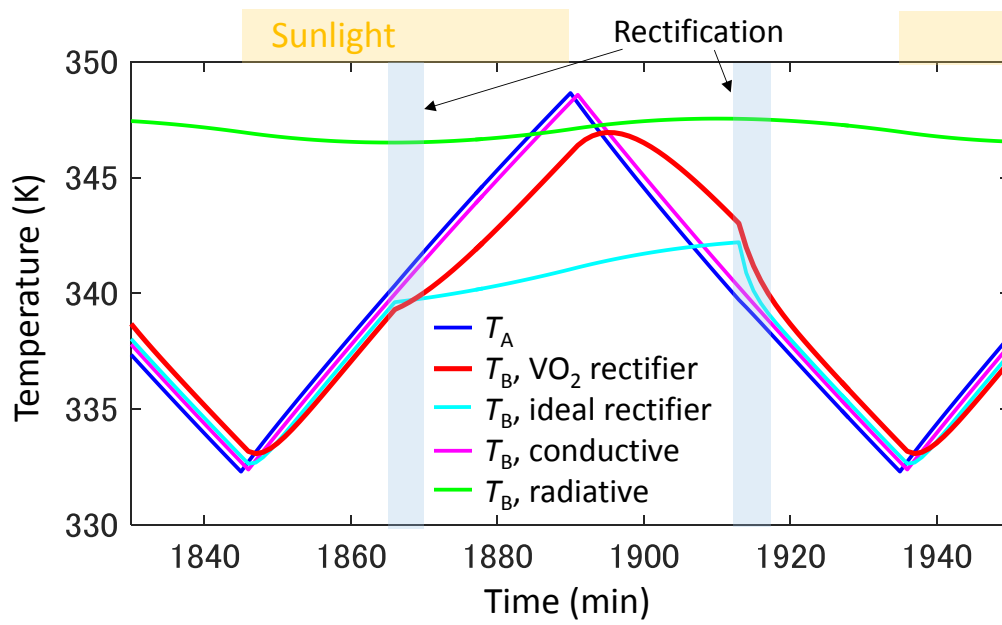


**Figure 7. 5 Transient response of the temperatures in the artificial satellite.**

### 7.5 Conclusion

In this study, four different types of thermal radiation control, namely dynamic modulation, monochromatic light source, thermal rectification, and near-field radiative heat transfer, have been investigated. These controls have been achieved by coupling surface polariton and guided mode resonance, proximity coupling between neighboring MIM resonators, metal-insulator transition of VO<sub>2</sub>, and submicron gaps formed by micromachined spacers, respectively. The obtained results are outstanding compared to other works. These achievements enable dynamic, monochromatic thermal emitter for non-dispersive infrared sensing, and intelligent thermal management system for artificial satellites. Furthermore, the achievements opens a pathway to more flexible thermal radiation control, which may be realized by merging the knowledge from other research fields including solid-state physics and material science.

**Reference**

- [1] T. Inoue, M. De Zoysa, T. Asano, and S. Noda. "Realization of dynamic thermal emission control." *Nat. Mat.* **13**, 928 (2014).
- [2] S. Vassant, I. Moldovan Doyen, F. Marquier, F. Pardo, U. Gennser, A. Cavanna, J. L. Pelouard, and J. J. Greffet. "Electrical modulation of emissivity." *Appl. Phys. Lett.* **102**, 081125 (2013).
- [3] V. W. Brar, M. C. Sherrott, M. S. Jang, S. Kim, L. Kim, M. Choi, L. A. Sweatlock, and H. A. Atwater. "Electronic modulation of infrared radiation in graphene plasmonic resonators." *Nat. Comm.* **6** (2015).
- [4] B. J. Lee, L. P. Wang, and Z. M. Zhang. "Coherent thermal emission by excitation of magnetic polaritons between periodic strips and a metallic film." *Opt. Exp.* **16**, 11328 (2008).
- [5] J. Hao, L. Zhou, and M. Qiu. "Nearly total absorption of light and heat generation by plasmonic metamaterials." *Phys. Rev. B* **83**, 165107 (2011).
- [6] W. Streyer, K. Feng, Y. Zhong, A. J. Hoffman, and D. Wasserman. "Selective absorbers and thermal emitters for far-infrared wavelengths." *Appl. Phys. Lett.* **107**, 081105 (2015).
- [7] T. Inoue, M. D. Zoysa, T. Asano, and S. Noda. "Single-peak narrow-bandwidth mid-infrared thermal emitters based on quantum wells and photonic crystals." *Appl. Phys. Lett.* **102**, 191110 (2013).
- [8] F. Costa, S. Genovesi, A. Monorchio, and G. Manara. "A circuit-based model for the interpretation of perfect metamaterial absorbers." *IEEE Trans. Ant. Prop.* **61**, 1201 (2013).

- [9] X. Liu, T. Tyler, T. Starr, A. F. Starr, N. M. Jokerst, and W. J. Padilla. "Taming the blackbody with infrared metamaterials as selective thermal emitters." *Phys. Rev. Lett.* **107**, 045901 (2011).
- [10] A. Sakurai, B. Zhao, and Z. M. Zhang. "Resonant frequency and bandwidth of metamaterial emitters and absorbers predicted by an RLC circuit model." *J. Quant. Spec. Rad. Trans.* **149**, 33 (2014).
- [11] C. W. Chang, D. Okawa, A. Majumdar, and A. Zettl, Solid-state thermal rectifier. *Science*, **314**, 1121 (2006).
- [12] W. Kobayashi, Y. Teraoka, and I. Terasaki, An oxide thermal rectifier. *Appl. Phys. Lett.* **95**, 171905 (2009).
- [13] R. Nakayama, T. Takeuchi, "Thermal Rectification in Bulk Material Through Unusual Behavior of Electron Thermal Conductivity of Al-Cu-Fe Icosahedral Quasicrystal" *J. Electronic Materials* **44**, 356 (2015).
- [14] C. R. Otey, W. T. Lau, and S. Fan, Thermal rectification through vacuum. *Phys. Rev. Lett.* **104**, 154301 (2012).
- [15] H. Iizuka, and S. Fan, Rectification of evanescent heat transfer between dielectric-coated and uncoated silicon carbide plates. *J. Appl. Phys.* **112**, 024304 (2012).
- [16] S. Basu, and Francoeur M. Near-field radiative transfer based thermal rectification using doped silicon. *Appl. Phys. Lett.* **98**, 113106 (2011).
- [17] Y. Yang, S. Basu, and L. Wang, Radiation-based near-field thermal rectification with phase transition materials, *Appl. Phys. Lett.* **103**, 163101 (2013).
- [18] P. Ben-Abdallah, and S. A. Biehs, Phase-change radiative thermal diode. *Appl. Phys. Lett.* **103**, 191907 (2013).

- [19] Z. Chen, C. Wong, S. Lubner, S. Yee, J. Miller, W. Jang, C. Hardin, A. Fong, J. E. Garay, and C. Dames. "A photon thermal diode." *Nat. Comm.* **5** (2014).
- [20] C. Y. Tso, and C. Y. H. Chao. "Solid-state thermal diode with shape memory alloys." *International Journal of Heat and Mass Transfer* **93**, 605 (2016).
- [21] P. Ben-Abdallah, and S. A. Biehs. "Near-field thermal transistor." *Phys. Rev. Lett.* **112**, 044301 (2014).
- [22] V. Kubytzkyi, S. A. Biehs, and P. Ben-Abdallah. "Radiative bistability and thermal memory." *Phys. Rev. Lett.* **113**, 074301 (2014).
- [23] K. Ito, K. Nishikawa, and H. Iizuka. "Multilevel radiative thermal memory realized by the hysteretic metal-insulator transition of vanadium dioxide." *Appl. Phys. Lett.* **108**, 053507 (2016).
- [24] S. A. Dyakov, J. Dai, M. Yan, and M. Qiu. "Thermal self-oscillations in radiative heat exchange." *Appl. Phys. Lett.* **106**, 064103 (2015).
- [25] J. Zhu, K. Hippalgaonkar, S. Shen, K. Wang, Y. Abate, S. Lee, J. Wu, X. Yin, A. Majumdar, and X. Zhang. "Temperature-gated thermal rectifier for active heat flow control." *Nano Lett.* **14**, 4867 (2014).
- [26] J. B. K. Kana, J. M. Ndjaka, G. Vignaud, A. Gibaud, and Malik Maaza. "Thermally tunable optical constants of vanadium dioxide thin films measured by spectroscopic ellipsometry." *Opt. Comm.* **284**, 807 (2011).
- [27] E. Rousseau, A. Siria, G. Jourdan, S. Volz, F. Comin, J. Chevrier, and J. J. Greffet. "Radiative heat transfer at the nanoscale." *Nat. Photo.* **3**, 514 (2009).
- [28] S. Shen, A. Narayanaswamy, and G. Chen. "Surface phonon polaritons mediated energy transfer between nanoscale gaps." *Nano Lett.* **9**, 2909 (2009).

- [29] K. Kim, B. Song, V. Fernández-Hurtado, W. Lee, W. Jeong, L. Cui, D. Thompson, J. Feist, M. H. Reid, F. J. García-Vidal, and J. C. Cuevas, "Radiative heat transfer in the extreme near field." *Nature* **528**, 387 (2015).
- [30] R. S. Ottens, V. Quetschke, S. Wise, A. A. Alemi, R. Lundock, G. Mueller, D. H. Reitze, D. B. Tanner, and B. F. Whiting. "Near-field radiative heat transfer between macroscopic planar surfaces." *Phys. Rev. Lett.* **107**, 014301 (2011).
- [31] T. Kralik, P. Hanzelka, M. Zobac, V. Musilova, T. Fort, and M. Horak. "Strong near-field enhancement of radiative heat transfer between metallic surfaces." *Phys. Rev. Lett.* **109**, 224302 (2012).
- [32] T. Ijiri, and N. Yamada. "Near-field radiative heat transfer between two parallel SiO<sub>2</sub> plates with and without microcavities." *Appl. Phys. Lett.* **106**, 023103 (2015).
- [33] M. Lim, S. S. Lee, and B. J. Lee. "Near-field thermal radiation between doped silicon plates at nanoscale gaps." *Phys. Rev. B* **91**, 195136 (2015).
- [34] R. St-Gelais, L. Zhu, S. Fan, and M. Lipson. "Near-field radiative heat transfer between parallel structures in the deep subwavelength regime." *Nat. Nanotech.* (2016).
- [35] B. Song, D. Thompson, A. Fiorino, Y. Ganjeh, P. Reddy, and E. Meyhofer. "Radiative heat conductances between dielectric and metallic parallel plates with nanoscale gaps." *Nat. Nanotech.* (2016).

## *Publications*

### **Journal paper:**

- [1] Kota Ito and Hideo Iizuka, "Highly efficient-1st-order reflection in Littrow mounted dielectric double-groove grating," *AIP Advances*, vol. 3, no. 6, pp. 062119 (2013).
- [2] Kota Ito, Takayuki Matsui, and Hideo Iizuka, "Thermal emission control by evanescent wave coupling between guided mode of resonant grating and surface phonon polariton on silicon carbide plate," *Applied Physics Letters*, vol. 104, no. 5, pp. 051127 (2014).
- [3] Kota Ito, Kazutaka Nishikawa, Hideo Iizuka, and Hiroshi Toshiyoshi, "Experimental investigation of radiative thermal rectifier using vanadium dioxide," *Applied Physics Letters*, vol. 105, no. 25, pp. 253503 (2014).
- [4] Kota Ito, Atsushi Miura, Hideo Iizuka, and Hiroshi Toshiyoshi, "Parallel-plate submicron gap formed by micromachined low-density pillars for near-field radiative heat transfer," *Applied Physics Letters*, vol. 106, no. 8, pp. 083504 (2015).
- [5] 伊藤晃太、松井崇行、飯塚英男、年吉洋、"表面波と結合した回折格子中共鳴モードによる熱輻射制御 ～光学解析と製作法検討～" *電気学会論文誌 E (センサ・マイクロマシン部門誌)*, vol. 135, no. 5, pp. 184-190 (2015).
- [6] Kota Ito, Hiroshi Toshiyoshi, and Hideo Iizuka. "Metal-insulator-metal metamaterial absorbers consisting of proximity-coupled resonators with the control of the fundamental and the second-order frequencies." *Journal of Applied Physics* vol. 119, no. 6, pp. 063101 (2016).
- [7] Kota Ito, Hiroshi Toshiyoshi, and Hideo Iizuka. "Densely-tiled metal-insulator-metal metamaterial resonators with quasi-monochromatic thermal emission." *Optics*

Express vol. 24, no. 12, pp. 12803-12811.

**International conference:**

- [1] Kota Ito, Takayuki Matsui, and Hideo Iizuka, “Thermal Emission Property of Silicon Resonant Grating Positioned above SiC Substrate”, The 2nd International Workshop on Nano-Micro Thermal Radiation: Energy, Manufacturing, Materials, and Sensing (NANORAD2014), Shanghai, China, 6-9 June, 2014, A0063 (oral)
- [2] Kota Ito, Kazutaka Nishikawa, Hideo Iizuka, and Hiroshi Toshiyoshi, “Experimental Observation of Radiative Thermal Rectification Using a Phase-Change Material,” MRS spring meeting, San Francisco, USA, 6-10 April, 2015, M14.11 (poster)
- [3] Kota Ito, Hiroshi Toshiyoshi, Hideo Iizuka, “Proximity-interaction between metamaterial resonators for the control of parasitic modes,” NFO-14: The 14th International Conference of Near-Field Optics, Nanophotonics and Related Techniques, Hamamatsu, Japan, 4-8 September, 2016 (poster)
- [4] Kota Ito, Atushi Miura, Kazutaka Nishikawa, Hideo Iizuka, and Hiroshi Toshiyoshi, “Experimental study on electromagnetic heat transfer: near-field coupling, thermal diode, and thermal information storage,” NFO-14: The 14th International Conference of Near-Field Optics, Nanophotonics and Related Techniques, Hamamatsu, Japan, 4-8 September, 2016 (oral)

**Domestic conference:**

- [1] 伊藤晃太, 松井崇行, 飯塚英男, 年吉洋 : “表面波と結合した回折格子中共鳴モードによる熱輻射制御 ～理論的解析と製作法検討～,” 電気学会 E 部門総合研究会, 東京, 27-28 May, 2014, MSS-14-021 (oral)
- [2] 伊藤晃太, 西川和孝, 三浦篤志, 飯塚英男, 年吉洋 : “二酸化バナジウム薄膜を用いた熱輻射の整流,” 第 52 回伝熱シンポジウム, 福岡, 3-5 June, 2015, G123 (oral)
- [3] 伊藤晃太, 三浦篤志, 西川和孝, 飯塚英男, 年吉洋 : “近接場熱輻射の応用に向けたサブミクロンギャップの形成”, 第 76 回応用物理学会秋季学術講演会, 名古屋, 13-16 Sep, 2015 (oral)
- [4] 伊藤晃太, 西川和孝, 三浦篤志, 飯塚英男, 年吉洋 : “エバネッセント熱輻射の応用に向けたサブミクロンギャップの形成”, 第 32 回センサ・マイクロマシンと応用システム, 新潟, 28-30 Oct, 2015 (oral)
- [5] 伊藤晃太 : “熱ふく射の波長特性・方向・熱量の制御,” 第 53 回伝熱シンポジウム, 大阪, 24-26 May, 2016, 日本伝熱学会特定推進研究特別セッション「エネルギー・環境戦略と特定推進研究による伝熱研究の展開」 (oral)

## *Acknowledgements*

I would like to express my deepest gratitude to my supervisor, Prof. Toshiyoshi. He has guided me to wisdom which is necessary to survive as a professional researcher. A number of comments from his insight have driven this thesis in a bold tone. The discussion with him encouraged me to progress this thesis, especially in the first year of my doctoral course, which was the one of the hardest period in my life. I am very grateful to the committee members, Prof. Fujita, Prof. Takahashi, Prof. Nakamura, and Prof. Mita for their fruitful suggestions to this thesis, which span from the perspective of this thesis to the details. Especially, I would like to thank Prof. Fujita for the discussion of the measurement of near-field radiative heat transfer and coaching me when I was a master student, and Prof. Nakamura for the coursework in RCAST “Proposal”.

I would like to thank all members in Toshiyoshi lab and Fujita lab including Mr. Takahashi, Dr. Han, Dr. Jalabert, Dr. Zhengxi, Mr. Misawa, Mr. Mori, Dr. Higo, Dr. Yamashita, and Mr. Inoue. The discussion with them were fruitful and the chatting relaxed the mood during hard days. I acknowledge Ms. Koizumi for the administrative help in all the steps in the doctoral course. I am also thankful to Dr. Ishida, whose research style encourages me to continue hard experimental trials. I am grateful to the staff in Takeda CR including Prof. Mita, Dr. Lebrasseur, Dr. Sawamura, and Dr. Kubota for their effort for the maintenance. I would like to thank again Prof. Mita for training me when I was a bachelor student.

I am grateful to my colleagues in Toyota Central R&D Labs., Inc. I would like to acknowledge Dr. Iizuka for his support based on the inspiring research strategy, and the

help in the field of electromagnetic analysis. I would like to acknowledge Mr. Nishikawa for the kind cooperation related to vanadium dioxide, and Mr. Miura, Mr. Takahashi, and Mr. Iwasaki for the great support in micromachining. I would like to thank Dr. Matsui for the discussion on the electromagnetic analysis. I am grateful to Dr. Sato for the continuous support to SRD. I am thankful to Dr. Matsunaga, Dr. Tani, Dr. Ohmori, Dr. Mitsukawa, Dr. Takao, and Dr. Nakano for the administrative help. Thanks to Dr. Tanaka for daily discussions.

Finally, I would like to thank my family members. Thanks to my parents for raising me and giving good educations. I would like to thank my wife Masako. Without her, I cannot finish this thesis. My daughter Akane, who was born on this February, gives me lots of energies.

I cannot write down all who help, support, guide, discuss, inspire, and collaborate with me, but I am thankful to all of them. Here I remember again that I am standing on these fruitful support and collaborations.